Metal-Support Interaction and Electrochemical Promotion of Nano-Structured Catalysts for the Reverse Water Gas Shift Reaction

Christopher Panaritis

Thesis submitted to the University of Ottawa

in partial Fulfillment of the requirements for the

Degree of Doctor of Philosophy

Department of Chemical and Biological Engineering

Faculty of Engineering

University of Ottawa

Abstract

The continued release of fossil-fuel derived carbon dioxide (CO_2) emissions into our atmosphere led humanity into a climate and ecological crisis. Converting CO_2 into valuable chemicals and fuels will replace and diminish the need for fossil fuel-derived products. Through the use of a catalyst, CO_2 can be transformed into a commodity chemical by the reverse water gas shift (RWGS) reaction, where CO_2 reacts with renewable hydrogen (H_2) to form carbon monoxide (CO). CO then acts as the source molecule in the Fischer-Tropsch (FT) synthesis to form a range of hydrocarbons to manufacture chemicals and fuels. While the FT synthesis is a mature process, the conversion of CO_2 into CO has yet to be made commercially available due to the constraints associated with high reaction temperature and catalytic stability.

Noble metal ruthenium (Ru) has been widely used for the RWGS reaction due to its high catalytic activity, however, several constraints hinder its practical use, associated with its high cost and its susceptibility to deactivation. The doping or bimetallic use of non-noble metals iron (Fe) and cobalt (Co) is an attractive option to lower material cost and tailor the selectivity of the CO_2 conversion towards the RWGS reaction without compromising catalytic activity. Furthermore, employing nanostructured catalysts as nanoparticles is a viable solution to further lower the amount of metal used and utilize the highly active surface area of the catalyst. Dispersing nanoparticles on ionically conductive supports/solid electrolytes which contain species like O^{2-}, H^+, Na^+, and K^+, provide an approach to further enhance the reaction. This phenomenon is referred to as metal-support interaction (MSI), allowing for the ions to back spillover from the support and onto the catalyst surface. An in-situ approach referred to as Non-Faradaic Modification of catalytic activity (NEMCA), also known as electrochemical promotion of catalysis (EPOC) is used to in-situ control the movement of ionic species from the solid electrolyte to and away from the catalyst. Both the MSI and EPOC phenomena have been shown to be functionally equivalent, meaning the ionic species act to alter the work function of the catalyst by forming an effective neutral double layer on the surface, which in turn alters the binding energy of the reactant and intermediate species to promote the reaction.

The main objective of this work is to develop a catalyst that is highly active and selective to the RWGS reaction at low temperatures (< 400 °C) by employing the MSI and EPOC

phenomena to enhance the catalytic conversion. The electrochemical enhancement effect will lower energy requirements and allow the RWGS reaction to take place at moderate temperatures. Catalysts composed of Ru, Fe and Co were synthesized through the polyol synthesis technique and deposited on mixed-ionically conductive and ionically conductive supports to evaluate their performance towards the RWGS reaction and the MSI effect. The nano-structured catalysts are deposited as free-standing nanoparticles on solid electrolytes to in-situ promote the catalytic rate through the EPOC phenomenon. Furthermore, Density Functional Theory (DFT) calculations were performed to correlate theory with experiment and elucidate the role polarization has on the binding energy of reactant and intermediate species.

The high dispersion of RuFe nanoparticles on ion-containing supports like samarium-doped ceria (SDC) and yttria-stabilized zirconia (YSZ) led to an increase in the RWGS activity due to the MSI effect. A direct correlation between experimental and DFT modeling was established signifying that polarization affected the binding energy of the CO molecule on the surface of Ru regardless of the type of ionic species in the solid electrolyte. The electrochemical enhancement towards the RWGS reaction has been achieved with iron-oxide (FeO_x) nanowires on YSZ. The in-situ application of O^{2-} ions from YSZ maintained the most active state of Fe_3O_4 and FeO towards the RWGS reaction and allowed for persistent-promoted state that lasted long after potential application. Finally, the deposition of FeO_x nanowires on Co_3O_4 resulted in the highest CO_2 conversion towards the RWGS reaction due to the metal-oxide interaction between both metals, signifying a self-sustained electro-promoted state.

Résumé

La production continue d'émissions de dioxyde de carbone (CO_2) provenant des énergies fossiles dans notre atmosphère a conduit l'humanité à une crise climatique et écologique. La conversion du CO_2 en produits chimiques et en carburants de valeur remplacera et réduira le besoin de produits dérivés de combustibles fossiles. Grâce à l'utilisation d'un catalyseur, le CO_2 peut être transformé en un produit chimique de base par la réaction <<reverse water gas shift>> (RWGS), où le CO_2 réagit avec l'hydrogène renouvelable (H_2) pour former du monoxyde de carbone (CO). Le CO agit alors comme molécule source dans la synthèse Fischer-Tropsch (FT) pour former une gamme d'hydrocarbures permettant de fabriquer des produits chimiques et des carburants. Bien que la synthèse FT soit un processus mature, la conversion du CO_2 en CO n'est pas encore commercialisée en raison des contraintes liées à la température de réaction élevée et à la stabilité catalytique.

Le ruthénium (Ru), un métal noble, a été largement utilisé pour la réaction RWGS en raison de sa forte activité catalytique. Cependant, plusieurs contraintes entravent son utilisation pratique, liées à son coût élevé et à sa susceptibilité à la désactivation. Le dopage ou l'utilisation bimétallique de métaux non nobles comme le fer (Fe) et le cobalt (Co) est une option intéressante pour réduire le coût des matériaux et adapter la sélectivité de la conversion du CO_2 à la réaction RWGS sans compromettre l'activité catalytique. En outre, l'utilisation de catalyseurs nanostructurés sous forme de nanoparticules est une solution viable pour réduire encore la quantité de métal utilisée et utiliser la surface hautement active du catalyseur, qui peut être encore améliorée en les dispersant sur un support. La dispersion de nanoparticules sur des supports ioniquement conducteurs/électrolytes solides contenant des espèces telles que O^{2-}, H^+, Na^+ et K^+, permet d'améliorer encore la réaction. Ce phénomène est appelé <<Metal-Support Interaction>> (MSI), permettant aux ions de se répandre du support à la surface du catalyseur. Une approche in-situ appelée <<Non-Faradic Modification of Catalytic Activity>> (NEMCA), également connue sous le nom de <<Electrochemical Promotion of Catalysis>> (EPOC), est utilisée pour contrôler in-situ le mouvement des espèces ioniques de l'électrolyte solide vers et à partir du catalyseur. Les phénomènes MSI et EPOC se sont avérés fonctionnellement équivalents, ce qui signifie que les espèces ioniques agissent pour modifier la fonction de travail du catalyseur en

formant une double couche neutre efficace à la surface, qui à son tour modifie l'énergie de liaison du réactif et des espèces intermédiaires pour favoriser la réaction.

L'objectif principal de ce travail est de développer un catalyseur qui soit hautement actif et sélectif pour la réaction RWGS à basse température (< 400 °C) en utilisant les phénomènes MSI et EPOC pour améliorer la vitesse catalytique. L'effet d'amélioration électrochimique réduira les besoins en énergie et permettra à la réaction RWGS de se dérouler à des températures modérées. Des catalyseurs composés de Ru, Fe et Co ont été synthétisés par la technique de synthèse des polyols et déposés sur des supports mixtes à conductivité ionique et à conductivité ionique afin d'évaluer leur performance vis-à-vis de la réaction RWGS et de l'effet MSI. Les catalyseurs nano-structurés sont déposés sous forme de nanoparticules autonomes sur des électrolytes solides pour favoriser in-situ la vitesse catalytique par le phénomène EPOC. En outre, des calculs de la <<Density Functional Theory>> (DFT) ont été effectués pour corréler la théorie avec l'expérience et élucider le rôle de la polarisation sur l'énergie de liaison des espèces réactives et intermédiaires.

La forte dispersion des nanoparticules de RuFe couplées sur des supports contenant des ions comme le <<samarium-doped ceria>> (SDC) et la <<yttria-stabilized zirconia>> (YSZ) a entraîné une augmentation de l'activité des RWGS en raison de l'effet MSI. Une corrélation entre la modélisation expérimentale et la DFT a été établie, ce qui signifie que la polarisation a affecté l'énergie de liaison de la molécule de CO à la surface du Ru, quel que soit le type d'espèce ionique dans l'électrolyte solide. L'amélioration électrochimique vers la réaction RWGS a été réalisée avec des nanofils d'oxyde de fer (FeO_x) sur YSZ. L'application in-situ d'ions O^{2-} provenant d'YSZ a permis de maintenir l'état le plus actif de Fe_3O_4 et FeO vers la réaction RWGS et a permis un état persistant qui a duré longtemps après l'application potentielle. Enfin, le dépôt de nanofils de FeO_x sur du Co_3O_4 a entraîné la conversion de CO_2 la plus élevée vers la réaction RWGS en raison de l'interaction métal-oxyde entre les deux métaux, ce qui signifie un état électro-promu autonome.

Statement of Contributors of Collaborators and Co-Authorship

I hereby declare that I am the sole author of this thesis.

Chapter 1, and 2 were solely authored by myself and editorial comments by Prof. Elena Baranova.

Chapter 3 was written by me with editorial comments by Prof. Elena Baranova. The synthesis, catalytic setup, EPOC experimentation were conducted by me. Catalyst characterization was performed by Dr. Martin Couillard.

Chapter 4 was majority written by me with editorial comments by Dr. Carine Michel and Dr. Steinmann from Ecole Normal de Superior (ENS) de Lyon in Lyon, France and Prof. Elena Baranova. The synthesis, catalytic setup, EPOC experimentation were conducted by me. The experimental work was assisted by the undergraduate thesis student Kiran Patel. Density Functional theory (DFT) calculations were performed by me at ENS. Catalyst characterization was performed by Dr. Martin Couillard.

Chapter 5, was done in collaboration with PhD candidate Dimitrios Zagoraios (co-authorship) and editorial comments by his supervisor's Prof. Katsaounis and Prof. Vayenas from the Laboratory of Chemical and Electrochemical Processes (L.C.E.P.) in the University of Patras in Patras, Greece and Prof. Baranova. Experimental work was assisted by undergraduate students Katrina Krassakopoulou and Homer Giagousis.

Chapter 6 was written by me with editorial comments by Prof. Elena Baranova. The synthesis, catalytic setup, EPOC experimentation were conducted by me. The experimental work was assisted by the Master of Engineering (M.Eng) students Johnny Zgheib and Sayed Ebrahim. Catalyst characterization was performed by Dr. Martin Couillard.

Chapter 7 was written by me with editorial comments by Prof. Elena Baranova. The synthesis, catalytic setup, EPOC experimentation were conducted by me. The experimental work was assisted by M.Eng student Johnny Zgheib. Catalyst characterization was performed by Dr. Martin Couillard.

Chapter 8 was written by me with editorial comments by Prof. Elena Baranova. The synthesis, catalytic setup, EPOC experimentation were conducted by me. The experimental work was assisted by the M. Eng student Shuo Yang. Catalyst characterization was performed by Dr. Martin Couillard.

Acknowledgements

I would like to thank *Professor Elena A. Baranova* for selecting me as a Master and Ph.D. student to further gain experience in combating the climate crisis through innovated design to utilize carbon dioxide. She granted me the opportunity to explore my own ideas, come up with new ideas together and collaborations. I have a learned a great deal under her supervision which has strengthened my passion in developing sustainable technologies, in research and development were greatly enhanced due to this experience.

Thank you to *Dr. Carine Michel* and *Dr. Stephan Steinmann* who taught me how to perform density functional theory (DFT) calculations and granted me the opportunity to examine catalytic reactions at an atomic perspective. Thank you to *Dr. Martin Couillard* who is a co-author in all my publications, who provided beautiful STEM images for the variety of synthesized nano-structured catalysts. I would like to thank *Prof. Alexandros Katsaounis* and *Prof. Constantinos Vayenas* from the University of Patras in Patras, Greece, who hosted me for two months in the Laboratory of Chemical and Electrochemical Processes. It was unforgettable experience to work under the supervision of the founder of the EPOC effect. A special thanks to the laboratory, friendships and co-author *Dimitris Zagoraios* for the memories that I made during the short time period. Thank you to the past, present and future lab co-workers and friends *Evans Monyoncho*, *Natalia Alzate-Carvajal* (& David), *Yasmine Hajar*, *Mohamed Houache*, *Emily Cossar*, *Niloofar Aligholizadeh*, *Najmeh Ahledel*, *Arash Fella Jahromi*, *Asma Shubair,* and *Ju Wang*. Thank you to everyone else I had the pleasure of befriending (especially in D218) at the University of Ottawa.

A huge thank you to my Ottawa family (*i.e.* originally Lavalers) Vanessa, Marko, Steph and Orad, and Christine, who not only was great company and friends, but made my Ottawa experience feel like home. A tremendous thank you to my main visitors, friends turned family (*ie.* Koumbs) Nick/Niko, Anthoula, and Marianne, who were by my side throughout this degree and encourage me throughout the way. A special thank you to my cousin Eleni who helped me with my presentation and organization skills and supporting me along the way. And thank you to all my family and friends for the support.

Finally, and certainly not least, my parents Voula and George, and my brother Nico. Without their guidance and support, this degree would not have been possible. This thesis is for you.

Table of Contents

List of Figures

Nomenclature

ADF	Annular Dark-Field
ASF	Anderson-Schulz-Flory
BE	Binding Energy
CCS	Carbon Capture and Storage
CCU	Carbon Capture and Utilization
CE	Counter Electrode
CV	Cyclic Voltammetry
DFT	Density Functional Theory
EDX/EDS	Energy Dispersive X-ray
EELS	Energy Electron Loss Spectrometry
EG	Ethylene Glycol
EPOC	Electrochemical Promotion of Catalysis
FT	Fischer-Tropsch
FTIR	Fourier Transform Infrared
FWHM	Full-Width at Half Maximum
GDC	Gadolinium-doped Ceria
GHG	Greenhouse Gas
GHSV	Gas Hourly Space Velocity
HAADF	High-Angle Annular Dark-Field
ICP-ES	Inductively-Coupled Plasma Emission Spectroscopy
IPPC	Intergovernmental Panel on Climate Change
MIEC	Mixed Ionic-Electronic Conducting
MS	Mass Spectrometer
MSI	Metal-Support Interaction
NEMCA	Non-Faradaic Electrochemical Modification of Catalytic Activity
NP	Nanoparticle

p-EPOC	Permanent/Persistent EPOC
O.C.	Open-circuit
RE	Reference Electrode
RLS	Rate Limiting Step
RWGS	Reverse Water Gas Shift
SDC	Samarium-doped Ceria
SEM	Scanning Electron Microscopy
SMSI	Strong Metal-Support Interaction
SSA	Specific Surface Area
STEM	Scanning Transmission Electron Microscopy
TEM	Transmission Electron Microscopy
TGA	Thermogravimetric Analysis
TOF	Turnover Frequency
TPD	Three-Phase Boundary
VASP	Vienna Ab-ignition Simulation Package
WE	Working Electrode
WF	Work Function
WGS	Water Gas Shift
XPS	X-Ray Photoelectron Spectroscopy
XRD	X-Ray Diffraction
YSZ	Yttria-Stabilized Zirconia

List of Symbols

A	Pre-exponential factor
D	Dispersion
d	Average Particle Size
E_a	Activation Energy
F	Faraday's constant
I	Current
i	Current density
k_A	Equilibrium constant of electron acceptor
k_D	Equilibrium constant of electron donor
p_A	Partial pressure of electron acceptor
p_D	Partial pressure of electron donor
Q	Charge
r	Closed-circuit catalytic rate
r_o	Open-circuit catalytic rate
SA_{NP}	Surface area of the nanoparticle
T	Reactor temperature
U	Cell potential
U_{WR}/V_{WR}	Catalyst-working electrode potential
V_{NP}	Volume of nanoparticle
W	Weight of catalyst

List of Greek Symbols

γ	Permanent/persistent EPOC
γ -Al_2O_3	Gamma-alumina
Λ	Apparent Faradaic efficiency
ρ	Rate enhancement ratio
τ	Time constant

Chapter 1 : Literature Review

1.1 Rationale for CO_2 Utilization

The ever-growing use of fossil fuels for anthropogenic energy needs has led to the release of greenhouse gases (GHG) into the atmosphere resulting in effects of climate change and ocean acidification [1–3]. GHGs consist of water vapor (H_2O), carbon dioxide (CO_2), methane (CH_4), nitrous oxide (N_2O) and ozone (O_3) [4]. Among these emissions, carbon dioxide (CO_2) makes up two-thirds of the total, significantly influencing the greenhouse gas effect in radiating heat back to Earth. Since 2002, the concentration of CO_2 has increased by 35% worldwide at a rate of 2.0 ± 0.1 ppm per year [1,5,6]. CO_2 is a very stable molecule that retains heat and remains in the atmosphere for over 200 years [2,7]. This entrapment of heat leads to the greenhouse effect, radiating heat back to the Earth's surface overall increasing global temperature. While this effect is crucial for life on Earth in maintaining a certain temperature, emissions from fossil fuel sources has led to an excess of CO_2 being released at a much faster rate than can be utilized by natural processes like photosynthesis and ocean absorption. In 2015, the global Paris climate agreement was adopted by most countries in an effort to limit the increase in global temperature to 1.5 °C before the end of the century, by reducing overall CO_2 emissions [5]. As of July 2020, efforts seem futile since the largest CO_2 concentration of 414 ppm was recorded [8,9]. It is believed that a temperature increase above 2 °C will result in irreversible consequences on the planet. Current strategies include improving energy efficiency, increase use of renewable energy and capturing and utilizing CO_2 [2,10–12].

In order to achieve this goal, energy sources must move away from fossil fuels and towards renewable and carbon-neutral sources. Currently, renewable energy is dependent on weather, geographical location and battery storage. Renewable technology is constantly improving; however, at the moment it is unable to compete and fully replace fossil fuel energy. Therefore, the implementation of CO_2 capture from fossil fuel combustion is on the rise to reduce emissions until renewable energy is improved [10]. The environmental issue with this method is that it still relies on fossil fuels for energy needs, thus the ideal scenario should consist of CO_2 being separated directly from air. As renewable energy in the form of electricity continues to dominate in residential and industrial sectors, there lacks a viable fossil-free energy source for transportation. For example, alternatives like biofuel and hydrogen are still a long way from replacing fossil fuels,

since they require engine modification, storage, and further research and development for the opportunity to become economically viable [13,14]. Thus, current research is focused on mitigating CO_2 through carbon capture and storage. However, storing the carbon in a location where it can be inert is the major issue with this technology [1]. The suggested solution is to store it in depleted fossil fuel reserves, but some experts worry that earthquakes and other natural events can cause it to escape into the atmosphere in dangerously high concentrations. Thus, an ideal method for decarbonization is through the utilization of CO_2 to create useful chemicals in the form of synthetic fuel to accommodate with transportation needs [2,7,14,15].

Various methods exist in utilizing CO_2, however most of them are currently in the laboratory and pilot phase [16]. Large scale processes that are currently using CO_2 are in enhanced oil recovery, in carbonated beverages and as feedstock for agriculture. Currently research is focused on storing CO_2 through the process of mineralization where it can be used to make calcium carbonate and cement, but this makes it unavailable for further use [17]. Finally, the research involved in converting CO_2 into valuable chemicals like synthetic fuel is being effectively studied to determine the best suitable way to scale it up. Ideally, in the near future larger scale CO_2 separators will be able to efficiently obtain CO_2 from the air and not from fossil fuel combustion sources.

A promising solution to this pressing issue is to treat CO_2 as a resource by reacting it with hydrogen (H_2) to produce high-value chemicals, plastics and fuels [10,12,18], which can be applied in future human exploration missions to Mars [19]. When paired with energy provided by renewable energy sources (*i.e.* wind, hydro, solar, etc.), will lead to a carbon-neutral energy source that will allow vehicles and infrastructures that depend on fossil fuel sources to continue to be employed [20,21]. The advancements can be applied to make a profit economically, provide eco-conscious opportunity for consumers and of course lead humanity into a sustainable future [22].

1.2 CO_2 Hydrogenation

CO_2 is a highly stable molecule that requires a large amount of energy usually in the form of heat and/or electricity to be transformed from one form to another [23,24]. Since it is a highly oxidize molecule it must be reduced with a hydrogen source to be transformed. To overcome the large thermodynamic barriers, the conversion of CO_2 is possible through the use of a catalyst, which increases the chemical rate of reaction by reducing the activation energy allowing the

conversion to reach theoretical values [25,26]. A catalytic reaction can be a homogeneous where the catalyst and reactants are in the same phase (*i.e.* liquid reactants and liquid catalyst) or heterogeneous, where the reactants and catalyst occur in different phases (*i.e.* gas reactants and solid catalyst) [26]. Undertaking a heterogeneous catalytic reaction is much more beneficial since it allows for easy separation of catalyst and products, and overall, more ideal for the gaseous conversion of CO_2 into valuable chemicals. Additionally, the catalyst is not consumed once the reaction is complete, allowing it to be used again

The conversion of CO_2 is achieved through a hydrogenation reaction, where it is reacted with hydrogen (H_2) to yield various chemicals. Hydrogen is not a feasible feedstock to obtain since it is not found in nature, therefore it must be removed from a compound, like hydrocarbons and/or water. A mature process of producing hydrogen is done through the steam reforming of hydrocarbons, which is obtained from non-renewable energy sources [27]. In efforts to reduce dependence on fossil fuel sources, H_2 is currently being optimized to be developed using renewable sources for the electrolysis of water [28–30]. Thus, use of the most abundant resource on Earth – water, is electrolytically split into H_2 and O through the application of an electrical current. This is advantageous since energy obtained from renewable sources like hydro, wind and solar is sufficient to undertake the reaction. Electrical energy is stored in the form of chemical energy in the H_2 molecule, which can be used for off-peak periods in fuel cells and/or to reduce CO_2. As this process is still in development and is not at the stage that it can be industrially available, it can provide promising results for CO_2 hydrogenation and H_2 fuel cells in the near future.

CO_2 hydrogenation reactions can be selective in end-products by altering the parameters of pressure, temperature, amount of H_2, catalysts size and other various others [31]. Typical CO_2 hydrogenated end-products that can be produce with high selectivity include CO and CH_4 and CH_3OH obtained by the reverse water gas (RWGS) reaction, methanation and methanol synthesis, respectively. The end-products are useful in multiple applications since they can be used as feedstock to further be processed into chemicals and hydrocarbons. The overall CO_2 hydrogenation reaction for the synthesis of hydrocarbons is related to the following equation:

$$xCO_2 + \left(2x - z + \frac{y}{2}\right) H_2 \rightarrow C_x H_y O_z + (2x - z) H_2 O \qquad 1\text{-}1$$

Direct conversion of CO_2 into long chain hydrocarbons of CH-CH (*i.e.* z=0) is difficult since multiple reactants and products are taking place, making it difficult to construct a catalyst that is able to build CH bonds with incoming CO_2. However, following eq. 1-1, C_1 hydrocarbons CH_4 (x=1, y=4, z=0) and CH_3OH (x=1,y=4, z=1) can be produced. The methanation and methanol synthesis reactions are displayed in further detail in eq. 1-2 and 1-3.

$$CO_2 + 4H_2 \rightarrow CH_4 + 2H_2O, \Delta H = -49.5\ kJ\ mol^{-1} \quad 1\text{-}2$$

$$CO_2 + 3H_2 \rightarrow CH_3OH + H_2O, \Delta H = -167.0\ kJ\ mol^{-1} \quad 1\text{-}3$$

The methanation reaction, is an exothermic reaction which directly produces methane by reacting 4 molecules of H_2 with 1 of CO_2. The methane produced can be used as an energy storage system for excess energy generated by renewable energy to later be used as synthetic natural in periods of need. However, the combustion of methane is difficult and often results in a portion of unburnt methane into the atmosphere [32]. Methanol can be used in a similar manner, with the advantage in being utilized in transportation, either mixed with gasoline or be applied in a direct fuel cell. However, use in a direct fuel is challenging since the technological advancement is not fully optimized. Finally, aimed to produce high-value fuels the RWGS reaction is a promising chemical reaction which reacts CO_2 and H_2 to produce CO and water (H_2O), as displayed in eq. 1-4.

$$CO_2 + H_2 \leftrightarrow CO + H_2O, \Delta H = 42.1\ kJ\ mol^{-1} \quad 1\text{-}4$$

The RWGS reaction is an endothermic reaction that requires a high temperature to allow for the cleavage of the double bond between the carbon and oxygen atom [16,33]. Unlike the previous reactions, the RWGS requires a 2 e^- transfer of one mole of each reactant to produce one mole of CO and one mole of H_2O. Further hydrogenation of CO with H_2, or synthetic gas (or syngas) through the Fischer-Tropsch (FT) synthesis reaction leads to the production of hydrocarbons. The FT reaction is displayed in eq. 1-5 [34].

$$(2n + 1)H_2 + nCO \rightarrow C_nH_{2n+2} + nH_2O \quad 1\text{-}5$$

The value of *n* can be increased to produce longer hydrocarbon chains, depending on the desired end refined product (*i.e.,* gasoline, diesel, etc.). The FT reaction is a well-known, mature process developed during the industrial revolution to produce liquid fuels from syngas ($CO:H_2$ ratios of 1:1 to 1:2) through the gasification of fossil fuels [2,10,27]. Pairing the RWGS reaction with the FT reaction to convert CO_2 obtained from carbon capture and H_2 from water electrolysis offers a

promising solution in reducing climate change effects and solving transportation needs [35]. For the overall process to be carbon neutral, the conversion reactions and production of H_2 must run on renewable energy; otherwise it is counterproductive [12].

Initially the FT process was developed to combat the shortage of fuel and now it used in South Africa (Sasol One) to produce fuel relying on coal as the source of carbon to produce syngas [36]. Even though this technology is mature, it is not sustainable to rely on fossil fuels to produce a carbon fuel, since it releases a large number of harmful greenhouse gas emissions in the process. The FT follows the Anderson-Schulz-Flory (ASF) distribution, which determines the hydrocarbon chain formation [16]. The same metals as the RWGS can be used; Ru, Co and Fe are employed to undertake the FT process, however typically Co and Fe are the preference of choice [20,37]. Research is aimed to tailor transportation hydrocarbons like gasoline, jet fuel, and diesel fuel which are limited by their theoretical ASF distribution of 48, 41, and 40%, respectively [38,39].The ideal pathway will be to directly hydrogenate CO_2 which requires a multifunctional catalyst able to reduce CO_2 and then hydrogenated CO into hydrocarbons. Regardless, the initial mechanism requires CO_2 to be split first into CO to commence the C-C chain growth. Thus, examining the catalysts for the RWGS will provide insight on the initial, indirect pathway to manufacture hydrocarbons.

1.3 Reverse Water Gas Shift (RWGS) Reaction

Extensive work has been carried out in determining a suitable catalyst for the RWGS reaction [2,7,40]. The ideal RWGS catalyst should be highly active in converting CO_2, selective to CO formation and display a high thermal stability for prolonged periods. Given that the RWGS is an endothermic reaction, it requires high temperatures ranging from 300 to 800 °C for sufficient conversion to take place, depending solely on thermodynamic processes. The high operating temperature is the major drawback in the RWGS reaction, which is why it is difficult to rely on renewable energy to run the reaction on an industrial level without having to improve the reaction conditions and setup. The equilibrium constant for the RWGS reaction was determined by Twigg [41] and Smith et al., [42] which summarize the calculations to calculate the equilibrium constant of the water gas shift reaction. Taking the reciprocal of the water gas shift (WGS) reaction equilibrium determines the RWGS equilibrium constant (K_{eq}) (eq. 1-6) and eq. 1-7 displays the Z value.

$$K_{eq} = \frac{1}{\exp(-0.29353 * Z^3 + 0.63508 * Z^2 + 4.1778 * Z + 0.31688)} \quad 1\text{-}6$$

$$Z = \frac{1000}{T} - 1 \quad 1\text{-}7$$

Figure 1-1 displays the thermodynamic limitation of the RWGS reaction for corresponding the CO_2:H_2 ratios ranging from 1:1 – 1:7 as calculated by eq. 1-6 and 1-7, following an improvement in conversion with an increase in H_2 in the feed and temperature from 200-800°C. At 800 °C it is observed that the maximum conversion achieved is ~90%, increasing further will almost reach full conversion, however it is not ideal conditions in terms of the energy required, catalyst stability and reactor design. Thus, attaining theoretical conversion at lower temperatures is more sustainable.

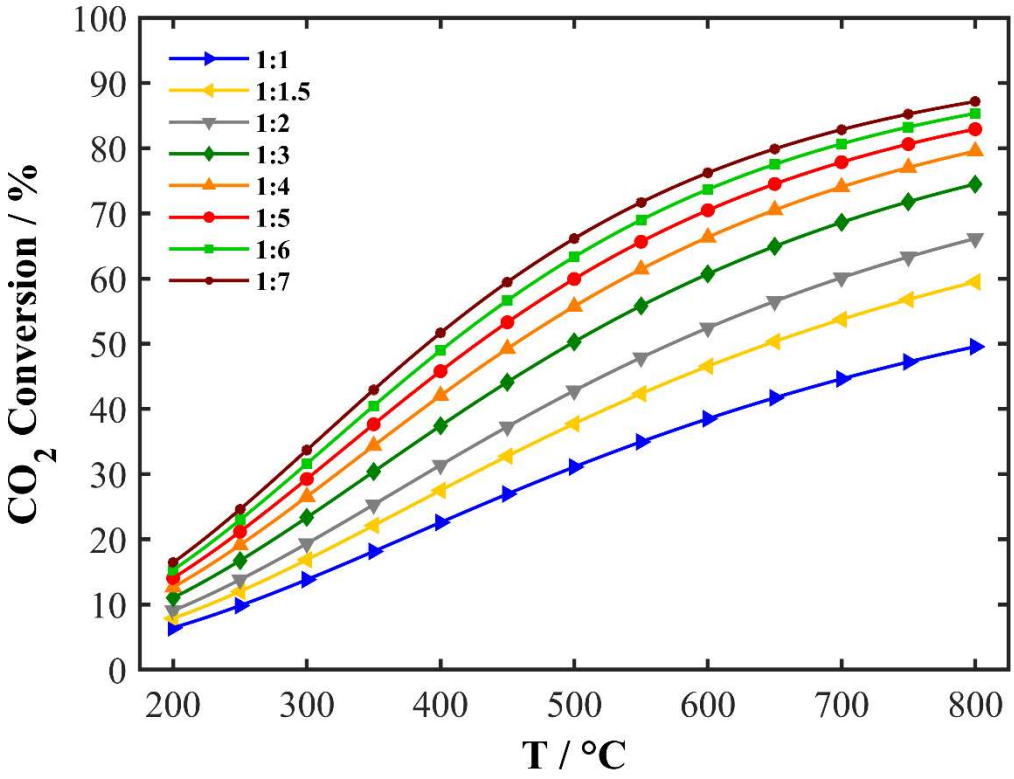

Figure 1-1. RWGS equilibrium constants as a function of temperature for the CO_2:H_2 ratios of 1:1, 1:1.5, 1:2, 1:3, 1:4, 1:5, 1:6 and 1:7.

1.4 Catalysts & Supports

A typical heterogeneous catalyst consists of metal or metal oxide dispersed on a support to increase the number of active sites, improve gas diffusion, increase resistance to attrition, and improve thermal conductivity [25]. Catalytic reactions typically take place on the surface of the metal, while the bulk of the metal is bypassed by the reaction. Employing nanostructured catalysts can greatly enhance the catalytic rate due to the increase of its surface-to-volume ratio ensuring only the surface is utilized [26]. Additionally, with nanostructured catalysts the amount of material used is greatly reduced without compromising the catalytic activity and sometimes enhancing the rate. Furthermore, in terms of the RWGS reaction, nano-structured catalysts have shown to be highly selective to CO production and inhibit the selectivity to CH_4 [43]. This is due to the change in catalyst structure which does not favour the further hydrogenation of CO into CH_4 [43]. Thus, allowing several techniques that can be employed to favour the RWGS reaction and increase its catalytic activity.

1.4.1 *Noble Metals*

Noble metals such as platinum (Pt), rhodium (Rh) and ruthenium (Ru) have been successfully used in the RWGS reaction and display CO_2 conversions close to equilibrium [44–50]. They are advantageous over transition metals since they typically do not exhibit coke deposition and CH_4 formation does not occur passed 500 °C [45]. Pt catalysts are most widely used due to their ability to be easily reduced by H_2 and form CO as their product [44,45,51]. The main issue with noble metals is their high cost and low availability. Ru is the most economical amongst the noble metals, and has shown to display catalytic activity similar to Pt, but is favourable in CH_4 formation [47,52,53]. Additionally, it accounts for several oxidation states that exhibit high electron transfers, making it a suitable candidate for CO_2 hydrogenation [26]. Thus, the properties of the catalyst are altered through its change in size, by increasing its dispersion and favouring the exposure of active sites for CO formation. One study performed by Kwak *et al.*, [54] show that increasing the loading of Ru supported on Al_2O_3 to 5 wt.% tailors its selectivity to CH_4 (>80%), while decreasing the loading to 0.1 wt.% highly favours CO (>80%). They concluded that above 1 wt.% Ru agglomerated into larger clusters that tailor the further hydrogenation of CO_2 into CH_4, while less than 1 wt.% highly dispersed Ru nanoparticles or even atomic Ru favours CO desorption. Thus, the more highly dispersed and smaller particle size, the less likelihood of CO being further hydrogenated into CH_4.

1.4.2 *Non-Noble Metals*

Many non-noble metals have been studied for the RWGS reaction and each exhibit some sort of concern. Transition metals like copper (Cu), nickel (Ni), and cobalt (Co) are commonly used in the water gas shift (WGS) reaction due to their high activity in the forward direction and have been extensively studied for the reverse direction [55–61].The main challenges in dealing with these inexpensive metals are lower conversion rates, selectivity to CH_4, coke deposition and stability issues [51,60,62]. Cu has shown to display poor activity since the particles tend to agglomerate, lowering their stability and increasing their deactivation rate [56]. To deal with the issue of thermal stability, it was observed that when iron (Fe) was combined with Cu, its stability was improved, allowing for a stable conversion for long periods, eventually deactivating before 100 hours [56,61]. For Cu and Ni, coke deposition rates are typically proportional to increases in temperature. The conversion rate is therefore limited by operating at lower temperatures to avoid a buildup of coke, thereby deactivating the catalyst. Ni exhibits similar properties to noble metals but displays lower catalytic activity and is more prone to methane formation [58,63]. Co is a well-known catalyst for the Fischer-Tropsch process in converting CO into long-chain hydrocarbons, on its own it does react with CO_2 however with the addition of a metal that can adsorbed CO_2, direct hydrogenation into fuels can be possible [60,64]. Yin *et al.*, [65] studied a Co-CoO_x core-shell catalyst which displayed high selectivity (>96%) and CO_2 conversion affiliated to the interactions at the Co-CoO interface and that the CoO shell enhanced the adsorption and activation of CO_2, while the metallic core Co functioned as a site for H_2 adsorption and activation. Continued research is being done to optimize the performance of transition metal catalysts in order to benefit from their abundance and price when compared to noble metals.

Iron, one of the most abundant and economical metal, is the typical catalyst used for the Fischer-Tropsch synthesis of producing hydrocarbon fuels from syngas (mixture of CO + H_2) and the water gas shift reaction [66]. However, when compared with noble metals its catalytic activity is inferior, but where it lacks in activity, it is superior in thermal stability and affordability [67]. Recent studies have demonstrated that iron-based catalysts are efficient for the RWGS reaction [57,68–70]. Fe-oxide's activity is due to an existence of several activation states of iron: Fe_2O_3, Fe_3O_4, FeO and Fe acting as oxygen storage exchange reservoir, cycling through redox reactions induced in the presence of CO_2 and H_2 [71,72]. Kim *et al.,* studied the RWGS reaction using unsupported Fe-oxide nanoparticles with a CO_2 conversion close to equilibrium and long-term

stability at 600 ºC that was not studied at lower temperatures. Wenzel *et al.,* have studied the oxygen storage effect of FeO_x and how it can be feasibly cycled between redox reactions [73]. Among the transition metals, Fe has shown to have the highest CO_2 adsorption energy, as determined through DFT studies for Fe (face-centered cubic) [67]. Furthermore, proven through temperature programmed reduction (TPR) studies, iron-oxide has shown to be able to reduce to FeO between 320-340 ºC due the increase in H_2 dissociation that is able to spillover and reduce the FeO_x bulk [33,74–76].

1.4.3 *CO_2 Hydrogenation Mechanism for Late Transition Metals*

The CO_2 hydrogenation mechanism for late transition metals has been proposed to be catalyst dependent and can vary from three pathways observed from Fourirer-transform infrared (FTIR) spectroscopy and Density Functional Theory (DFT) studies [77,78]. The CO_2 hydrogenation mechanism has been performed by Avanesian *et al.*, [77] where Ru(0001) slab was used to undertake the reaction, since it's the most active metals for the CO_2 hydrogenation and can be evaluated as its reduced metallic state.

The potential energy diagram of the pathway and corresponding mechanism is displayed in Figure 1-2 as purposed by Avanesian *et al.* [77]. The first pathway is direct CO_2 hydrogenation, where CO_2 interacts with dissociated H* (adsorbed species denoted by the asterisk) to form COOH*, followed by its dissociation into CO* and OH*. Thus, CO can be desorbed and OH* can be further reduced into H_2O to follow the RWGS reaction. The second pathway typically observed follows the dissociation of CO_2 into CO* and O*, where CO* is directly hydrogenated to follow the CO methanation pathway to yield CH_4 or other CH_x products. Finally, the less common pathway is the direct dissociation of CO_2 into CO*, followed by CO* dissociation to C* and further hydrogenation to CH_x compounds [77]. The latter is less likely to occur, since two sets of double carbon bonds must be cleaved, which is very energy intensive. In all cases, the binding energy of CO* is the rate limiting step (RLS) which governs the selectivity of the final product by either desorbing as CO or remaining binded to the surface to be further hydrogenated into CH_x compounds. Overall, evaluating the mechanism through DFT calculations allows the opportunity to comprehend how end-product selectivity varies from catalyst-to-catalyst and aims at developing methods to improve the catalytic reaction. To further comprehend the CO_2 hydrogenation mechanism on a specific metal, DFT calculations using the Ru(0001) surface have been evaluated, accurately depicting Ru nanoparticles (<10 nm) for CH_4 and CO yields [77,78]. It was observed

that for the Ru(0001) surface, the hydrogenation mechanism favours the direct CO_2 hydrogenation pathway over the direct hydrogenation into COOH* or HCOO*. Avanesian *et al.,* determined that the RLS for both the RWGS and methanation reaction for Ru(0001) depends on the desorption tendency of CO*, usually governed by the reaction conditions (*i.e.* CO_2:H_2 ratio, temperature and pressure) [77].

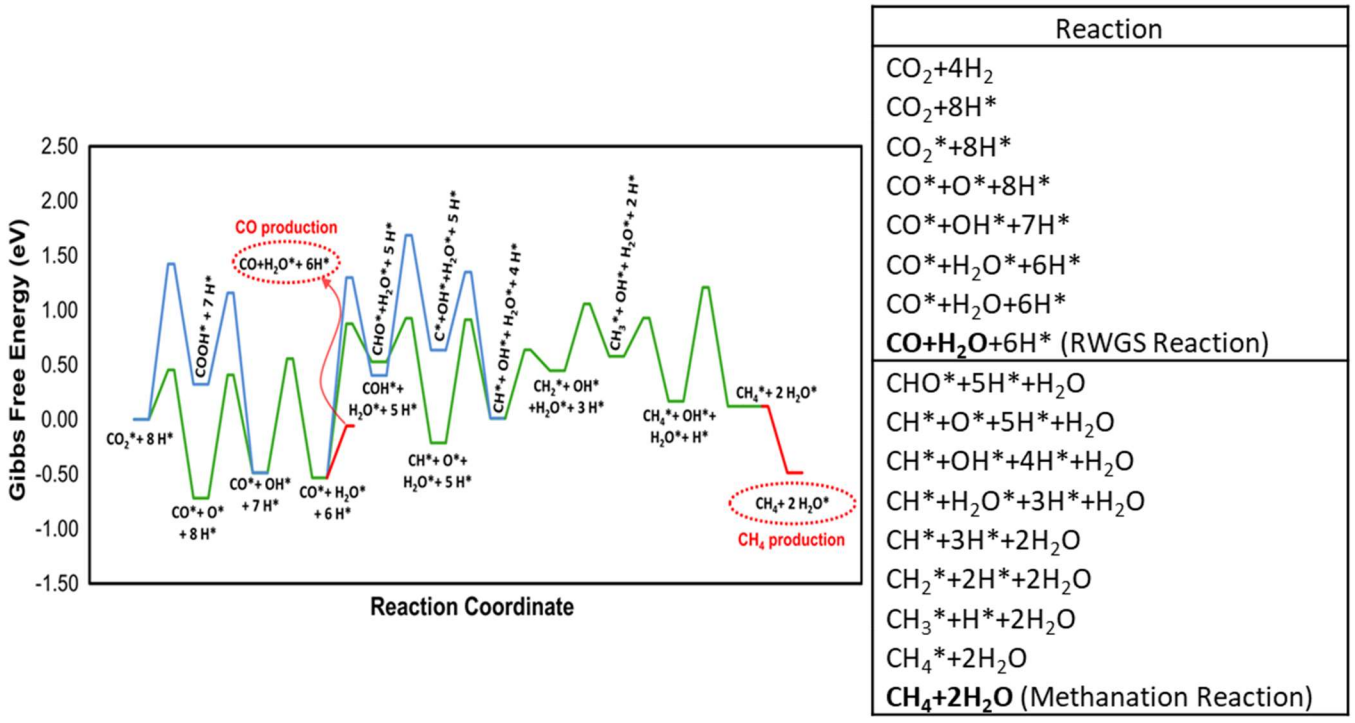

Figure 1-2. Potential energy diagram and corresponding reaction mechanism depicting the CO_2 hydrogenation pathway on Ru(0001) for the production of CO and CH_4. Reprinted with permission from [77]. Copyright Elsevier 2016.

1.5 Promotion in Catalysis

The performance of all forms of catalytic reactions can be improved through the addition of electronic promoters. Common promoters include potassium (K) and sodium (Na), which are added in during the synthesis preparation [79]. K has been shown to decrease the rate of sintering and increase overall the stability when paired with Pt since it creates new active sites for the reaction to take place [7,80,81]. Addition of Na to noble metal catalysts have shown to suppress CO_2 methanation and favour the RWGS reaction [51,82]. Methanation is suppressed in basic conditions and promoted in acidic conditions since the chemisorption of CO_2 increases, while that

of H_2 decreases [83]. Structural promoters affect the formation and stabilization of the catalysts active phase resulting in a superior distribution of NPs over the support [7,79]. The addition of Na results in a structural promotion effect that blocks the surface sites at which methanation takes place, or the location where subsequent carbon hydrogenation into CH_4 occurs.

1.5.1 *Metal-Support Interaction Effect*

It is well known that the catalytic activity of a catalyst depends on many factors: particle size, size distribution, catalyst dispersion, surface and bulk composition, and the nature of the support [26]. The latter is known as the metal-support interaction (MSI) effect [84–86]. The MSI can be tailored to enhance the RWGS reaction through the selection of the metal and support used and the catalyst preparation method. Dispersion of the metal catalyst on a support greatly increases the surface to volume ratio and in turn increases the number of active sites available for the reaction. Due to the increase in the number of exposed sites, the loading amount of active catalyst on support can be reduced to 5 wt.% or less, because more than has not shown to drastically change performance [44]. Most common catalyst supports include aluminum oxide (Al_2O_3), silica (SiO_2), and activated carbon, which simply function as structural supports to enhance the exposure of active sites [59]. Additionally, the support reduces the rate at which at which the metal deactivates since it stabilizes them against agglomeration, thermal sintering and improvement in thermal conductivity [25].

The use of mixed ionic-electronic conductive (MIEC) oxide supports such as ceria (CeO_2), titania (TiO_2) samarium doped ceria (Sm-CeO_2 or SDC), beta-alumina (β-Al_2O_3), and ionically conductive yttria-stabilized zirconia (YSZ) have been on the rise since they enhance the MSI effect [86,87]. MIEC ceramics entail a balance of ionically and electronically conductive properties. They are typically used in fuel cells to act as membrane to conduct electrons or protons from the cathode to the anode. The relationship between metal and oxide support results in a bifunctional relationship at the metal-oxide interphase which increase the number of active sites and alters the binding strength of reactant and intermediate species [54,76,88]. Promotional species, like O^{2-} in the case of CeO_2 and YSZ migrate from the support onto the surface of the catalyst, altering the catalyst work function and in turn the chemisorption energies of the reactant and intermediate species [89–92]. This effect occurs for nanoparticles of < 5 nm that allow O^{2-} to migrate the short nanoparticle distance through an increase temperature [84,90,93–95]. Thus, the MIEC and

ionically conductive supports do not only provide support but takes part in the reaction by their promoting species that can be regenerated by the reactants in the feed.

1.5.2 *Oxygen Conducting Supports*

The redox reaction induced through the metal-support interaction between deposited metal nanoparticles on mixed-ionic (CeO_2, TiO_2, ZrO_2, perovskites) and ionically conductive (YSZ) oxygen supports has been shown by various authors to be the main reason for the increase in catalytic activity [96]. CeO_2 has been proven to be an active support for the RWGS due to its high reducibility, high ability to adsorb CO_2 and its high oxygen ion (O^{2-}) conductivity [59,91,92,97,98]. Oxygen vacancies for CeO_2 are created through redox cycles between Ce^{4+} and Ce^{3+} where the vacancies act as storage and release sites. The mechanism follows a reduction-oxidation process which requires the presence of both reactants (i.e. CO_2 and H_2) [99]. Nolan *et al.* determined that the activity of ceria is due to an oxygen hopping mechanism where one O molecule from CO_2 fills up the oxygen vacancy resulting in CO desorption, and two H molecules adsorbs to the O molecule to produce H_2O [100]. The first step consists of H_2 adsorption on the supported metal, which dissociated H_2 into H* (where * denotes adsorbed species). Following its dissociation H spillovers to CeO_x, adsorbing on O forming O-H*, followed by the reduction of another H* to form H_2O*. H_2O* then desorbs from the surface leaving behind an oxygen vacancy in the lateral structure of the support freeing up a location for CO_2 to adsorb and oxidize [101]. One of the double bonds from CO_2 forms a lock and key process filling up the vacancy and cleaving the double bond to form CO. The cycle then repeats itself all over again. Thus, the removal of surface oxygen to an oxygen vacant site (O_v) allows for a site for CO_2 to reduce, following a mechanism (eq. 1-8 and 1-9) proposed by various authors [99,102].

$$2H^* + CeO_2 \rightarrow H_2O + O_{v\,CeO2-\delta} \quad 1\text{-}8$$

$$CO_2 + O_{v\,CeO2-\delta} \rightarrow CO + CeO_2 \quad 1\text{-}9$$

Where $O_{v\,CeO2-}$ represents the oxygen vacancy in CeO_2.

There is a consensus on the high catalytic activity of CeO_2 attributed to the generation of oxygen vacancies which are the reason for the high activity. Doped-ceria results in a structural defect which generates additional oxygen vacancies and turn increases the catalytic activity of CO_2. Additionally, doping ceria with samarium (Sm), gadolinium (Gd) or dysprosium (Dy) has been shown to enhance catalytic activity even further [103]. CeO_2 doped with Sm – otherwise

known as samarium doped-ceria (SDC) - displayed the highest conductivity and high oxygen vacancy generation due to Sm causing strain on the ceria structure [103,104]. Given the high conductivity and reducibility of SDC, it is a promising support when paired with active metal nanoparticles in the RWGS reaction, and can provide a high selectivity to CO and high thermal stability.

1.5.3 *Proton Conducting Support*

The use of a proton conductor is a fairly new area of solid electrolytes and is grabbing the attention of scientists and researchers since it allows to cycle H^+ ions, similar to the oxygen conductors [105]. Thus, it is more applicable for CO_2 reductions since H_2 is available in the feed and is dissociated into H. Proton conductors use a hydrogen hoping mechanism due to the lattice structure of the solid electrolyte composed of hydroxide (OH^-) bonds. Furthermore, protonic ceramics are more conductive at lower temperatures (<300°C) due to the lower energy barrier for proton migration to occur [106]. The most commonly used proton solid electrolyte is yttria-doped barium zirconate (BZY) doped with nickel-oxide (NiO) [105], where the use of barium (Ba) is to enhance the basicity of the catalyst and improve the adsorption of CO_2 [107]. Doping BZY with NiO has shown to be crucial during its synthesis since it lowers the sintering temperature and increases the conductivity of the final product [108]. Thus, ensuring a less energy intensive approach in the manufacturing process, while providing a high conductivity. Kim *et al*., [107] studied different doping concentrations on BZY for the RWGS reaction at 600 °C. They show that Zr doping of $BaZr_{0.8}Y_{0.16}Zn_{0.04}O_3$ (BZYZ) displayed the highest catalytic activity close to equilibrium values, allowing for the possibility of high conversion at lower temperatures and promoting supported nanoparticle catalysts. The addition of Ce increased proton conductivity but did not increase the CO_2 conversion and yield to CO due to the blocking of ZnO active sites. Overall, with ongoing research with the use of a proton conductor for CO_2 hydrogenation reactions, BZY has the capability of enhancing the CO_2 conversion rate and the selectivity of the reaction.

1.5.4 *Electrochemical Promotion of Catalysis*

In the last decades, aiming to enhance the MSI effect, Vayenas and colleagues discovered an approach to in-situ control the migration of ionic species within a solid electrolyte to promote the catalytic rate of a reaction [89,90,109]. This phenomenon was first referred to as the Non-Faradaic Electrochemical Modification of Catalytic Activity (NEMCA) and more recently referred to as Electrochemical Promotion of Catalysis (EPOC). The EPOC phenomenon has been evaluated for over 100 experimental tests, mostly oxidation reactions [86,87,109–114]. The advantageous effect of the EPOC phenomenon is displayed in Figure 1-3 where in the direct application of a very small current (1 μA), the reaction increases by 35 times without the need of altering other parameters [115]. The process is termed Non-Faradaic since it does not follow Faraday's Law (solid straight line in Figure 1-3) under the application of potential or electrical current, meaning the increase in the catalytic rate is greater than the rate of suppling or removing ions to the catalyst, correlated with electrons transfer. The promotional effect is due to electrochemically controlled formation of an effective neutral double layer induced by the ion spillover/backspillover of migration species from the solid electrolyte support onto the surface of the catalyst. The migration of species is induced through the application of a potential difference or current between the counter electrode and the catalyst-working electrode where the promoting ionic species travel through the electrolyte-gas-catalyst interface or the three-phase boundary (TPB). The catalyst work function is altered due to the generation of surface dipoles that alters the binding strength of chemisorbed species. Thus leading to a promotional increase in catalytic activity which has shown to control end-product selectivity for CO_2 hydrogenation reactions [82,116–119]. The origin of EPOC has been confirmed using a range of in-situ (TPD, isotopic oxygen exchange, cyclic voltammetry) and ex-situ (XPS, STEM, etc.) techniques [86,120–123]. Typically, the solid electrolytes used include yttria-stabilized zirconia (YSZ) (O^{2-} conductor) [85,86,124,125], K-β"-Al_2O_3 (K^+ conductor), Na- β"-Al_2O_3 (Na^+ conductor) [117,126,127] and $BaZrO_{0.85}Y_{0.15}O_{3-\alpha}$ (BZY) (H^+ conductor) [118,119], that allow for the ions to migrate between the catalyst/support interface, towards and away the catalyst [112,128].

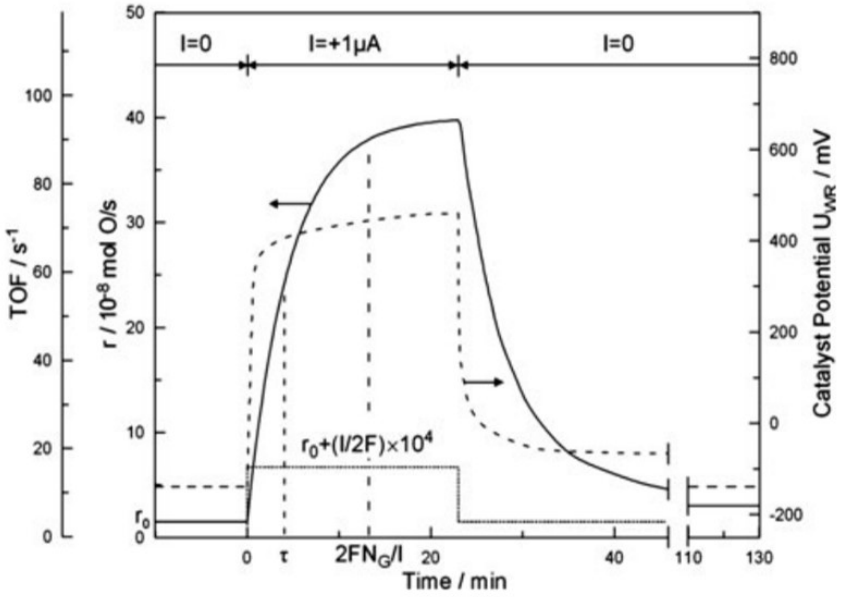

Figure 1-3. EPOC effect using YSZ as the O^{2-} conducting support for the application of 1 μA displays a 35-fold increase in production rate. Reprinted from with permission from [115]. Copyright Elsevier 2013.

The EPOC setup is schematically represented in Figure 1-4, where the typical cell resembles an electrocatalytic cell, where the catalyst is represented as the catalyst-working electrode deposited as film (typical thickness of > 2μm) and the counter and reference electrodes are typically inert gold. The electrochemical cell consists of a metal catalyst (working electrode) in-contact with an ionically conductive ceramic support (solid electrolyte) to allow potential and electrical current to conduct through the catalyst and counter electrode. Unlike traditional catalyst promotion, where promoters like Na and K are added during the synthesis procedure, electrical promotion is controlled in-situ during the reaction [51,62,109]. Taking the O^{2-} conductor YSZ as an example, during positive polarization, a potential or current is applied between the counter and working-catalyst electrode which allows for the supply of $O^{\delta-}$ (denoted as δ- partial charge) through the three-phase boundary (TPB) (YSZ-gas-catalyst interface) onto the catalyst. When negative polarization is applied, a potential difference or current passing traveling from the working-catalyst towards the current electrode results in the removal of $O^{\delta-}$ from the catalyst towards YSZ. The same mechanism occurs for K-β"-Al_2O_3 (K^+), Na- β"-Al_2O_3 (Na^+) and BZY (H^+), except the

charges are reversed. Thus, positive polarization leads to the removal of protonic species from the catalyst and negative polarization leads to the addition of protonic species onto the catalyst surface.

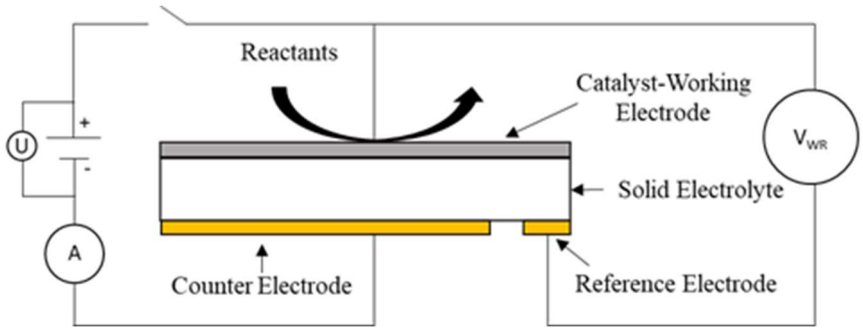

Figure 1-4. Schematic representation of the EPOC phenomenon.

The EPOC phenomenon abides to a set of rules that govern its promotional behaviour, in terms of open-circuit catalytic rate versus closed-circuit promoted rate. Altering the open-circuit kinetics of the reaction by examining the electron donor with respect to the electron acceptor results in a method in predicting the catalytic rate of the catalyst under applied [129]. Figure 1-5 summarizes the set of four electrochemical rules established by Vayenas and Brosda [130], which are discussed below.

Rule 1 (R1): The catalytic rate increases with potential, referred to as electrophobic behaviour when it is positive order in the electron donor (D) species and zero or negative order in the electron acceptor (A) species. Thus, species A is more strongly adsorbed on the surface than species D.

Rule 2 (R2): The catalytic rate decreases with potential, referred to as electrophilic behaviour when the rate is positive order in A and zero or negative order in D. In this case, species D is more strongly adsorbed on the surface than species A.

Rule 3 (R3): The catalytic rate goes through a maximum, referred to as volcano type behaviour where the rate changes from a positive order in A and negative order in D to a negative order in A and a positive order in D. In this case, species A and D are strongly adsorbed on the surface.

Rule 4 (R4): The catalytic rate goes through a minimum, referred to as inverted volcano type behaviour when the kinetics are positive order for A and D. In this case, species A and D are weakly adsorbed on the surface.

Depending on the catalyst, reaction and reaction parameters the rules can vary. Ideally inverted-volcanic behaviour is most ideal since the catalyst can be employed as both the working and the counter electrode to enhance the reaction rate for the whole cell. Regarding the CO_2 hydrogenation reaction, CO_2 is the electron acceptor and H_2 is the electron donor.

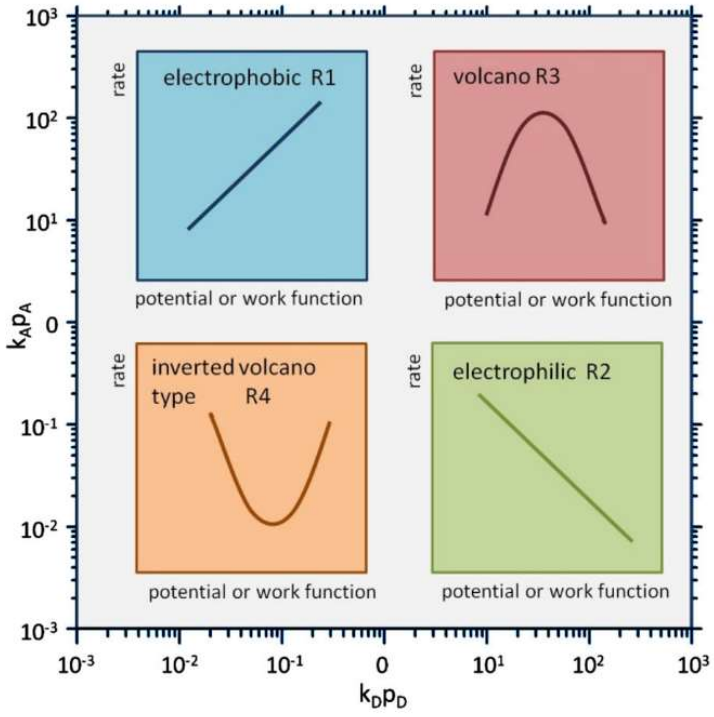

Figure 1-5. Rules of electrochemical behaviour: (a) electrophobic, (b) electrophilic, (c) volcano and (d) inverted volcano. Reprinted with permission from [130]. Copyright Elsevier 2014.

The EPOC phenomenon is usually reversible and the rate returns to its initial state, however for metal oxide catalysts (RuO_2, IrO_2, PdO) the permanent or persistent (p-EPOC) has been reported by Comninnelis and co-workers [131,132], as displayed in Figure 1-6, where after polarization the open-circuit rate is greater than it was before potential application. The O^{2-} supplied during positive polarization leads to oxygen storage in the form of metal oxides that remain after current interruption which can permanently alter the state of the catalyst into an active

one. Additionally, the effect can be persistent-EPOC when the catalytic rate returns to its initial open-circuit conditions after a long period (sometimes >2 h) affiliated to the consumption of stored oxygen during the reaction, which is dependent on the polarization period. This is a practical approach since the active state of the catalyst can be permanently altered favouring a high catalytic rate and control over end-product selectivity.

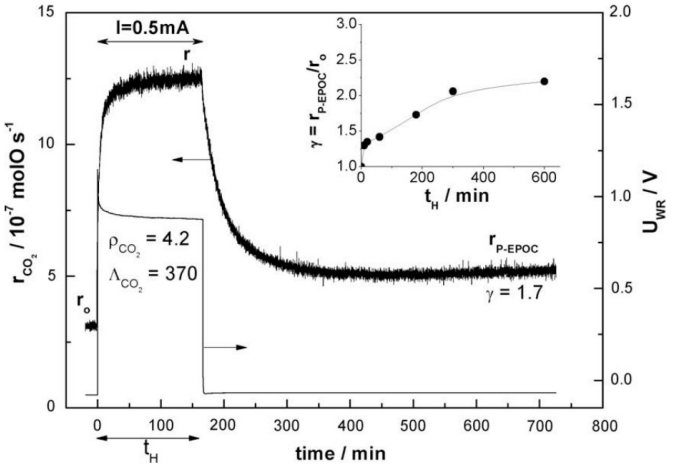

Figure 1-6. The phenomenon of permanent-EPOC. Reprinted with permission from [131]. Copyright Elsevier 2010.

To measure the effect of EPOC, the enhancement ratio (ρ) (eq. 1-10), apparent Faradaic efficiency (Λ) (eq. 1-11), and p-EPOC (γ) (eq. 1-12) are used.

$$\rho = \frac{r}{r_o} \qquad 1\text{-}10$$

$$|\Lambda| = \frac{\Delta r}{\frac{I}{nF}} \qquad 1\text{-}11$$

$$\gamma = \frac{r_{p-EPO}}{r_o} \qquad 1\text{-}12$$

Where r_o represents the open-circuit catalytic rate (*i.e.* no polarization), r represents the catalytic rate when potential is applied and Δr is the rate difference. The Faradaic efficiency is used to determine if the reaction is following the rules of electrochemical promotion, thus going against Faradays Law [109]. The denominator in eq. 1-11; (I/zF), where z is the number of electrons transferred (2 for CO and 8 for CH_4), F is Faraday's constant and I is the applied current, represents the rate at which $O^{\delta-}$ travels through the TPB to form the neutral double layer on working-catalyst

electrode. The $r_{p\text{-}EPOC}$ in eq. 1-12 represents the open-circuit catalytic rate after potential/current application. In oxidation reactions, it is non-Faradaic when $|\Lambda| > 1$ since the rate of promotional value outweighs the amount being supplied from the YSZ electrolyte. In the case of hydrogenation reactions, the Λ can be regarded as any value when $\rho \neq 1$ since the $O^{\delta-}$ promoter is not a reactant and is not being consumed [82].

1.5.4.1 EPOC for CO_2 Hydrogenation

Having made impressive progress in oxidation reactions, to this day electrochemical promoting CO_2 hydrogenation been observed in a handful of studies. It was not until a decade later, in 2008 after the discovery of the EPOC effect where it was applied for CO_2 hydrogenation reactions. With the interest in a carbon neutral economy, its utilization is increasing since the electricity required can be easily supplied through renewable energy sources and the need to limit greenhouse gas emissions continues to be crucial.

Bebelis *et al*. [133,134], studied the reaction of CO_2 and H_2 on electro-promoted rhodium (Rh) and palladium (Pd) working-catalyst electrodes. The Rh and Pd electrodes were composed of paste film deposited through thermal decomposition, consisting of a micrometer thick film. They first studied Rh/YSZ in the temperature range of 346-477 °C and observed the simultaneous production of CH_4 and CO. During positive polarization (*i.e.* $O^{\delta-}$ supply to the catalyst) the CH_4 rate increase by 2.7 times while the CO rate was suppressed. Negative polarization led to the opposite effect where the CO rate increased by 1.4 times and the CH_4 rate was suppressed. Thus, the methanation reaction follows electrophobic behaviour (R1) favouring electron donor species (H_2) and the RWGS reaction is electrophilic (R2) favouring the electron acceptors (CO_2). This was one of the first rare occasions where the EPOC effect varied the selectivity of one end-product over the other. The same group, evaluated Pd on YSZ and β”-Al_2O_3 (Na^+) at 533-605 °C under reducing conditions (where CO_2:H_2 = 1:7) [134]. Pd is not typically used as a catalyst for CO_2 hydrogenation reactions since it does not favour CO_2 adsorption. Only CO was produced at the elevated temperature for Pd/YSZ and followed inverted-volcano behaviour, thus the CO rate increased under positive and negative polarization. For Pd/β”-Al_2O_3 (Na^+), the catalytic activity increased throughout the evaluated temperature range as the potential decreased. During cathodic polarization Na^+ ions are sent to the surface of the catalyst resulting in a decrease in the work

function of Pd, favouring CO_2 adsorption and CO desorption. For both solid electrolytes, the high temperature favours the selectivity to the RWGS reaction at elevated temperatures.

In 2012, Theleritis *et al.*, evaluated the EPOC effect for a Ru film (3 mg of catalyst and 2-3 μm film thickness) deposited through thermal decomposition. They examined the performance under reducing conditions (CO_2:H_2 = 1:7) between 200-300°C with YSZ as the solid electrolyte. Following the same behaviour as the Rh/YSZ study, under positive polarization the CH_4 rate increased and the CO rate decreased, while the opposite occurred for negative polarization. Figure 1-7 displays the proposed mechanism occurring during closed-circuit conditions for the supply and removal of O^{2-} during polarization. During positive polarization (Figure 1-7 (a)) O^{2-} supplied to the surface generates an effective neutral double layer of $O^{\delta-}$ compensated with the positive charge of $Ru^{\delta-}$ to form the neutral double layer favouring the adsorption strength of H due to the generation of OH bonds (eq. 1-13). This effect is similar to increasing the H_2 feed due to the greater H species on the surface favouring the hydrogenation of CO_2 into CH_4 and decreasing the formation of CO. Under negative polarization, $O^{\delta-}$ is removed decreasing the amount of H adsorption sites and increasing CO_2 adsorption sites. Additionally, the adsorption strength of CO is weakened allowing CO to be easily desorbed.

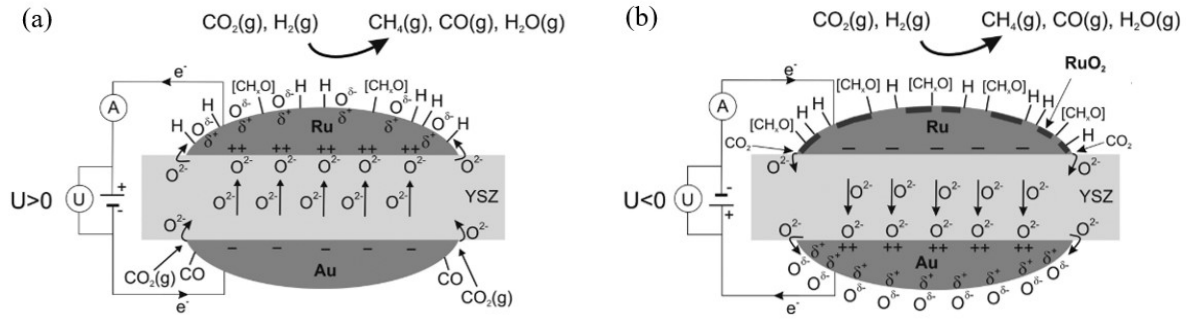

Figure 1-7. EPOC induced CO_2 hydrogenation mechanism under (a) positive and (b) negative application. Reprinted with permission from [82]. Copyright Elsevier 2012.

$$O^{2-}(YSZ) + Ru + \frac{1}{2}H_2 \rightarrow \left(OH^{\delta-} - \delta^{+}\right)Ru + 2e^{-} \qquad 1\text{-}13$$

Makri *et al.*, examined a Ru film on K-β"-Al_2O_3 (K^+) under similar conditions as Ru/YSZ by Theleritis *et al*. The addition of potassium ions (K^+) was shown to aid in the binding of CO_2

and in turn decrease the activation energy required to cleave an oxygen molecule, overall lowering the work function of Ru and improvement in the desorption of CO. Similar to Ru/YSZ, the EPOC behaviour for Ru/K-β"-Al_2O_3 was the same, however the overall CO rate is greater.

Kalaitzidou *et al.*, studied Ru/BZY (H^+) to determine how H^+ species influence catalytic activity and the EPOC effect [119]. Under open-circuit conditions the selectivity to CO was greater than CH_4, due to the backspillover of H^+ onto the Ru surface that can occur spontaneously. Furthermore, they evaluated the effect of lowering the catalytic loading and found an enhancement in the catalytic rate, which can be linked to the greater exposure of active sites and increase in the length of three-phase boundary, as indicated by the larger current required (high Λ). During negative polarization, the effect has shown to be nearly Faradaic ($\Lambda \sim 1$) due to the size of H^+ which cannot form a stable neutral double layer, under reducing conditions, while $\Lambda > 10$ is observed under oxidizing conditions by the absorbed oxygen species. However, even with the new observations with BZY, the electrochemical promotional response remained the same with Ru, where the methanation reaction was electrophobic, while the RWGS reaction followed electrophilic behaviour.

In addition to the previous study, Kalaitzidou *et al*., performed a comparative study with Ru deposited on YSZ, BZY, Na-β"-Al_2O_3 and K-β"-Al_2O_3 and confirmed the same electrochemical behaviour for all solid electrolytes [117]. Kinetic studies confirm that the methanation reaction is positive order in H_2 and zero order for CO_2, while for the RWGS reaction the opposite is true. Thus, there is a universal electrochemical behaviour for Ru under polarization that is exists for the CO_2 hydrogenation reaction regardless of the type of ionic species used. Out of the four commonly studied solid electrolytes, YSZ and BZY are most attractive since their ionic species can be regenerated by the CO_2+H_2 reaction mixture. YSZ can be partially regenerated by directly supplying the electrochemical cell with O through the dissociation of CO_2 on the surface of the catalyst, allowing O to spillover onto YSZ. While for BZY H_2 dissociation into H and spillovers onto BZY, regenerating it. However, Na and K cannot be regenerated in-situ since they are added in the initial material of the solid electrolyte and as the ions are consumed over time as sacrificial promoters the electrochemical cell will short-circuit and promotion will end.

Until recently, most EPOC CO_2 hydrogenation studies have employed thick catalytic films. One approach to use nano-structured catalysts from Kotsiras *et al*., was performed utilizing Ru-

Co nanoparticles (5-8 nm) deposited on an interlayer Ru film deposited on BZY [135]. The Ru film was added to ensure conductivity for the Ru-Co nanoparticles and to close the electrochemical circuit. They examined Ru-Co loading (0.5 mg/cm^2 and 2.9 mg/cm^2) under reducing conditions (CO_2:H_2 = 1:7). Under open-circuit potential (O.C.) the CO rate is highly selective (> 60%) that is affiliated to the dispersion of the Ru-Co nanoparticles and the use of BZY due to the spontaneous migration of H^+ species to the surface. Behaving similar to the previous discussed Ru catalysts in this section, under anodic polarization the CH_4 rate increases while the CO rate decreases and under cathodic polarization the opposite behaviour occurs. They conclude the possibility of promoting nanoparticles with a higher selectivity to CO under O.C. is due to the high dispersion of supported nanoparticles favouring the RWGS reaction. Furthermore, the use of the Ru intermediate film utilizes a large amount of noble metal and thus, an alternative way to electro-promoted nanoparticles is required.

Table 1-1 summarizes the catalytic activity and electrochemical enhancement for the discussed catalysts. Overall, EPOC was shown not only to enhance catalytic activity it also provides a method to tailor selectivity that is reversible. There are a handful of CO_2 EPOC studies that deal with the RWGS reaction and there remains a lot to explore. One approach is to utilized nanostructured catalysts, non-noble metals and electrochemical cell configurations. Furthermore, fundamental studies like density functional theory (DFT) and FTIR will provide great understanding in the overall mechanisms occurring in-situ on the surface of the catalyst.

Table 1-1. Summary of CO_2 hydrogenation reactions under the influence of EPOC with their highest CO_2 conversion reported.

Catalyst	Deposition	Temperature (°C)	CO_2:H_2	X_{CO2} (%)	ρ_{max}	Λ_{max}	Ref
Rh/YSZ	Thermal decomposition	425-477	1:1	< 1	2.7	210	[133]
Pd/YSZ and Pd/β"-A_2O_3	Paste coating	533-605	1:7	< 1	7	150	[136]
Ru/YSZ	Impregnation	240-300	1:7	~9	2.5	10^3	[82]
Ru/K^+-β"-Al_2O_3	Impregnation	280-420	1:7	--	3	--	[137]
Ru/BZY	Impregnation	300-450	1:7	~14	4.5	500	[119]
(Ru-Co)/Ru/BZY	Ru-Co powder on Ru impregnated film	260-460	1:7	6	2.5	60	[135]

1.5.5 *EPOC and free-standing Nanoparticles*

To further enhance the EPOC effect and improve the affordability of the reaction, nano-structured catalysts in the form of free-standing nanoparticles deposited directly on YSZ have been employed by the group of Baranova. Several studies have shown the promoting behaviour of free-standing nanoparticles for oxidation reactions regarding volatile organic compounds CO, CH_4 [138,139] and ethylene (C_2H_4) [87,140,141]. The addition of gold mesh to act as a current collector was placed on the free-standing nanoparticles and was mechanically pressed to ensure constant contact to close the circuit [142]. The promotion of capability of nanoparticles was established without the use of a thick intermediate film, making progress toward more efficient EPOC electrocatalytic systems.

Furthermore, one particular study by Isaifan *et al.*, demonstrates the attractiveness in using nanoparticles supported on ionically conductive supports, where the use of Pt nanoparticles (<2 nm) supported on YSZ resulted in the oxidation of CO and ethylene (C_2H_4) in the absence of O_2

in the gas phase [143]. The combustion of the volatile gases occurred at the three-phase boundary at the interface between Pt and the oxygen ionically conductive support. The driving force behind this effect is due to the difference in work function between Pt and YSZ, granting oxygen ions the ability to backspillover from YSZ onto Pt as low at 75°C and 120°C for CO and C_2H_4, respectively. This behaviour was referred to as self-induced EPOC, which is used to described the metal-support interaction (MSI) for noble metal nanoparticles supported on purely ionic conductive or metal-oxide supports, which was later coined by Vernoux [144], to be self-sustained electro-promotion (SSEP). Applying the use of nanoparticles for the CO_2 hydrogenation will allow to limit the amount of noble metal used and will improve the CO selectivity.

1.5.6 *Insight into the EPOC phenomenon using Density Functional Theory (DFT)*

Density Functional Theory (DFT) is a technique used to provide a precise atomistic understanding of the origin of the promotional activity is lacking. Comprehending the atomistic origin of this process clarifies the role of promotional species, *i.e.*, if they act as spectator species or directly participate in the bond formation/scission processes. This detailed insight will also improve the understanding of metal-support interactions and chemical promotion effects since these phenomena are functionally equivalent [86].

The EPOC effect for the CO_2 hydrogenation has never been evaluated through DFT calculations. Instead, it was evaluated for oxidation reactions through quantum-chemistry to evaluate how the change in work function alters the chemisorption of promoting ions, specifically O^{2-}, Na^+ and F^+. These ions lead to the formation of an electric field, in turn changing the adsorption energies of the reactants, intermediates and products, confirming a promotional behaviour [145]. The study performed by Pacchioni *et al.*, concluded that the effect induced by the electric field/dipole layer is an electrostatic force that is strongly dependent on the reactants, catalyst and electrolytes (*i.e.* promoting species) [146]. Furthermore, Leiva *et al.*, studied the effect of O^{2-} and Na^+ pumping to the surface of the Pt(111) to determine how the catalytic surface is altered affecting the work function [147]. The study supported EPOC experimental results where the addition of O^{2-} lead to an increase in work function due to a positive change induced on the surface and the opposite is observed for the adsorption of Na^+, decreasing the work function. More recently, Che *et al.*, studied the anodic reaction for methane steam reforming, simulated through an electric field,

confirming that the structure of the surface did not alter but influenced the adsorption energies of the species [148–150].

Currently, a new model proposed by Steinmann *et al*., allows for a more accurate depiction of an electric field, tailoring to the EPOC polarization effect [151]. The model evaluates the binding energies of the adsorbed species induced by the application of an electrochemical potential difference. Essentially, the electrical double layer / electric field is represented as an addition to the classical DFT approach. Using the linearized Poisson-Boltzmann distribution function, the addition or removal of electrons on the structure results in the application of a different potential, to simulate an electric field and a change in work function, thereby determining the effect of potential on the intermediates and in turn end-product selectivity. This effect was recently studied by Hajar *et al*., for the oxidation of ethylene on free-standing RuO_2 nanoparticles on YSZ comparing experiment with theory (RuO_2 (110) slab) [152]. They evaluated the addition of oxygen as a function of potential to simulate the backspillover effect induced by EPOC effect with YSZ. The experimental catalytic rate followed inverted-volcano behaviour meaning the rate increased under positive and negative polarization. The most stable surface was selected and the adsorption and dissociation of C_2H_4 and O_2 was evaluated. Under positive polarization the adsorption and cleavage of the C-C bond of ethylene was enhanced, while under negative polarization the activation of oxygen was enhanced. Thus, the DFT calculations explained the reason for the catalytic behaviour, allowing the model and process to be used for future experiment to provide insights on the fundamentals of EPOC.

References

[1] P. Ciais, C. Sabine, G. Bala, L. Bopp, V. Brovkin, J. Canadell, A. Chhabra, R. DeFries, J. Galloway, M. Heimann, C. Jones, C. Le Quéré, R.B. Myneni, S. Piao, P. Thornton, The physical science basis. Contribution of working group I to the fifth assessment report of the intergovernmental panel on climate change, Chang. IPCC Clim. (2013) 465–570. doi:10.1017/CBO9781107415324.015.

[2] M.D. Porosoff, B. Yan, J.G. Chen, Catalytic reduction of CO2 by H2 for synthesis of CO, methanol and hydrocarbons: challenges and opportunities, Energy Environ. Sci. 9 (2016) 62–73. doi:10.1039/C5EE02657A.

[3] W. Steffen, et al., Trajectories of the Earth System in the Anthropocene, Proc. Natl. Acad. Sci. U. S. A. 115 (2018) 8252–8259. doi:10.1073/pnas.1810141115.

[4] G.M. Masters, W.P. Ela, Introduction to Environmental Engineering and Science, Pearson Education, Inc., 2013.

[5] Government of Canada, Canada's Mid-century Long-term Low-greenhouse Gas Development Strategy, 2016. http://www.onxeo.com/en/nos-produits/strategie-de-developpement/.

[6] D. Yang, Y. Liu, Z. Cai, X. Chen, L. Yao, D. Lu, First Global Carbon Dioxide Maps Produced from TanSat Measurements, Adv. Atmos. Sci. 35 (2018) 621–623.

[7] S. Saeidi, N.A.S. Amin, M.R. Rahimpour, Hydrogenation of CO2 to value-added products - A review and potential future developments, J. CO2 Util. 5 (2014) 66–81. doi:10.1016/j.jcou.2013.12.005.

[8] Earth System Research Laboratory, Trends in Atmospheric Carbon Dioxide, (n.d.). https://www.esrl.noaa.gov/gmd/ccgg/trends/ (accessed August 27, 2020).

[9] NASA, Carbon Dioxide Emissions, (n.d.). https://climate.nasa.gov/vital-signs/carbon-dioxide/ (accessed August 27, 2020).

[10] A. Rafiee, M. Panahi, K.R. Khalilpour, CO2 utilization through integration of post-combustion carbon capture process with Fischer-Tropsch gas-to-liquid (GTL) processes, J. CO2 Util. 18 (2017) 98–106. doi:10.1016/j.jcou.2017.01.016.

[11] Z. Yuan, M.R. Eden, R. Gani, Toward the Development and Deployment of Large-Scale Carbon Dioxide Capture and Conversion Processes, Ind. Eng. Chem. Res. 55 (2016) 3383–3419. doi:10.1021/acs.iecr.5b03277.

[12] F.D. Meylan, V. Moreau, S. Erkman, CO2 utilization in the perspective of industrial ecology, an overview, J. CO2 Util. 12 (2015) 101–108. doi:10.1016/j.jcou.2015.05.003.

[13] D. Bratt, M. Fan, Catalytic CO2 Hydrogenation -Literature Review: Technology Development since 2014, Chem. Eng. Plan B. Pap. 1. (2016). https://hdl.handle.net/20.500.11919/779.

[14] A.A. Olajire, Valorization of greenhouse carbon dioxide emissions into value-added products by catalytic processes, J. CO2 Util. 3–4 (2013) 74–92. doi:10.1016/j.jcou.2013.10.004.

[15] J. Wei, Q. Ge, R. Yao, Z. Wen, C. Fang, L. Guo, H. Xu, J. Sun, Directly converting CO2 into a gasoline fuel, Nat. Commun. 8 (2017) 15174. doi:10.1038/ncomms15174.

[16] W. Zhou, K. Cheng, J. Kang, C. Zhou, V. Subramanian, Q. Zhang, Y. Wang, New horizon in C1 chemistry: Breaking the selectivity limitation in transformation of syngas and hydrogenation of CO2 into hydrocarbon chemicals and fuels, Chem. Soc. Rev. 48 (2019) 3193–3228. doi:10.1039/c8cs00502h.

[17] J.M. Matter, M. Stute, S.O. Snaebjornsdottir, E.H. Oelkers, S.R. Gislason, E.S. Aradottir, B. Sigfusson, I. Gunnarsson, H.A. Alfredsson, D. Wolff-boenisch, K. Mesfin, K. Dideriksen, W.S. Broecker, Rapid carbon mineralization for permanent disposal of anthropogenic carbon dioxide emissions, 2016. doi:10.1126/science.aad8132 Inject,.

[18] D.U. Nielsen, X.-M. Hu, K. Daasbjerg, T. Skrydstrup, Chemically and electrochemically catalysed conversion of CO2 to CO with follow-up utilization to value-added chemicals, Nat. Catal. 1 (2018) 244–254. doi:10.1038/s41929-018-0051-3.

[19] C. Vogt, M. Monai, G.J. Kramer, B.M. Weckhuysen, The renaissance of the Sabatier reaction and its applications on Earth and in space, Nat. Catal. 2 (2019) 188–197. doi:10.1038/s41929-019-0244-4.

[20] R.G. Grim, Z. Huang, M.T. Guarnieri, J.R. Ferrell, L. Tao, J.A. Schaidle, Transforming the carbon economy: Challenges and opportunities in the convergence of low-cost electricity and reductive CO2 utilization, Energy Environ. Sci. 13 (2020) 472–494. doi:10.1039/c9ee02410g.

[21] J. Artz, T.E. Müller, K. Thenert, J. Kleinekorte, R. Meys, A. Sternberg, A. Bardow, W. Leitner, Sustainable Conversion of Carbon Dioxide: An Integrated Review of Catalysis and Life Cycle Assessment, Chem. Rev. 118 (2018) 434–504. doi:10.1021/acs.chemrev.7b00435.

[22] C. Hepburn, E. Adlen, J. Beddington, E.A. Carter, S. Fuss, N. Mac Dowell, J.C. Minx, P. Smith, C.K. Williams, The technological and economic prospects for CO2 utilization and removal, Nature. 575 (2019) 87–97. doi:10.1038/s41586-019-1681-6.

[23] S. Roy, A. Cherevotan, S.C. Peter, Thermochemical CO2 Hydrogenation to Single Carbon Products: Scientific and Technological Challenges, ACS Energy Lett. 3 (2018) 1938–1966. doi:https://doi.org/10.1021/acsenergylett.8b00740.

[24] A.D. Handoko, F. Wei, Jenndy, B.S. Yeo, Z.W. Seh, Understanding heterogeneous electrocatalytic carbon dioxide reduction through operando techniques, Nat. Catal. 1 (2018) 922–934. doi:10.1038/s41929-018-0182-6.

[25] I. Chorendorff, J.W. Niemantsverdriet, Concepts o Modern Catalysis and Kinetics, Wiley-VCH Verlag GmbH & Co. KGaA, Weinheim, 2003. doi:10.1002/anie.200461440.

[26] B. Cornils, W.A. Herrmann, C. Wong, H. Zanthoff, R. Eds, Catalysis from A to Z, Wiley-VCH Verlag GmbH & Co. KGaA, Weinheim, 2007. doi:10.1016/S1351-4180(07)70462-2.

[27] J.D. Holladay, J. Hu, D.L. King, Y. Wang, An overview of hydrogen production technologies, Catal. Today. 139 (2009) 244–260. doi:10.1016/j.cattod.2008.08.039.

[28] I. Dincer, C. Acar, Review and evaluation of hydrogen production methods for better sustainability, Int. J. Hydrogen Energy. 40 (2014) 11094–11111. doi:10.1016/j.ijhydene.2014.12.035.

[29] J. Chi, H. Yu, Water electrolysis based on renewable energy for hydrogen production, Cuihua Xuebao/Chinese J. Catal. 39 (2018) 390–394. doi:10.1016/S1872-2067(17)62949-8.

[30] E. Cossar, A.O. Barnett, F. Seland, E.A. Baranova, The performance of nickel and nickel-iron catalysts evaluated as anodes in anion exchange membrane water electrolysis, Catalysts. 9 (2019) 814. doi:10.3390/catal9100814.

[31] A. V. Puga, On the nature of active phases and sites in CO and CO2 hydrogenation catalysts, Catal. Sci. Technol. 8 (2018) 5681–5707. doi:10.1039/c8cy01216d.

[32] C. Jiménez-Borja, S. Brosda, M. Makri, F. Sapountzi, F. Dorado, J.L. Valverde, C.G. Vayenas, Methane oxidation on Pd/YSZ by electrochemical promotion, Solid State Ionics. 225 (2012) 376–381. doi:10.1016/j.ssi.2012.03.004.

[33] Y.H. Choi, Y.J. Jang, H. Park, W.Y. Kim, Y.H. Lee, S.H. Choi, J.S. Lee, Carbon dioxide Fischer-Tropsch synthesis: A new path to carbon-neutral fuels, Appl. Catal. B Environ. 202 (2017) 605–610. doi:10.1016/j.apcatb.2016.09.072.

[34] A.N. Pour, M.R. Housaindokht, A new kinetic model for direct CO 2 hydrogenation to higher hydrocarbons on a precipitated iron catalyst: Effect of catalyst particle size, J. Energy Chem. 26 (2017) 359–367. doi:https://doi.org/10.1016/j.jechem.2016.12.006.

[35] G. Centi, S. Perathoner, Opportunities and prospects in the chemical recycling of carbon dioxide to fuels, Catal. Today. 148 (2009) 191–205. doi:10.1016/j.cattod.2009.07.075.

[36] J.C. van Dyk, M.J. Keyser, M. Coertzen, Syngas production from South African coal sources using Sasol-Lurgi gasifiers, Int. J. Coal Geol. 65 (2006) 243–253. doi:10.1016/j.coal.2005.05.007.

[37] M.K. Gnanamani, G. Jacobs, H.H. Hamdeh, W.D. Shafer, F. Liu, S.D. Hopps, G.A. Thomas, B.H. Davis, Hydrogenation of Carbon Dioxide over Co-Fe Bimetallic Catalysts, ACS Catal. 6 (2016) 913–927. doi:10.1021/acscatal.5b01346.

[38] J. He, Z. Liu, Y. Yoneyama, N. Nishiyama, N. Tsubaki, Multiple-functional capsule catalysts: A tailor-made confined reaction environment for the direct synthesis of middle isoparaffins from syngas, Chem. - A Eur. J. 12 (2006) 8296–8304. doi:10.1002/chem.200501295.

[39] J. Li, Y. He, L. Tan, P. Zhang, X. Peng, A. Oruganti, G. Yang, H. Abe, Y. Wang, N.

Tsubaki, Integrated tuneable synthesis of liquid fuels via Fischer–Tropsch technology, Nat. Catal. 1 (2018) 787–793. doi:10.1038/s41929-018-0144-z.

[40] S. Saeidi, S. Najari, F. Fazlollahi, M.K. Nikoo, F. Sefidkon, J.J. Klemeš, L.L. Baxter, Mechanisms and kinetics of CO 2 hydrogenation to value-added products: A detailed review on current status and future trends, Renew. Sustain. Energy Rev. 80 (2017) 1292–1311. doi:10.1016/j.rser.2017.05.204.

[41] M. V. Twigg, Catalyst Handbook, Wolfe Publishing Ltd, 1989.

[42] B. Smith R J, M. Loganathan, M.S. Shantha, A review of the water gas shift reaction kinetics, Int. J. Chem. React. Eng. 8 (2010). doi:10.2202/1542-6580.2238.

[43] Y. Yan, Q. Wang, C. Jiang, Y. Yao, D. Lu, J. Zheng, Y. Dai, H. Wang, Y. Yang, Ru/Al2O3catalyzed CO2hydrogenation: Oxygen-exchange on metal-support interfaces, J. Catal. 367 (2018) 194–205. doi:10.1016/j.jcat.2018.08.026.

[44] X. Chen, X. Su, H. Duan, B. Liang, Y. Huang, T. Zhang, Catalytic performance of the Pt/TiO2 catalysts in reverse water gas shift reaction: Controlled product selectivity and a mechanism study, Catal. Today. 281 (2017) 312–318. doi:10.1016/j.cattod.2016.03.020.

[45] S.G. Jadhav, P.D. Vaidya, B.M. Bhanage, J.B. Joshi, Kinetics of reverse water-gas shift reaction over Pt/Al2O3 catalyst, Can. J. Chem. Eng. 94 (2016) 101–106. doi:10.1002/cjce.22370.

[46] V. Arunajatesan, B. Subramaniam, K.W. Hutchenson, F.E. Herkes, In situ FTIR investigations of reverse water gas shift reaction activity at supercritical conditions, Chem. Eng. Sci. 62 (2007) 5062–5069. doi:10.1016/j.ces.2007.01.010.

[47] D.C. Upham, A.R. Derk, S. Sharma, H. Metiu, E.W. McFarland, CO 2 methanation by Ru-doped ceria: the role of the oxidation state of the surface, Catal. Sci. Technol. 5 (2015) 1783–1791. doi:10.1039/C4CY01106F.

[48] S.S. Kim, K.H. Park, S.C. Hong, A study of the selectivity of the reverse water-gas-shift reaction over Pt/TiO2 catalysts, Fuel Process. Technol. 108 (2013) 47–54. doi:10.1016/j.fuproc.2012.04.003.

[49] K. Zhao, L. Wang, M. Calizzi, E. Moioli, A. Züttel, In Situ Control of the Adsorption Species in CO2 Hydrogenation: Determination of Intermediates and Byproducts, J. Phys. Chem. C. 122 (2018) 20888–20893. doi:10.1021/acs.jpcc.8b06508.

[50] K. Jalama, Carbon dioxide hydrogenation over nickel-, ruthenium-, and copper-based catalysts: Review of kinetics and mechanism, Catal. Rev. - Sci. Eng. 59 (2017) 95–164. doi:10.1080/01614940.2017.1316172.

[51] K. Yaccato, R. Carhart, A. Hagemeyer, A. Lesik, P. Strasser, A.F. Volpe, H. Turner, H. Weinberg, R.K. Grasselli, C. Brooks, Competitive CO and CO2 methanation over supported noble metal catalysts in high throughput scanning mass spectrometer, Appl. Catal. A Gen. 296 (2005) 30–48. doi:10.1016/j.apcata.2005.07.052.

[52] S. Sharma, Z. Hu, P. Zhang, E.W. McFarland, H. Metiu, CO2 methanation on Ru-doped ceria, J. Catal. 278 (2011) 297–309. doi:10.1016/j.jcat.2010.12.015.

[53] J. Ma, N. Sun, X. Zhang, N. Zhao, F. Xiao, W. Wei, Y. Sun, A short review of catalysis for CO2 conversion, Catal. Today. 148 (2009) 221–231. doi:10.1016/j.cattod.2009.08.015.

[54] J.H. Kwak, L. Kovarik, J. Szanyi, CO2 Reduction on Supported Ru/Al2O3 Catalysts: Cluster Size Dependence of Product Selectivity, ACS Catal. 3 (2013) 2449–2455. doi:10.1021/cs400381f.

[55] S. Choi, B.-I. Sang, J. Hong, K.J. Yoon, J.-W. Son, J.-H. Lee, B.-K. Kim, H. Kim, Catalytic behavior of metal catalysts in high-temperature RWGS reaction: In-situ FT-IR experiments and first-principles calculations, Sci. Rep. 7 (2017) 41207. doi:10.1038/srep41207.

[56] X. Zhang, X. Zhu, L. Lin, S. Yao, M. Zhang, X. Liu, X. Wang, Y. Li, C. Shi, D. Ma, Highly dispersed Copper over β-Mo2C as Efficient and Stable Catalysts for RWGS Reaction, ACS Catal. 7 (2017) 912–918. doi:10.1021/acscatal.6b02991.

[57] B. Dai, G. Zhou, S. Ge, H. Xie, Z. Jiao, G. Zhang, K. Xiong, CO2 reverse water-gas shift reaction on mesoporous M-CeO2 catalysts, Can. J. Chem. Eng. 95 (2017) 634–642. doi:10.1002/cjce.22730.

[58] R. V. Gonçalves, L.L.R. Vono, R. Wojcieszak, C.S.B. Dias, H. Wender, E. Teixeira-Neto, L.M. Rossi, Selective hydrogenation of CO 2 into CO on a highly dispersed nickel catalyst obtained by magnetron sputtering deposition: A step towards liquid fuels, Appl. Catal. B Environ. 209 (2017) 240–246. doi:10.1016/j.apcatb.2017.02.081.

[59] D.L. Jurković, A. Pohar, V.D.B.C. Dasireddy, B. Likozar, Effect of Copper-based Catalyst Support on Reverse Water-Gas Shift Reaction (RWGS) Activity for CO_2 Reduction, Chem. Eng. Technol. (2017) 1–9. doi:10.1002/ceat.201600594.

[60] L. Wang, H. Liu, Y. Chen, S. Yang, Reverse water–gas shift reaction over co-precipitated Co–CeO2 catalysts: Effect of Co content on selectivity and carbon formation, Int. J. Hydrogen Energy. 42 (2016) 3682–3689. doi:10.1016/j.ijhydene.2016.07.048.

[61] C.S. Chen, W.H. Cheng, S.S. Lin, Enhanced activity and stability of a Cu/SiO2 catalyst for the reverse water gas shift reaction by an iron promoter., Chem. Commun. (Camb). (2001) 1770–1771. doi:10.1039/b104279n.

[62] X. Su, J. Xu, B. Liang, H. Duan, B. Hou, Y. Huang, Catalytic carbon dioxide hydrogenation to methane: A review of recent studies, J. Energy Chem. 25 (2016) 553–565. doi:10.1016/j.jechem.2016.03.009.

[63] B. Lu, K. Kawamoto, Preparation of mesoporous CeO 2 and monodispersed NiO particles in CeO 2 , and enhanced selectivity of NiO / CeO 2 for reverse water gas shift reaction, 53 (2014) 70–78. doi:10.1016/j.materresbull.2014.01.043.

[64] R.W. Dorner, D.R. Hardy, F.W. Williams, H.D. Willauer, Heterogeneous catalytic CO2 conversion to value-added hydrocarbons, Energy Environ. Sci. 3 (2010) 884–890. doi:10.1039/c001514h.

[65] G. Yin, X. Yuan, X. Du, W. Zhao, Q. Bi, F. Huang, Efficient Reduction of CO2 to CO Using Cobalt–Cobalt Oxide Core–Shell Catalysts, Chem. - A Eur. J. 24 (2018) 2157–2163. doi:10.1002/chem.201704596.

[66] M. V. Landau, N. Meiri, N. Utsis, R. Vidruk Nehemya, M. Herskowitz, Conversion of CO2, CO, and H2 in CO2 Hydrogenation to Fungible Liquid Fuels on Fe-Based Catalysts, Ind. Eng. Chem. Res. 56 (2017) 13334–13355. doi:10.1021/acs.iecr.7b01817.

[67] C. Liu, T.R. Cundari, A.K. Wilson, CO2 reduction on transition metal (Fe, Co, Ni, and Cu) surfaces: In comparison with homogeneous catalysis, J. Phys. Chem. C. 116 (2012) 5681–5688. doi:10.1021/jp210480c.

[68] V. V Galvita, H. Poelman, V. Bliznuk, C. Detavernier, G.B. Marin, CeO 2 -Modified Fe 2 O 3 for CO 2 Utilization via Chemical Looping, Ind. Eng. Chem. Res. 52 (2013) 8416–8426. doi:10.1021/ie4003574.

[69] D.H. Kim, S.W. Han, H.S. Yoon, Y.D. Kim, Reverse water gas shift reaction catalyzed by Fe nanoparticles with high catalytic activity and stability, J. Ind. Eng. Chem. 23 (2014) 67–71. doi:10.1016/j.jiec.2014.07.043.

[70] X. Nie, L. Meng, H. Wang, Y. Chen, X. Guo, C. Song, DFT insight into the effect of potassium on the adsorption, activation and dissociation of CO2 over Fe-based catalysts, Phys. Chem. Chem. Phys. 20 (2018) 14694–14707. doi:10.1039/c8cp02218f.

[71] J.A. Loiland, M.J. Wulfers, N.S. Marinkovic, R.F. Lobo, Fe/γ-Al2O3and Fe-K/γ-Al2O3as reverse water-gas shift catalysts, Catal. Sci. Technol. 6 (2016) 5267–5279. doi:10.1039/c5cy02111a.

[72] S. Kattel, P. Liu, J.G. Chen, Tuning Selectivity of CO2 Hydrogenation Reactions at the Metal/Oxide Interface, J. Am. Chem. Soc. 139 (2017) 9739–9754. doi:10.1021/jacs.7b05362.

[73] M. Wenzel, N.V.R. Aditya Dharanipragada, V. V. Galvita, H. Poelman, G.B. Marin, L. Rihko-Struckmann, K. Sundmacher, CO production from CO2 via reverse water-gas shift reaction performed in a chemical looping mode: Kinetics on modified iron oxide, J. CO2 Util. 17 (2017) 60–68. doi:10.1016/j.jcou.2016.10.015.

[74] M. Albrecht, U. Rodemerck, M. Schneider, M. Bröring, D. Baabe, E. V. Kondratenko, Unexpectedly efficient CO2 hydrogenation to higher hydrocarbons over non-doped Fe2O3, Appl. Catal. B Environ. 204 (2017) 119–126. doi:10.1016/j.apcatb.2016.11.017.

[75] J. Zieliński, I. Zglinicka, L. Znak, Z. Kaszkur, Reduction of Fe2O3 with hydrogen, Appl. Catal. A Gen. 381 (2010) 191–196. doi:10.1016/j.apcata.2010.04.003.

[76] D. Zhang, J. Luo, J. Wang, X. Xiao, Y. Liu, W. Qi, D.S. Su, W. Chu, Ru/FeOx catalyst performance design: Highly dispersed Ru species for selective carbon dioxide hydrogenation, Chinese J. Catal. 39 (2018) 157–166. doi:10.1016/S1872-2067(17)62967-X.

[77] T. Avanesian, G.S. Gusmão, P. Christopher, Mechanism of CO2 reduction by H2 on

Ru(0 0 0 1) and general selectivity descriptors for late-transition metal catalysts, J. Catal. 343 (2016) 86–96. doi:10.1016/j.jcat.2016.03.016.

[78] S.-T. Zhang, H. Yan, M. Wei, D.G. Evans, X. Duan, Hydrogenation mechanism of carbon dioxide and carbon monoxide on Ru(0001) surface: a density functional theory study, RSC Adv. 4 (2014) 30241. doi:10.1039/C4RA01655F.

[79] P. Kangvansura, L.M. Chew, C. Kongmark, P. Santawaja, H. Ruland, W. Xia, H. Schulz, A. Worayingyong, M. Muhler, Effects of Potassium and Manganese Promoters on Nitrogen-Doped Carbon Nanotube-Supported Iron Catalysts for CO2 Hydrogenation, Engineering. 3 (2017) 385–392. doi:10.1016/J.ENG.2017.03.013.

[80] M.D. Porosoff, J.W. Baldwin, X. Peng, G. Mpourmpakis, H.D. Willauer, Potassium-promoted molybdenum carbide as a highly active and selective catalyst for CO2 conversion to CO, ChemSusChem. 15261 (2017) 1–9. doi:10.1002/cssc.201700412.

[81] B. Liang, H. Duan, X. Su, X. Chen, Y. Huang, X. Chen, J.J. Delgado, T. Zhang, Promoting role of potassium in the reverse water gas shift reaction on Pt/mullite catalyst, Catal. Today. 281 (2017) 319–326. doi:10.1016/j.cattod.2016.02.051.

[82] D. Theleritis, S. Souentie, A. Katsaounis, C.G. Vayenas, Hydrogenation of CO2 over Ru electropromoted catalysts, ACS Catal. 2 (2012) 770–780. doi:dx.doi.org/10.1021/cs300072a.

[83] U. Rodemerck, M. Holeňa, E. Wagner, Q. Smejkal, A. Barkschat, M. Baerns, Catalyst development for CO2 hydrogenation to fuels, ChemCatChem. 5 (2013) 1948–1955. doi:10.1002/cctc.201200879.

[84] R.J. Isaifan, E.A. Baranova, Effect of ionically conductive supports on the catalytic activity of platinum and ruthenium nanoparticles for ethylene complete oxidation, Catal. Today. 241 (2015) 107–113. doi:10.1016/j.cattod.2014.03.061.

[85] R.J. Isaifan, H.A.E. Dole, E. Obeid, L. Lizarraga, P. Vernoux, E.A. Baranova, Metal-Support Interaction of Pt Nanoparticles with Ionically and Non-Ionically Conductive Supports for CO Oxidation, Electrochem. Solid-State Lett. 15 (2012) E14. doi:10.1149/2.024203esl.

[86] P. Vernoux, L. Lizarraga, M.N. Tsampas, F.M. Sapountzi, A. De Lucas-Consuegra, J.L. Valverde, S. Souentie, C.G. Vayenas, D. Tsiplakides, S. Balomenou, E.A. Baranova, Ionically conducting ceramics as active catalyst supports, Chem. Rev. 113 (2013) 8192–8260. doi:10.1021/cr4000336.

[87] Y.M. Hajar, K.D. Patel, U. Tariq, E.A. Baranova, Functional equivalence of electrochemical promotion and metal support interaction for Pt and RuO2 nanoparticles, J. Catal. 352 (2017) 42–51. doi:10.1016/j.jcat.2017.05.001.

[88] G.C. Wang, J. Nakamura, Structure sensitivity for forward and reverse water-gas shift reactions on copper surfaces: A DFT study, J. Phys. Chem. Lett. 1 (2010) 3053–3057. doi:10.1021/jz101150w.

[89] C.G. Vayenas, Bridging electrochemistry and heterogeneous catalysis, J. Solid State Electrochem. 15 (2011) 1425–1435. doi:10.1007/s10008-011-1336-5.

[90] J. Nicole, C. Comninellis, D. Tsiplakides, C. Pliangos, X.E. Verykios, C.G. Vayenas, Electrochemical promotion and metal-support interactions, J. Catal. 204 (2001) 23–34. doi:10.1006/jcat.2001.3360.

[91] F. Wang, C. Li, X. Zhang, M. Wei, D.G. Evans, X. Duan, Catalytic behavior of supported Ru nanoparticles on the {100}, {110}, and {111} facet of CeO2, J. Catal. 329 (2015) 177–186. doi:10.1016/j.jcat.2015.05.014.

[92] F.S. Sangsefidi, M. Salavati-Niasari, S. Mazaheri, M. Sabet, Controlled green synthesis and characterization of CeO2nanostructures as materials for the determination of ascorbic acid, J. Mol. Liq. 241 (2017) 772–781. doi:10.1016/j.molliq.2017.06.078.

[93] H.A.E. Dole, A.C.G.S.A. Costa, M. Couillard, E.A. Baranova, Quantifying metal support interaction in ceria-supported Pt, PtSn and Ru nanoparticles using electrochemical technique, J. Catal. 333 (2016) 40–50. doi:10.1016/j.jcat.2015.10.015.

[94] H.A.E. Dole, E.A. Baranova, Ethylene Oxidation in an Oxygen-Deficient Environment: Why Ceria is an Active Support?, ChemCatChem. 8 (2016) 1977–1986. doi:10.1002/cctc.201600142.

[95] H.A.E. Dole, E.A. Baranova, Implementation of Nano-structured Catalysts in the Electrochemical Promotion of Catalysis, in: A.S.H. (Eds. . Aliofkhazraei, M., Makhlouf (Ed.), Handb. Nanoelectrochemistry Electrochem. Synth. Methods, Prop. Charact. Tech., Springer International Publishing, Switzerland, 2015: pp. 1095–1124.

[96] M. Boaro, S. Colussi, A. Trovarelli, Ceria-based materials in hydrogenation and reforming reactions for CO 2 valorization, Front. Chem. 7 (2019) 28. doi:10.3389/fchem.2019.00028.

[97] A. Trovarelli, Catalysis by ceria and related materials, Catal. Sci. Ser. 2 (2005) 508. doi:10.1016/j.cattod.2004.12.016.

[98] F.S. Sangsefidi, M. Salavati-niasari, H. Khojasteh, M. Shabani-nooshabadi, Synthesis , characterization and investigation of the electrochemical hydrogen storage properties of CuO-CeO 2 nanocomposites synthesized by green method, Int. J. Hydrogen Energy. 42 (2017) 14608–14620. doi:10.1016/j.ijhydene.2017.04.103.

[99] M. Grünbacher, B. Klötzer, S. Penner, CO2 Reduction by Hydrogen Pre-Reduced Acceptor-Doped Ceria, ChemPhysChem. 20 (2019) 1706–1718. doi:10.1002/cphc.201900314.

[100] M. Nolan, J.E. Fearon, G.W. Watson, Oxygen vacancy formation and migration in ceria, Solid State Ionics. 177 (2006) 3069–3074. doi:10.1016/j.ssi.2006.07.045.

[101] S.M. Lee, H. Eom, S.S. Kim, A study on the effect of CeO2 addition to a Pt/TiO2 catalyst on the reverse water gas shift reaction, Environ. Technol. (United Kingdom). 3330 (2019). doi:10.1080/09593330.2019.1625954.

[102] B. Dai, S. Cao, H. Xie, G. Zhou, S. Chen, Reduction of CO2 to CO via reverse water-gas

shift reaction over CeO2 catalyst, Korean J. Chem. Eng. 35 (2018) 421–427. doi:10.1007/s11814-017-0267-y.

[103] S. Kuharuangrong, Ionic conductivity of Sm, Gd, Dy and Er-doped ceria, J. Power Sources. 171 (2007) 506–510. doi:10.1016/j.jpowsour.2007.05.104.

[104] G. Avgouropoulos, M. Manzoli, F. Boccuzzi, T. Tabakova, J. Papavasiliou, T. Ioannides, V. Idakiev, Catalytic performance and characterization of Au/doped-ceria catalysts for the preferential CO oxidation reaction, J. Catal. 256 (2008) 237–247. doi:10.1016/j.jcat.2008.03.014.

[105] E. Fabbri, L. Bi, D. Pergolesi, E. Traversa, Towards the next generation of solid oxide fuel cells operating below 600 °c with chemically stable proton-conducting electrolytes, Adv. Mater. 24 (2012) 195–208. doi:10.1002/adma.201103102.

[106] N. Shi, Y. Xie, D. Huan, Y. Yang, S. Xue, Z. Qi, Y. Pan, R. Peng, C. Xia, Y. Lu, Controllable CO2 conversion in high performance proton conducting solid oxide electrolysis cells and the possible mechanisms, J. Mater. Chem. A. 7 (2019) 4855–4864. doi:10.1039/c8ta12458b.

[107] D.H. Kim, J.L. Park, E.J. Park, Y.D. Kim, S. Uhm, Dopant Effect of Barium Zirconate-Based Perovskite-Type Catalysts for the Intermediate-Temperature Reverse Water Gas Shift Reaction, ACS Catal. 4 (2014) 3117–3122. doi:10.1021/cs500476e.

[108] S.P. Shafi, L. Bi, S. Boulfrad, E. Traversa, Y and Ni Co-Doped BaZrO3 as a Proton-Conducting Solid Oxide Fuel Cell Electrolyte Exhibiting Superior Power Performance, J. Electrochem. Soc. 162 (2015) F1498–F1503. doi:10.1149/2.0701514jes.

[109] C.G. Vayenas, S. Bebelis, C. Pliangos, S. Brosda, D. Tsiplakides, Electrochemical Activation of Catalysis, Springer US, 2001.

[110] S.G. Neophytides, C.G. Vayenas, TPD and cyclic voltammetric investigation of the origin of electrochemical promotion in catalysis, J. Phys. Chem. 99 (1995) 17063–17067. doi:10.1021/j100047a001.

[111] P. Tsiakaras, C.G. Vayenas, Non-faradaic electrochemical modification of catalytic activity. VII. The case of methane oxidation on platinum, J. Catal. 140 (1993) 53–70. doi:10.1006/jcat.1993.1068.

[112] C.G. Vayenas, S. Ladas, S. Bebelis, I. V. Yentekakis, S. Neophytides, J. Yi, C. Karavasilis, C. Pliangos, Electrochemical promotion in catalysis: non-faradaic electrochemical modification of catalytic activity, Electrochim. Acta. 39 (1994) 1849–1855. doi:10.1016/0013-4686(94)85174-3.

[113] G.G. Vayenas, S. Bebelis, S. Ladas, Dependence of catalytic rates on catalyst work function, Nature. 343 (1990) 625–627. doi:https://doi.org/10.1038/343625a0.

[114] C. Wagner, Adsorbed Atomic Species as Intermediates in Heterogeneous Catalysis, Adv. Catal. 21 (1970) 323–381. doi:10.1016/S0360-0564(08)60567-2.

[115] C.G. Vayenas, Promotion, electrochemical promotion and metal-support interactions: Their common features, Catal. Letters. 143 (2013) 1085–1097. doi:10.1007/s10562-013-1128-x.

[116] E.I. Papaioannou, S. Souentie, A. Hammad, C.G. Vayenas, Electrochemical promotion of the CO2 hydrogenation reaction using thin Rh, Pt and Cu films in a monolithic reactor at atmospheric pressure, Catal. Today. 146 (2009) 336–344. doi:10.1016/j.cattod.2009.06.008.

[117] I. Kalaitzidou, M. Makri, D. Theleritis, A. Katsaounis, C.G. Vayenas, Comparative study of the electrochemical promotion of CO2 hydrogenation on Ru using Na+, K+, H+ and O2- conducting solid electrolytes, Surf. Sci. 646 (2016) 194–203. doi:10.1016/j.susc.2015.09.011.

[118] D. Theleritis, M. Makri, S. Souentie, A. Caravaca, A. Katsaounis, C.G. Vayenas, Comparative study of the electrochemical promotion of CO2 hydrogenation over Ru-supported catalysts using electronegative and electropositive promoters, ChemElectroChem. 1 (2014) 254–262. doi:10.1002/celc.201300185.

[119] I. Kalaitzidou, A. Katsaounis, T. Norby, C.G. Vayenas, Electrochemical promotion of the hydrogenation of CO2 on Ru deposited on a BZY proton conductor, J. Catal. 331 (2015) 98–109. doi:10.1016/j.jcat.2015.08.023.

[120] M.N. Tsampas, F.M. Sapountzi, A. Boréave, P. Vernoux, Investigation of the Electrochemical Promotion of Catalysis origins on electrochemical catalysts with oxygen ion conductive supports: Isotopic labeling mechanistic studies, Solid State Ionics. 262 (2014) 257–261. doi:10.1016/j.ssi.2014.01.008.

[121] X. Li, F. Gaillard, P. Vernoux, Investigations under real operating conditions of the electrochemical promotion by O2temperature programmed desorption measurements, Top. Catal. 44 (2007) 391–398. doi:10.1007/s11244-006-0131-5.

[122] M.N. Tsampas, F.M. Sapountzi, A. Boréave, P. Vernoux, Isotopical labeling mechanistic studies of electrochemical promotion of propane combustion on Pt/YSZ, Electrochem. Commun. 26 (2013) 13–16. doi:10.1016/j.elecom.2012.09.043.

[123] M. Makri, G.G. Vayenas, S. Bebelis, K.H. Besocke, C. Cavalca, Atomic resolution STM imaging of electrochemically controlled reversible promoter dosing of catalysts, Surf. Sci. 369 (1996) 351–359. doi:10.1016/S0039-6028(96)00911-9.

[124] H.A.E. Dole, R.J. Isaifan, F.M. Sapountzi, L. Lizarraga, D. Aubert, A. Princivalle, P. Vernoux, E.A. Baranova, Low temperature toluene oxidation over Pt nanoparticles supported on yttria stabilized-zirconia, Catal. Letters. 143 (2013) 996–1002. doi:10.1007/s10562-013-1071-x.

[125] R.J. Isaifan, M. Couillard, E.A. Baranova, Low temperature-high selectivity carbon monoxide methanation over yttria-stabilized zirconia-supported Pt nanoparticles, Int. J. Hydrogen Energy. 42 (2017) 13754–13762. doi:10.1016/j.ijhydene.2017.01.049.

[126] A. de Lucas-Consuegra, A. Caravaca, M.J. Martín de Vidales, F. Dorado, S. Balomenou,

D. Tsiplakides, P. Vernoux, J.L. Valverde, An electrochemically assisted NOx storage/reduction catalyst operating under fixed lean burn conditions, Catal. Commun. 11 (2009) 247–251. doi:10.1016/j.catcom.2009.10.004.

[127] E. Ruiz, D. Cillero, P.J. Martínez, Á. Morales, G.S. Vicente, G. De Diego, J.M. Sánchez, Bench scale study of electrochemically promoted catalytic CO2 hydrogenation to renewable fuels, Catal. Today. 210 (2013) 55–66. doi:10.1016/j.cattod.2012.10.025.

[128] S. Brosda, C.G. Vayenas, J. Wei, Rules of chemical promotion, Appl. Catal. B Environ. 68 (2006) 109–124. doi:10.1016/j.apcatb.2006.07.021.

[129] D. Grigoriou, D. Zagoraios, A. Katsaounis, C.G. Vayenas, The role of the promoting ionic species in electrochemical promotion and in metal-support interactions, Catal. Today. (2019). doi:10.1016/j.cattod.2019.08.024.

[130] C.G. Vayenas, S. Brosda, Electron Donation-Backdonation and the Rules of Catalytic Promotion, Top. Catal. 57 (2014) 1287–1301. doi:10.1007/s11244-014-0294-4.

[131] S. Souentie, C. Xia, C. Falgairette, Y.D. Li, C. Comninellis, Investigation of the "permanent" electrochemical promotion of catalysis (P-EPOC) by electrochemical mass spectrometry (EMS) measurements, Electrochem. Commun. 12 (2010) 323–326. doi:10.1016/j.elecom.2009.12.031.

[132] C. Falgairette, A. Jaccoud, G. Fóti, C. Comninellis, The phenomenon of "permanent" electrochemical promotion of catalysis (P-EPOC), J. Appl. Electrochem. 38 (2008) 1075–1082. doi:10.1007/s10800-008-9554-y.

[133] S. Bebelis, H. Karasali, C.G. Vayenas, Electrochemical promotion of CO2 hydrogenation on Rh/YSZ electrodes, J. Appl. Electrochem. 38 (2008) 1127–1133. doi:10.1007/s10800-008-9574-7.

[134] S. Bebelis, H. Karasali, C.G. Vayenas, Electrochemical promotion of the CO2 hydrogenation on Pd/YSZ and Pd/b"-Al2O3 catalyst-electrodes, Solid State Ionics. 179 (2008) 1391–1395. doi:10.1016/j.ssi.2008.02.043.

[135] A. Kotsiras, I. Kalaitzidou, D. Grigoriou, A. Symillidis, M. Makri, A. Katsaounis, C.G. Vayenas, Electrochemical promotion of nanodispersed Ru-Co catalysts for the hydrogenation of CO 2, Appl. Catal. B Environ. 232 (2018) 60–68. doi:10.1016/j.apcatb.2018.03.031.

[136] S. Bebelis, H. Karasali, C.G. Vayenas, Electrochemical promotion of the CO2hydrogenation on Pd/YSZ and Pd/β″-Al2O3catalyst-electrodes, Solid State Ionics. 179 (2008) 1391–1395. doi:10.1016/j.ssi.2008.02.043.

[137] M. Makri, A. Katsaounis, C.G. Vayenas, Electrochemical promotion of CO2 hydrogenation on Ru catalyst-electrodes supported on a K-β″-Al2O3 solid electrolyte, Electrochim. Acta. 179 (2015) 556–564. doi:10.1016/j.electacta.2015.03.144.

[138] Y.M. Hajar, B. Venkatesh, M.S.E. Houache, H. Liu, R. Safari, S. Prabhudev, G.A. Botton, E.A. Baranova, Electrochemical promotion of Bi-metallic Ni9Pd core double-shell

nanoparticles for complete methane oxidation, J. Catal. 374 (2019) 127–135. doi:10.1016/j.jcat.2019.04.026.

[139] Y.M. Hajar, B. Venkatesh, E.A. Baranova, Electrochemical promotion of nanostructured palladium catalyst for complete methane oxidation, Catalysts. 9 (2019) 48. doi:10.3390/catal9010048.

[140] H.A.E. Dole, L.F. Safady, S. Ntais, M. Couillard, E.A. Baranova, Electrochemically enhanced metal-support interaction of highly dispersed Ru nanoparticles with a CeO2 support, J. Catal. 318 (2014) 85–94. doi:10.1016/j.jcat.2014.07.003.

[141] Y.M. Hajar, H.A. Dole, M. Couillard, E.A. Baranova, Investigation of heterogeneous catalysts by electrochemical method: Ceria and titania supported iridium for ethylene oxidation, ECS Trans. 72 (2016) 161–172. doi:10.1149/07207.0161ecst.

[142] H.A.E. Dole, L.F. Safady, S. Ntais, M. Couillard, E.A. Baranova, Improved Catalytic Reactor for the Electrochemical Promotion of Highly Dispersed Ru Nanoparticles with CeO2 support, ECS Trans. 61 (2014) 65–74. doi:10.1149/06101.0065ecst.

[143] R.J. Isaifan, E.A. Baranova, Catalytic electrooxidation of volatile organic compounds by oxygen-ion conducting ceramics in oxygen-free gas environment, Electrochem. Commun. 27 (2013) 164–167. doi:10.1016/j.elecom.2012.11.021.

[144] P. Vernoux, Recent advances in electrochemical promotion of catalysis, Catalysis. 29 (2017) 29–59. doi:10.1039/9781788010634-00029.

[145] G. Pacchioni, F. Illas, S. Neophytides, C.G. Vayenas, Quantum-chemical study of electrochemical promotion in catalysis, J. Phys. Chem. 100 (1996) 16653–16661. doi:10.1021/jp9612386.

[146] G. Pacchioni, J.R. Lomas, F. Illas, Electric field effects in heterogeneous catalysis, J. Mol. Catal. A Chem. 119 (1997) 263–273. doi:10.1016/S1381-1169(96)00490-6.

[147] E.P.M. Leiva, C. Vázquez, M.I. Rojas, M.M. Mariscal, Computer simulation of the effective double layer occurring on a catalyst surface under electro-chemical promotion conditions, J. Appl. Electrochem. 38 (2008) 1065–1073. doi:10.1007/s10800-008-9539-x.

[148] F. Che, R. Zhang, A.J. Hensley, S. Ha, J.-S. McEwen, Density functional theory studies of methyl dissociation on a Ni(111) surface in the presence of an external electric field, Phys. Chem. Chem. Phys. 16 (2014) 2399–2410. doi:10.1039/C3CP54135E.

[149] F. Che, J.T. Gray, S. Ha, J.-S. McEwen, Improving Ni Catalysts Using Electric Fields: A DFT and Experimental Study of the Methane Steam Reforming Reaction, ACS Catal. 7 (2017) 551–562. doi:10.1021/acscatal.6b02318.

[150] F. Che, S. Ha, J.S. McEwen, Elucidating the field influence on the energetics of the methane steam reforming reaction: A density functional theory study, Appl. Catal. B Environ. 195 (2016) 77–89. doi:10.1016/j.apcatb.2016.04.026.

[151] S.N. Steinmann, P. Sautet, Assessing a First-Principles Model of an Electrochemical

Interface by Comparison with Experiment, J. Phys. Chem. C. 120 (2016) 5619–5623. doi:10.1021/acs.jpcc.6b01938.

[152] Y.M. Hajar, L. Treps, C. Michel, E.A. Baranova, S.N. Steinmann, Theoretical insight into the origin of the electrochemical promotion of ethylene oxidation on ruthenium oxide, Catal. Sci. Technol. 9 (2019) 5915–5926. doi:10.1039/c9cy01421g.

Chapter 2 : Thesis Objectives

2.1 Background and Motivation

Decarbonization is the greatest challenge of the 21st century. CO_2 is a very stable molecule, which requires a large energy input to convert it into valuable products. Reacting CO_2 with renewable hydrogen leads to carbon-neutral products and decreases anthropogenic dependence on fossil fuel use. Current research attempts to address the energy requirement and end-product selectivity by designing catalysts to undertake the reaction. Catalytic enhancement can be accomplished by a promotional effect induced through chemical promoters added in during the synthesis or in-situ controlled during the reaction. This is done by using ionically conductive material containing ionic species (*i.e.* O^{2-}, H^+, Na^+ and K^+) within its structure that can promote the reaction through a thermal input and electrical stimulus. The material acts a support which supplies promoters to the surface of the catalyst, altering the chemisorption of reactant and intermediate species. This effect is referred to as the metal-support interaction (MSI) with the use of nanoparticles that are dispersed on the conductive support.

To in-situ control the promotional effect, the non-Faradaic enhancement of catalytic activity (NEMCA) or electrochemical promotion of catalysis (EPOC) is applied. The cell configuration is a three-electrode electrochemical cell where the ionically conductive support is the solid electrolyte and the catalyst is the working electrode. By closing the electrical circuit, ions like O^{2-}, H^+, Na^+ and K^+ migrate to the surface of the catalyst which alter the binding energy of the reaction species. Both the MSI and EPOC effect are functionally equivalent which have shown to typically enhance the reaction by altering the activation energy and end-product selectivity of reactions. Evaluating these phenomena through the use of density functional theory (DFT) calculations provide an understanding in the reaction mechanisms and catalytic design.

The release of CO_2 into the atmosphere will continue to remain a climate crisis issue. Increasing the incentives to utilize it as a resource and develop products that replace the need for fossil fuels, the economy will not need to depend on non-sustainable energy sources. At the time of this writing, the field of CO_2 conversion has evolved in popularity and is vastly researched worldwide bringing forth new discoveries allowing for friendly competition and collaborations

between research teams that will undoubtfully result in scientific breakthroughs in decarbonizing society.

2.2 Research Objectives

The overall objective of this research was to study and develop a catalyst and reactor setup to undertake the reverse water gas shift (RWGS) reaction by reacting CO_2 and H_2 to produce CO and H_2O efficiently and economically to address the constraints discussed in Chapter 1. To employ the MSI and EPOC phenomena and study their enhancement effect on nanostructured catalysts under experimental and theoretical evaluation.

The following objectives have been executed:

- Synthesis of nanoparticles with an average particle size of less than 10 nm, including ruthenium (Ru) and iron (Fe) and bimetallic catalyst, RuFe of various atomic compositions.
- Characterize the physicochemical properties of the catalysts through transmission electron microscopy (TEM), scanning transmission electron microscopy (STEM), scanning electron microscopy (SEM), X-ray diffraction (XRD), X-ray photoelectron spectroscopy (XPS), thermal gravimetric analysis (TGA), ionically-coupled plasma emission spectroscopy (ICP-ES) and cyclic voltammetry (CV).
- Evaluate the catalytic activity of the MSI effect and self-induced EPOC for noble and non-noble metal nanoparticles supported on ionically conductive, mixed-ionically conductive, non-conductive supports, and semi-conductor metal-oxide for various CO_2:H_2 ratios and temperature.
- Apply and compare the EPOC phenomenon for noble and non-noble metal free-standing and supported nanoparticles to enhance the selectivity and catalytic rate for the RWGS reaction. Measure the enhancement ratio and apparent non-Faradaic efficient and incorporate metal-oxides for the permanent-EPOC effect.
- Study the influence O^{2-} and H^{+} ions have on the RWGS reaction.
- Gain insight towards the EPOC effect for RWGS reaction and selectivity using Density Functional Theory (DFT).

2.3 Thesis Structure

The overall objective of the research is obtained through the progression of Chapter 3-8. To begin, Chapter 1 discusses the literature review of the importance of utilizing CO_2, the RWGS reaction and catalysts, methods to promote the catalytic rate by the MSI and EPOC phenomena and concluding with theoretical DFT calculations to provide insights at what occurs at the atomic scale. To evaluate and understand the concept of the MSI effect Chapter 3 begins with the use of supported nano-catalysts. Following the high catalytic activity observed in Chapter 3 for the ionically conductive support, the remaining Chapters employ the use of solid electrolytes to evaluate the EPOC phenomenon and the selectivity towards the RWGS reaction. Chapter 4 and 5 employ the same nano-catalyst deposited on oxygen and proton conducting solid electrolyte, respectively. Independent on the type of solid electrolyte, the response to electrochemical polarization remained the same. To provide insight on how the EPOC effect can affect reaction selectivity, theoretical DFT calculations are performed in Chapter 4. This led to the understanding on how polarization affects the binding energy of the CO molecule playing a role in the selectivity of the reaction. After understanding the behaviour of noble metals, Chapter 6 moves towards practical application by employing non-noble transition metal catalysts. It was determined that polarization for non-noble metal-oxides did not only affect the catalytic activity but also the oxidation state of the catalyst. Chapter 7 non-noble metal-oxide is doped with a noble metal to evaluate its EPOC effect. After further understanding on the oxidation state of the catalyst, Chapter 8 concludes with the use a metal-oxide paired with a metal-oxide semiconductor nanostructured catalyst, resulting in the highest catalytic activity.

The main hypothesis is that non-conductive supports do not enhance the reaction rate as much as conductive supports. Since the catalytic reaction take places mainly on the surface, employing nanostructured catalysts amplifies the catalytic activity due to its high surface-to-volume ratio. Furthermore, the use of highly dispersed nanoparticles will tailor the selectivity towards the RWGS reaction. Polarization of the catalyst will allow the reaction to take place at lower temperatures and provide a way to in-situ control catalyst selectivity. The use of O^{2-} from YSZ can be used to alter the oxidation state of the catalyst. Non-noble metal thick films have not responded to the effect EPOC, while the use of nano-catalysts have yet to be investigated. The addition of an intermediate layer between nanoparticles and the solid electrolyte can increase catalyst dispersion and improve conductivity.

The sub-objective was achieved by synthesizing nanoparticles though the polyol method and dispersing them on various supports. Chapter 3 discusses the synthesis of monometallic Ru and bimetallic Ru_xFe_{100-x} (x=20, 45, 80) nanoparticles (1-2.5 nm) supported on mixed-ionic electronic (CeO_2, SDC, Gd-CeO_2, Y_2O_3-CeO_2), ionically conductive (YSZ) and non-conductive (carbon) supports by various loadings. It was determined that the addition of Fe improved the thermal stability of Ru without drastically compromising catalytic activity. Furthermore, $Ru_{45}Fe_{55}$/YSZ displayed the highest catalytic at lower temperatures affiliated to its ionically conductive properties and used as the preferred supports (solid electrolytes YSZ and BZY) in Chapters 4-8. Chapter 4 and 5 employ Ru nanoparticles (1-2 nm) deposited on YSZ and BZY, respectively. Additionally, in Chapter 4 Ru nanoparticles are dispersed on the semi-conductor Co_3O_4 to act as intermediate layer support for Ru. Chapter 6 employs FeO_x nanowires (Ø = 5 nm) on YSZ, showing for the first time non-noble metals to be electrochemically active for the RWGS reaction. From the breakthrough of FeO_x nanowires, Chapter 7 combines Ru nanoparticles with FeO_x nanowires through a 2-step synthesis method and deposited on YSZ. Finally, Chapter 8 entails the combination of FeO_x nanowires with Co_3O_4 greatly enhancing the MSI interaction allowing the catalyst to display the highest catalytic activity discussed in this research.

Several characterization techniques were used to undertake this project. All catalysts have been examined through STEM analysis (Chapter 3-8) and TEM (Chapter 5 and 8) to determine the catalyst size, while SEM (Chapter 3, 5, 6 and 8) was used to determine the morphology of the catalyst. EDX mapping (Chapter 3, 5, 6 and 8) of STEM images was performed to provide elemental composition. EELS mapping (Chapter 5, 6 and 8) was performed to distinguish and visualize the various elemental compositions on the STEM images. To determine the physical properties of the catalyst in Chapter 3, TGA and ICP-EPS were used. XRD (Chapter 5) was done to provide crystallographic insight and oxidation state of the catalyst. XPS spectra (Chapter 5 and 6) were collected to provide information on the oxidation state of the catalyst. Electrochemical CV characterizations (Chapter 6) were done to investigate the change in oxidation state of the catalyst with respect to potential application.

The MSI effect of nano-catalysts were examined in a fixed-bed reactor (Chapter 3 and 8) in the temperature range of 200-800°C with varied catalyst loading amount and ratio of CO_2 and H_2. In Chapter 3 the catalyst atomic composition, loading, reaction conditions and stability were

optimized taking into consideration the catalytic activity towards the RWGS reaction. In Chapter 5 and 8 the self-induced EPOC effect for Ru and FeO_x supported on the semi-conductor Co_3O_4 under various CO_2:H_2 ratios was evaluated.

The EPOC phenomenon was evaluated for each catalyst mentioned in Chapter 4, 5, 6, 7, and 8. Open-circuit catalytic activity was achieved followed by the application of constant potential or current. The EPOC effect was measured according to the enhancement ratio (ρ), apparent Faradaic efficiency (Λ) and permanent-EPOC (γ).

To investigate the influence of the type of ionic species, the same Ru nanoparticles were deposited on YSZ (O^{2-}) (Chapter 4) and BZY (H^+) (Chapter 5) and evaluated under the same reaction conditions. To provide further insight on how the EPOC phenomenon and polarization affects reaction selectivity, DFT modeling is employed to elucidate the reaction mechanism. This study was achieved by modeling the CO_2 hydrogenation over a Ru(0001) slab and evaluating the EPOC phenomenon by adding and removing electrons to simulate the effect of potential.

Chapter 3 : Insight towards the role of ceria-based supports for the reverse water gas shift reaction over RuFe nanoparticles

Adapted from: ***C. Panaritis****, M. Edake, M. Couillard, R. Einakchi, E.A. Baranova, Journal of CO_2 Utilization, 26 (2018) 350–358.*

Abstract

Utilization of CO_2 through the reverse water gas shift (RWGS) reaction is a promising solution in managing greenhouse gas emissions. Here, we used the RWGS reaction to evaluate the catalytic conversion of CO_2 over Ru-Fe nanoparticles supported on samarium-doped ceria (SDC) support. Catalysts of different Ru_xFe_{100-x} compositions (x = 100, 80, 45, 20, 0 at.%) have been studied under steady-state conditions in a packed bed reactor in the temperature range 300-800 °C to determine their catalytic activity and selectivity towards CO. The metal-support interaction (MSI) effect for SDC was evaluated to determine its promotional behaviour for the RWGS reaction. The catalyst was characterized using TEM, TGA, and ICP-ES techniques. Among all investigated catalysts, $Ru_{45}Fe_{55}$/SDC (2 wt.%) displayed the overall best activity and CO selectivity. A stability test of 100 h at 650 °C confirmed an excellent stability of the $Ru_{45}Fe_{55}$/SDC catalyst. Overall, the use of $Ru_{45}Fe_{55}$/SDC (2 wt.%) is a promising catalyst in the utilization of CO_2, reaching a maximum CO yield of ~47.5% at 800 °C and 100% CO selectivity above 500 °C. Furthermore, $Ru_{45}Fe_{55}$ (2 wt.%) nanoparticles were deposited on un-doped CeO_2 and doped ceria: Gd-CeO_2, Y_2O_3-CeO_2, as well as yttria-stabilized zirconia (YSZ) and carbon supports. Contrary to carbon support, all catalysts containing oxygen conducting-ceramic supports displayed 100% selectivity to CO at temperatures above 600 °C, which can be attributed to the synergistic relationship between Ru-Fe nanoparticles being promoted through the MSI and thermally induced migration of promoting ionic species ($O^{\delta-}$) from oxygen conducting ceramics to the nanoparticles.

3.1 Introduction

Ru is the most economical amongst the noble metals, and has shown to display catalytic activity similar to Pt, but is favourable in CH_4 formation [1,2]. Additionally, it accounts for a large number of oxidation states that exhibit high electron transfers, making it a suitable candidate for

CO_2 hydrogenation [3]. Previous studies show Fe to display properties of high stability at elevated temperatures [4]. Pairing Ru with Fe presents the opportunity of using less noble metals, while not compromising activity and allowing for a synergistic relationship between different metals. Methanol (CH_3OH) has not been shown to be formed through the Sabatier side reaction using these metals.

In this chapter, the catalytic activity of mono- and bimetallic Ru, Fe and Ru_xFe_{100-x} (x = 100, 80, 45, 20, 0 at.%) nanoparticles (1.5 - 2 nm) supported on CeO_2, ,mixed-ionic electronical conductive (MIEC) and ionically conductive doped-CeO_2 (Sm-CeO_2 (SDC), Gd-CeO_2 and Y_2O_3-CeO_2) and YSZ, and non-ionic carbon were examined for the RWGS reaction in order to shed light on MSI effect and role of O^{2-} from the support. The effect of Ru to Fe atomic ratio along with the overall metal loading on SDC support was examined to reduce the amount of Ru while ensuring high activity. Furthermore, the gas composition (CO_2:H_2 ratios) and the stability of the best-performed catalyst, as well as its activity for water gas shift reaction have been investigated.

3.2 Experimental

3.2.1 *Synthesis of colloidal nanoparticles*

Ru, Fe and Ru-Fe nanoparticles were synthesized using the polyol synthesis method. This method consists of mixing metal precursors with ethylene glycol and sodium hydroxide (NaOH): ethylene glycol acting as a reaction medium and a reducing agent [5], and NaOH to increase the pH of the solution, which governs the size of the nanoparticles by allowing the ethylene glycol to act as a stabilizer. Ruthenium chloride ($RuCl_3$) (anhydrous, Sigma Aldrich) and iron (III) nitrate ($Fe(NO_3)_3$) (nanohydrate, Fischer Scientific) were synthesized in 50 mL ethylene glycol (Fischer-Scientific certified grade) containing 0.08 M NaOH. For example, the $Ru_{45}Fe_{55}$ (atomic composition) colloid solution was prepared with 0.123 g and 0.2916 g of $RuCl_3$ and $Fe(NO_3)_3$, respectively. The colloid solution was mixed for 1 h at room temperature where the pH increased to 11. It was then refluxed for 3 h at 160 °C, cooled, and then stored at room temperature. The final mixture for bimetallic $Ru_{45}Fe_{55}$ colloid was dark brown in colour. The remainder of the colloids were prepared by the same method with their respective concentrations and were all dark brown in colour.

3.2.2 *Supported mono- and bi-metallic Ru and Fe nanoparticles*

The supported nanoparticles were prepared as follows: the colloid amount was determined in terms of metal loading and was mixed with 500 mg of SDC (Fuel Cell Materials, specific surface area (SSA) 33.8 $m^2\ g^{-1}$) and 40 mL deionized water (18 MΩ cm) and stirred at room temperature for 48 hours. The mixture was then centrifuged three times, being rinsed with deionized water between each step to remove any remaining salt and ethylene glycol from the synthesis. The catalyst was left to dry in a fume hood for two days and further oven dried at 120 °C for 3 h. Multiple catalysts were prepared to contain the same SDC support amount of 500 mg. The compositions of the catalyst were Ru/SDC (0.5 and 5 wt.%), Fe/SDC (5 wt.%), $Ru_{20}Fe_{80}$/SDC (5 wt.%) and $Ru_{45}Fe_{55}$/SDC (0.5, 1, 2, 3, and 5 wt.%). The best performing Ru_xFe_{100-x} catalyst was prepared on supports CeO_2 (Alfa Aesar, SSA 30-50 $m^2\ g^{-1}$), Gd-CeO_2 (Sigma Aldrich, SSA 10-14 $m^2\ g^{-1}$), Y_2O_3-CeO_2 (Sigma Aldrich, SSA 33-38 $m^2\ g^{-1}$), YSZ (Tosoh, SSA 13 $m^2\ g^{-1}$) and C (Cabot, 250 $m^2\ g^{-1}$).

3.2.3 *Physicochemical Characterization*

The size of the catalysts was determined using scanning transmission electron microscopy (STEM) performed on a FEI Titan^3 80-300 TEM operated at 300 keV, equipped with a CEOS aberration corrector for the probe-forming lens. Annular dark field (ADF) images were taken using a Fishione detector to provide a contrast between the nanoparticles and support. The convergence and collection angles were 17 and 60 mrad, respectively. The TEM samples were prepared through sonicating the powder catalyst in ethanol and then one drop deposited onto a 200 mesh TEM copper grid coated with a lacey carbon support film (Ted Pella). Scanning transmission electron microscopy (SEM) and energy dispersive spectroscopy (EDS) were taken using JSM-7500F (JEOL) to further determine the size of the catalyst and to confirm the presence of Ru and Fe. X-Ray Diffraction (XRD) patterns did not show any peaks because the monometallic Ru and bimetallic Ru_xFe_{100-x} were amorphous making it difficult to confirm the formation of an alloy. The weight loss of the catalyst was measured from 25 °C to 900 °C in increments of 10 °C/min using thermal gravimetric analysis (TGA) (Q5000 IR). Confirmation of the metal composition of the powder catalyst was determined through inductively coupled plasma emission spectroscopy (ICP-ES) (Agilent 8800).

3.2.4 *Reaction Experiment*

The catalytic performances of the synthesized catalysts were evaluated using the RWGS reaction in the temperature range of 300-800 °C under atmospheric pressure. An increase in pressure did not affect the reaction [6]. The setup is displayed in Figure 3-1. The temperature was monitored by a thermocouple (OMEGA®) placed directly in contact with the outside of the reactor at the location of the catalyst. Each experiment followed the same procedure where 50 mg of the powder catalyst was placed into the packed bed 4 mm tubular quartz reactor supported by inert quartz wool. A gas mixture of 2 kPa CO_2 (Linde, 99.99%), 2 kPa H_2 (Linde, 100%) and 96 kPa He (Linde, 100%) was sent through mass flow controllers (MFC, MKS Instruments) and then to the reactor. The total pressure and flow rate of the mixture of gas was 100 kPa and 100 mL min^{-1}, respectively. Prior to each experiment, the catalyst underwent a pretreatment step, where it was reduced under a flow of 20% H_2:He at a rate of 60 mL min^{-1} at 400 °C for 1 hour. The reaction was performed at 50 °C intervals in the range of 300-800 °C and held constant at each interval for 20-30 minutes or until rate concentrations were stabilized. The gas hourly space velocity *GHSV* was 1,020,000 h^{-1}, calculated using the following equation (eq. 3-1):

$$GHSV = \frac{F * d}{W} \qquad 3\text{-}1$$

Where *F* is the flow rate, *d* is the support bulk density and *W* is the mass of the support. The product gases were analyzed using a non-dispersive infrared CO analyzer (Horiba VIA-510) and a quadrupole mass spectrometer (QMS, Ametek Proline DM 100), with values for CO_2, CO, H_2O, CH_4, He and H_2 corresponding to the m/z (mass-to-charge) ratios 44, 28, 18, 15, 4 and 2, respectively.

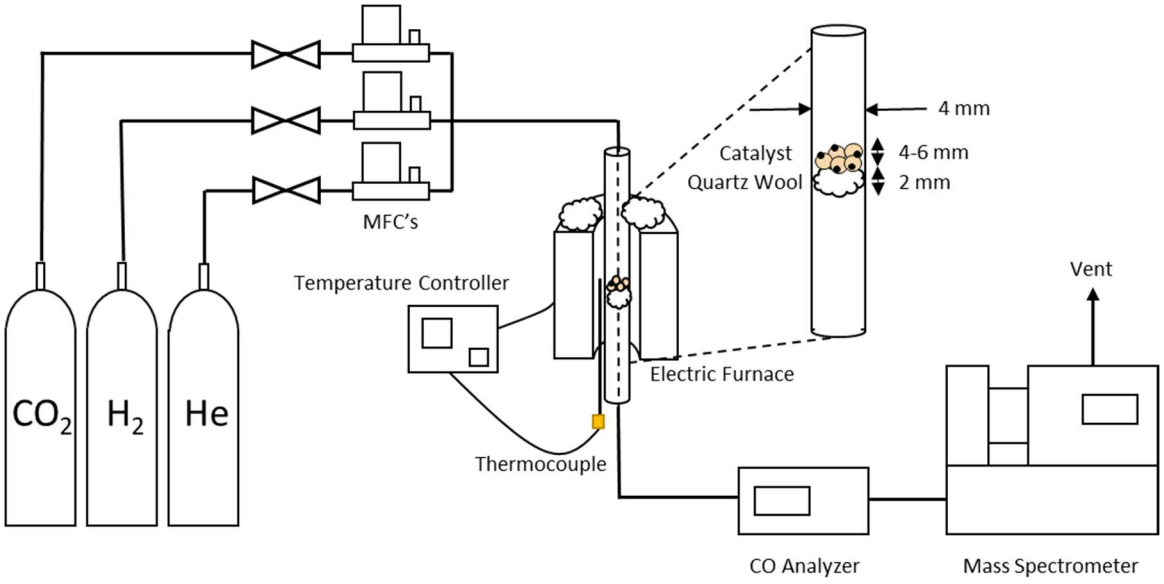

Figure 3-1. Experimental set-up for the fixed-bed RWGS reactor.

Each set of experiments was repeated 2-3 times to evaluate the stability and reproducibility. The 2nd and 3rd runs were identical for all catalysts investigated as shown in Figure A-1 in Appendix A. The results of the second run are shown in all figures, unless otherwise stated. The catalyst that displayed the best results, namely $Ru_{45}Fe_{55}$/SDC, underwent a stability test at 650 °C for 100 hours, following the same reaction procedure. The yield of CO and CH_4 was calculated as displayed in the following equations:

$$Conversion\ of\ CO_2 = \frac{[CO_2]_{in} - [CO_2]_{out}}{[CO_2]_{in}} * 100 \quad 3\text{-}2$$

$$Yield\ of\ CO = \frac{[CO]_{out}}{[CO_2]_{out} + [CO]_{out} + [CH_4]_{out}} * 100 \quad 3\text{-}3$$

$$Yield\ of\ CH_4 = \frac{[CH_4]_{out}}{[CO_2]_{out} + [CO]_{out} + [CH_4]_{out}} * 100 \quad 3\text{-}4$$

The turnover frequency (TOF) values were calculated using the average size of the nanoparticles from the STEM analysis. The dispersion values for Ru, $Ru_{20}Fe_{80}$ and $Ru_{45}Fe_{55}$ nanoparticles were done using the following equation [7]:

$$D = \frac{6 * \frac{V_{NP}}{SA_{NP}}}{d} \quad 3\text{-}5$$

Where V_{NP} and SA_{NP} represents the volume and surface area of a Ru atom, represented by the values 13.65 Å^3 and 6.35 Å^2 respectively, and d is the average particle size of the Ru atoms from the STEM analysis [7]. The Ru_xFe_{100-x} nanoparticles were calculated using the values of Ru. TOF values were calculated using the following equation:

$$TOF = \frac{F_{CO2} * X_{CO} * M}{W * D * x} \quad 3\text{-}6$$

Where F_{CO2} is the flow rate of CO_2 at the inlet, X_{CO} is the proportion of CO at the outflow, M is the atomic mass of Ru, W is the weight of the catalyst, D is the dispersion, and x is the loading amount of Ru on the SDC.

Additionally, the water gas shift reaction was conducted using the same reactor setup as the RWGS, with the addition of a humidifier before the reactor. The best performing catalyst was studied in the temperature range of 250-600 °C. A gas mixture of 1% CO and He balance (Linde, 1/99%) was sent through the mass flow controller at a rate of 83 mL min^{-1}. The gas was sent through deionized water (18 MΩ cm) to humidify the CO before entering the reactor. Prior to the experiment, the catalyst was reduced with 20% H_2:He at 400 °C for 1 h.

3.3 Results & Discussion

3.3.1 *Catalyst Characterization*

Mono- and bi-metallic Ru, FeO_x and Ru_xFe_{100-x} nanoparticles were prepared using the polyol synthesis method. Larger particles are not appropriate for RWGS since they have been proven to promote methane formation and tend to agglomerate promoting catalyst deactivation [8,9]. STEM analysis was performed for Ru/SDC (0.5 wt.%), $Ru_{20}Fe_{80}$/SDC (5 wt.%), $Ru_{45}Fe_{55}$/SDC (5 wt.%) and Ru/CeO_2 (1 wt. %), and representative micrographs are shown in Figure 3-2 (a), (b), (c), and (d), respectively. STEM image of as-prepared monometallic Ru is shown in Figure A-2 (a). Ru and Ru-Fe nanoparticles are spherical in shape and could be distinguished at the surface of SDC only due to poor contrast between nanoparticles and the support. Nanoparticle size falls in the range of 1-2.5 nm. SEM image Figure A-2 (b) shows the roughness of the support material. EDS analysis (Figure A-3) showed the presence of both Ru and

Fe in bimetallic NPs. ICP-ES analysis confirmed that nominal and actual Ru to Fe at. ratio and metal loading are in good agreement (+/- 2-5% difference between nominal and actual values). TGA was performed for $Ru_{45}Fe_{55}$/SDC (Figure A-4) in nitrogen. The results display a small initial weight loss from room temperature to 100 °C that can be attributed to loss through volatilization and/or water desorption. The total weight loss was 3.3%, which remained constant from 550 °C to 900 °C, suggesting that the catalyst is thermally stable up to 900 °C.

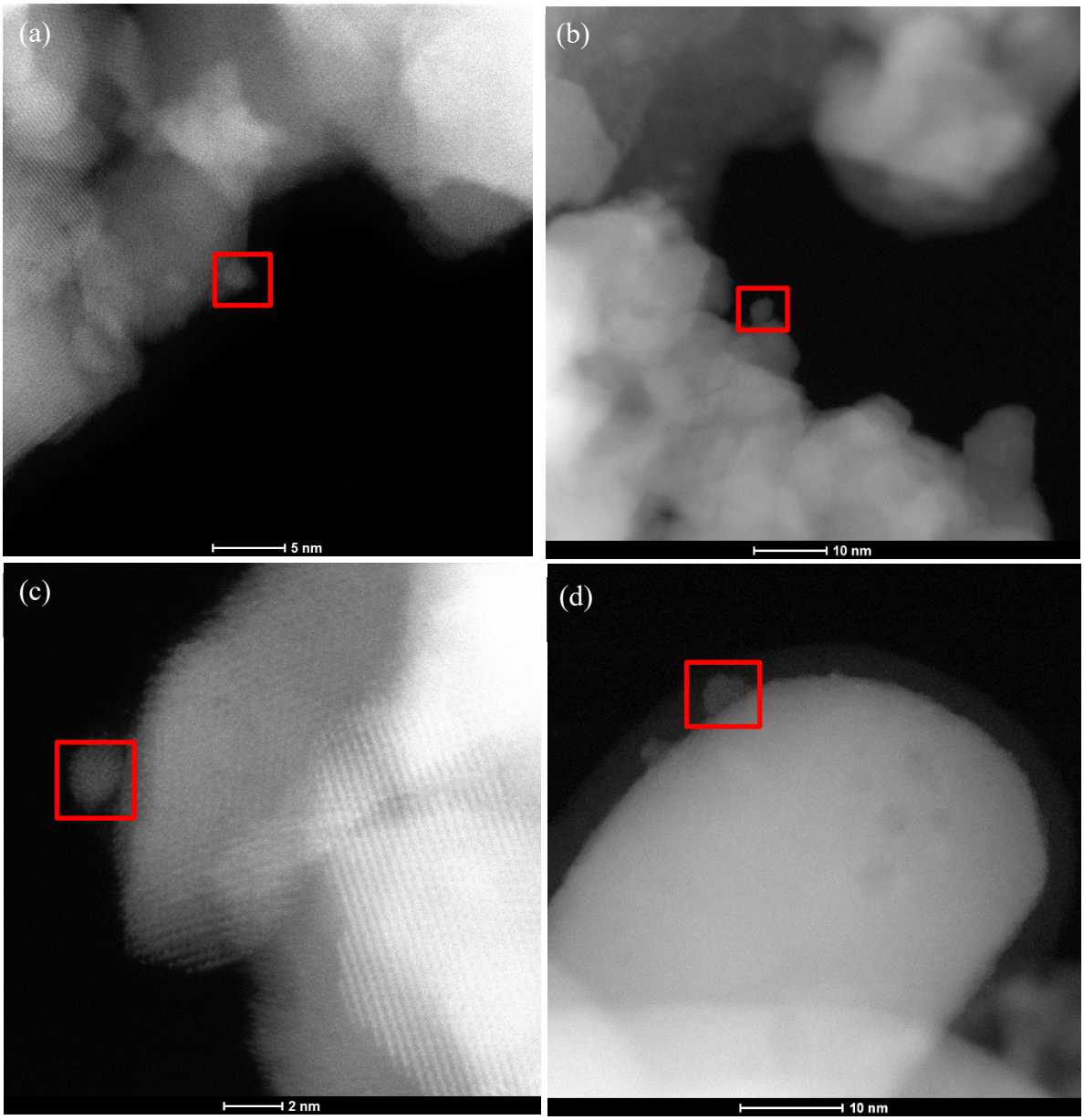

Figure 3-2. STEM images of mono- and bi-metallic Ru nanoparticles supported on SDC. (a) Ru/SDC (0.5 wt.%), (b) $Ru_{20}Fe_{80}$/SDC (5 wt.%), (c) $Ru_{45}Fe_{55}$/SDC (5 wt.%) and (d) Ru/CeO_2 (1 wt.%).

3.3.2 ***RWGS catalyst performance***

3.3.2.1 Monometallic Ru/CeO_2 and Ru/SDC nanoparticles

The CO yield results over Ru/CeO_2 (5 wt.%) and Ru/SDC (5 wt.%) in the temperature range 300-750 °C are displayed in Figure 3-3 (a), in addition, the activity of bare SDC and CeO_2 are also shown. Doping ceria with samarium (Sm), gadolinium (Gd) or dysprosium (Dy) has been shown to enhance the catalytic activity of CO and C_2H_4 complete oxidation [10–12]. Both bare supports, SDC and CeO_2 show CO production starting from 500 °C and reach almost 40% CO yield at 750 °C. This indicates that both oxide supports are catalytically active and their activity is related to their ionic conductivity as non-conductive supports, e.g. γ-Al_2O_3, SiO_2, C where no activity has been reported [9,13,14]. SDC has a slightly better performance above 600 °C, which can be attributed to its higher O^{2-} ionic conductivity and the presence of a higher number of oxygen vacancies due to Sm causing strain on the ceria structure [10,12]. When 5 wt.% of Ru was deposited on CeO_2 and SDC, the catalytic activity at lower temperatures increased significantly. The CO yield is similar for both catalysts above 500 °C, reaching ~ 46% and ~ 45% at 750 °C for Ru/CeO_2 and Ru/SDC, respectively. At temperatures below 500 °C, Ru/SDC outperformed Ru/CeO_2 and showed higher selectivity towards CO. Some CH_4 production was observed up to 500 °C on both catalysts, as can be seen in Figure 3-3 (b). CH_4 production for both Ru/CeO_2 and Ru/SDC reached a maximum of ~10% and ~5%, respectively at 350 °C. Additionally, to study the effect on CH_4 production on SDC supports, a study was conducted using Ru/SDC (0.5 wt.%) at CO_2:H_2 ratios of 1:1, 1:3 and 1:5 (Figure A-5 (a) and (b)). In Figure A-5 (b), the results for the second run depict that for ratios 1:3 and 1:5, CH_4 formation still occurred between 300 – 500 °C with a maximum yield of 10% at 400 °C and that for 1:1 CH_4 was formed in trace amounts. Formation of CH_4 during the second run can be due to the structure of Ru favouring CH_4 formation, which it is known to form at lower temperatures with high CO_2:H_2 ratios [1]. It was also noticed that during this study the Ru/SDC catalyst products required more than 20 minutes to stabilize on the mass spectrometer, suggesting that Ru on its own is less stable when compared with tests with Fe (discussed in the next sections). Furthermore, due to the bulk density of CeO_2 being lower than that of SDC, a greater volume reactor is required for CeO_2 to avoid a pressure build-up. Since SDC on its own displayed a better catalytic, stability performance, has a greater bulk density, lower CH_4 production and has been rarely studied for the RWGS reaction, it was used as the main support for this study [15].

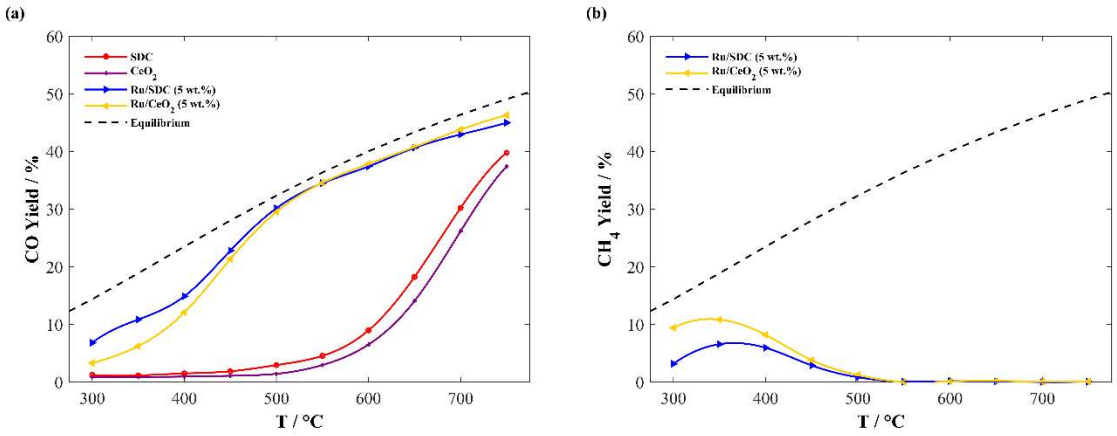

Figure 3-3. Yield of (a) CO and (b) CH_4 as a function of temperature for 5 wt.% Ru/CeO_2 and Ru/SDC catalysts for CO_2:H_2 1:1. 50 mg of catalyst and 100 mL min^{-1}.

3.3.2.2 Effect of Ru:Fe ratio on Ru_xFe_{100-x}/SDC catalysts

Mono- and bi-metallic compositions of Ru and Fe supported on SDC were investigated to determine the highest CO yields in the temperature range of 300-750 °C. The results for the CO yield are displayed in Figure 3-4 (a) for SDC, Ru/SDC (5 wt.%), Fe/SDC (5 wt.%), $Ru_{20}Fe_{80}$/SDC (5 wt.%), $Ru_{45}Fe_{55}$/SDC (5 wt.%) and $Ru_{80}Fe_{20}$/SDC (5 wt.%). All catalysts were highly active and reached a constant rate of reaction above 600 °C. The Fe/SDC catalyst displayed a similar activity trend to SDC with minimal activity at lower temperatures and becoming active above 500 °C. Ru/SDC was highly active at lower temperatures and remained at a constant reaction rate with respect to the theoretical yield. $Ru_{20}Fe_{80}$/SDC displayed a constant rate of reaction but with lower yields, which can be attributed to the high amount of Fe present, suppressing its activity, as seen for Fe/SDC. The $Ru_{80}Fe_{20}$/SDC catalyst displayed similar activity to Ru/SDC, which can be due to the large amount of Ru present. The final catalyst $Ru_{45}Fe_{55}$/SDC displayed the best activity, equally benefiting from the synergistic effect between the Ru and Fe metals. It displays a low activity under 450 °C and increases significantly after 550 °C with a constant CO yield close to equilibrium yields and reaching a CO yield (and CO_2 conversion) of ~48% at 750 °C. The initial low activity can be explained by the presence of Fe, as seen with the Fe/SDC and $Ru_{20}Fe_{80}$/SDC catalysts. Given that $Ru_{45}Fe_{55}$/SDC displayed the highest CO yields at higher temperatures it was chosen as the main focus of study. Even though Ru/SDC (5 wt.%) and $Ru_{80}Fe_{20}$/SDC (5 wt.%) displayed higher CO yields at lower temperatures than $Ru_{45}Fe_{55}$/SDC (5 wt.%), the yield amount is far less than what occurs at higher temperatures. The TOF values for catalysts Ru/SDC (0.5

wt.%), $Ru_{20}Fe_{80}$/SDC (5 wt.%) and $Ru_{45}Fe_{55}$/SDC (5 wt.%) are displayed in Figure 3-4 (b), where the activity is dependent on dispersion results. Similar trends are depicted for all catalysts suggesting that the preparation method ensures sufficient dispersion. The $Ru_{20}Fe_{80}$/SDC catalyst displayed the highest TOF trend with a lower CO_2 conversion and lower dispersion, suggesting that the sites are very active. The increased portion of Fe has caused the particles to agglomerate, increasing the exposure of Ru active sites.

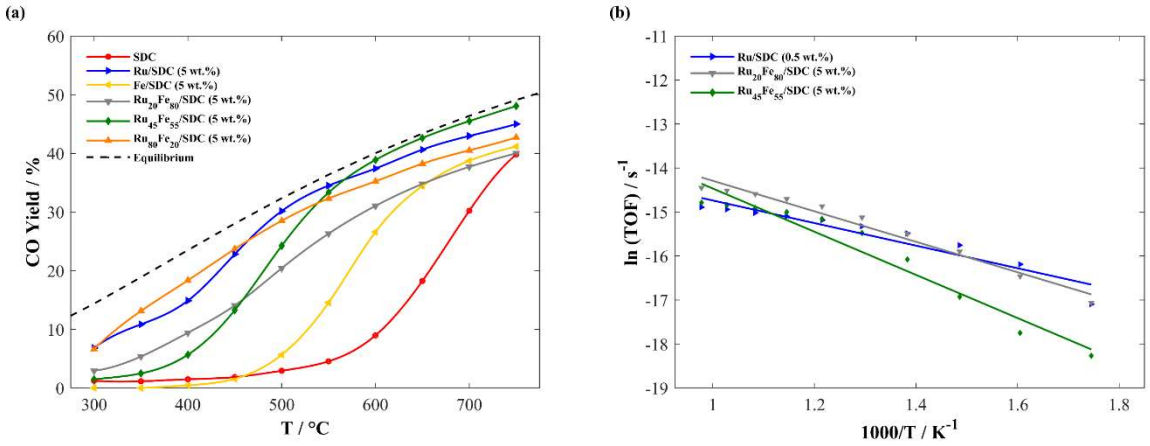

Figure 3-4. (a) Yield of CO and (b) TOF values as a function of temperature for various catalysts as indicated in the figure 50 mg of catalyst, CO_2:H_2 1:1 and 100 mL min^{-1}.

3.3.2.3 Effect of metal loading

The $Ru_{45}Fe_{55}$/SDC catalyst was analyzed with metal loadings of 0.5, 1, 2, 3 and 5 wt.% in the temperature range 400-800 °C to determine a suitable metal loading. A maximum metal loading of 5 wt.% was chosen because higher values were shown not to improve the activity and possibly cause deactivation due to the agglomeration of the nanoparticles [16]. Lowering the metal content reduces the amount of metal used, lowering the cost and susceptibility of deactivation from the nanoparticles not being highly dispersed. Displayed in Figure 3-5, the catalysts all exhibit a high conversion of CO_2 and a high selectivity to CO. The 5 wt.% and 3 wt.% catalysts showed similar activity of ~ 50% and ~ 51% CO yield at 800 °C, indicating that the difference in loading minimally affected its performance and can be assumed that metal loadings above 3 wt.% does not significantly increase CO yield. The 2 wt.% catalyst displayed a slightly lower activity when compared with the 5 wt.% and 3 wt.% catalyst, indicating that the catalyst is sufficiently active at a lower metal loading with a CO yield of ~ 47.5% at 800 °C. Additionally, the reason for the high

2 wt.% activity can be due to the high dispersion of particles on the support – allowing for less agglomeration and exposing a sufficient number of active sites. The 1 wt.% and 0.5 wt.% displayed CO yields of ~ 40% and ~ 41% at 800 °C, respectively. They were significantly lower than the 2 wt.%, 3 wt.% and 5 wt.% catalysts and performed worse than SDC alone at 800 °C, with a CO yield of ~ 45%. This can be due to the reduction in active sites by the reduction in metal loading. Additionally, a pattern is observed between the 0.5 wt.% and 1 wt.% catalysts, where the rate of conversion remains constant and highly active even at lower temperature, however, for the purpose of producing a large amount of CO, production at higher temperatures were desired. Since the reaction is 100% selective to CO, the CO yield also represents the CO_2 conversion.

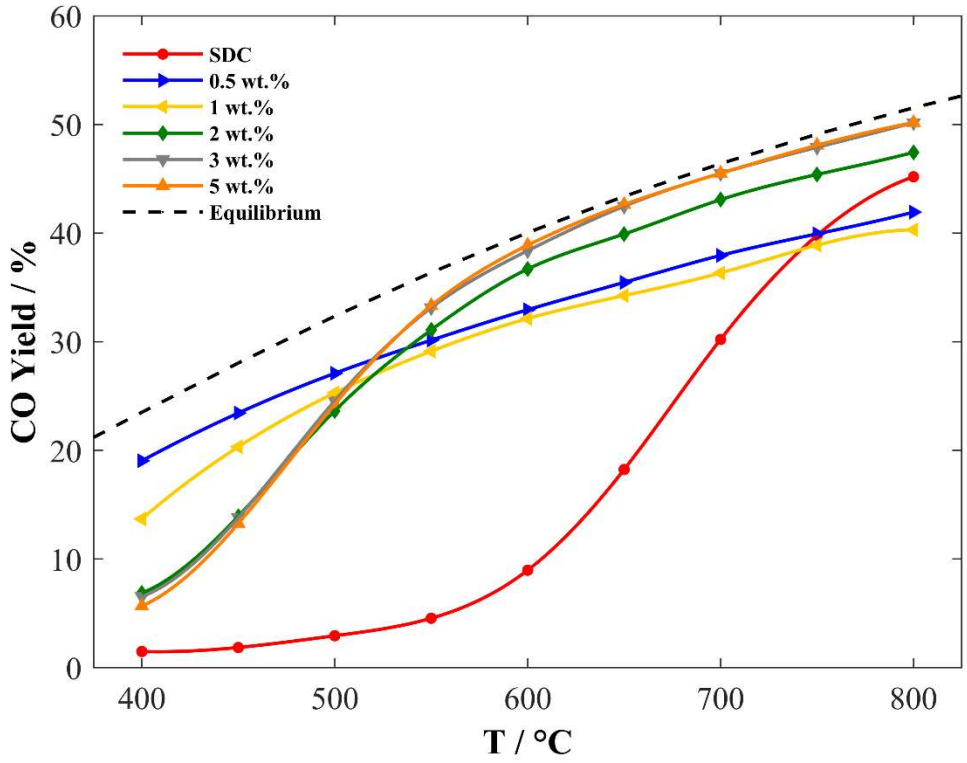

Figure 3-5. CO yield for $Ru_{45}Fe_{55}$/SDC metal loadings of 0.5 wt.%, 1 wt.%, 2 wt.%, 3 wt.% and 5 wt.%. 50 mg of catalyst, CO_2:H_2 1:1 and 100 mL min^{-1}.

3.3.2.4 Effect of CO_2:H_2 ratio

Given the performance of each catalyst, the 2 wt.% catalyst was chosen for further study since it is more economically viable (*i.e.,* less metal used) and still maintains a high catalytic activity. The effect of H_2 concentration for $Ru_{45}Fe_{55}$/SDC (2 wt.%) was examined with varying CO_2 to H_2 ratios to study the impact on CO_2 conversion, determining the CO and CH_4 selectivity. The CO_2:H_2 ratios used were 1:0.5, 1:1.5, 1:2, 1:3, 1:4 and 1:5, done so by alternating the flow rate of H_2 and He from the inlet, while keeping the total flow rate 100 mL min^{-1}. The yield of CO for the second run is displayed in Figure 3-6 (a), and the yield of CH_4 for the second run is displayed in Figure 3-6 (b). The CH_4 amount is measured since it is more likely to be formed due to the increased presence of H_2. During the second run all ratios displayed the same patterns that with increasing amounts of H_2, an increase in CO yield occurred. This is due to the overspill of H_2 onto the catalyst, promoting the MSI performance, allowing for more sites to be reduced, generating oxygen vacancies [3].The second run displayed close to equilibrium CO yields for temperatures above 600 °C with increasing conversions for increasing ratios and temperature. As expected, the highest CO_2:H_2 ratio of 1:5 exhibited the highest CO yield of ~ 77.5% at 750 °C, but was outperformed below 600 °C by the 1:4 to ratio suggesting that increasing the H_2 passed a ratio of 1:4 does not improve activity dramatically. This can be seen as beneficial since it sets a maximum of H_2 required to be adequate for the reaction. Given that it is a valuable feedstock, it is economically ideal to limit the amount used, unless it can be obtained easily. Furthermore, with an increase in CO_2:H_2 ratio, CO_2 conversion follows a negative reaction order in terms of CO production because H coverage dominates the surface, resulting in fewer sites for CO_2 to dissociate. [17] Additionally, at lower temperatures, the CO yield is low for all ratios, which can be attributed to the Fe present as seen in the initial tests. However, once the temperature reaches 500 °C, catalytic activity begins to approach theoretical values and eventually reaches a constant rate of reaction for increasing temperatures. Figure 3-6 (b) displays the effect of increasing the CO_2:H_2 on the yield of CH_4 for the second run. It is observed that for the CO_2:H_2 ratios of 1:3, 1:4 and 1:5, the CH_4 yield was trace amounts, which again can be attributed to the presence of Fe.

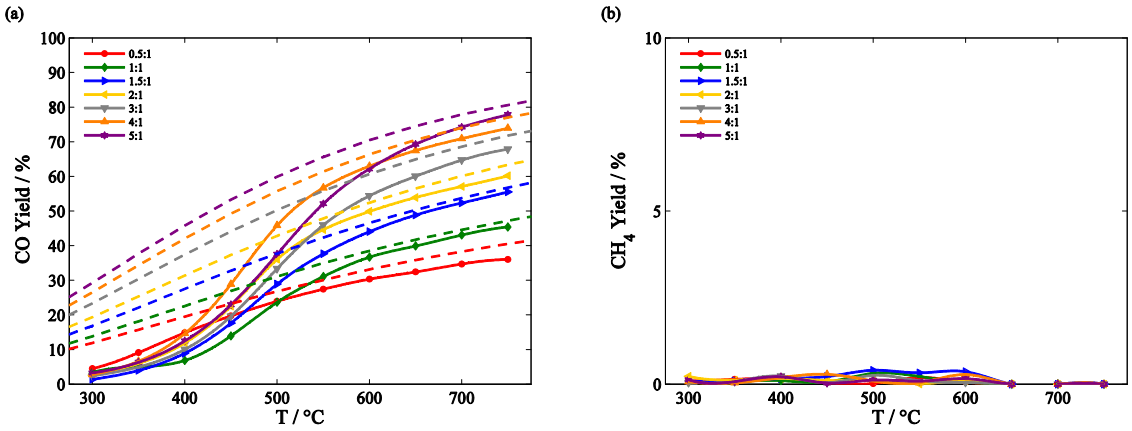

Figure 3-6. Catalytic performance for CO_2:H_2 ratios of 1:0.5, 1:1, 1:1.5, 1:2, 1:3, 1:4 and 1:5. (a) CO yield run 2, (b) CH_4 yield run 2. 50 mg of catalyst and 100 mL min^{-1}.

3.3.2.5 Stability performance

Figure 3-7 (a) displays the CO yield over $Ru_{45}Fe_{55}$/SDC (5 wt.%) at 650 °C for 100 h. 650 °C was selected in accordance with the data obtained from TGA, that since the weight loss did not change from 600 to 900 °C, there was no need to operate at temperatures above 650 °C. The stability is due to the presence of Fe since it has been proven to display high thermal resistance, along with the high thermal stability of SDC [9]. The conversion was stable at a constant rate of 38-40%, which is slightly lower than equilibrium values (~41%). This finding is significant because it can allow the catalyst to be used in industrial applications due to its capability of operating at high temperatures for long periods, all while maintaining a high conversion of reactants with little to no deactivation.

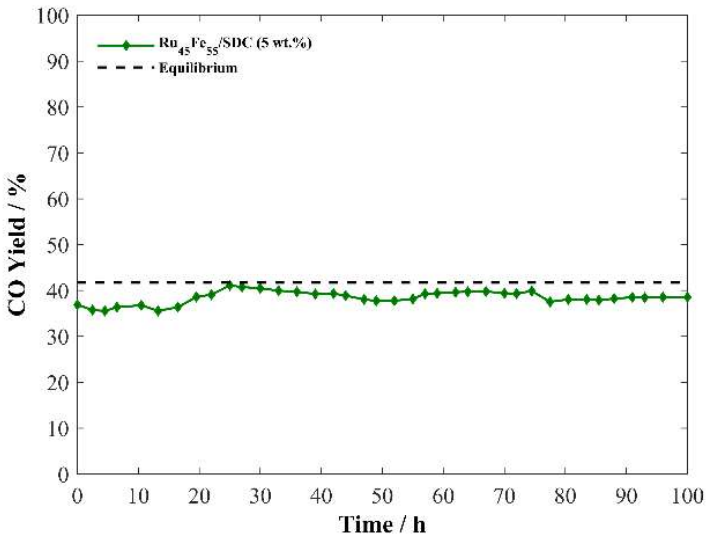

Figure 3-7. Stability of $Ru_{45}Fe_{55}$/SDC (5 wt.%) for 100 hours at 650 °C. 50 mg of catalyst, CO_2:H_2 1:1 and 100 mL min^{-1}.

3.3.3 *Water Gas Shift performance*

The $Ru_{45}Fe_{55}$/SDC (2 wt.%) then underwent the WGS reaction to evaluate its performance in the forward direction. Figure 3-8 displays the WGS reaction and it is observed that the conversion of CO decreases with increasing temperatures, since it is an exothermic reaction. The yield of H_2 was ~15% up to 600 °C, which was not as high as expected when compared with literature values of ~30% at 500 °C [18]. This can be due to the simple modification of the reactor and not operating at elevated pressures like mature processes [19]. The purpose of this test was to show that $Ru_{45}Fe_{55}$/SDC (2 wt.%) is active and suitable for the WGS reaction and can be further improved given the ideal conditions.

Knowing the ideal parameters and the reproduced patterns for the activities of Ru and Fe metals and the SDC support, further studies incorporating these catalysts can be performed for the optimization of the process. The synergistic relationship between Ru and Fe has proven to be effective at high temperatures, thus ensuring catalytic conversion and stability. The ability of Ru to adsorb CO_2 and dissociate H_2, combined with the stability properties of Fe supported on the generating oxygen vacancy properties of SDC has allowed for the use of a promising catalyst. Above 550°C, the yield of CO increases close to equilibrium values with a selectivity of ~100%. It was therefore determined that the optimal performance for bimetallic Ru-Fe supported on SDC

is achieved with compositions of $Ru_{45}Fe_{55}$. Furthermore, a metal loading of 2 wt.% was proven beneficial in achieving high catalytic activity, while keeping the amount of the noble metal – Ru, less than 1 wt.%.

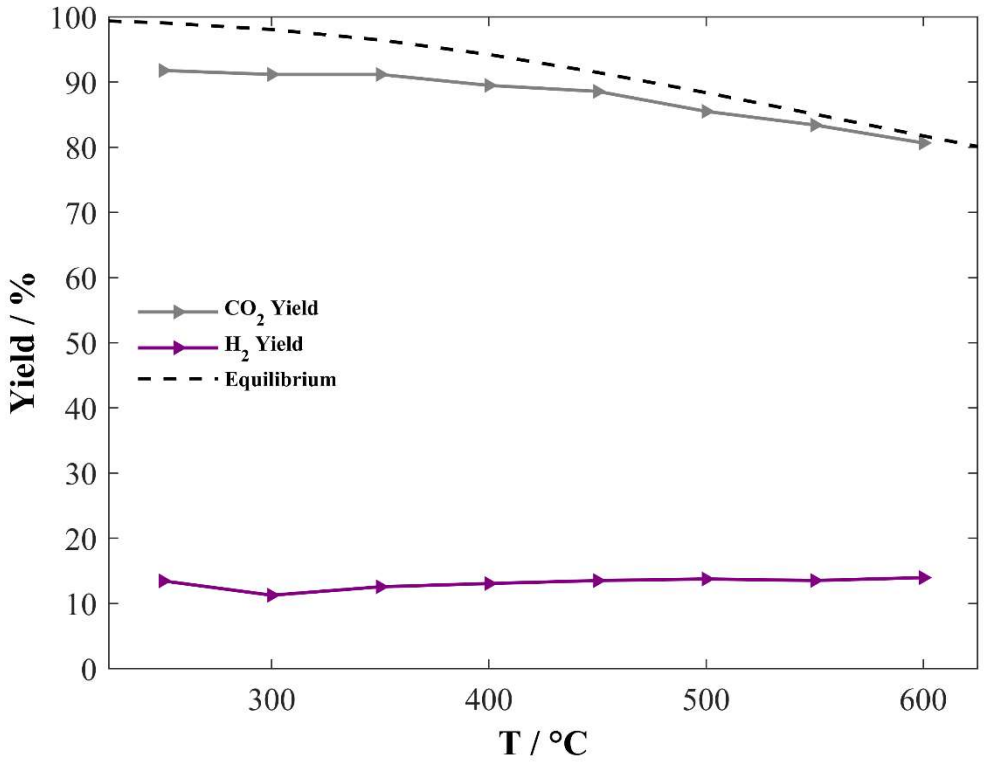

Figure 3-8. Water Gas Shift reaction for $Ru_{45}Fe_{55}$/SDC (2 wt.%). 50 mg of catalyst, H_2O:CO 1:1 and 50 mL min^{-1}.

3.3.4 *Effect of different supports*

Using the 2 wt.% loading of $Ru_{45}Fe_{55}$, new catalysts with different supports were tested to compare with the activity of SDC. The catalysts were deposited by the same impregnation technique described in Chapter 3.2.2 on the supports CeO_2, ceria doped-yttria (CeO_2-Y_2O_3), ceria doped-gadolinium (CeO_2-Gd), yttria-stabilized zirconia (YSZ), and carbon. The results are displayed in Figure 3-9. Whereas the ceria supports display similar activity, the YSZ support is slightly lower, and the carbon support performs worse than the ceria and SDC supports independently (as seen in Figure 3-3 (a)). However, at lower temperatures, YSZ performs slightly better than ceria, given that it is ionically conductive as opposed to mixed-ionically conductive

CeO_2-based supports. YSZ could provide a higher number of O^{2-} promotional species to the catalyst at lower temperatures [11,20]. The similar activity for the ceria supports suggest that any form of ceria paired with $Ru_{45}Fe_{55}$ nanoparticles is highly active for the RWGS reaction. However, as mentioned in section 3.3.2.1, it is less practical to use un-doped CeO_2 due to its low bulk density, requiring a greater reactor for similar catalytic activity. The CO yield for YSZ supported nanoparticles was 2-3% lower than CeO_2-Gd, suggesting that since it is ionically conductive, it displays similar activity to that of ceria. As for the carbon supported catalyst, it only became active above 500 °C and displayed very low activity, despite the fact that the specific surface area of carbon support is much larger (250 $m^2\ g^{-1}$) than doped-ceria or YSZ (< 30 $m^2\ g^{-1}$). The increased activity from the MIEC catalyst supports (i.e. CeO_2-based and YSZ) is due to the migration of promoting $O^{\delta-}$ ions (O^{2-} in the case of these supports) from the support to the surface of nanoparticles. This MSI effect is comparable to the EPOC (or NEMCA) effect, where the backspillover of ionic promoting species form a neutral double layer around the nanoparticles, in turn increasing its activity [21]. Due to the size of the $Ru_{45}Fe_{55}$ nanoparticles (< 2.5 nm) the O^{2-} ions from the support do not have to travel far and their migration is enhanced with an increase in temperature [21]. Unlike in EPOC, where the migration of promoting species is controlled in-situ through a current/potential difference, the MSI promotional effect is observed through the comparison of the nanoparticles dispersed on supports like C. Thus, the similar activity for MIEC supports is affiliated to the O^{2-} ionic species and CeO_2-based supports displays a slightly better performance than YSZ due to the increased presence of oxygen vacancies, which are more abundant when it is doped. Additionally, in terms of CO_2 hydrogenation, O^{2-} ions are not a reactant, so it is interesting to see a promotional effect taking place, unlike what is observed during an oxidation reaction where O^{2-} ions take part in the reaction as sacrificial promoters [22–24]. Further tests are required to understand how the O^{2-} are involved in the reaction. Furthermore, the utilization a H^+ ion conducting supports has the potential of promoting the hydrogenation reaction even more since they act as sacrificial promoters [25]. These results suggest that support selection is as important as the metal nanoparticle catalyst, concluding the MSI effect displayed for ceria and doped ceria supports are best towards the RWGS reaction in CO selectivity and thermal stability.

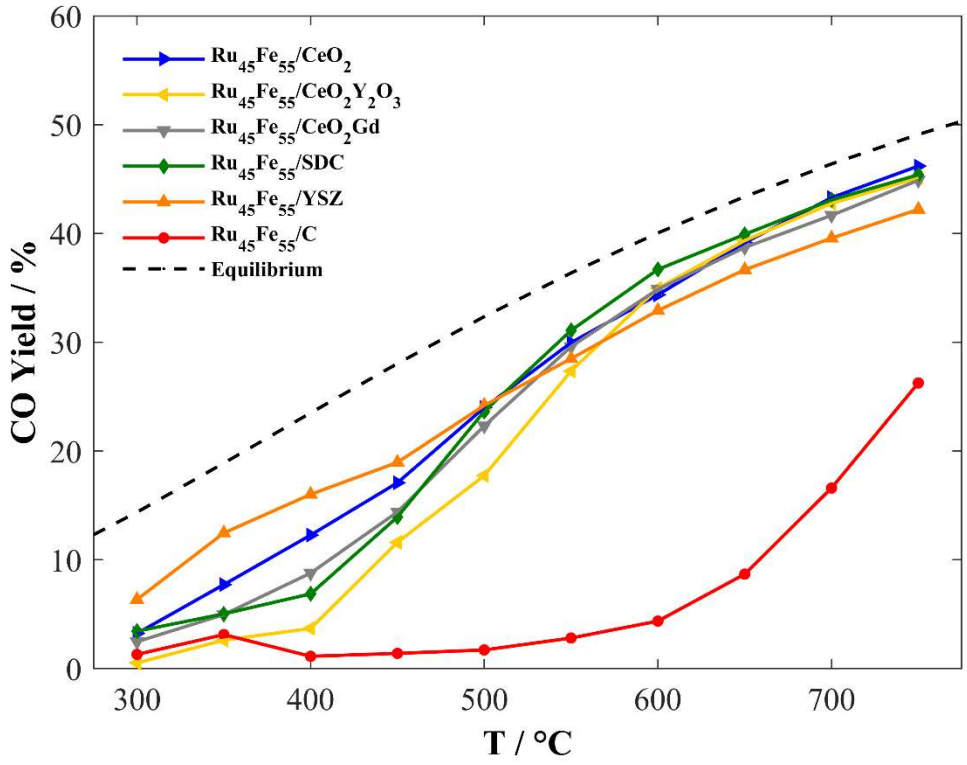

Figure 3-9. Comparison of $Ru_{45}Fe_{55}$ (2 wt.%) deposited on various supports for run 2. 50 mg of catalyst, CO_2:H_2 1:1 and 100 mL min^{-1}.

3.4 Conclusion

Overall, the RWGS is a promising chemical reaction in reducing GHG emissions by the utilization of CO_2 obtained through carbon storage and sequestration and H_2 through the electrolysis of water. Evaluation of the bimetallic Ru_xFe_{100-x} supported on SDC was highly active towards the RWGS reaction. The high selectivity to CO can be affiliated to the size of the nanoparticles being less 2.5 nm. It was determined that reducing the Ru metal content to less than 1 wt.% ($Ru_{45}Fe_{55}$/SDC 2 wt.%) utilized the ability of Ru, without compromising the catalytic conversion of CO_2 into CO at elevated temperatures. The 1 wt.% presence of Fe suppressed the conversion at lower temperatures but improved the performance of Ru at increased temperatures. Additionally, the mixed-ionic conductivity of the SDC support allowed for improved stability and improved activity through its promotional MSI effect. Future work can focus on further promoting the activity of Ru-Fe by the incorporation of different pretreatment steps, addition of new metals and reactor design to control in-situ an electrochemical promotion effect.

References

[1] D.C. Upham, A.R. Derk, S. Sharma, H. Metiu, E.W. McFarland, CO 2 methanation by Ru-doped ceria: the role of the oxidation state of the surface, Catal. Sci. Technol. 5 (2015) 1783–1791. doi:10.1039/C4CY01106F.

[2] S. Sharma, Z. Hu, P. Zhang, E.W. McFarland, H. Metiu, CO2 methanation on Ru-doped ceria, J. Catal. 278 (2011) 297–309. doi:10.1016/j.jcat.2010.12.015.

[3] B. Cornils, W.A. Herrmann, C. Wong, H. Zanthoff, R. Eds, Catalysis from A to Z, 2007. doi:10.1016/S1351-4180(07)70462-2.

[4] C.S. Chen, W.H. Cheng, S.S. Lin, Enhanced activity and stability of a Cu/SiO2 catalyst for the reverse water gas shift reaction by an iron promoter., Chem. Commun. (Camb). (2001) 1770–1771. doi:10.1039/b104279n.

[5] T. Milek, D. Zahn, Molecular simulation of Ag nanoparticle nucleation from solution: Redox-reactions direct the evolution of shape and structure, Nano Lett. 14 (2014) 4913–4917. doi:10.1021/nl502503t.

[6] M.D. Porosoff, B. Yan, J.G. Chen, Catalytic reduction of CO2 by H2 for synthesis of CO, methanol and hydrocarbons: challenges and opportunities, Energy Environ. Sci. 9 (2016) 62–73. doi:10.1039/C5EE02657A.

[7] G. Bergeret, P. Gallezot, Handbook of Heterogeneous Catalysis, Wiley-VCH, 2002.

[8] R. V. Gonçalves, L.L.R. Vono, R. Wojcieszak, C.S.B. Dias, H. Wender, E. Teixeira-Neto, L.M. Rossi, Selective hydrogenation of CO 2 into CO on a highly dispersed nickel catalyst obtained by magnetron sputtering deposition: A step towards liquid fuels, Appl. Catal. B Environ. 209 (2017) 240–246. doi:10.1016/j.apcatb.2017.02.081.

[9] L. Wang, H. Liu, Y. Chen, S. Yang, Reverse water–gas shift reaction over co-precipitated Co–CeO2 catalysts: Effect of Co content on selectivity and carbon formation, Int. J. Hydrogen Energy. 42 (2016) 3682–3689. doi:10.1016/j.ijhydene.2016.07.048.

[10] G. Avgouropoulos, M. Manzoli, F. Boccuzzi, T. Tabakova, J. Papavasiliou, T. Ioannides, V. Idakiev, Catalytic performance and characterization of Au/doped-ceria catalysts for the preferential CO oxidation reaction, J. Catal. 256 (2008) 237–247. doi:10.1016/j.jcat.2008.03.014.

[11] R.J. Isaifan, E.A. Baranova, Effect of ionically conductive supports on the catalytic activity of platinum and ruthenium nanoparticles for ethylene complete oxidation, Catal. Today. 241 (2015) 107–113. doi:10.1016/j.cattod.2014.03.061.

[12] S. Kuharuangrong, Ionic conductivity of Sm, Gd, Dy and Er-doped ceria, J. Power Sources. 171 (2007) 506–510. doi:10.1016/j.jpowsour.2007.05.104.

[13] B. Dai, G. Zhou, S. Ge, H. Xie, Z. Jiao, G. Zhang, K. Xiong, CO2 reverse water-gas shift reaction on mesoporous M-CeO2 catalysts, Can. J. Chem. Eng. 95 (2017) 634–642.

doi:10.1002/cjce.22730.

[14] W. Wang, Y. Zhang, Z. Wang, J.M. Yan, Q. Ge, C.J. Liu, Reverse water gas shift over In2O3-CeO2catalysts, Catal. Today. 259 (2016) 402–408. doi:10.1016/j.cattod.2015.04.032.

[15] M. Lortie, R. Isaifan, Y. Liu, S. Mommers, Synthesis of CuNi/C and CuNi/-Al2O3 Catalysts for the Reverse Water Gas Shift Reaction`, Int. J. Chem. Eng. 2015 (2015). doi:0.1155/2015/750689.

[16] X. Zhang, X. Zhu, L. Lin, S. Yao, M. Zhang, X. Liu, X. Wang, Y. Li, C. Shi, D. Ma, Highly dispersed Copper over β-Mo2C as Efficient and Stable Catalysts for RWGS Reaction, ACS Catal. 7 (2017) 912–918. doi:10.1021/acscatal.6b02991.

[17] T. Avanesian, G.S. Gusmão, P. Christopher, Mechanism of CO2 reduction by H2 on Ru(0 0 0 1) and general selectivity descriptors for late-transition metal catalysts, J. Catal. 343 (2016) 86–96. doi:10.1016/j.jcat.2016.03.016.

[18] A. Haryanto, S. Fernando, S. Adhikari, Ultrahigh temperature water gas shift catalysts to increase hydrogen yield from biomass gasification, Catal. Today. 129 (2007) 269–274. doi:10.1016/j.cattod.2006.09.039.

[19] I. Chorendorff, J.W. Niemantsverdriet, Concepts o Modern Catalysis and Kinetics, 2003. doi:10.1002/anie.200461440.

[20] R.J. Isaifan, E.A. Baranova, Catalytic electrooxidation of volatile organic compounds by oxygen-ion conducting ceramics in oxygen-free gas environment, Electrochem. Commun. 27 (2013) 164–167. doi:10.1016/j.elecom.2012.11.021.

[21] C.G. Vayenas, Promotion, electrochemical promotion and metal-support interactions: Their common features, Catal. Letters. 143 (2013) 1085–1097. doi:10.1007/s10562-013-1128-x.

[22] Y.M. Hajar, K.D. Patel, U. Tariq, E.A. Baranova, Functional equivalence of electrochemical promotion and metal support interaction for Pt and RuO2 nanoparticles, J. Catal. 352 (2017) 42–51. doi:10.1016/j.jcat.2017.05.001.

[23] H.A.E. Dole, R.J. Isaifan, F.M. Sapountzi, L. Lizarraga, D. Aubert, A. Princivalle, P. Vernoux, E.A. Baranova, Low temperature toluene oxidation over Pt nanoparticles supported on yttria stabilized-zirconia, Catal. Letters. 143 (2013) 996–1002. doi:10.1007/s10562-013-1071-x.

[24] D. Theleritis, S. Souentie, A. Katsaounis, C.G. Vayenas, Hydrogenation of CO2 over Ru electropromoted catalysts, ACS Catal. 2 (2012) 770–780. doi:dx.doi.org/10.1021/cs300072a.

[25] I. Kalaitzidou, M. Makri, D. Theleritis, A. Katsaounis, C.G. Vayenas, Comparative study of the electrochemical promotion of CO2 hydrogenation on Ru using Na+, K+, H+ and O2- conducting solid electrolytes, Surf. Sci. 646 (2016) 194–203. doi:10.1016/j.susc.2015.09.011.

Appendix A - Supplementary Information for Chapter 3

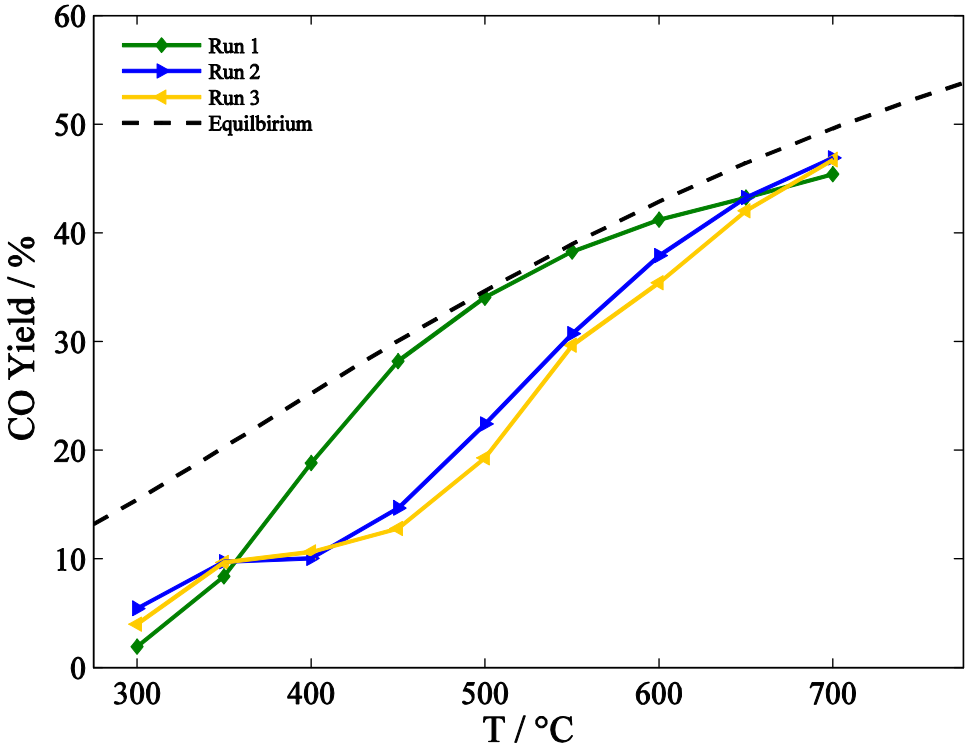

Figure A-1. CO Yield for $Ru_{45}Fe_{55}$/SDC (5 wt.%) run 1, 2 and 3, displaying minimal change between runs 2 and 3. 50 mg of catalyst, H_2:CO_2 1:1 and 100 mL min^{-1}.

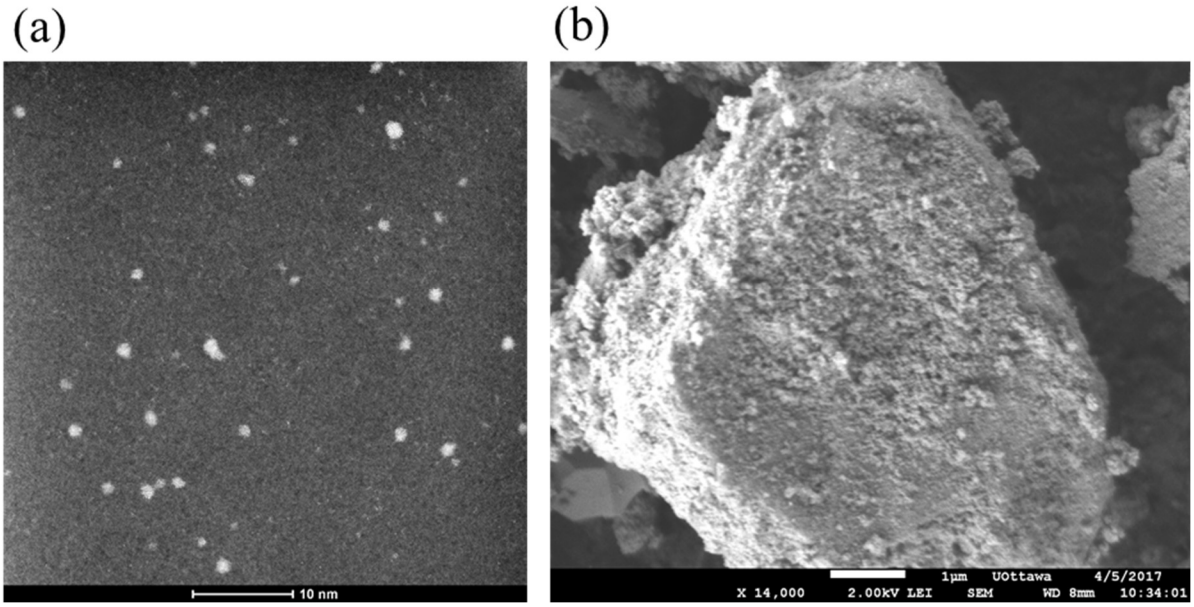

Figure A-2. (a) STEM image of Ru colloids and (b) SEM image of $Ru_{45}Fe_{55}$/SDC.

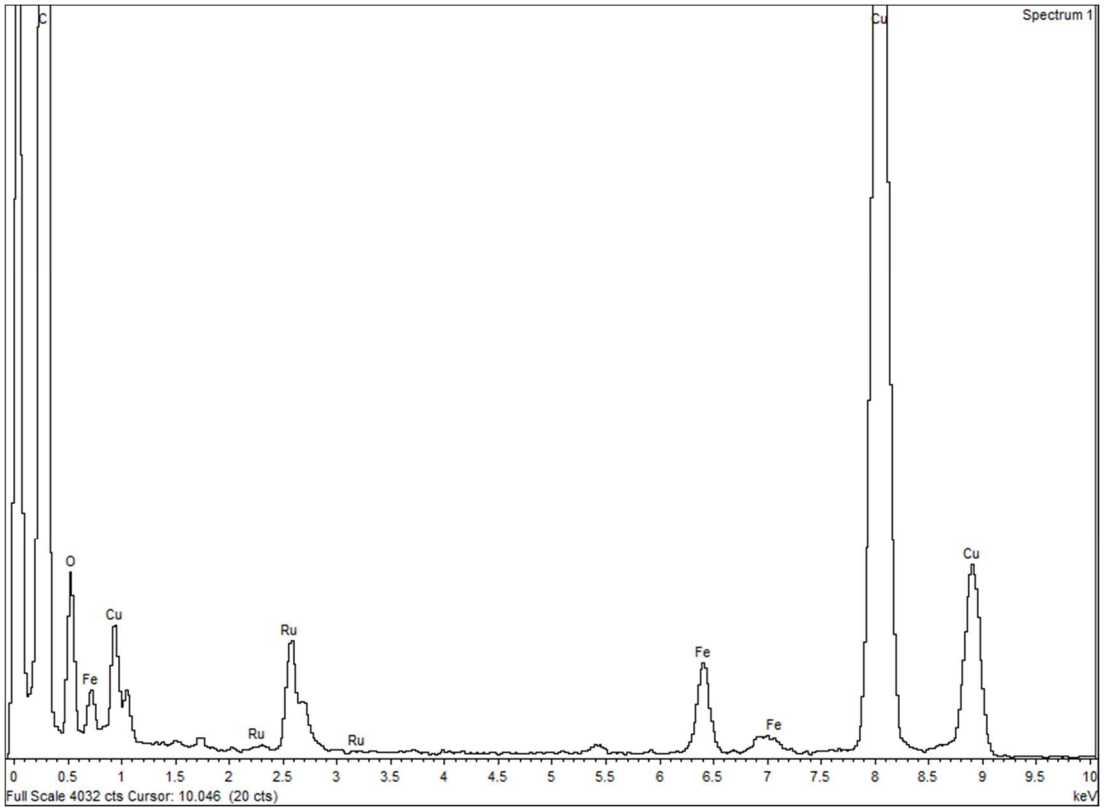

Figure A-3. EDS distribution for $Ru_{45}Fe_{55}$ colloid.

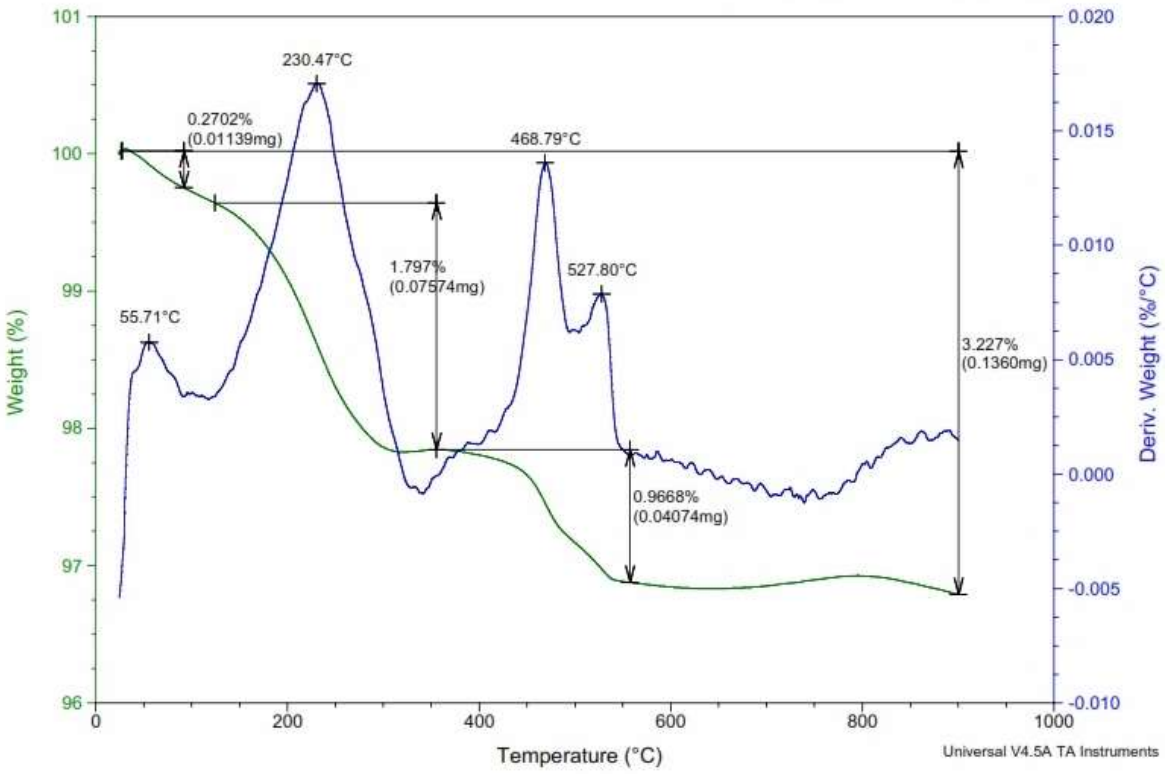

Figure A-4. TGA analysis for $Ru_{45}Fe_{55}$/SDC (5 wt.%).

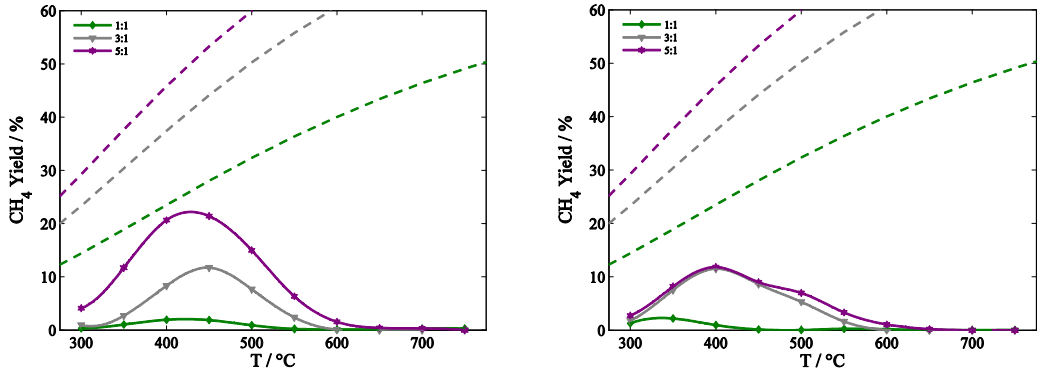

Figure A-5. CH_4 yields of Ru/SDC (0.5 wt.%) for CO_2:H_2 ratios of 1:1, 1:3 and 1:5 for (a) run 1 and (b) run 2. 50 mg of catalyst and 100 mL min^{-1}.

Chapter 4 : Elucidating the role of electrochemical polarization on the selectivity of the CO_2 hydrogenation reaction over Ru

Adapted from: ***C. Panaritis****, C. Michel, C. Martin, E. A. Baranova, and S. Steinmann, Electrochimica Acta, 350 (2020) 136405.*

Abstract

The hydrogenation of CO_2 into high-value fuels is a potentially effective approach to reduce anthropogenic dependence on fossil fuels and effects of climate change. In this study, we evaluated the hydrogenation of CO_2 into CO and CH_4 under the electrochemical promotion of catalysis (EPOC) effect through experimental and computational studies using Ru nanoparticles. Ru nanoparticles (1-2 nm) supported on yttria-stabilized zirconia (YSZ) solid electrolyte were evaluated at 250 °C at atmospheric pressure. Under positive polarization, the methanation reaction was promoted and the competitive reverse water gas shift (RWGS) reaction was impeded. On the other hand, negative polarization resulted in suppressing permanently the methanation reaction and minimally affecting the RWGS reaction. To qualitatively rationalize the tuning of selectivity via EPOC, Density Functional Theory (DFT) computations were used to model the EPOC effect induced on the Ru(0001) surface. DFT computations uncovered that electric field effects together with a change in surface electrochemical potential between intermediates are responsible for the contrasting influence of EPOC on the CH4 and CO formation over Ru catalysts.

4.1 Introduction

Depending on the catalyst and relative partial pressures, the RWGS or the methanation reaction is dominant, yielding carbon monoxide (CO) and methane (CH_4), respectively [1]. Ruthenium (Ru) has been used extensively due to its dual ability of activating CO_2 and H_2, and it is the most economical noble metal [2]. Based on experimental Fourier transform infrared (FTIR) spectroscopy and Density Functional Theory (DFT) studies, the main reaction pathways of CO_2

reduction over Ru catalysts is summarized in Figure 4-1 [2–5]. The first step consists of adsorbing CO_2 and dissociating it into chemisorbed CO and O. The next step is crucial for the selectivity: either CO desorbs or it hydrogenates further to CHO and ultimately to CH_4. This competition depends on the morphology and the presence of promoters as well as on the reaction conditions (temperature and H_2/CO_2 pressure ratio). Typically, CH_4 selectivity is favoured by temperatures of 200-300 °C. Above 250 °C the temperature is high enough to enable the endothermic formation of CO on Ru nanoparticles, although only at about 500 °C a high selectivity was reached previously in Chapter 3.

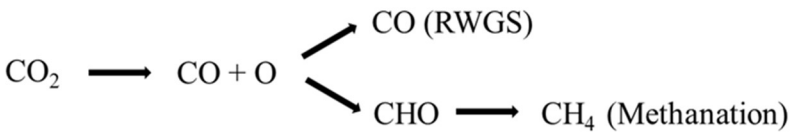

Figure 4-1. Schematic mechanism of the CO hydrogenation pathway under standard conditions on the Ru(0001) surface.

Previous EPOC studies of CO_2 hydrogenation over Ru films of 2 μm thickness, have demonstrated that the electrochemical polarization alters the CO to CH_4 ratio [6,7], independently from the promoting species used, such as O^{2-}, Na^+, K^+ and H^+, associated with yttria-stabilized zirconia (YSZ), Na-β"-Al_2O_3, K-β"-Al_2O_3, and $BaZrO_{0.85}Y_{0.15}O_{3-\alpha}$ (BZY) solid electrolytes, respectively [6,7]. This suggests a universal promoting mechanism, which is not primarily related to surface coverages of active species such as H and O but rather due to the polarization of the electrode and work function modification.

To elucidate the origin of the contrasting impact of the electrochemical potential of the catalyst surface on CH_4 and CO production rates, this chapter investigates the competition between CO and CH_4 production over Ru catalysts at moderate temperatures of 250 °C, where EPOC allows to tune the competition between the two pathways. We aim at providing qualitative but robust understanding of the EPOC effect. Our model of EPOC that includes the polarization at the interface without specifying the promoting species predicts trends in the competition that are in line with the experimental observations regarding the selectivity of the CO_2 reduction. It confirms that when using Ru-based catalysts, the selectivity of the reaction is not driven by the nature of the migrating species but by the induced polarization. The combination of periodic DFT and

experiments shows that the relative adsorption energy of CO and CHO as a function of the electrochemical potential at the catalyst surface is key for determining the selectivity between CO and CH_4 production.

4.2 Experimental

4.2.1 *Catalyst Preparation*

The ruthenium (Ru) nanoparticles were synthesized using the polyol synthesis method [8]. The method incorporates metal precursors, ethylene glycol (EG) and tetramethylammonium hydroxide (TMAOH). The addition of TMAOH serves to stabilize and increase the pH to govern the size of the nanoparticles. The Ru colloid was prepared using 0.105 g of ruthenium chloride ($RuCl_3$) (anhydrous, Sigma Aldrich) mixed in 15 mL ethylene glycol (Fischer-Scientific certified grade) containing 0.15 M TMAOH (Sigma Aldrich, pentahydrate). The solution was then heated up until it reached 160 °C and immediately turned off and cooled to room temperature. Initial pH of the solution was 12 and dropped to 7 after reflux. The final colloidal solution was black in colour and stored at room temperature.

4.2.2 *Physiochemical Characterization*

The size of the free-standing Ru nanoparticles was evaluated using scanning transmission electron microscopy (STEM) performed on a FEI Titan^3 80-300 TEM operated at 300 keV, equipped with a CEOS aberration corrector for the probe-forming lens. Annular Dark Field (ADF) images were taken using a Fishione detector to provide a contrast between the nanoparticles and support at convergence and collection angles of 17 and 60 mrad, respectively. The Ru colloidal sample was sonicated in ethanol and then one-drop was deposited onto a 200 mesh TEM copper grid coated with a lacey carbon support film (Ted Pella). The Image J software was used to measure the average size of the nanoparticles. X-Ray Diffraction (XRD) patterns did not show peaks for the free-standing Ru nanoparticles because they were amorphous.

4.2.3 *Electrochemical Cell and Reactor Setup*

The electrochemical cell consisted of the ionically conductive support 8 mol% Y_2O_3-stabilized ZrO_2 (YSZ) (Tosoh) as the solid electrolyte in the form of a disc (diameter = 19 mm and thickness = 1 mm) prepared as described elsewhere [9]. Gold (Au) counter and reference electrodes were painted using Au paste (C2090428D4, Gwent Group, CAS: 98- 55-5) next to each other with a surface area of 1 cm^2 and 0.2 cm^2, respectively. The Au counter and reference electrodes were

annealed in air at 500 °C for 1 h. Directly opposing the counter electrode, the working catalyst-electrode was deposited in a surface area of 1 cm^2. The Ru catalyst was deposited as a colloid solution enclosed in a tape mask mold. It was deposited 10 μL at a time with subsequent heating at 130 °C for 10 min in between deposits to dry the solution until the desired catalyst loading (0.2 mg of Ru free-standing nanoparticles) was achieved. A gold mesh was mechanically pressed on the catalyst-working electrode to act as a current collector, as previously shown [10].

Similar to the setup described in Chapter 3.2.4, the EPOC reactor (70 cm^3) is displayed in Figure 4-2. The total flow rate of 100 $mL.min^{-1}$ consisted of CO_2 (Linde, 99.999%), H_2 (Linde, 100%) and He (Linde, 100%) balance at 1.5 kPa, 9 kPa and 89.5 kPa, respectively. These were fed to the reactor through three independent mass flow controllers (MFC, MKS Instruments). The catalyst was pre-treated in 20 kPa of O_2 for 2 h at 200 °C to remove any residue ethylene glycol and TMAOH from the surface. The pre-treatment was then followed by He purging for 15 min and then H_2 (30% in He) for 3 h at 200 °C to reduce the RuO_2 surface to Ru. The CO_2:H_2 ratio of 1:7 was used since it was observed in all previous EPOC reactions that the this ratio displayed the highest selectivity to CH_4 with Ru films and additionally allows for CO and CH_4 end-products to be produced [7]. The high concentration of H_2 during reaction conditions ensures a complete reduction at 200 °C. These conditions are chosen in order to conveniently determine the influence of the electrochemical potential at the catalyst surface on product selectivity. The electrochemical cell is a modified version of the reactor described in Ref. [11]. Three gold wires were used to connect the working, counter and reference electrodes to the potentiostat-galvanostat (Arbin Instruments, MSTAT) that supplied the application of potential and constant current to the electrochemical cell.

The EPOC effect was evaluated through the enhancement ratio (ρ) (eq. 1-11) and apparent Faradaic efficiency (Λ) (eq. 1-11) defined in Chapter 1. The *z* variable in eq. 1-11 is the number of electrons transferred ($2e^-$ for CO and $8e^-$ for CH_4).

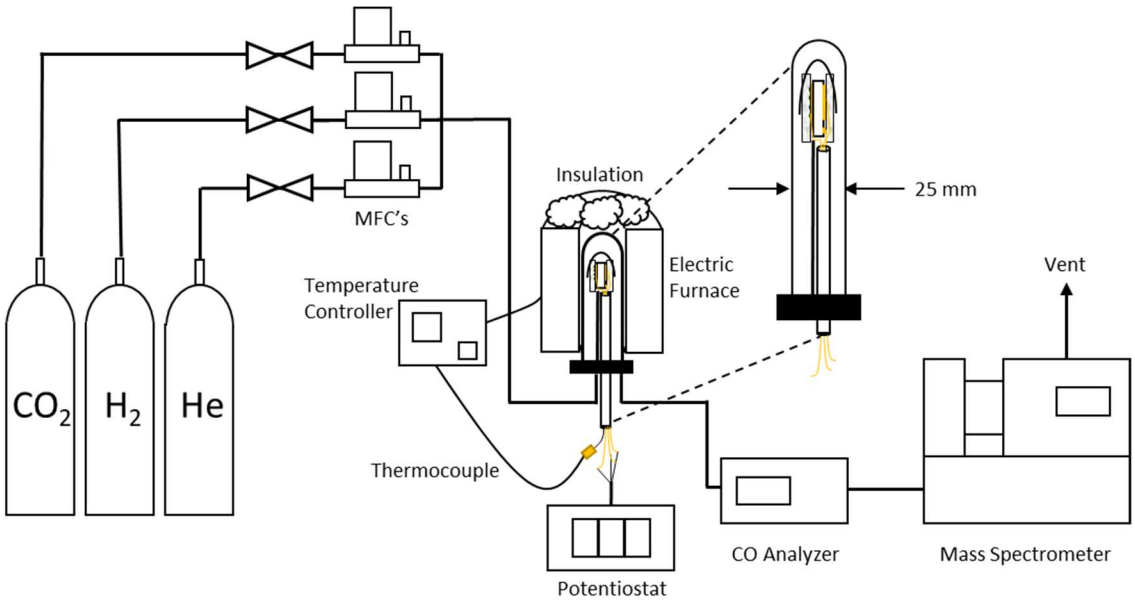

Figure 4-2. Experimental set-up for the EPOC reactor.

4.2.4 *Computational Model*

The VASP code (Vienna Ab-initio Simulation Package) was used to perform all DFT computations [12]. The dispersion corrected density functional approximation PBE-dDsC was applied. This method has been shown to reproduce experimental adsorption energies [12,13]. In the absence of experimental insight on the most representative surface sites, the most stable Ru(0001) surface was chosen [2,3]. A symmetric p(3x3) unit cell with of 5 metallic layers was used. A large (45.2 Å) vacuum layer separates the two surfaces to prevent interactions and provides the necessary space of the description of the double layer. [14] The Brillouin zone was integrated with a Monkhorst–pack k-point of 5x5x1. The basis-set cutoff was set to 400 eV. All geometries have been optimized to forces below 0.02 eV/Å with wave functions converged to 10^{-6} eV. Frequencies were computed with the harmonic approximation to determine the vibrational contribution to the enthalpy and entropy. The translational and rotational contributions for the gas molecules were computed within the ideal gas approximation and the rigid rotator approximation. The linearized Poisson-Boltzmann equation with default parameters as implemented in VASPsol module [15] has been used to model the influence of the electrochemical potential at the catalyst surface [14,16]. For detailed explanations on the computational model, we refer the reader to ref [17], where we have also demonstrated that the precise technical parameters do not considerably

influence the EPOC results. The investigated reaction pathway follows the proposal by Avanesian *et al.* [2].

The Gibbs Free Energy (G_{ads}) values for each reactant, intermediate and product adsorbed on Ru(0001) were calculated using equation 4-1.

$$G_{ads} = \frac{1}{2}\left[G_{surface+molecule} - \left(G_{surface} + 2\,G_{molecule}\right)\right] \quad 4\text{-}1$$

where $G_{surface+molecule}$ is the Gibbs Free Energy of the optimized configuration of the species on the surface, $G_{surface}$ is the Gibbs Free Energy of the optimized Ru(0001) surface and $G_{molecule}$ is the Gibbs Free energy of the molecule optimized in the gas phase. The factor ½ accounts for the use of a symmetric slab, which is also the reason for the use of two gas-phase molecules in the reference.

4.3 Results

4.3.1 *Catalyst Characterization*

The STEM image displayed in Figure 4-3 confirms that the Ru nanoparticles were between 0.5-1 nm in diameter, in accordance with the modified polyol method. Additionally, the free-standing (*i.e.* unsupported) nanoparticles were well dispersed and did not display significant agglomeration prior to reaction. Supported STEM images were not possible due to the presence of the solid electrolyte, which blocks the transmission and SEM does not provide enough resolutions to view the nanoparticles. The contrast provided by the ADF image represents the nanoparticles as bright spots on the darker background. Here, RuO_x ($x \leq 2$) are displayed since they are exposed to air; however, they were reduced back to metallic Ru during the hydrogenation pre-treatment step.

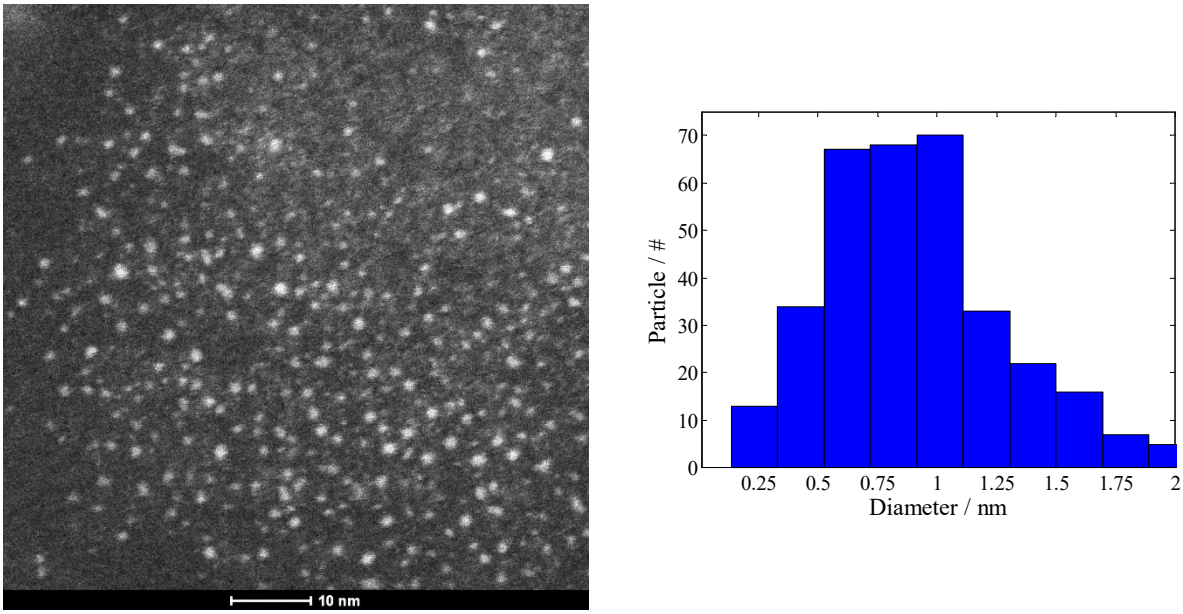

Figure 4-3. STEM image of free-standing Ru nanoparticles and corresponding particle size distribution histogram.

4.3.2 *EPOC Performance for Ru nanoparticles*

To evaluate the EPOC phenomenon for the methanation and RWGS reaction on Ru nanoparticles deposited on YSZ, 250 °C was chosen as reaction temperature, since simultaneous production of CO and CH_4 is observed at this temperature. Figure 4-4 (a) shows a representative transient rate response for application of a positive current of 50 μA at 250 °C, which corresponds to a potential difference between the catalyst-working and reference electrode (U_{WR}) of about 1 V. The open-circuit (O.C.) conditions were maintained for 1 h after reaching a steady-state, followed by 3 h polarization and return to open-circuit for 3 h. The duration of each time window was chosen to let the system reach a steady-state.

At open-circuit conditions, the production rate for CO is greater than for CH_4. When a positive current of 50 μA is applied, the methanation reaction is promoted, with $\rho > 1$ and $\Lambda = 34$ (Figure 4-4 (a)). Conversely, the RWGS reaction is impeded, with $\rho < 1$ and a low Faradic efficiency ($\Lambda = 15$). When the system is switched back to O.C. conditions, it requires over 2 h to return, in line with the slow increase in rate upon positive application. During positive polarization there is a continuous supply of oxygen ionic species to the gas-exposed catalyst surface that act as promoters for CH_4 and inhibitors for CO production. The slow return of CO production rate to

O.C. upon current interruption indicates that supplied oxygen ions remain on the surface of the catalyst and continue acting as inhibitors for CO formation for over 2 h. A $\Lambda > 1$ signifies non-Faradaic behaviour, which improves as the Λ value increases [18]. However, for hydrogenation reactions with O^{2-} solid electrolyte as the active support, since O^{2-} is not a reactant, the process is non-Faradaic when $\rho \neq 1$. The kinetic study performed by Theleritis *et al.* [6], and Kalaitzidou *et al.*[7], have shown that the selectivity to CH_4 can be influenced by three factors: H_2 partial pressure (1:7 CO_2:H_2) in the feed, reaction temperature (< 300 °C) and catalyst loading (>2 mg) under open-circuit conditions. Since the methanation reaction is positive order in the electron donor (*i.e.* H_2) and the application of polarization is equivalent to increasing the partial pressure of H_2 in the reaction, the CH_4 rate is favoured. The underlying hypothesis is that the positive surface charge, increases the coverage of H and thus the hydrogenation to CH_4. Therefore, positive potentials induce reducing conditions (*i.e.* high hydrogen coverage) without having to increase the amount of H_2.

Figure 4-4 (b) summarizes the EPOC response when varying the current from 50 to 150 μA and the corresponding enhancement ratio (ρ). As the current is increased, the CH_4 rate increases and the CO rate decreases. It is a rather robust behaviour since it was also observed on much thicker Ru films also deposited on YSZ and on other solid electrolytes (*i.e.* K-β"-Al_2O_3, Na- β"-Al_2O_3, and BZY), which generate other promoting ions (K^+, Na^+, H^+) [6,7].

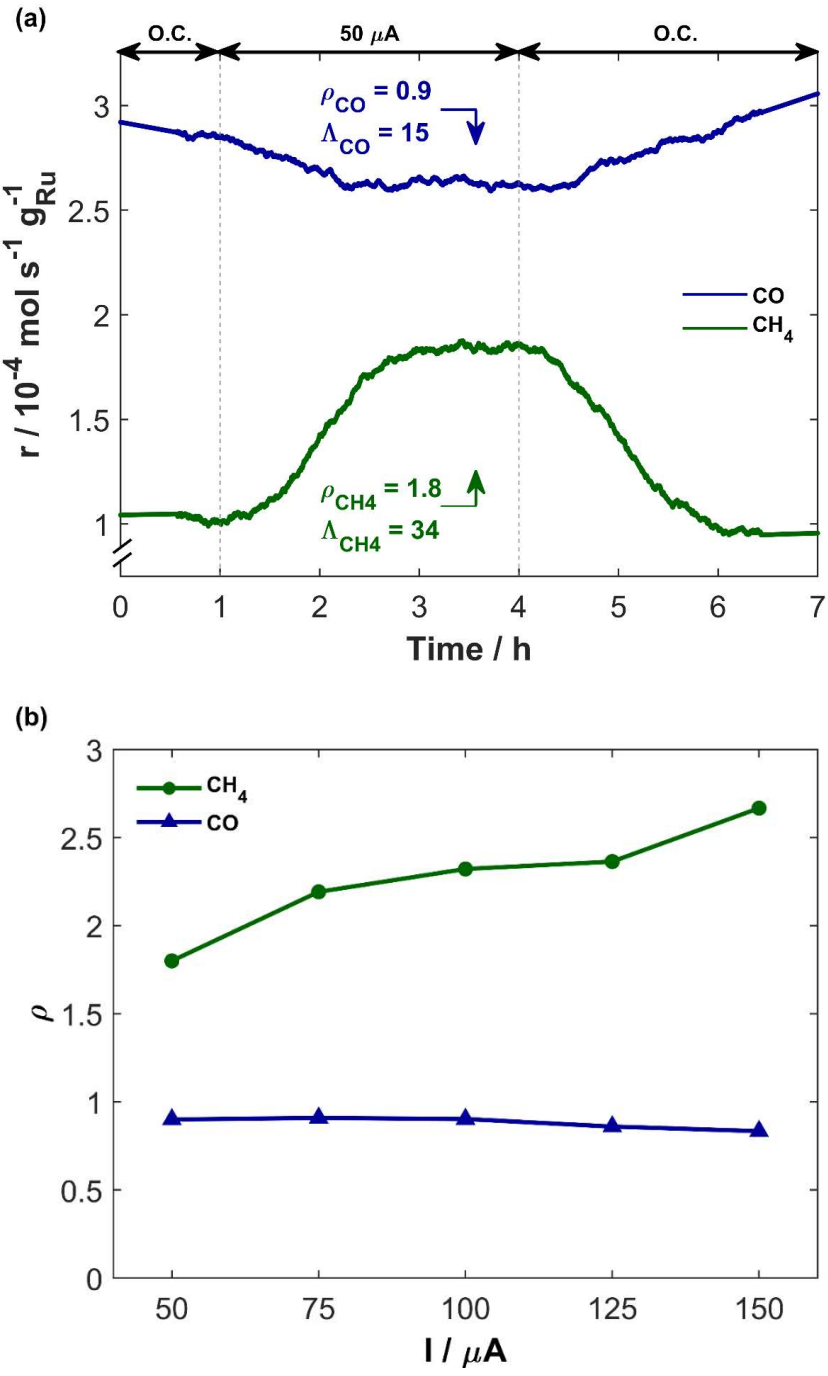

Figure 4-4. (a) Transient effect for application of 50 μA, and (b) Summary of ρ values under various currents at 250 °C for the production of CO and CH_4. 0.2 mg catalyst, CO_2:H_2 1:7 and total flow rate 100 mL min^{-1}.

The effect of negative polarization was investigated with application of a constant current of -25 μA (U_{WR} = ~-1 V) for 3 h, displayed in Figure B-1 (a) and (b) (in Appendix B) for CH_4 and

CO rate, respectively. The production rate of CO is barely affected ($\rho \sim 1$) while the one of methane is reduced ($\rho = 0.46$). Upon current interruption, the open-circuit CH_4 production rate did not return to its initial values, suggesting that the induced modification (reduction) of the surface state under a negative current and a negative potential difference is irreversible being maintained when the catalyst is left under open-circuit conditions. This is in line with the work by Theleritis *et al.*, [19], where Ru was in a reduced state inhibiting the formation of CH_4 which is favoured by the oxidation state. Additionally, once the CH_4 rate reached a new steady-state (not shown), negative potential was applied again, which resulted in further decrease in CH_4 production and minimally affected CO. This provides a way to permanently suppress unwanted CH_4 production and produce only CO at a temperature as low as 250 °C. Producing CO clean from CH_4 is important when aiming at the production of longer hydrocarbon chains in a downstream Fisher-Tropsch process [20].

4.3.3 *Computational Analysis*

Given the above reported EPOC effect on the methanation reaction, which is also in line with previous experiments, [7,19] let us now turn to the atomistic modeling. Computational studies to rationalize the EPOC effect are not very numerous and can be divided into two categories: (i) adsorbates are included explicitly [21,22] which results in a significant computational complexity, especially when investigating an entire reaction pathway (ii) the EPOC phenomenon is modelled by including a uniform electric field [23]. Herein, we rely on our recently proposed a third approach, which is to directly model the electrochemical potential at the catalyst surface instead of an electric field [17]. This method was successfully employed to highlight the influence of the electrode polarization on chemical steps involved in electrochemical processes, such as the rotation of adsorbed formate in the electro-oxidation of formic acid to CO_2 [24]. In short, the potential dependence is determined treating the electrons in a grand-canonical ensemble. Grand-canonical DFT allows to keep the potential constant from one elementary step to the next by varying the number of electrons [25–27]. The linearized Poisson-Boltzmann equation is used to model a thermodynamic average for the effective double layer, necessary to neutralize the surface charge. The resulting surface polarization is associated with a varying number of electrons as a function of the reaction coordinate in order to keep the potential constant and in agreement with the experimental setup [17,25,26,28,29]. This approach does not require specifying the chemical nature of the promotional species. Note, however, that we have chosen a model Ru(0001) surface at an intermediate coverage and in the absence of co-adsorption to qualitatively understand the

EPOC effect. This approximation prohibits quantitative comparisons to experiments, especially ones that assess the influence of the nanoparticle size or differences in promoting species. Furthermore, in contrast to simulations with an explicit electrostatic field, the potential dependent simulations facilitate the comparison with experiment where the potential is the measurable quantity. All computational details follow closely the one of Ref. [17].

To begin with, we considered the hydrogenation pathway in open-circuit conditions over Ru(0001), theoretically modeled by steady-state, equilibrium thermodynamics. The formation of methane is the thermodynamic product (computed $\Delta G_{250°C}$ = -0.74 eV) while CO is the kinetic product (computed $\Delta G_{250°C}$ = 0.2 eV). A catalytic cycle beginning with the adsorption of CO_2 and 4 H_2 was calculated to allow for the formation of CH_4. Avanesian *et al*. proposed that the formation of CO and CH_4 over Ru(0001) begins with the direct dissociation of H_2 into H*, followed by the adsorption of CO_2 and its dissociation into CO* and O* [2,3]. Then, to yield CH_4, CO* is hydrogenated either to CHO* or to COH*. The CHO* pathway was selected since transition states conducted by Avanesian *et al*., show that CHO* is more favourable, even though COH* is thermodynamically more stable [2]. The C-O bond can break in the CHO* intermediate, yielding CH* that undergoes successive hydrogenations to reach CH_4. In parallel, O* is hydrogenated to OH* and then H_2O. Following this pathway, the open-circuit Gibbs Free energy profile was evaluated at 250 °C and at standard pressure conditions and displayed in Figure 4-5. Desorption of close-shell molecules was systematically included when feasible (typically, desorption of water as soon as generated along the path). Competitive pathways were also considered, as shown in Figure B-2. For instance, the hydrogenation of CO_2, yielding COOH*, results in an intermediate that is less stable than the CO*+O* by at least 1 eV. The dissociation of CO* into C*+O* has been shown by Zhang *et al*., to require a high energy transition state (2.63 eV) when compared to its desorption or its hydrogenation into CHO* or COH* and thus was not included in this study [3].

CO* is a critical intermediate for the overall selectivity of the hydrogenation of CO_2. It can either desorb or be further reduced into CHO* and then to CH_4 through the sequence shown in Figure 4-5. With a slightly smaller desorption energy of CO (ΔG_{des}= 1.10 eV), desorption of CO is more likely than its hydrogenation into CHO* (ΔG= 1.15 eV). This is in line with our experimental results in open-circuit (O.C.) conditions, displaying a higher selectivity in CO over CH_4 (shown in the first hour in Figure 4-4 (a)).

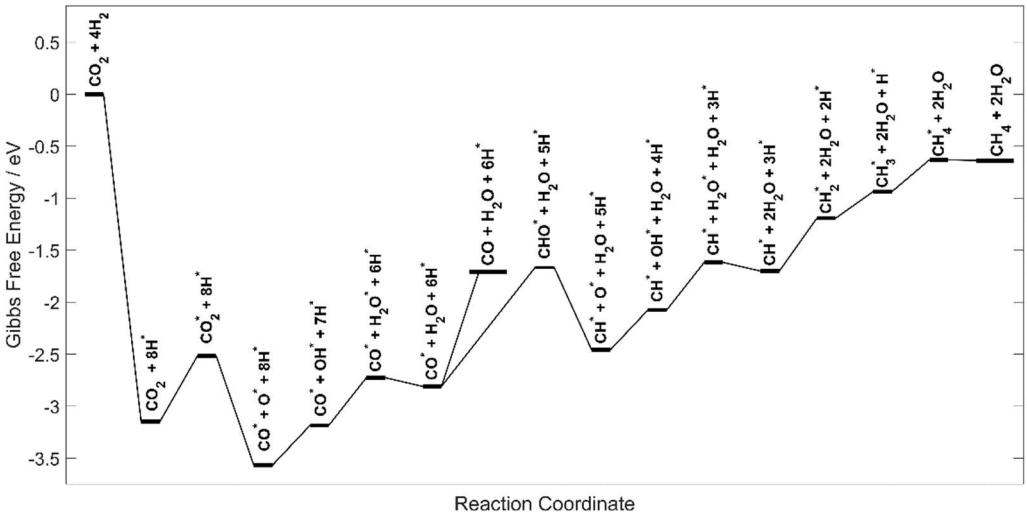

Figure 4-5. Computed Gibbs Free energy profile at 250 °C and atmospheric pressure of the CO_2 hydrogenation into CO and CH_4 on Ru(0001) in open-circuit conditions.

Let us now turn to the influence of an applied electrochemical potential at the catalyst surface on the selectivity. The reduction of CO into the CHO* was identified to be the selectivity determining step. We selected a maximum range of ±1 V since it is the typical experimental range evaluated in EPOC reactions [6,7]. The Gibbs free energy values at 250 °C are summarized in Table B-1 for open-circuit and ±1 V and the full profiles are shown in Figure B-3.

The CO_2 chemisorption is improved by the application of a negative potential (from ΔG_{ads}= 0.63 eV in O.C. conditions to 0.21 eV at -1V). In agreement with previous studies, the CO chemisorption is not very much affected at constant potential [30] or constant fields [31], but it is still stronger under a negative polarization that favours stronger back-bonding (from ΔG_{des}= 1.10 eV in O.C. conditions to 1.18 eV at -1V). This is in agreement with EPOC rules [32], where CO is an electron acceptor and its chemisorption increases upon negative polarization (decrease of work function). Because this effect is less pronounced in the present case, where CO is a reaction intermediate or product, it may indicate that the effect of polarization on CO adsorption depends on the presence of other adsorbed species (electron donor or acceptor) on the Ru surface during the RWGS reaction. However, our DFT calculations do not explicitly include co-adsorption; therefore, this requires further investigation. H_2O is the most impacted, with an opposite behaviour: the chemisorption is strengthened by a positive polarization, switching from exergonic desorption under a negative polarization (ΔG_{des}= -0.25 eV at -1V) to endergonic desorption

(ΔG_{des}= +0.61 eV) under a positive polarization while it was athermic under O.C. conditions (ΔG_{des}= -0.08 eV). These general trends are in agreement with empirically established rules of electrochemical promotion where the chemisorption of electron acceptor (*i.e.* CO_2) is favoured by a negative polarization and electron donor (*i.e.* H_2O) by positive polarization [6,32]. The resulting overall profiles (shown in Figure B-3 (a) and (b)) are hence modulated by the polarization.

The influence of polarization on the CO/CH_4 selectivity is illustrated in Figure 4-6 focusing on the branching from CO* to CO and CHO*. As already mentioned, the influence on CO chemisorption is rather weak (less than 0.1 eV). The CO*+H* → CHO* is more sensitive with variations up to 0.23 eV in the reaction Gibbs energy. As previously seen, under O.C. the difference is small between these two competing reactions (0.05 eV), in favour of CO desorption. This difference in favour of CO desorption increases under negative polarization (0.15 eV), due to a destabilization of the CHO intermediate. This is in line with the decrease in CH_4 production under a negative polarization which was observed experimentally. Under a positive polarization, this branching turns slightly, by 0.03 eV, in favour of the hydrogenation of CO* into CHO*. In addition, the steps that follow are less endothermic, overall facilitating CH_4 production as seen in our experiments (see Figure 4-4). However, inferring a quantitative picture on the overall production rates of CO and CH_4 would require more advanced modeling, including transition states but also likely an improved description of the active sites of the Ru nanoparticles and perhaps even the effect of co-adsorbed species.

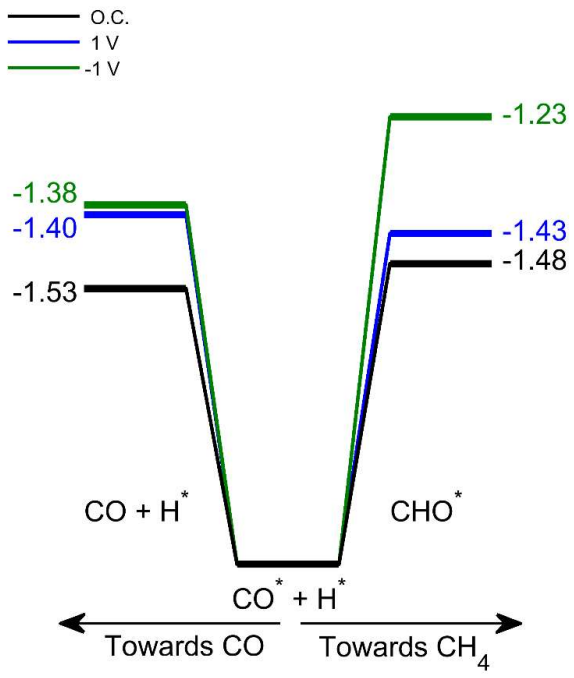

Figure 4-6. Branching from the CO*+H* intermediate to CO and to CHO* in function of the polarization. Energies are provided in eV.

4.4 Conclusion

Our computational model of EPOC that includes the polarization at the interface without specifying the promoting species predicts selectivity trends that are qualitatively in line with the experimental observations. It confirms that the selectivity of this reaction is not sensitive to the type of migrating species but to the change of surface electrochemical potential and the associated surface polarization. Hence, we can safely assume that the main EPOC effect stems from the electric field in the effective double layer and the varying number of electrons during the reaction which keep the potential constant as a function of the reaction coordinate. The combination of periodic DFT and experiments shows that the relative energy of CHO as a function of the electrochemical potential of the catalyst surface is key for determining the selectivity between CO and CH_4 production. The computational simplicity of our model allows it to be used in future studies to depict the polarization effect for various reactions and catalysts, as well as MSI and other promotional phenomena in catalysis.

References

[1] S. Saeidi, S. Najari, F. Fazlollahi, M.K. Nikoo, F. Sefidkon, J.J. Klemeš, L.L. Baxter, Mechanisms and kinetics of CO 2 hydrogenation to value-added products: A detailed review on current status and future trends, Renew. Sustain. Energy Rev. 80 (2017) 1292–1311. doi:10.1016/j.rser.2017.05.204.

[2] T. Avanesian, G.S. Gusmão, P. Christopher, Mechanism of CO2 reduction by H2 on Ru(0 0 0 1) and general selectivity descriptors for late-transition metal catalysts, J. Catal. 343 (2016) 86–96. doi:10.1016/j.jcat.2016.03.016.

[3] S.-T. Zhang, H. Yan, M. Wei, D.G. Evans, X. Duan, Hydrogenation mechanism of carbon dioxide and carbon monoxide on Ru(0001) surface: a density functional theory study, RSC Adv. 4 (2014) 30241. doi:10.1039/C4RA01655F.

[4] X. Wang, H. Shi, J. Szanyi, Controlling selectivities in CO2 reduction through mechanistic understanding, Nat. Commun. 8 (2017) 513. doi:10.1038/s41467-017-00558-9.

[5] K. Yaccato, R. Carhart, A. Hagemeyer, A. Lesik, P. Strasser, A.F. Volpe, H. Turner, H. Weinberg, R.K. Grasselli, C. Brooks, Competitive CO and CO2 methanation over supported noble metal catalysts in high throughput scanning mass spectrometer, Appl. Catal. A Gen. 296 (2005) 30–48. doi:10.1016/j.apcata.2005.07.052.

[6] D. Theleritis, M. Makri, S. Souentie, A. Caravaca, A. Katsaounis, C.G. Vayenas, Comparative study of the electrochemical promotion of CO2 hydrogenation over Ru-supported catalysts using electronegative and electropositive promoters, ChemElectroChem. 1 (2014) 254–262. doi:10.1002/celc.201300185.

[7] I. Kalaitzidou, M. Makri, D. Theleritis, A. Katsaounis, C.G. Vayenas, Comparative study of the electrochemical promotion of CO2 hydrogenation on Ru using Na+, K+, H+ and O2- conducting solid electrolytes, Surf. Sci. 646 (2016) 194–203. doi:10.1016/j.susc.2015.09.011.

[8] E.A. Baranova, C. Bock, D. Ilin, D. Wang, B. MacDougall, Infrared spectroscopy on size-controlled synthesized Pt-based nano-catalysts, Surf. Sci. 600 (2006) 3502–3511. doi:10.1016/j.susc.2006.07.005.

[9] I.R. Gibson, G.P. Dransfield, J.T.S. Irvine, Sinterability of commercial 8 mol% yttria-stabilized zirconia powders and the effect of sintered density on the ionic conductivity, J. Mater. Sci. 33 (1998) 4297–4305. doi:10.1023/A:1004435504482.

[10] H.A.E. Dole, A.C.G.S.A. Costa, M. Couillard, E.A. Baranova, Quantifying metal support interaction in ceria-supported Pt, PtSn and Ru nanoparticles using electrochemical technique, J. Catal. 333 (2016) 40–50. doi:10.1016/j.jcat.2015.10.015.

[11] Y.M. Hajar, H.A. Dole, M. Couillard, E.A. Baranova, Investigation of heterogeneous catalysts by electrochemical method: Ceria and titania supported iridium for ethylene oxidation, ECS Trans. 72 (2016) 161–172. doi:10.1149/07207.0161ecst.

[12] G. Kresse, J. Furthmiiller, Efficiency of ab-initio total energy calculations for metals and semiconductors using a plane-wave basis set, Comput. Mater. Sci. 6 (1996) 15–50. doi:10.1016/0927-0256(96)00008-0.

[13] G. Kresse, J. Hafner, Ab initio molecular dynamcis for liquid metals, Phys. Rev. B. 47 (1993) 558–561. doi:10.1103/PhysRevB.47.558.

[14] S.N. Steinmann, P. Sautet, Assessing a First-Principles Model of an Electrochemical Interface by Comparison with Experiment, J. Phys. Chem. C. 120 (2016) 5619–5623. doi:10.1021/acs.jpcc.6b01938.

[15] Kresse, G.; Furthmiiller, J. Efficiency of Ab-Initio Total Energy Calculations for Metals and Semiconductors Using a Plane-Wave Basis Set. Comput. Mater. Sci. 1996, 6,15−50. doi: 10.1016/0927-0256(96)00008-0

[16] K. Mathew, V.S.C. Kolluru, S. Mula, S.N. Steinmann, R.G. Hennig, Implicit self-consistent electrolyte model in plane-wave density-functional theory, J. Chem. Phys. 151 (2019) 234101. doi:10.1063/1.5132354.

[17] Y.M. Hajar, L. Treps, C. Michel, E.A. Baranova, S.N. Steinmann, Theoretical insight into the origin of the electrochemical promotion of ethylene oxidation on ruthenium oxide, Catal. Sci. Technol. 9 (2019) 5915–5926. doi:10.1039/c9cy01421g.

[18] Vayenas, C. G.; Bebelis, S.; Pliangos, C.; Brosda, S.; Tsiplakides, D. Electrochemical Activation of Catalysis: Promotion, Electrochemical Promotion, and Metal-Support Interactions; Springer: New York, 2001

[19] D. Theleritis, S. Souentie, A. Katsaounis, C.G. Vayenas, Hydrogenation of CO2 over Ru electropromoted catalysts, ACS Catal. 2 (2012) 770–780. doi:dx.doi.org/10.1021/cs300072a.

[20] Y. Daza, J.N. Kuhn, CO2 conversion by reverse water gas shift catalysis: Comparison of catalysts and mechanisms and their consequences for CO2 conversion to liquid fuels, RSC Adv. 6 (2016) 49675–49691. doi:10.1039/C6RA05414E.

[21] G. Pacchioni, F. Illas, S. Neophytides, C.G. Vayenas, Quantum-chemical study of electrochemical promotion in catalysis, J. Phys. Chem. 100 (1996) 16653–16661. doi:10.1021/jp9612386.

[22] E.P.M. Leiva, C. Vázquez, M.I. Rojas, M.M. Mariscal, Computer simulation of the effective double layer occurring on a catalyst surface under electro-chemical promotion conditions, J. Appl. Electrochem. 38 (2008) 1065–1073. doi:10.1007/s10800-008-9539-x.

[23] G. Pacchioni, J.R. Lomas, F. Illas, Electric field effects in heterogeneous catalysis, J. Mol. Catal. A Chem. 119 (1997) 263–273. doi:10.1016/S1381-1169(96)00490-6.

[24] S.N. Steinmann, C. Michel, R. Schwiedernoch, J.S. Filhol, P. Sautet, Modeling the HCOOH/CO2 Electrocatalytic Reaction: When Details Are Key, ChemPhysChem. 16 (2015) 2307–2311. doi:10.1002/cphc.201500187.

[25] N.G. Hörmann, O. Andreussi, N. Marzari, Grand canonical simulations of electrochemical interfaces in implicit solvation models, J. Chem. Phys. 150 (2019) 041730. doi:10.1063/1.5054580.

[26] M.M. Melander, M.J. Kuisma, T.E.K. Christensen, K. Honkala, Grand-canonical approach to density functional theory of electrocatalytic systems: Thermodynamics of solid-liquid interfaces at constant ion and electrode potentials, J. Chem. Phys. 150 (2019). doi:10.1063/1.5047829.

[27] R. Sundararaman, W.A. Goddard, T.A. Arias, Grand canonical electronic density-functional theory: Algorithms and applications to electrochemistry, J. Chem. Phys. 146 (2017) 114104. doi:10.1063/1.4978411.

[28] S.N. Steinmann, P. Sautet, C. Michel, Solvation free energies for periodic surfaces: comparison of implicit and explicit solvation models, Phys. Chem. Chem. Phys. 18 (2016) 31850–31861. doi:10.1039/c6cp04094b.

[29] H. Zhang, W.A. Goddard, Q. Lu, M.J. Cheng, The importance of grand-canonical quantum mechanical methods to describe the effect of electrode potential on the stability of intermediates involved in both electrochemical CO2 reduction and hydrogen evolution†, Phys. Chem. Chem. Phys. 20 (2018) 2549–2557. doi:10.1039/c7cp08153g.

[30] M. Mamatkulov, J.S. Filhol, An ab initio study of electrochemical vs. electromechanical properties: The case of CO adsorbed on a Pt(111) surface, Phys. Chem. Chem. Phys. 13 (2011) 7675–7684. doi:10.1039/c0cp01444c.

[31] S. González, C. Sousa, F. Illas, Electric field effects in the chemisorption of CO on bimetallic RhCu surface models, Surf. Sci. 548 (2004) 209–219. doi:10.1016/j.susc.2003.11.009.

[32] S. Brosda, C.G. Vayenas, J. Wei, Rules of chemical promotion, Appl. Catal. B Environ. 68 (2006) 109–124. doi:10.1016/j.apcatb.2006.07.021.

Appendix B: Supplementary Information for Chapter 4

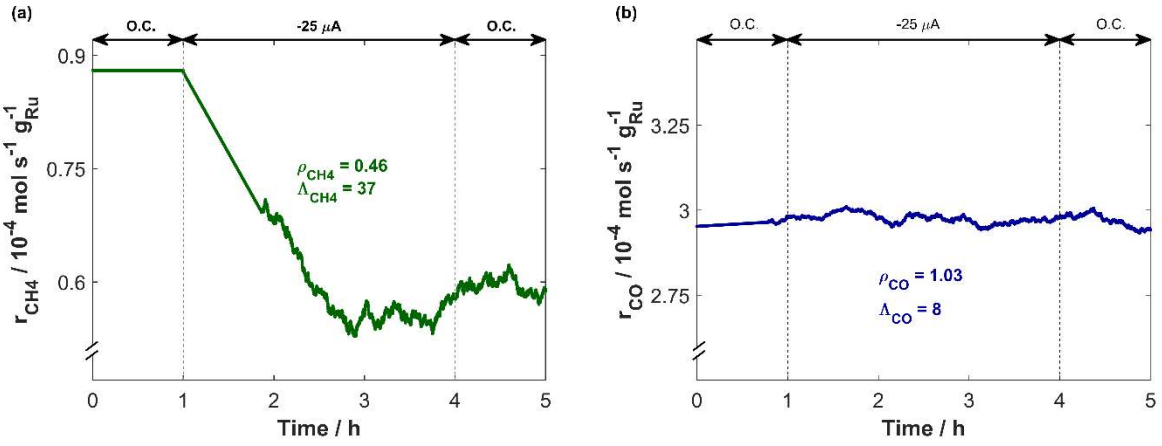

Figure B-1. Transient effect upon application of -25 μA at 250 °C for the production of (a) CH_4 and (b) CO. 0.2 mg catalyst, CO_2:H_2 = 7:1 and 100 mL min^{-1}.

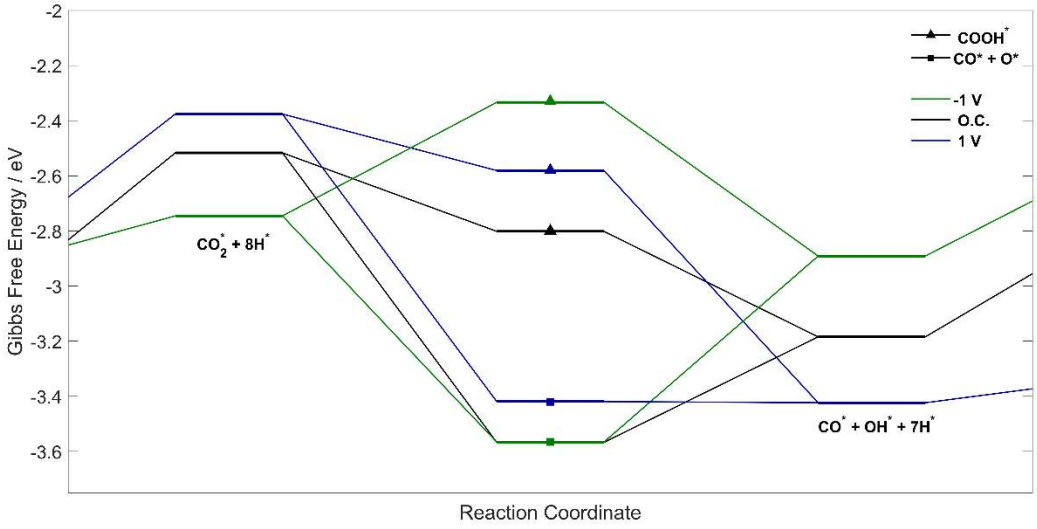

Figure B-2. Competitive pathway for COOH* and CO*+O* at open-circuit, 1 V and -1 V at 250 °C and atmospheric pressure.

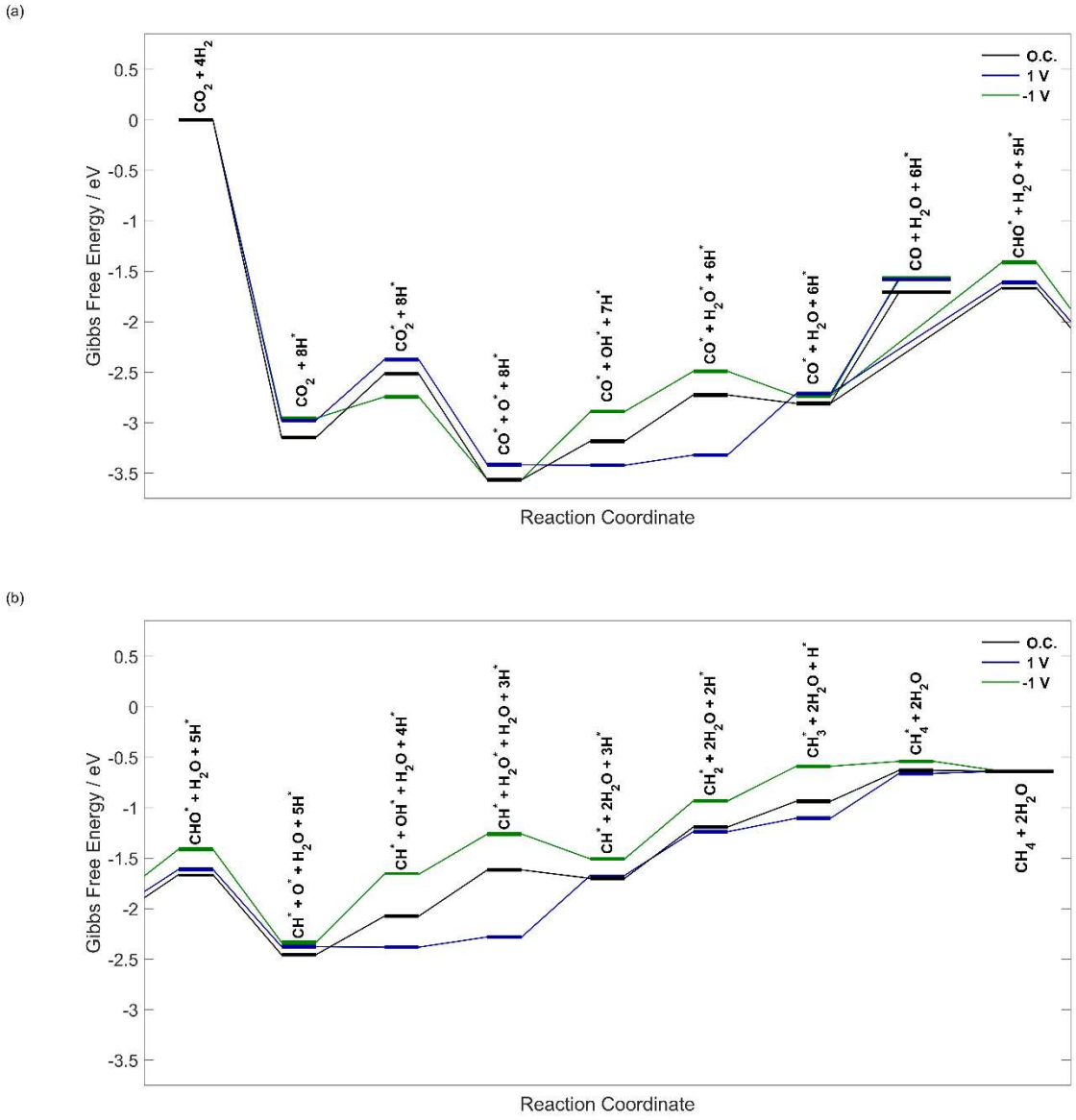

Figure B-3. CO_2 hydrogenation pathway for (a) CO desorption and (b) CH_4 desorption on Ru(0001) for open-circuit conditions and closed circuit conditions of -1 V and 1 V at 250 °C, standard conditions.

Table B-1. Calculated Gibbs Free energy for each intermediate species at open-circuit, 1 V and -1 V of polarization, at 525K (250ºC). Associated with Figure 4-5, Figure B-2 and Figure B-2.

Intermediate Step	Gibbs Free Energy (eV)		
	Open-Circuit	1V	-1V
CO_2+4H_2	0	0	0
CO_2+8H*	-3.15	-2.98	-2.96
CO_2*+8H*	-2.52	-2.38	-2.75
CO*+O*+8H*	-3.57	-3.42	-3.57
CO*+OH*+7H*	-3.18	-3.42	-2.89
CO*+H_2O*+6H*	-2.73	-3.32	-2.49
CO*+H_2O+6H*	-2.81	-2.71	-2.74
CO+H_2O+6H*	-1.71	-1.58	-1.56
CO+H_2O+3H_2	0.65	0.65	0.65
CHO*+5H*+H_2O	-1.66	-1.61	-1.41
CH*+O*+5H*+H_2O	-2.46	-2.38	-2.34
CH*+OH*+4H*+H_2O	-2.08	-2.38	-1.66
CH*+H_2O*+3H*+H_2O	-1.62	-2.28	-1.26
CH*+3H*+2H_2O	-1.70	-1.67	-1.51
CH_2*+2H*+2H_2O	-1.19	-1.24	-0.93
CH_3*+H*+2H_2O	-0.94	-1.11	-0.59
CH_4*+2H_2O	-0.63	-0.66	-0.54
CH_4+2H_2O	-0.64	-0.64	-0.64
Competitive Species (Figure B-3)			
COOH*+7H*	-2.8	-2.58	-2.33

Chapter 5 : Electrochemical promotion of Ru nanoparticles deposited on a proton conductor electrolyte during CO_2 hydrogenation

*Adapted from: D. Zagoraios[#], **C. Panaritis**[#], A. Krassakopoulou, E. A. Baranova, A. Katsaounis, C. G. Vayenas. Journal of Applied Catalysis B: Environmental, 276 (2020) 119148.*

Abstract

Recycling CO_2 into a carbon-neutral source is a beneficial approach in reducing non-renewable energy sources. Herein, the electrochemical promotion of catalysis (EPOC) effect has been exploited to enhance the catalytic activity of Ru nanoparticles (0.7-1 nm) deposited on the proton conductor yttria-doped barium zirconate (BZY), as free-standing nanoparticles and supported on Co_3O_4 semiconductor, for CO_2 hydrogenation. Under 250-450 ºC and atmospheric pressure, both methanation and reverse water-gas shift (RWGS) reaction take place simultaneously over the Ru nanoparticles with a superior selectivity to CO. Under anodic polarization, free-standing Ru nanoparticles displayed an increase in CH_4 and a decrease in CO production, while the opposite effect was observed under cathodic polarization. Ru supported on Co_3O_4 displayed a superior catalytic activity mostly due to enhanced metal-support interactions. The electronic effects induced by the pairing of Co_3O_4 and BZY resulted in a new approach to EPOC applications that brings it closer to industrial application.

5.1 Introduction

Comparing the fundamentals of the EPOC effect with the metal-support interaction effect, have been shown to be functionally identical, *i.e.* it is catalysis in the presence of a controllable double layer at the gas-exposed catalyst interface [1,2]. Proportionally, a metal-support interaction is mechanistically equivalent with a 'wireless' NEMCA configuration, that allow ionic species from the solid electrolyte to migrate to the gas-exposed metal surface without the application of potential [1,3]. One of the most important 'wireless' NEMCA study, was the comparison between Rh film on YSZ and Rh particles supported on TiO_2 [3]. Upon application of positive potentials

(O^{2-} migration from YSZ to the catalyst), authors observed the same trend in catalytic rate as in the case of Rh/TiO_2 due to the MSI effect. The proposed mechanism is that the support displayed a higher work function (higher ability to donate O^{2-}) than the supported metal, allowing it to initially receive electrons from the metal and the positive charge on Rh will induce O^{2-} reverse spillover to neutralize it [3]. This is an important operational advantage of EPOC, as it permits the use of a wide variety of promoters (e.g., O^{2-}, H^{+}), which have short life times for classical promotion applications [2].

In the present chapter, we studied the electrochemical promotion of CO_2 hydrogenation reaction under atmospheric pressure over three different catalysts: free-standing Ru nanoparticles (NPs), Ru NPs supported on Co_3O_4 and pure Co_3O_4. All of them were deposited on the proton conductor yttria-doped barium zirconate (BZY) and were tested for their catalytic and electrocatalytic behaviour. This is one of the first electrochemical promotion studies, where an oxide semiconductor is used as a support and as an active catalyst on a proton conductor electrolyte for CO_2 hydrogenation. Furthermore, the catalysts were characterized before and after electrochemical promotion experiments in order to investigate the consequential changes in the samples' physicochemical characteristics during reaction conditions

5.2 Experimental

5.2.1 *Deposition of Ru nanoparticles*

Ru nanoparticles (synthesis in Chapter 4.2.1) were mixed with Co_3O_4 (637025, Sigma - Aldrich, Cobalt(II,III) oxide nanopowder, <50 nm particle size (TEM), 99.5% trace metals basis) and 40 mL distilled (3D) water (18 MΩ·cm) and stirred at room temperature for 48 h. The mixture was then centrifuged four times with distilled (3D) water between each step. The catalyst was stirred dried at 50 ºC and further oven dried at 120 °C for 3h. The final composition of the catalyst was Ru/Co_3O_4 (2 wt.%). Previous work in Chapter 3 has displayed 2 wt.% to be sufficient Ru metal loading.

5.2.2 *Electrochemical cell*

A BZY ($BaZr_{0.85}Y_{0.15}O_3$ + 1 w% NiO) disc with a diameter of 18 mm and a thickness of 2 mm (NorECs AS, Norway) was utilized as the solid electrolyte, same size as YSZ (Chapter 4.2.3) [22]. On one side of the electrolyte, gold (Au) reference and counter electrodes were deposited using Au organometallic paste (Metalor A1118) following calcination at 450 °C for 30 minutes

and then at 700 °C for 1h. Blank experiments showed that gold electrodes were catalytically inactive both for the methanation and the RWGS reactions. All the examined catalysts/working electrodes (free-standing Ru NPs, supported Ru/Co_3O_4 (2 wt.%) and Co_3O_4) were deposited on the other side of the solid electrolyte (opposite to the counter electrode). In the case of free-standing NPs, Ru colloidal solution was directly deposited on the BZY electrolyte disc, inside a square (1 cm^2) tape mask followed by air-drying at 80 °C, forming a nanofilm. In the supported case, both catalysts Ru/Co_3O_4 (2 wt.%) and Co_3O_4 were drop-deposited on BZY via a micropipette containing the catalyst powder-isopropanol solution followed by subsequent drying at 60 ºC for 5 min after each deposit. The final mass of the Ru nanofilm was 0.5 mg, while the mass of Ru/Co_3O_4 (2 wt.%) and Co_3O_4 were both 2.6 mg. The samples were all calcined in air at 350 ºC for 1 h and then reduced in an H_2 atmosphere for at least 5 h.

5.2.3 *Experimental Setup*

Catalytic and electrocatalytic experiments were carried out in an atmospheric pressure single chamber reactor with a volume of 70 cm^3, as described in detail elsewhere [2,4]. Reactants consisted of Air Liquide certified standards of 5% CO_2 in He and 14.6% H_2 in He, that could be further diluted in ultrapure (99.999%) He (Air Liquide). Analysis of the reactants and products was performed using online CO_2-CO-CH_4 infrared gas analyzer (Futzi Electric ZRE) for the continuous and quantitative concentration measurements. Application of current or potential difference was performed by means of a galvanostat/potentiostat (AMEL 2053). Under these experimental conditions, only CO and CH_4 production was observed at temperatures up to 450 °C. The EPOC effect can be quantified through the rate enhancement ratio (eq. 4.1) and apparent Faradaic efficiency (eq. 4.2).

5.2.4 *Characterization of Ru NPs deposited on BZY*

The morphology of free-standing Ru NPs deposited on BZY solid electrolyte was also explored through scanning electron microscopy (SEM). SEM images were obtained using a JEOL 6300 microscope, equipped with an Oxford energy dispersive spectrometer (EDS). The images were taken under a magnification of 300,000 times with a distinctive limit of 3.5 nm (W.D. = 8 mm, 30 kV / SEI). The XPS spectra were measured on a Kratos Axis Nova spectrometer equipped with an Al X-ray source. As-prepared Ru nanoparticles were deposited on a Si grid and analyzed in an ultrahigh vacuum (10-10 Torr) chamber of the spectrometer. The XPS data were collected

using AlKα radiation at 1486.69 eV (150 W, 10 mA), a charge neutralizer and a delay-line detector (DLD) consisting of three multi-channel plates. High resolution of Ru3p, O1s and C1s were taken with a pass energy of 20 eV. Binding energies are referred to the C1s peak at 285 eV.

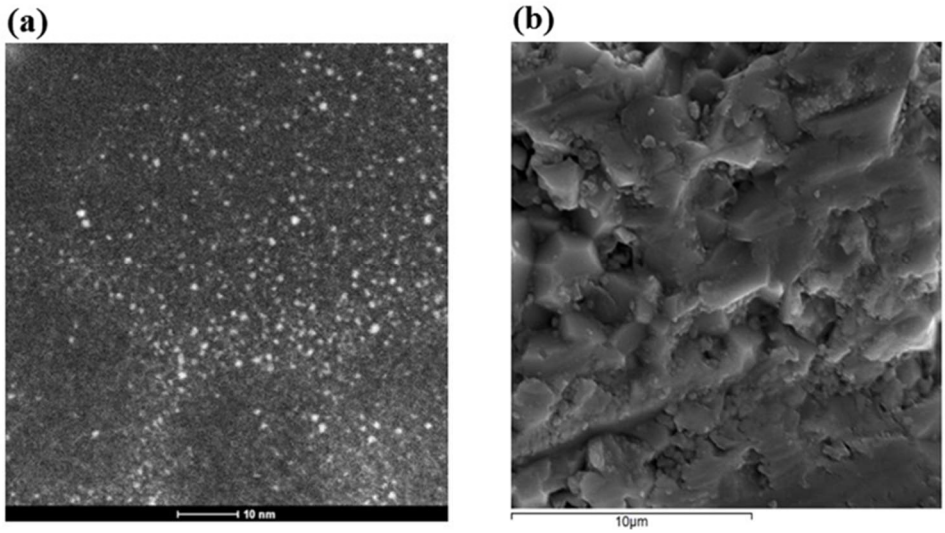

Figure 5-1. (a) STEM image of free-standing Ru nanoparticles, (b) SEM image of pure BZY surface.

Figure 5-1 (a) shows the STEM distribution of the free-standing Ru nanoparticles. The nanoparticles are assumed to be in an oxidized state as RuO_x (displayed as the white spots) and be reduced to metallic Ru under catalyst pretreatment. In accordance with the polyol synthesis method the average size of the Ru NPs is approximately 0.7-1 nm (Figure C-1 of Appendix C). The roughness of the BZY surface is displayed in Figure 5-1 (b), showing a rough structure allowing for sufficient adhesion/attachment between the Ru nanoparticles and the solid electrolyte. Furthermore, EDS analysis confirmed the presence of elemental traces of Ba, Zr and traces of Ni (Figure C-2). Furthermore, the presence of RuO_2 state for the as-prepared nanoparticles is displayed in the high-resolution XPS spectra in Figure C-3. Similar conclusion can be drawn by the previous analysis in our lab, where the Ru3p peak is located at 461.7 eV [5,6]. The presence of RuO_2 is confirmed through the full width at half maximum (FWHM) which is around ~5 eV and in Figure C-3 (b) showing the O1s spectrum of the RuO_2 oxidized state.

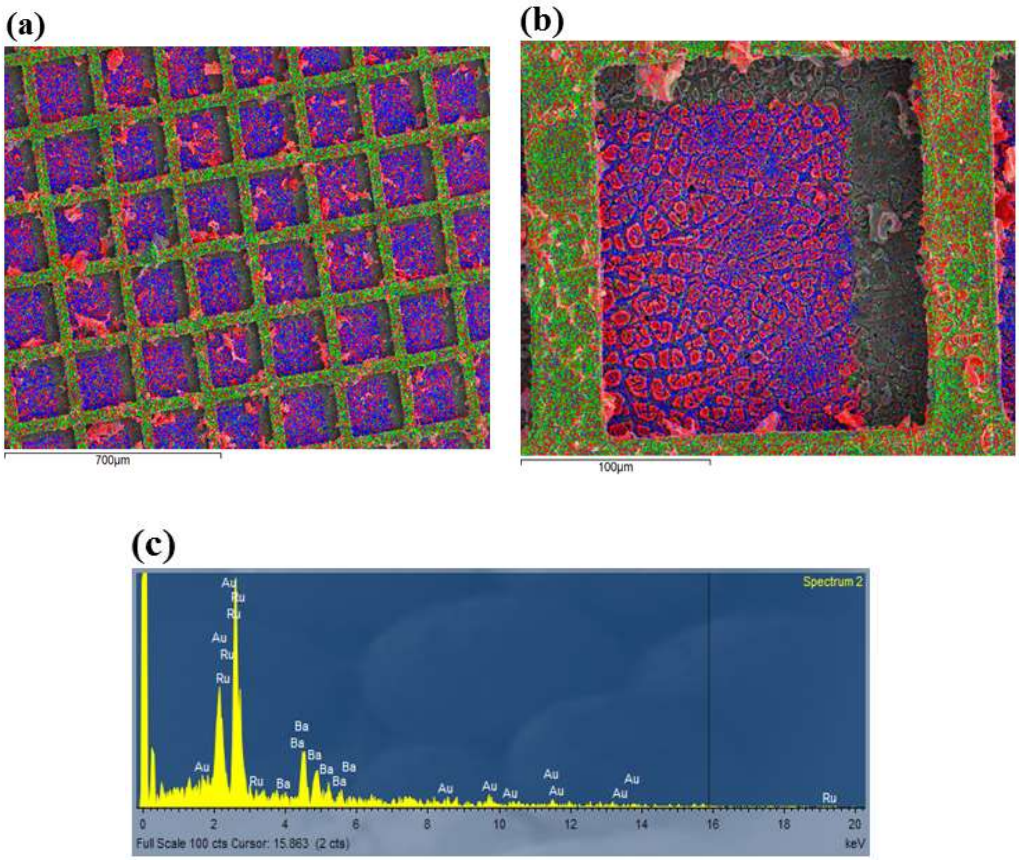

Figure 5-2. SEM mapping images of (a) Ru NPs/BZY, (b) a zoom in of a section of the gold grid (Ru: red, Ba: blue, and Au: green) and (c) EDS analysis spectrum.

Figure 5-2 (a) and (b) display the SEM images of the spent Ru working electrode surface. The gold grid that was used to increase the conductivity of the working electrode during the reaction was left on the catalyst to ensure conductivity for the SEM measurements. A distant view of the catalytic film after the reaction is shown in Figure 5-2 (a), where Ru, Ba, and Au are represented by the colours red, blue, and green, respectively. EDS analysis (Figure 5-2 (c)) confirms the presence of only Ru, Ba and Au. As it was expected, Au is mainly located as the squared golden grid and Ba occupies the majority of the rough surface. This is consistent with the idea that at elevated reaction temperatures the Ru NPs agglomerate and form bigger particles with mean size of about to 30 µm on the surface of BZY. Islands of Ru are observed on the top surface (Figure 5-2 (b)) and not in between the crevices of the BZY substrate. Furthermore, Ru agglomeration takes place at the edges of the square, correlated with the way the film is evaporated,

also known as coffee stain/ring effect, where particles move and deposit to the edge of the gold grid [7]. The casted shadow in Figure 5-2 (b) is due to the way the electron beam scattered on the surface and the position where the detector is located.

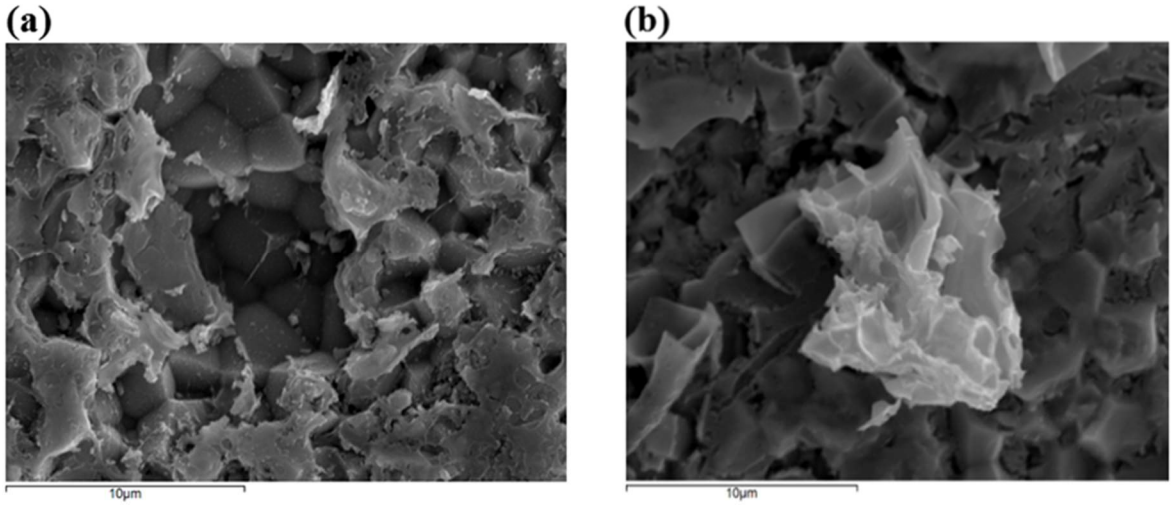

Figure 5-3. SEM morphological images of the Ru NPs/BZY (a) porous and (b) agglomerated particles.

The morphology of the catalytic film deposited on BZY is shown in Figure 5-3. The film is uniform (Figure 5-3 (a)), while defects (such as holes) are also present. Figure 5-3 (b) demonstrates agglomerated Ru particles deposited on the BZY electrolyte. It is worth noting that there are different sized particles and from the analysis this is correlated with the position of the particles. Particles tend to agglomerate near the gold grid, while those directly on BZY are more dispersed.

5.2.5 ***Characterization of Ru/Co_3O_4 powder***

5.2.5.1 STEM and TEM Analysis

In order to investigate the physicochemical properties of the Ru/Co_3O_4 (2 wt.%) catalyst, STEM analysis described in Chapter 4.2.2 was used to determine the mean metal particle size distribution and the morphology of the as-prepared (without reduction pretreatment) catalyst (Figure 5-4 (a)). Transmission Electron Microscopy (TEM) characterization was carried out using a JEOL JEM-2100 transmission electron microscope operating at 200 kV to characterize the used sample after reaction conditions (Figure 5-4 (b)). Sample preparation involved the ultrasonic

dispersion of the sample (1 min) in water, followed by a drop suspension on a carbon coated copper grid (dia. 3mm, Electron Microscopy Sciences).

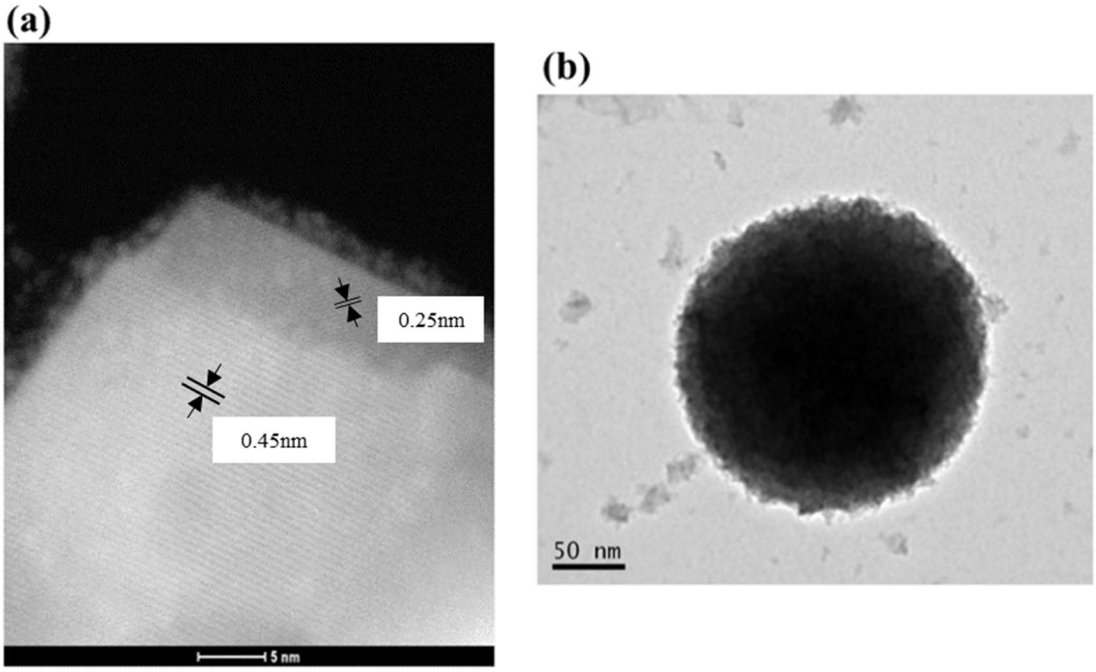

Figure 5-4. (a) STEM images of fresh and (b) TEM image of used Ru/Co_3O_4 (2 wt.%) powder.

Displayed in Figure 5-4 (a), are the supported Ru NPs on Co_3O_4 represented by the whiter dots on the Co_3O_4, through the use of STEM analysis. Moreover, spinel Co_3O_4 crystalline structure is clearly observed, with a d-spacing of 2.5 Å and 4.5 Å corresponding to CoO(111) and Co_3O_4(111), respectively, which is line with previous literature data [8,9]. Figure 5-4 (b) displays the Ru/Co_3O_4 (2 wt.%) catalyst after the reaction. In contrast with the fresh sample, the catalyst experiences a structural change, where the Co_3O_4 has formed a spherical shape. The change in structure is due to the high elevated temperature and exposure to the various reducing conditions, reducing it from Co_3O_4 to CoO [10]. The reducing conditions include: reducing reaction conditions, and the spontaneous and electrochemical migration of protons (H^+) from the support (BZY). The reduction of Co_3O_4 to CoO, results in the formation of oxygen vacancies, allowing the Ru NPs present to migrate into the CoO_x structure during the reduction pre-treatment [11–13]. Elevated temperatures also result in agglomeration of both Ru and Co_3O_4 particles. Finally, the only oxidizing conditions the catalyst experiences is through the dissociation of CO_2 into CO and O, which is assumed not to be suffice to keep the Ru in an oxidized state, unlike supplying direct

oxygen to the catalyst. STEM images taken of the used sample was difficult to distinguish the Ru nanoparticles on Co_3O_4, however the presence of Ru is confirmed through Energy-dispersive X-ray spectroscopy (EDX) mapping, provided in Figure C-4. A reason to why Ru nanoparticles were not visible, can be related to the work done by Yang *et al*. [14], where they determined that nanoparticles embedded in the structure and/or adhere strongly on the surface of the support can result in a low contrast resolution.

5.2.5.2 XRD Analysis

In order to confirm the results from TEM analysis, X-Ray Diffraction (XRD) measurements have been carried out for both fresh and used Ru/Co_3O_4 (2 wt.%). As shown in Figure 5-5 (a), the fresh sample (red line) demonstrates a typical XRD pattern of Co_3O_4. Some of the characteristic peaks are at $2\theta = 31.5, 37, 45, 55.8, 60, 65.5^{o}$, associated with the standard XRD pattern generated through the Crystallographica Search-Match software (Figure C-5). No crystallinity for the free-standing Ru nanoparticles was observed due to their small size and amorphous structure, which has been shown previously [15]. Additionally, the amorphous phase of NPs can be attributed to the low percentage (2 wt.%) of Ru on Co_3O_4.

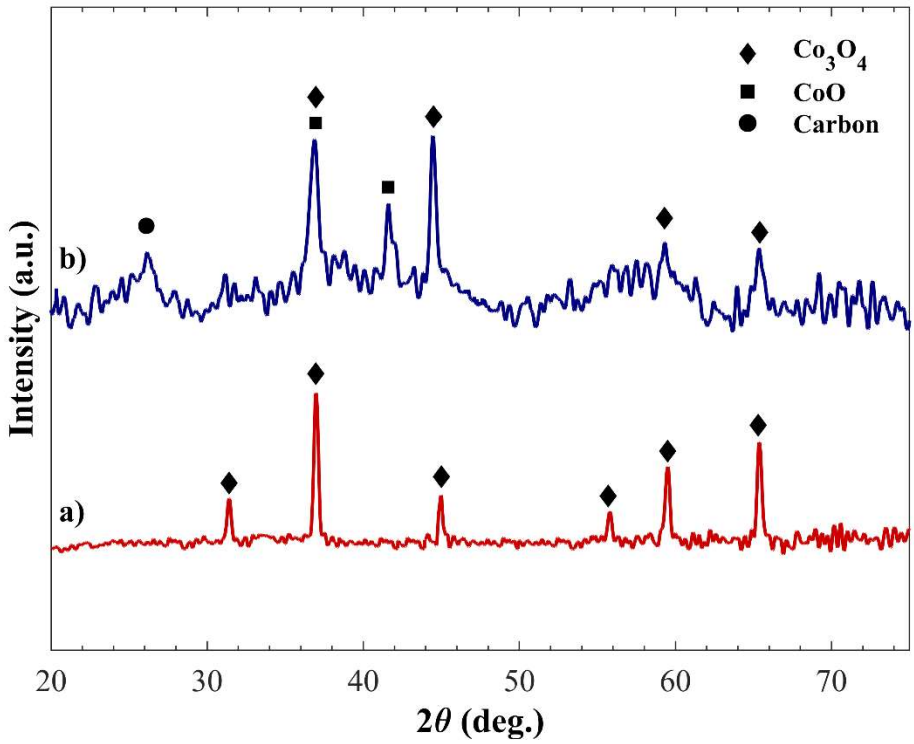

Figure 5-5. Comparison XRD pattern for (a) fresh and (b) used Ru/Co_3O_4 (2 wt.%) catalytic powder.

The XRD pattern for the used sample (blue line) is different from the fresh one (red line). The peaks in Figure 5-5 (b) are not as sharp when compared with the fresh sample, indicating a decrease in crystallinity. The peak at $2\theta \sim 26^{o}$, indicates that carbon is present in the sample as the form of coke [16,17]. This is acceptable due to the deposition of carbon during the reaction process, possibly through the Boudouard reaction. Moreover, this carbon peak is not present in the fresh sample (red line) indicating that carbon was formed during the reaction. More importantly, in the case of the used sample (Figure 5-5 (b)) there is a new peak at $2\theta \sim 42^{o}$, correlating to one of the characteristic peaks in the CoO XRD pattern [9,18]. This result is consistent with the TEM result; where the change of cobalt oxide shape was assigned the formation of CoO. At higher 2θ values, the broad peak from 55 to 60^{o} includes peaks associated with Co_3O_4, CoO, and other oxidation states of CoO_x that can be affiliated with a proportion of the powder consisting of CoO. These results are in full agreement with the TEM results and indicate the formation of CoO during the reaction either via reducing conditions or H^+ migration/removal from BZY solid electrolyte.

5.3 Results

5.3.1 *Free-Standing Ru NPs*

Free-standing Ru nanoparticles deposited on BZY were evaluated in the temperature range 250–450 ºC. Figure 5-6 displays the open-circuit catalytic response under various CO_2:H_2 ratios (1:1, 1:4, 1:7). The selectivity towards methane increases as the partial pressure of H_2 increases, mainly at lower temperatures, displaying a maximum selectivity of 40% at 250 ºC. Even though the reaction takes place in high reducing conditions (1:7), the selectivity of methane remains below 50%, indicating that CO is the dominant product even at low temperatures. This observation could be explained by the low loading and high dispersion of Ru NPs spread over the rough BZY surface, as shown in Figure 5-2 (a) and (b). The high dispersion of active Ru sites hinders the hydrogenation of CO into CH_4 to take place, overall decreasing the likelihood of CH_4 formation [19,20]. Increase in temperature, leads to the production of CO according to the endothermicity of the RWGS reaction. Furthermore, as reported in previous studies [21–24], proton conductors (such as BZY) favour the production of CO due to the thermal formation of a double layer of protons at the metal-support interface resulting in an alteration (and more specifically decrease) of the work function of the metal. Thus, instead of further hydrogenation, the thermal migration of H^+ aids in the direct reduction of CO_2 into CO.

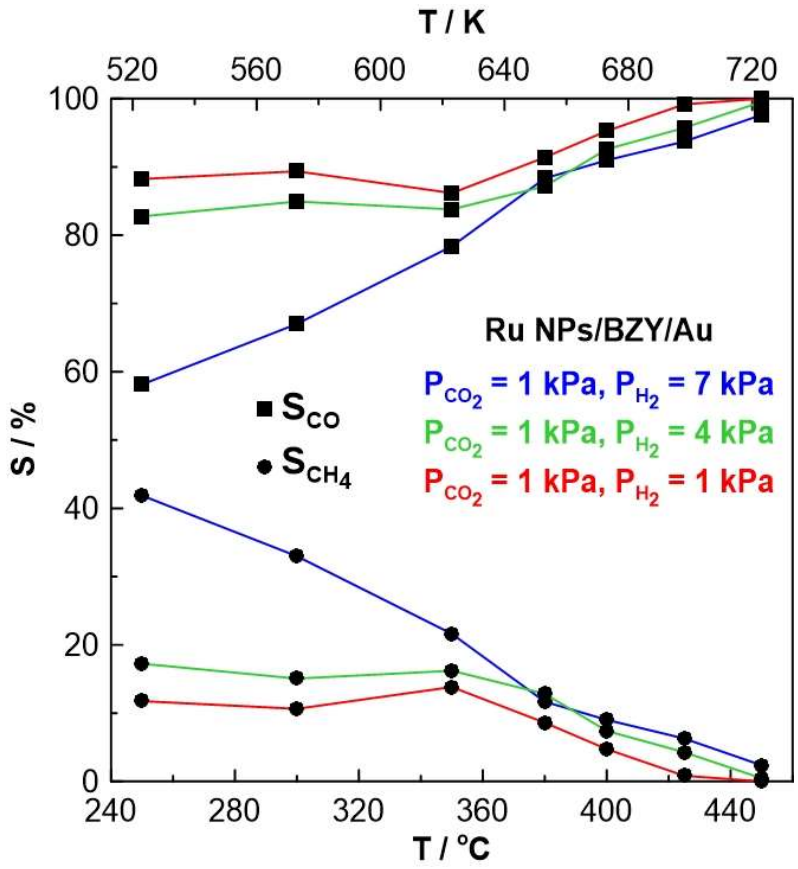

Figure 5-6. Catalytic performance of free-standing Ru nanoparticles for CO_2:H_2 ratios of 1:1, 1:4 and 1:7. 0.5 mg of catalyst and 100 mL min^{-1}.

Figure 5-7 (a)-(d), evaluates various CO_2:H_2 ratios and temperatures, under application of 1 mA (~2 V). Application of positive current or potential between the working electrode (WE) and counter electrode (CE) results in H^+ removal from the WE towards BZY, influencing the catalytic rates of both CO and CH_4 formation in agreement with the EPOC rules and previous studies [21,22]. Based on the EPOC transients (Figure 5-7), the CH_4 catalytic rate increases independently of the reaction conditions. The maximum rate enhancement ratio (ρ) for methane is about 2 in all cases, while the Λ values are above unity, indicating that the catalytic rate increase is non-Faradaic. Indeed, Λ values up to 10 are observed in the case of the most reducing conditions (1:7), while lower concentrations of H_2 in the gas mixture result in a decrease of apparent Faradaic efficiency down to 4. In most of the cases (Figure 5-7), the rate of CO production does not return to its initial value, indicating a suppressed permanent EPOC effect, with an average value γ of ~0.92. The parameter γ (P-EPOC) is expressed by eq. 1-12 [2,25].

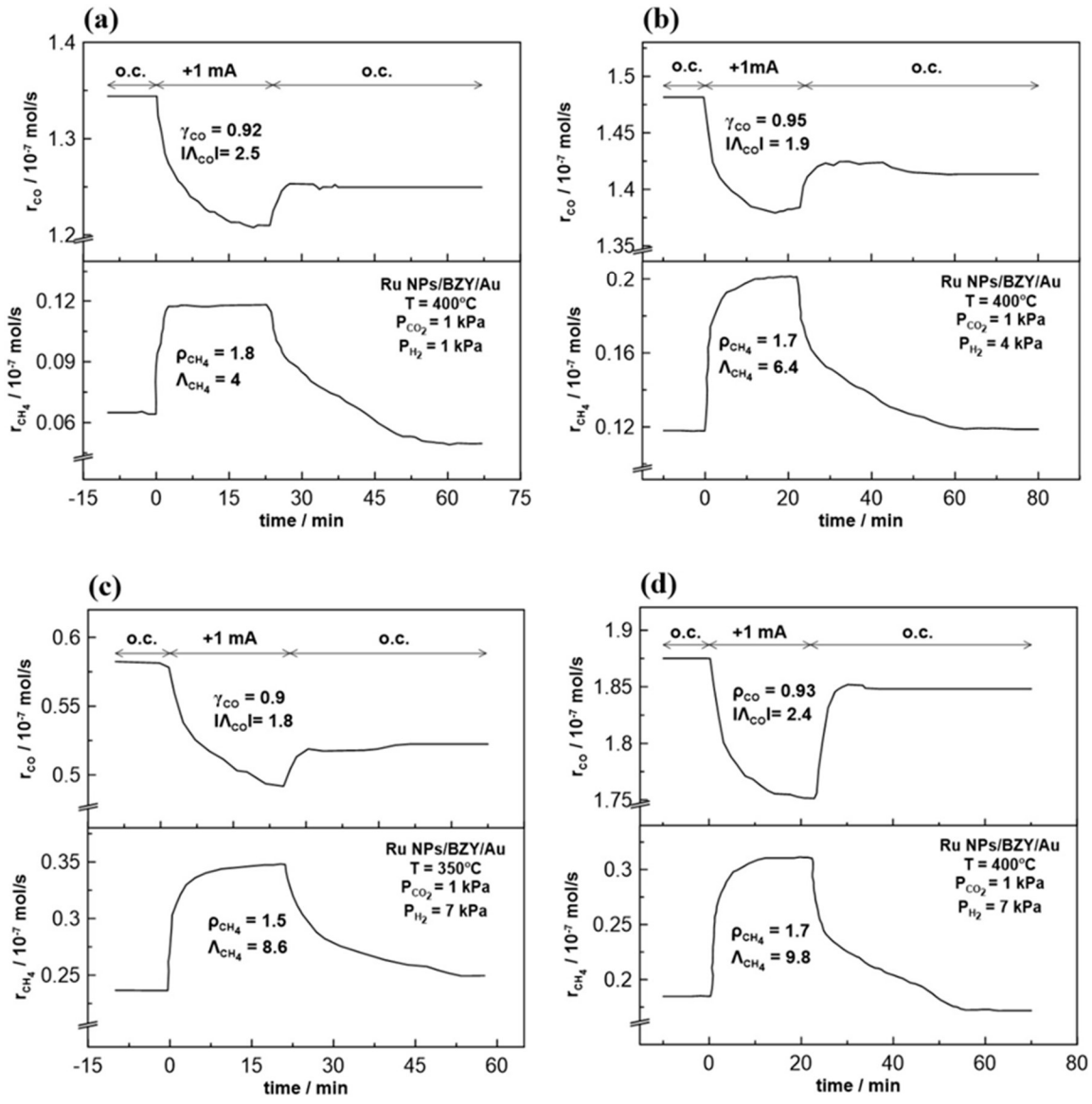

Figure 5-7. Transient response of Ru free-standing nanoparticles under current application of +1 mA at (a) 400 °C and CO_2:H_2, (b) 400 °C and CO_2:4H_2, (c) 350 °C and CO_2:7H_2, and (d) 400 °C and CO_2:7H_2. 0.5 mg of catalyst and 100 mL min^{-1}.

Transient experiments with negative polarization were also carried out. According to Figure 5-8 neither CH_4 rate, nor CO rate returned to their initial open-circuit rate value, revealing a permanent change in both catalytic rates. Negative polarization leads to the migration of H^+ from the BZY onto the gas-exposed Ru surface through the three-phase boundary. Only application of a positive current (removal of H^+ from Ru nanofilm) can force the catalytic rates to return to their

initial values. The permanent effect could be attributed to the presence of H^+ over the catalytic surface after current interruption, allowing Ru to remain in an electropromoted state. This is a synergestic effect between the Ru NPs and the formed proton double layer that cannot be destabilzed at low temperatures. Only above 425 °C does the permanent EPOC (p-EPOC) effect decrease (γ_{co}=1) as shown in Figure 5-8 (d), due to the easier destruction of the double layer, since the rise in temperatures grants the ions with energy that facilitates their desoprtion from the surface and/or reaction with CO_2. Furthermore, the permanent effect is beneficial since it provides a way to permanently suppress the methanation reaction and ensure selectivity towards the RWGS reaction.

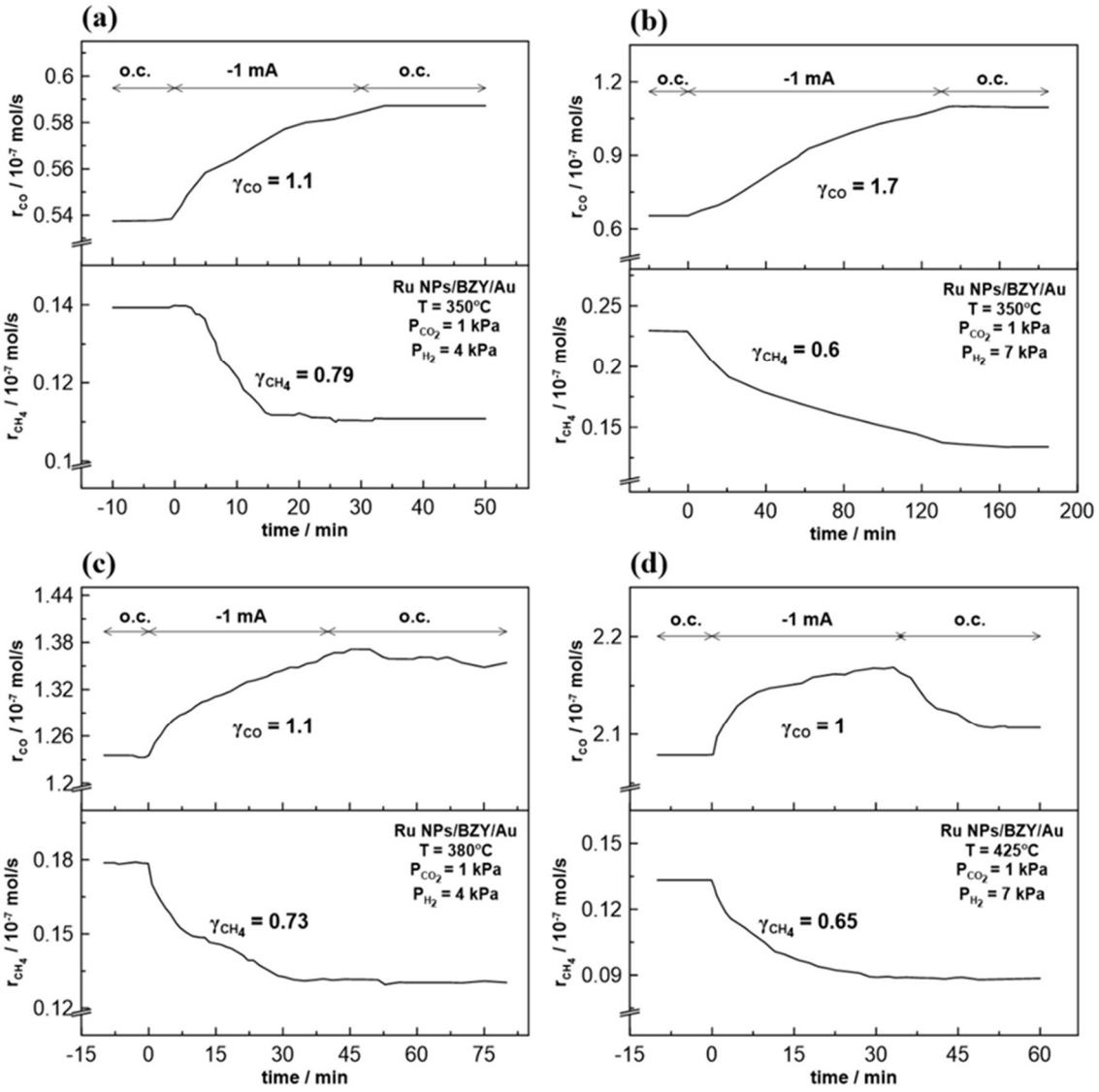

Figure 5-8. Transient response of Ru free-standing nanoparticles under current application of –1 mA at (a) 350 °C and CO_2:4H_2, (b) 350 °C and CO_2:7H_2, (c) 380 °C and CO_2:4H_2, and (d) 425 °C and CO_2:7H_2. 0.5 mg of catalyst and 100 mL min^{-1}.

Based on the results in Figure 5-7 and Figure 5-8 the methanation reaction exhibits electrophobic behaviour (*i.e.* the catalytic rate increases with positive polarization and decreases with negative polarization), while the RWGS reaction exhibits electrophillic bahaviour (*i.e.* the catalytic rate increases with negative polarization and decreases with positive polarization). Thus in aggrement with kinetic experiments (not shown here), which shows that the Sabatier reaction is positive order with respect to the electron donor (i.e. H_2) and negative or zero order with respect

to the electron acceptor (i.e. CO_2), whereas RWGS reaction exhibits the opposite kinetic behaviour. The current results are in agreement with previous EPOC studies on CO_2 hydrogenation [21–23], with the added benefit of the permanent behaviour.

5.3.2 *Ru/Co_3O_4 (2 wt.%)*

To evaluate the initial performance of the Ru/Co_3O_4 (2 wt.%) composite catalyst, light-off experiments were carried out in the temperature range of 250 – 450 °C. Selectivity trends performed under various CO_2:H_2 ratios (1:1, 1:4, 1:7) are shown in Figure 5-9. Under ratios 1:1 and 1:4, the selectivity to CO is dominant throughout the temperature range, similar to the behaviour of Ru NPs. However, under reducing conditions (1:7) and temperatures up to 300 °C, methane is the dominant product with selectivity up to 90%. This result owes to the presence of the semiconductor, Co_3O_4 providing an additional interaction between the Ru NPs and BZY and the additional promoting O species. The presence of Co_3O_4 provides active sites for CO_2 adsorption, granting Ru the affinity in directly dissociating H_2 into H [19,20,26], and spillover to reduce Ru [27]. Increasing the temperature above 300 °C results in the increase of CO selectivity in agreement with the thermodynamic analysis. Overall, the Co_3O_4 follows the redox mechanism of the reaction and follows an oxygen vacancy cycle exchange in line with the metal-support interaction mechanism [28]. Furthermore, the spontaneous migration of H^+ from BZY is suggested to aid in the reduction of the Co_3O_4 resulting in a vacant oxide which improves the oxygen cycling and operates like a high surface area support, where Ru NPs dispersed leads to a uniform distribution over BZY.

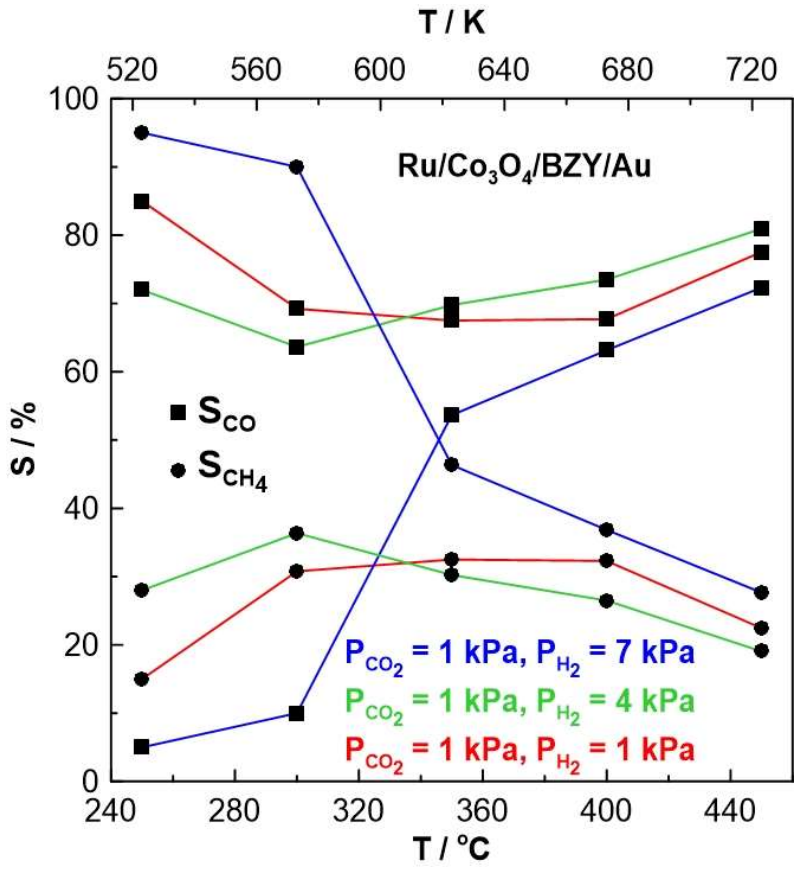

Figure 5-9. Catalytic performance of Ru/Co_3O_4 (2 wt.%) for CO_2:H_2 ratios of 1:1, 1:4, and 1:7. 2.6 mg of catalyst and 100 mL min^{-1}.

Evaluating the effect in terms of EPOC, above 350 °C Co_3O_4 serves as an electronic conductor [29], providing a migration pathway for the protons to travel from BZY toward the supported Ru NPs. Thus, having the dual function of operating like a mixed ionic-electronic conductor for the conduction of both protons and electrons. In low temperatures (below 350 °C), Co_3O_4 behaves like a semiconductor blocking the electron conduction and in turn, not able to close the electrical circuit. At higher temperatures the presence of Co_3O_4 results in a conductive film, similar to the EPOC studies with a conductive Ru film [22,30,31]. The higher selectivity of CH_4 (Figure 5-9) up to 350 °C in reducing conditions is due to the fact the Co_3O_4 is an oxygen capacitor and has the ability to spontaneously oxidize Ru NPs. The migration of oxygen species to metallic Ru results in higher CH_4 selectivity (as in the case of Ru/YSZ) due to the formation of RuO_2 [31]. Thus, up to 350 °C, oxygen migration is the dominant mechanism, while at temperatures above 350 °C the semiconductor turns into a conductive film for proton and electron conduction. With

the additional proton migration from BZY, increase in CO production and suppression of CH_4 formation occurs, due to the decrease of the work function of the Ru/Co_3O_4 (2 wt.%) composite catalyst.

Ru/Co_3O_4 (2 wt.%) was also evaluated under a range of applied potentials and reaction conditions, where only catalytic rate of CO was affected under oxidizing conditions (CO_2:H_2 = 3:1 and 4:1), demonstrating an electrophilic behaviour (Figure 5-10). The low-rate enhancement ratios could be explained by the fact that the catalyst is already in a promoted state. This is already known in the literature as 'wireless' EPOC effect or self-sustained electro-promotion (SSEP); where the catalyst operates as if it is induced under polarized conditions and further application of potential alters slightly the catalytic rate [3,32]. The permanent effect possibly originates from the high work function exhibited by the Co_3O_4 support enhancing the propensity of O spillover on the surface of the catalyst [33]. Another different feature is that the composite catalyst was electro-affected mainly under oxidizing conditions, instead of free-standing Ru NPs. Transient experiments were carried out at 400 and 425 °C (Figure 5-10) due to relatively low conductivity between the catalyst and BZY which arises from the presence of the Co_3O_4 semiconductor [29]. Another possible explanation why EPOC effect is not intense (*i.e.* ρ values close to unity) is that a part of the migrating protons partially reduces Co_3O_4 (as confirmed through TEM and XRD analysis) instead of stabilizing the effective double layer. Negative polarization results in the migration of H^+ onto Ru/Co_3O_4, while positive polarization results in the increase in the bond strength of H_2 from the gas mixture, thus both cases result in the reduction of CoO. This explains the negligible polarization effect on CH_4 formation, since the H species are used to reduce Co_3O_4 instead of hydrogenating CO_2 into CH_4. Which further confirms why operating in reducing conditions did not have an EPOC effect and hydrogen lean conditions was required to be promoted (Figure 5-10).

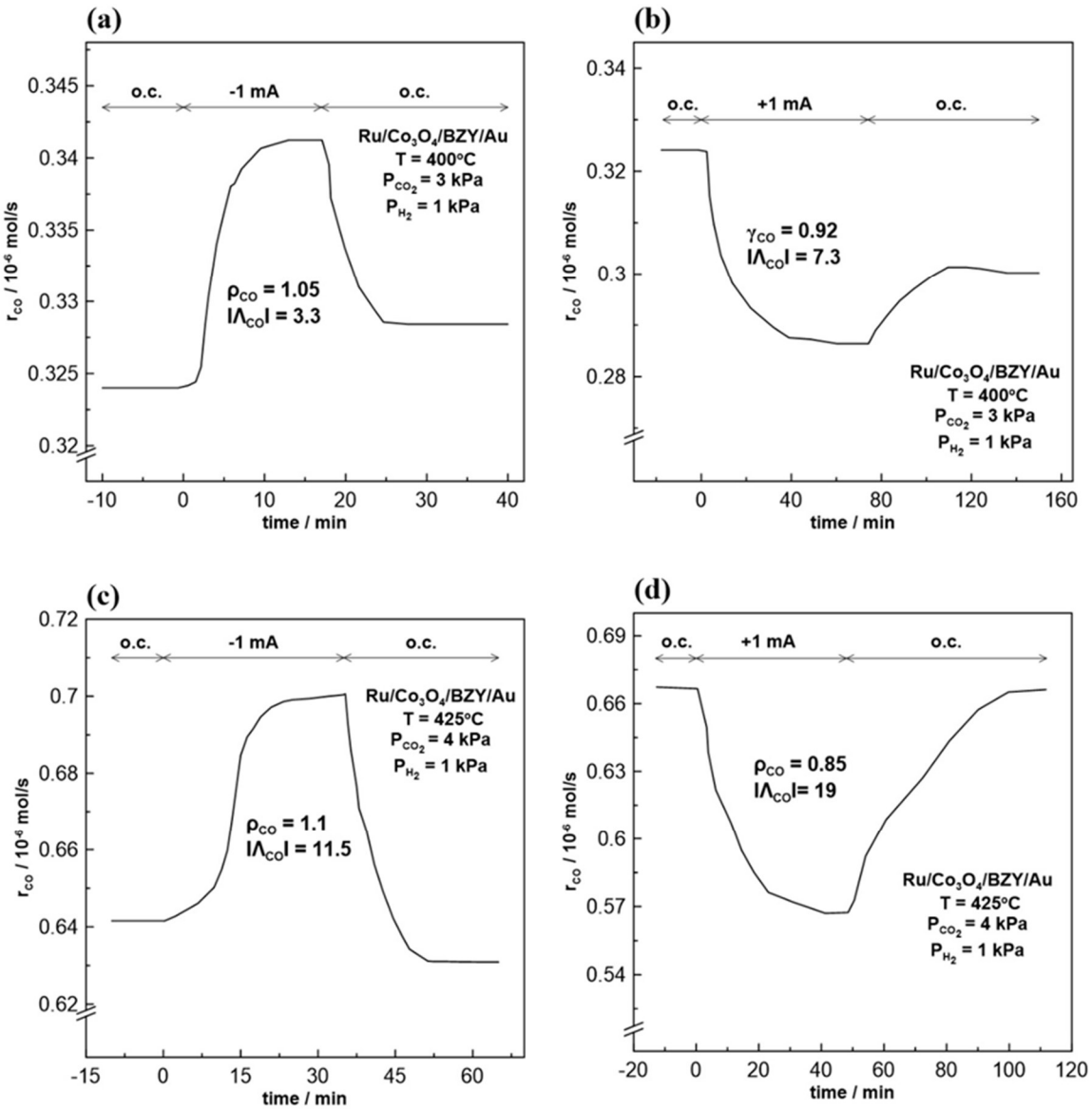

Figure 5-10. Transient response of Ru/Co_3O_4 (2 wt.%) under current application of –1 mA at (a) 400 °C and $3CO_2$:H_2 and (c) 425 °C and $4CO_2$:H_2, and +1 mA at (b) 400 °C and $3CO_2$:H_2, and (d) 425 °C and $4CO_2$:H_2. 2.6 mg of catalyst and 100 mL min^{-1}.

To elucidate the role of Co_3O_4, experiments were carried out using pure Co_3O_4 as working/catalyst electrode in the same operation conditions as the free-standing Ru NPs and Ru/Co_3O_4 (2 wt.%) catalysts. As shown in Figure 5-11, Co_3O_4 as a catalytic film displays selectivities to CH_4 up to 40% at low temperatures and reducing conditions, while CO is dominant at high temperatures and oxidizing conditions (with selectivities up to 95%). It should be noted that in the whole temperature range (250-450 °C) no electrochemical promotion was observed.

This result confirms that the electrochemical promotion in the case of composite Ru/Co_3O_4 (2 wt.%) catalyst is due to the modification of the Ru work function, causing the change of the reactant bond strength.

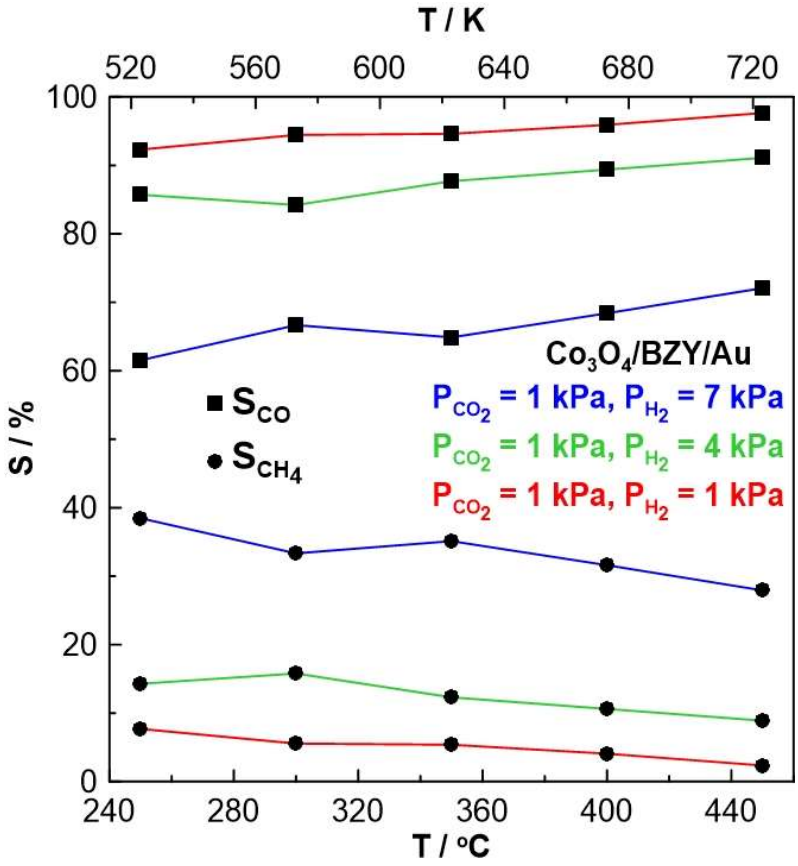

Figure 5-11. Catalytic performance Co_3O_4 for CO_2:H_2 ratios of 1:1, 1:4, and 1:7. 2.6 mg of catalyst and 100 mL min^{-1}.

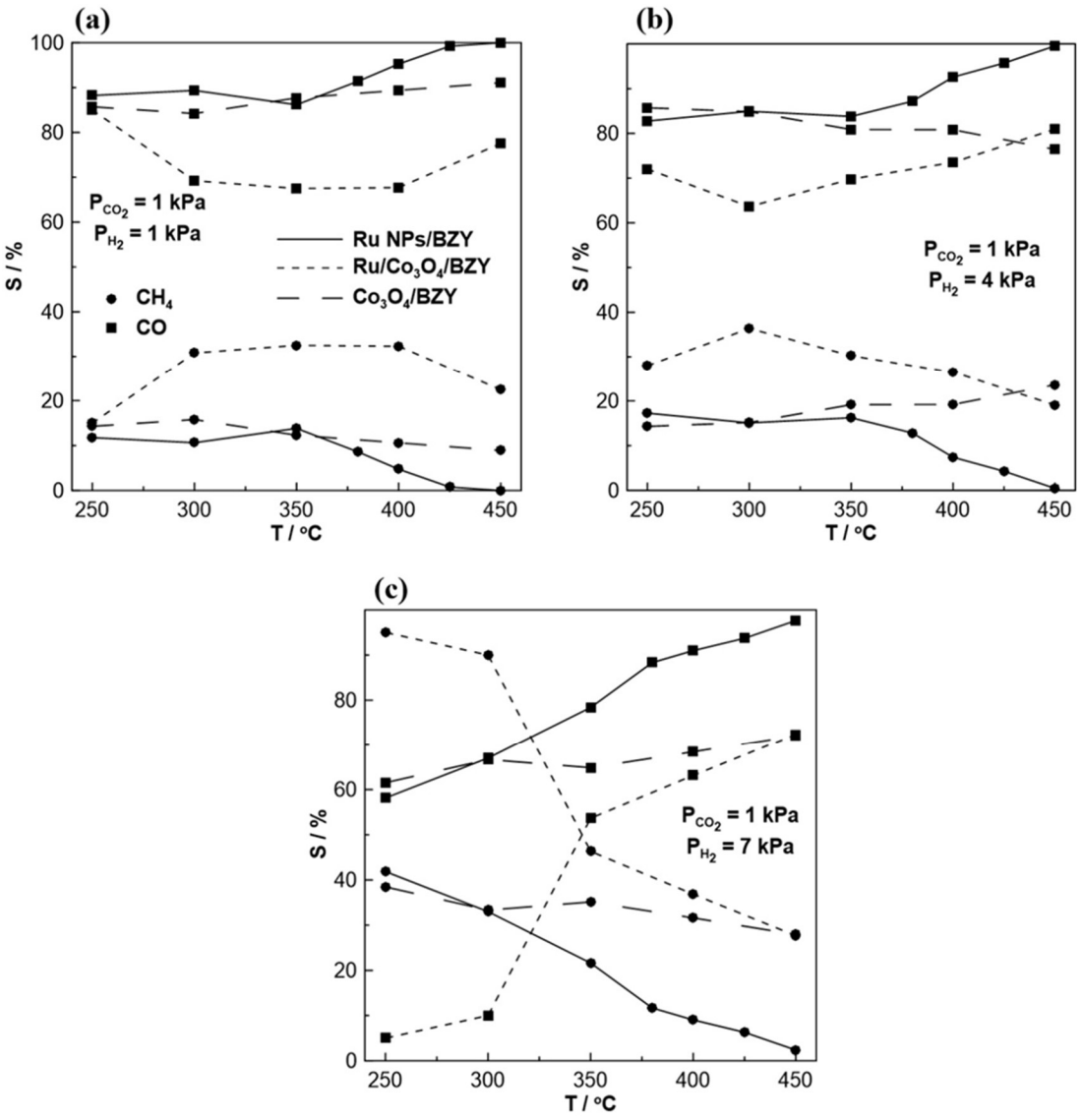

Figure 5-12. Comparison plot of product selectivity for free-standing Ru nanoparticles, Ru/Co_3O_4 (2 wt.%) and Co_3O_4 for CO_2:H_2 ratios (a) 1:1, (b) 1:4 and (c) 1:7.

Figure 5-12 presents the product selectivity for both free-standing Ru NPs, Ru/Co_3O_4 (2 wt.%) and Co_3O_4 catalysts in all experimental conditions, where the CO and CH_4 rates were normalized to the amount of Ru. In all P_{CO2}:P_{H2} cases, the selectivity of Ru/Co_3O_4 (2 wt.%) to CH_4 is higher than the corresponding selectivity of free-standing Ru NPs. This behaviour is more pronounced under reducing conditions (Figure 5-12 (c)). According to this result, a synergetic effect arises when Ru is combined with an oxide semiconductor, resulting in greater selectivities to CH_4, which could not be achieved with individual materials.

The enhanced performance of the supported catalyst in relation to the free-standing Ru NPs can also be explained by comparing the active surface areas of these two samples established by equation 5-1 using the transient experiments described in Figure 5-7 and Figure 5-10.

$$N_g = \frac{\tau I}{F} \qquad 5\text{-}1$$

where τ is the relaxation time constant upon current imposition (defined as the time required for the catalytic rate increase to reach 63% of its final steady-state value upon current application), I is the applied current, F is the Faraday constant and N_g is the catalyst-electrode surface area [2]. The active surface area for the supported catalyst is one order of magnitude ($N_g \sim 10^{-6}$ mol) higher that the unsupported one ($N_g \sim 10^{-7}$ mol). Thus, the active surface area of the supported Ru is 10 times greater than its unsupported counterpart, thus resulting in a superior catalytic activity.

The highest CO_2 conversion of this study was 25% for the free-standing nanoparticles and 22% for Ru/Co_3O_4 (2 wt.%) at 425°C. Even through, the conversion is lower for Ru/Co_3O_4, the CO_2:H_2 ratio of 4:1 utilizes a lot less H_2 when compared to free-standing Ru nanoparticles (CO_2:H_2 = 1:7).

Table **1-1** from Chapter 1.5.4.1 summarizes the best performing catalysts from previous CO_2 hydrogenation reaction studies under the EPOC phenomenon. Compared with the present study, the activity for Ru/BZY and Ru/Co_3O_4 (2 wt.%) is superior to the previous studies signifying advantages in using nanoparticles, semi-conducting supports and proton-conducting solid electrolytes.

5.4 Conclusion

The catalytic activity of Ru nanoparticles as free-standing and supported on Co_3O_4 deposited on BZY has been promoted through the combination of EPOC and MSI effect. CO production dominated in most cases associated to the nanostructured Ru and was manipulated through EPOC to display a permanent effect. The combined synergetic effect of proton and electron conductivity related to BZY and Co_3O_4 gives rise to a superior electronic catalytic activity resulting in a "wireless" EPOC effect. This effect is crucial since it brings the fundamentals of EPOC closer to industrial application without complex environmental setups, allowing for an efficient approach in utilizing CO_2.

References

[1] C.G. Vayenas, S. Brosda, C. Pliangos, The double-layer approach to promotion, electrocatalysis, electrochemical promotion, and metal-support interactions, J. Catal. 216 (2003) 487–504. doi:10.1016/S0021-9517(02)00127-6.

[2] C.G. Vayenas, S. Bebelis, C. Pliangos, S. Brosda, D. Tsiplakides, Electrochemical Activation of Catalysis: Promotion, Electrochemical Promotion, and Metal-Support Interactions, Springer, New York, 2001. doi:10.1007/b115566.

[3] J. Nicole, C. Comninellis, D. Tsiplakides, C. Pliangos, X.E. Verykios, C.G. Vayenas, Electrochemical promotion and metal-support interactions, J. Catal. 204 (2001) 23–34. doi:10.1006/jcat.2001.3360.

[4] C.G. Vayenas, C.G. Koutsodontis, Non-Faradaic electrochemical activation of catalysis, J. Chem. Phys. 128 (2008) 182506. doi:10.1063/1.2824944.

[5] H.A.E. Dole, L.F. Safady, S. Ntais, M. Couillard, E.A. Baranova, Electrochemically enhanced metal-support interaction of highly dispersed Ru nanoparticles with a CeO2 support, J. Catal. 318 (2014) 85–94. doi:10.1016/j.jcat.2014.07.003.

[6] E.A. Monyoncho, S. Ntais, F. Soares, T.K. Woo, E.A. Baranova, Synergetic effect of palladium-ruthenium nanostructures for ethanol electrooxidation in alkaline media, J. Power Sources. 287 (2015) 139–149. doi:10.1016/j.jpowsour.2015.03.186.

[7] R.G. Larson, In Retrospect: Twenty years of drying droplets, Nature. 550 (2017) 466–467. doi:10.1038/550466a.

[8] H. Liang, J.M. Raitano, L. Zhang, S.W. Chan, Controlled synthesis of Co3O4 nanopolyhedrons and nanosheets at low temperature, Chem. Commun. (2009) 7569–7571. doi:10.1039/b914447a.

[9] G. Huang, S. Xu, Y. Yang, Y. Chen, Z. Li, Rapid-rate capability of micro-/nano-structured CoO anodes with different morphologies for lithium-ion batteries, Int. J. Electrochem. Sci. 10 (2015) 10587–10596.

[10] C. Hernández Mejía, T.W. van Deelen, K.P. de Jong, Activity enhancement of cobalt catalysts by tuning metal-support interactions, Nat. Commun. 9 (2018) 1–8. doi:10.1038/s41467-018-06903-w.

[11] S. Sadasivan, R.M. Bellabarba, R.P. Tooze, Size dependent reduction-oxidation-reduction behaviour of cobalt oxide nanocrystals, Nanoscale. 5 (2013) 11139–11146. doi:10.1039/c3nr02877a.

[12] D. Zhang, J. Zhu, N. Zhang, T. Liu, L. Chen, X. Liu, R. Ma, H. Zhang, G. Qiu, Controllable fabrication and magnetic properties of double-shell cobalt oxides hollow particles, Sci. Rep. 5 (2015) 1–6. doi:10.1038/srep08737.

[13] X. Chen, L. Gu, D. Xiao, G. Cui, L. Chen, L. Zhang, C. Shang, P. Hu, S. Dong, J. Guan, Compatible interface design of CoO-based Li-O2 battery cathodes with long-cycling stability, Sci. Rep. 5 (2015) 1–7. doi:10.1038/srep08335.

[14] H. Yang, X. Chen, G. Hu, W.T. Chen, S.J. Bradley, W. Zhang, G. Verma, T. Nann, D.E. Jiang, P.E. Kruger, X. Wang, H. Tian, G.I.N. Waterhouse, S.G. Telfer, S. Ma, Highly efficient electrocatalytic hydrogen evolution promoted by O-Mo-C interfaces of ultrafine β-Mo2C nanostructures, Chem. Sci. 11 (2020) 3523–3530. doi:10.1039/d0sc00427h.

[15] L. Zhu, Z. Yang, J. Zheng, W. Hu, N. Zhang, Y. Li, C.J. Zhong, H. Ye, B.H. Chen, Decoration of Co/Co3O4 nanoparticles with Ru nanoclusters: A new strategy for design of highly active hydrogenation, J. Mater. Chem. A. 3 (2015) 11716–11719. doi:10.1039/c5ta02452h.

[16] F.-L. Du, Y.-M. Li, P.-D. Tang, J.-S. Qiu, S.-Y. Long, R.-B. Huang, K. Huang, Q.-S. Du, N.-Z. Xie, H.-L. Huang, A new type of two-dimensional carbon crystal prepared from 1,3,5-trihydroxybenzene, Sci. Rep. 7 (2017) 1–11. doi:10.1038/srep40796.

[17] S. Petrovska, Y. Zaulychnyy, T. Nakamura, E. Shibata, O. Foya, O. Ilkiv, R. Sergiienko, B. Ilkiv, Electronic Structure of Hollow Graphitic Carbon Nanoparticles Fabricated from Acetylene Carbon Black, Fullerenes, Nanotub. Carbon Nanostructures. 23 (2014) 449–454. doi:10.1080/1536383x.2014.885957.

[18] D.P. Dutta, G. Sharma, P.K. Manna, A.K. Tyagi, S.M. Yusuf, Room temperature ferromagnetism in CoO nanoparticles obtained from sonochemically synthesized precursors, Nanotechnology. 19 (2008) 245069–245075. doi:10.1088/0957-4484/19/24/245609.

[19] J.H. Kwak, L. Kovarik, J. Szanyi, Heterogeneous catalysis on atomically dispersed supported metals: CO2 reduction on multifunctional Pd catalysts, ACS Catal. 3 (2013) 2094–2100. doi:10.1021/cs4001392.

[20] J.H. Kwak, L. Kovarik, J. Szanyi, CO2 Reduction on Supported Ru/Al2O3 Catalysts: Cluster Size Dependence of Product Selectivity, ACS Catal. 3 (2013) 2449–2455. doi:10.1021/cs400381f.

[21] A. Kotsiras, I. Kalaitzidou, D. Grigoriou, A. Symillidis, M. Makri, A. Katsaounis, C.G. Vayenas, Electrochemical promotion of nanodispersed Ru-Co catalysts for the hydrogenation of CO 2, Appl. Catal. B Environ. 232 (2018) 60–68. doi:10.1016/j.apcatb.2018.03.031.

[22] I. Kalaitzidou, A. Katsaounis, T. Norby, C.G. Vayenas, Electrochemical promotion of the hydrogenation of CO2 on Ru deposited on a BZY proton conductor, J. Catal. 331 (2015) 98–109. doi:10.1016/j.jcat.2015.08.023.

[23] I. Kalaitzidou, M. Makri, D. Theleritis, A. Katsaounis, C.G. Vayenas, Comparative study of the electrochemical promotion of CO2 hydrogenation on Ru using Na+, K+, H+ and O2- conducting solid electrolytes, Surf. Sci. 646 (2016) 194–203. doi:10.1016/j.susc.2015.09.011.

[24] D. Grigoriou, D. Zagoraios, A. Katsaounis, C.G. Vayenas, The role of the promoting ionic species in electrochemical promotion and in metal-support interactions, Catal. Today. (2019) . doi:10.1016/j.cattod.2019.08.024.

[25] S. Souentie, C. Xia, C. Falgairette, Y.D. Li, C. Comninellis, Investigation of the

"permanent" electrochemical promotion of catalysis (P-EPOC) by electrochemical mass spectrometry (EMS) measurements, Electrochem. Commun. 12 (2010) 323–326. doi:10.1016/j.elecom.2009.12.031.

[26] S. Kattel, P. Liu, J.G. Chen, Tuning Selectivity of CO2 Hydrogenation Reactions at the Metal/Oxide Interface, J. Am. Chem. Soc. 139 (2017) 9739–9754. doi:10.1021/jacs.7b05362.

[27] D. Zhang, J. Luo, J. Wang, X. Xiao, Y. Liu, W. Qi, D.S. Su, W. Chu, Ru/FeOx catalyst performance design: Highly dispersed Ru species for selective carbon dioxide hydrogenation, Chinese J. Catal. 39 (2018) 157–166. doi:10.1016/S1872-2067(17)62967-X.

[28] J. Liu, V. Fung, Y. Wang, K. Du, S. Zhang, L. Nguyen, Y. Tang, J. Fan, D. en Jiang, F.F. Tao, Promotion of catalytic selectivity on transition metal oxide through restructuring surface lattice, Appl. Catal. B Environ. 237 (2018) 957–969. doi:10.1016/j.apcatb.2018.05.013.

[29] D. Zagoraios, A. Athanasiadi, I. Kalaitzidou, S. Ntais, A. Katsaounis, A. Caravaca, P. Vernoux, C.G. Vayenas, Electrochemical promotion of methane oxidation over nanodispersed Pd/Co 3 O 4 catalysts, Catal. Today. 355 (2020) 910–920. doi:10.1016/j.cattod.2019.02.030.

[30] M. Makri, A. Katsaounis, C.G. Vayenas, Electrochemical promotion of CO2 hydrogenation on Ru catalyst-electrodes supported on a K-β″-Al2O3 solid electrolyte, Electrochim. Acta. 179 (2015) 556–564. doi:10.1016/j.electacta.2015.03.144.

[31] D. Theleritis, S. Souentie, A. Siokou, A. Katsaounis, C.G. Vayenas, Hydrogenation of CO2 over Ru/YSZ electropromoted catalysts, ACS Catal. 2 (2012) 770–780. doi:10.1021/cs300072a.

[32] P. Vernoux, Recent advances in electrochemical promotion of catalysis, Catalysis. 29 (2017) 29–59. doi:10.1039/9781788010634-00029.

[33] P. Vernoux, L. Lizarraga, M.N. Tsampas, F.M. Sapountzi, A. De Lucas-Consuegra, J.L. Valverde, S. Souentie, C.G. Vayenas, D. Tsiplakides, S. Balomenou, E.A. Baranova, Ionically conducting ceramics as active catalyst supports, Chem. Rev. 113 (2013) 8192–8260. doi:10.1021/cr4000336.

Appendix C - Supplementary Information for Chapter 5

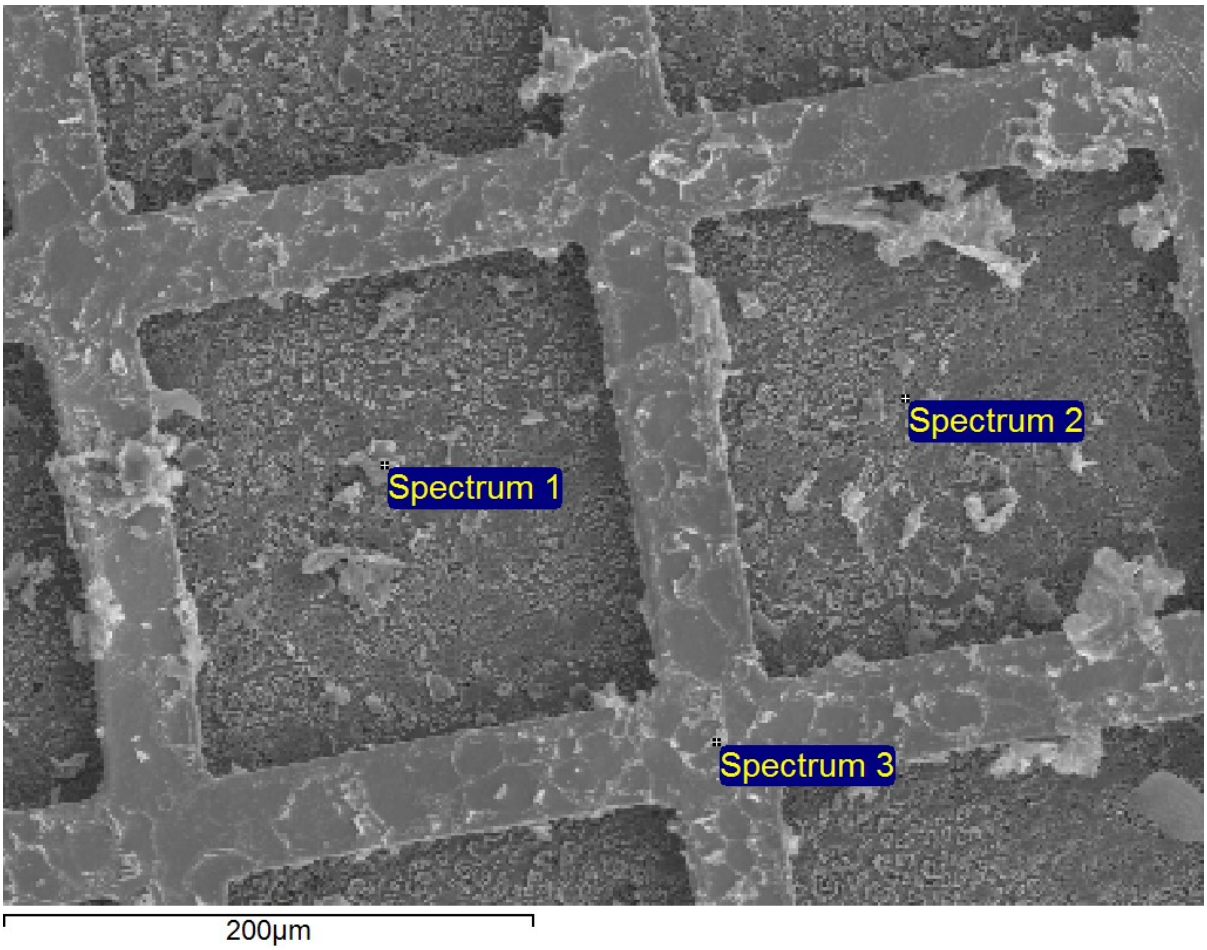

Figure C-1. EDS mapping of BZY for Figure 5-2 (b).

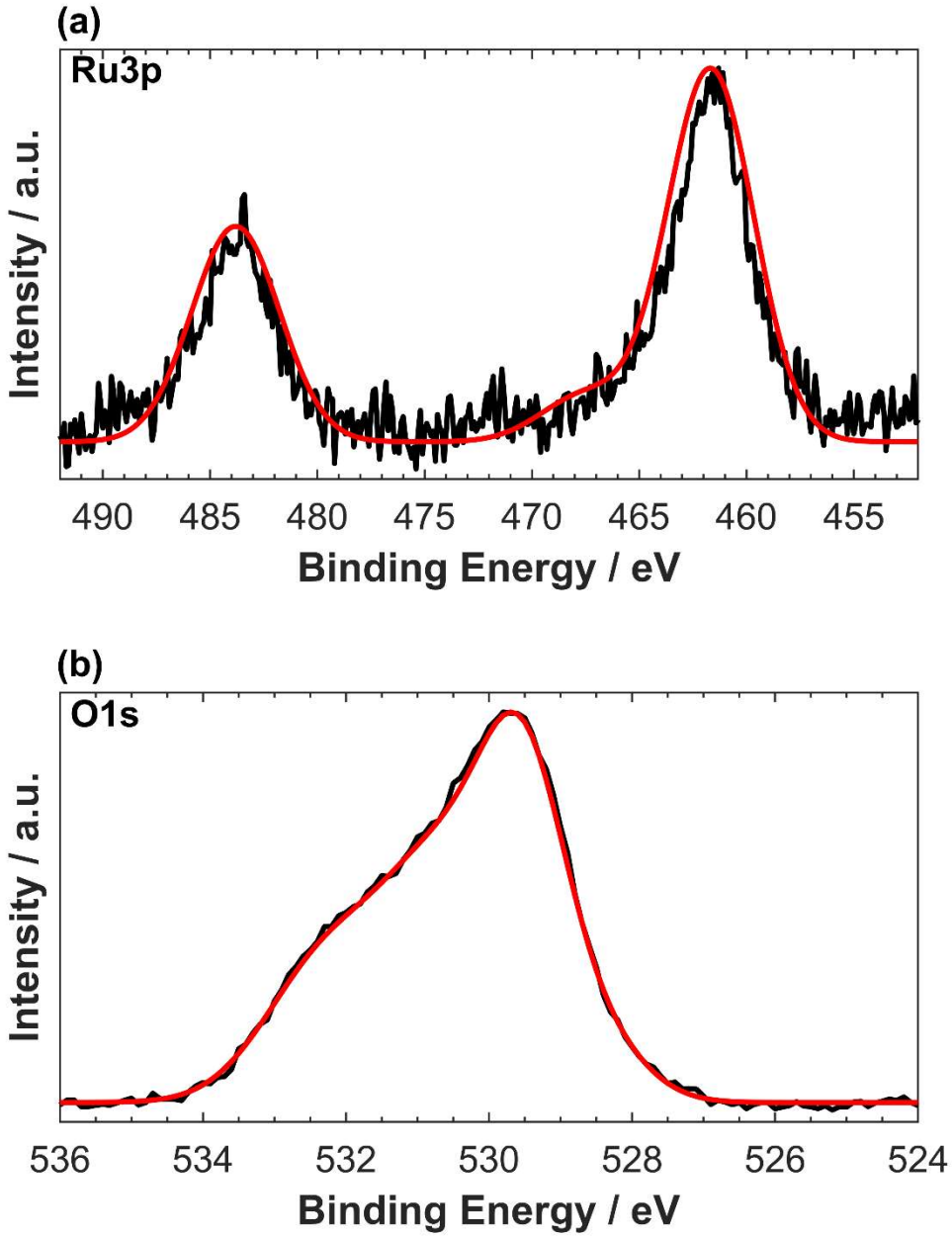

Figure C-2. High resolution XPS spectra of as-prepared Ru nanoparticles. (a) Ru3p and (b) O1s. Black lines represent the acquired XPS spectra and red lines represent the best fit.

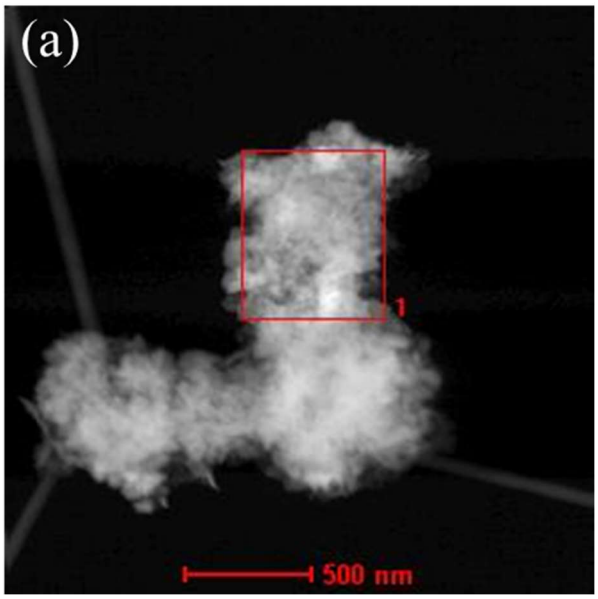

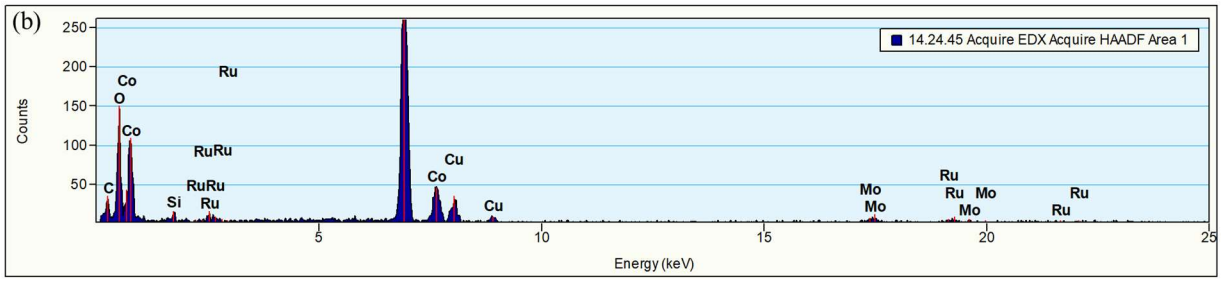

Figure C-3. (a) STEM image and (b) EDX mapping of used Ru/Co_3O_4 (2 wt.%). EDX mapping was taken with EDAX Analyzer, DPP-II.

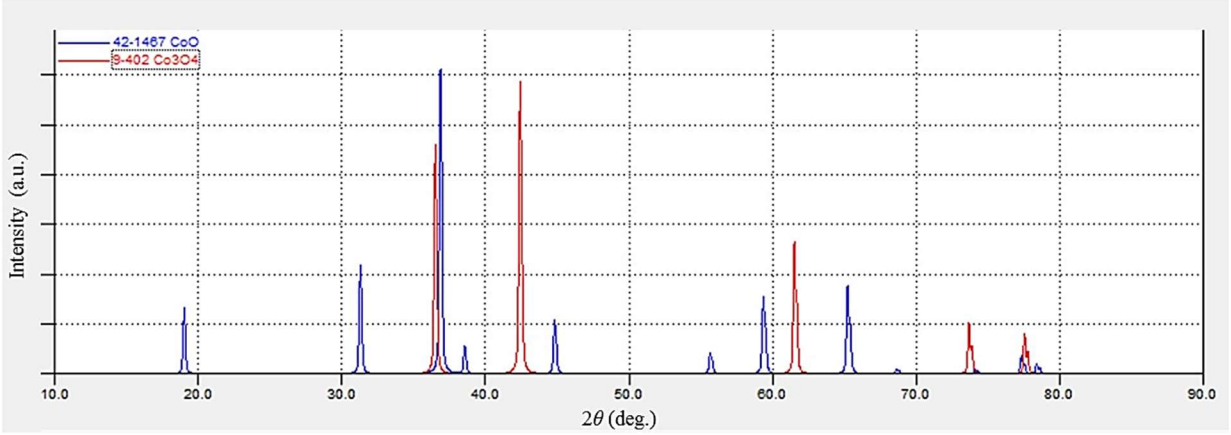

Figure C-4. Standard XRD of Co_3O_4 and CoO phase, generated through the Crystallographica Search-Match software.

Chapter 6 : Electrochemical In-situ Activation of Fe-Oxide Nanowires for the Reverse Water Gas Shift Reaction

Adapted from: ***C. Panaritis****, J. Zgheib, S. A. H. Ebrahim, M. Couillard, E. A. Baranova, Journal of Applied Catalysis B: Environmental, 269 (2020) 118826.*

Abstract

The catalytic activity of FeO_x nanowires (Ø = 5-6 nm) deposited on yttria-stabilized zirconia (YSZ) solid-electrolyte was enhanced through the application of external current or potential for the reverse water gas shift (RWGS) reaction. As shown by XPS, the as-prepared FeO_x nanowires consist of the mixture of oxides: Fe_2O_3, Fe_3O_4 and some FeO. The nanowires showed 99% selectivity to CO under both open-circuit and electrochemical polarization. We found that the oxidation state of iron depended on the reaction temperature and was in-situ controlled and modified upon anodic and cathodic polarization. Anodic polarization at 335 and 400 ºC led to a 200% increase in the reaction rate due to the electrooxidation of inactive Fe_xC and supply of oxygen ions from YSZ to FeO_x resulting in the formation of an active oxide. Cathodic polarization resulted in up to a 4-fold rate increase due to catalyst reduction increasing the coverage of CO_2 on the surface.

6.1 Introduction

The use of Fe for the EPOC effect has only been studied for the CO_2 hydrogenation reaction using large Fe particles on a TiO_2 film which was deposited on yttria-stabilized zirconia (YSZ) by Ruiz *et al.* [1]. Results have shown to abide to the rules of electrochemical promotion, however the influence of the TiO_2 film remains to be further evaluated under the electro-oxidation conditions induced by the use of YSZ and they do not focus on the RWGS reaction. The lack of Fe use in EPOC studies allows for new applications of Earth abundant metals.

In this chapter, we report in-situ modification of the catalytic activity of FeO_x nanowires deposited on oxygen conducting YSZ solid-electrolyte for the RWGS reaction in the temperature range of 300 and 400 ºC. First, physicochemical properties of FeO_x nanowires before and after the reaction are presented followed by open-circuit catalytic tests and finally induced under

polarization. The role of polarization is investigated using the cyclic voltammetry, chronoamperometry and chronopotentiometry under a CO_2:H_2 ratio of 1:1 reaction mixture. Additionally, in-situ activation of inactive Fe-carbide is achieved through an electro-oxidation process.

6.2 Experimental

6.2.1 *Synthesis of nanostructured FeO_x*

The FeO_x nanowires were synthesized according to the polyol synthesis method [2]. Fe nanowires were synthesized by mixing iron precursor (iron (III) nitrate ($Fe(NO_3)_3$)) with ethylene glycol (Fischer Scientific certified grade) and tetramethylammonium hydroxide (TMAOH). Ethylene glycol acts as reaction medium and reducing agent, and TMAOH is used to increase the pH of the solution – serving as a mean to control the size of the produced nanowires. After weighing the desired mass of the iron precursor, a solution containing 0.12 M TMAOH solution was added, 1 ml at a time, measuring the pH after each addition. Once the pH of the solution reached 12, ethylene glycol was added until the desired volume was reached. The mixture, which had a turbid yellow colour, was stirred at room temperature for 30 min and then heated from room temperature until it reached 160 ºC, and ceased heating to be cooled and stored at room temperature, until further use. The colour of the solution became rusty brown and pH dropped from ~12 to ~9.

6.2.2 *Physicochemical Characterization*

Scanning Transmission Electron Microscopy (STEM) was performed on the fresh Fe colloidal solution to determine its size and morphology. STEM images were taken on a FEI Titan 80-300 TEM operated at 300 keV. The sample preparation and analysis was done through the same procedure described in Chapter 3.2.3. Scanning electron microscope (SEM) images of the Fe nanofilm deposited on YSZ were taken using Phenom SEM (NanoScience Instruments, USA). The X-Ray Photoelectron Spectroscopy (XPS) spectra for Fe 2p and O 1s of the fresh sample were taken using the Kratos AXIS Nova spectrometer equipped with an AI X-ray source. Sample was deposited on a silicon wafer, where it was dried at 130 ºC – following the same conditions when deposited on YSZ. Analysis took part in an ultrahigh vacuum (10^{-10} Torr) chamber and was performed using AlK_a radiation at 1486.69 eV (150 W, 15 kV), a charge neutralizer and a three multi-channel plate delay-line detector (DLD). Survey spectra was done from -5 to 1200 eV, where

the C1s peak of 285 eV was taken as the reference and the incident angle was 54.74º. Due to the amorphous structure and oxidized phase of the Fe nano-structured catalyst, X-Ray Diffraction (XRD) patterns did not provide insight in its crystallinity.

6.2.3 *Reaction Experiment*

The EPOC effect was evaluated through the enhancement ratio (ρ) (eq. 1-10), apparent Faradaic efficiency (Λ) (eq. 1-11) and permanent or persistent EPOC (γ) (eq. 1-12). The effect is known to follow non-Faradaic behaviour when $|\Lambda| > 1$, or in the case of hydrogenation reactions when $\rho \neq 1$ since $O^{\delta-}$ is not directly consumed in the reaction. Furthermore, the best potential or current response was plotted alongside the CO rate in the results.

Cyclic voltammetry (CV) characterization was performed in a potential window of -1.6V to 1.6V with a scan rate of 20 mV s^{-1} using the potentiostat-galvanostat (Arbin Instruments, MSTAT) at 350 °C under reaction conditions of 1:1 (CO_2:H_2). To evaluate the effect of holding potential time, the potential was held at 1.6V for 5, 30 and 45 minutes, beginning from 1.6V to -1.6V and cycled back to 1.6V for 10 cycles. The charge (Q), for each cathodic peak was obtained by numerically integrating the area under the second and third cathodic peaks in a potential window of 300 mV, following the same procedure described in Ref. [3].

6.3 Results and Discussion

6.3.1 *Physiochemical Characterization*

Figure 6-1 (a) and (b) show the STEM images of the as-prepared FeO_x nanostructured catalyst. The polyol synthesis resulted in the formation of nanowires of 5 nm in diameter and various length in the range of 5 to 50 nm. Since STEM transmission is not possible for Fe/YSZ, SEM images were taken instead of the as-prepared FeO_x nanowires deposited onto the YSZ solid-electrolyte disk (Figure D-1 (a) and (b) from Appendix D). In the fresh sample, upon deposition of the colloidal solution containing FeO_x nanowires, the catalyst is shown to form a porous layer indicating a high active surface area. The porosity of the structure is important for the electrochemical promotion effect since it ensures a large three-phase boundary, allowing promoting ions to migrate effectively to the active area of the catalyst. The used sample (Figure D-1 (c) and (d)) taken after several weeks of the reaction between 300 and 400 ºC, displays a thinner porous structure, mainly caused by reduction under hydrogen and sintering at elevated temperatures. The EDX spectrum in Figure D-2, taken after the reaction confirms the presence of

Fe, Y and Zr – the Cu represent the Cu grid for the analysis with no other impurities. Figure 6-1 (c) and (d), displays the STEM image of the agglomerated used FeO_x particle and its corresponding composition EELS breakdown, respectively. The composition of the red square in Figure 6-1 (d), is displayed in Figure D-3 as EELS mapping. The colours in Figure 6-1 (d) of blue, green and red represent Fe, O and C, respectively. Thus, FeO_x takes the form of a core-shell, with Fe at the core, O intermediate layer and an outer layer of C.

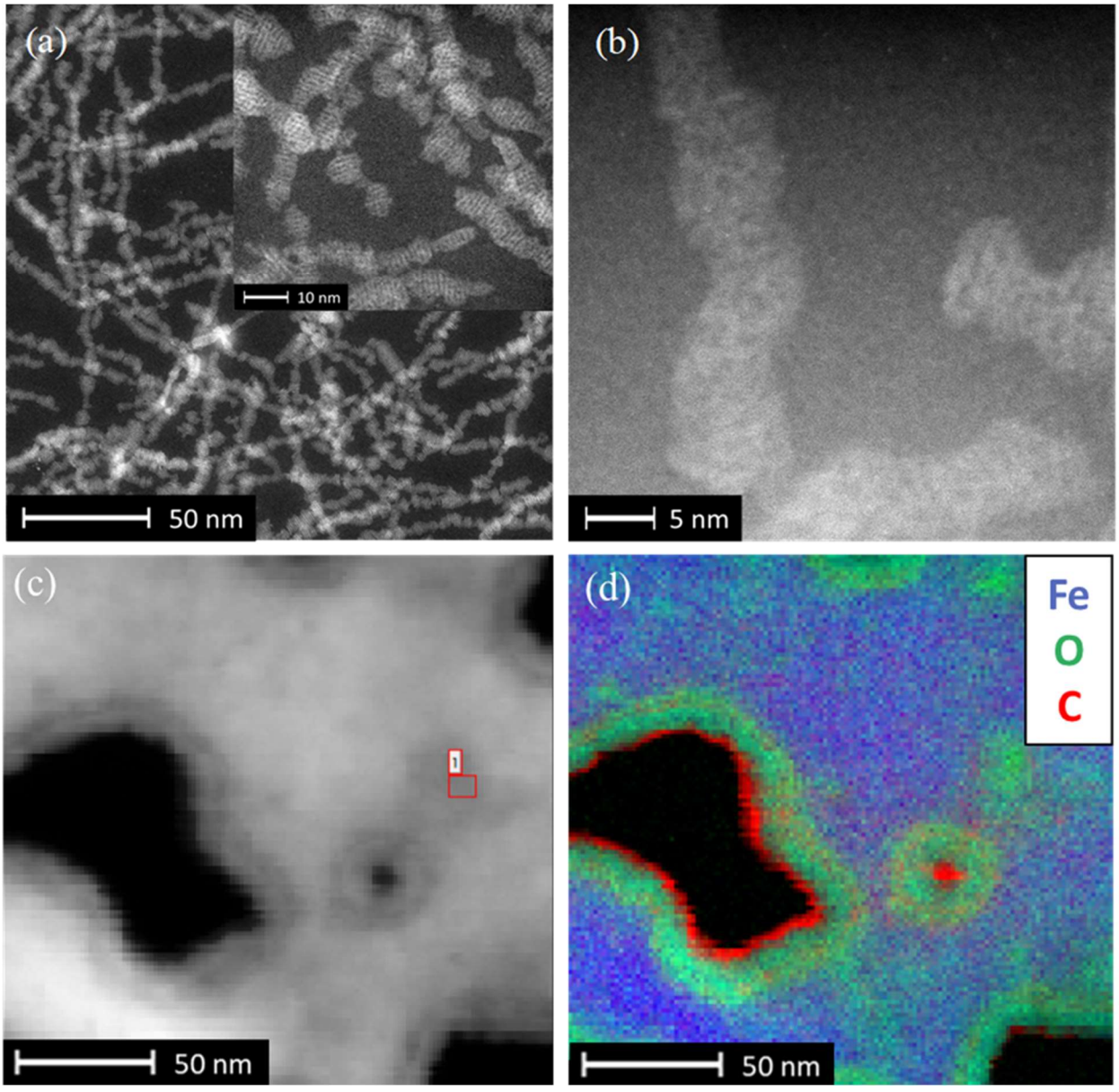

Figure 6-1. STEM images of as-prepared FeO_x nanowires displaying (a) uniform distribution and (b) localization of the FeO_x nanowires, (c) used FeO_x and (d) EELS mapping, where blue represents Fe, green is oxygen and red is carbon.

The high resolution XPS spectra for Fe2p, C1s, and O1s of the nanofilm are displayed in Figure 6-2 (a), (b) and (c), respectively. The XPS data shows that the as-prepared FeO_x nanowires are only present in an oxidized state and no presence of metallic Fe was found. The ratio of Fe_2O_3 states to Fe_3O_4 states is about 5:1 for the fresh sample.

Table 6-1 summarizes the XPS species associated with the Fe2p, C1s and O1s and their deconvolution. The FeO_x state consist of a mix of Fe_2O_3 and Fe_3O_4 at 710.25 eV, which is in agreement with previous studies [4,5]. The Fe-carbide present for the fresh sample at 709.1 eV and 283.7 eV for the Fe2p and C1s spectrum is related to the carbide from the ethylene glycol in the colloid solution. The O1s peaks at a maximum at 530.9 eV in Figure 6-2 (b), which is again in agreement with previous studies [4,5]. For the purpose of this study, the initial state of the catalyst was crucial to ensure it was an oxide that will aid in the analysis of the EPOC effect using the oxygen-conductive solid electrolyte YSZ. Analysis of the used sample, the red line in Figure 6-2 (a) and (b) represents Fe-carbide, while the red line in the O1s spectrum (Figure 6-2 (c)) corresponds to the oxidation state of FeO_x. A significant increase in Fe-carbide formation is evident with a binding energy of 710.8 eV and 284.4 eV for Fe2p and C1s [4]. For the O1s spectrum in Figure 6-2 (c), there is an increase in the metallic state of FeO_x with a binding energy of 530.1 eV. Thus, analysis of FeO_x after reaction conditions confirms a reduced oxidation state and the formation of Fe-carbide.

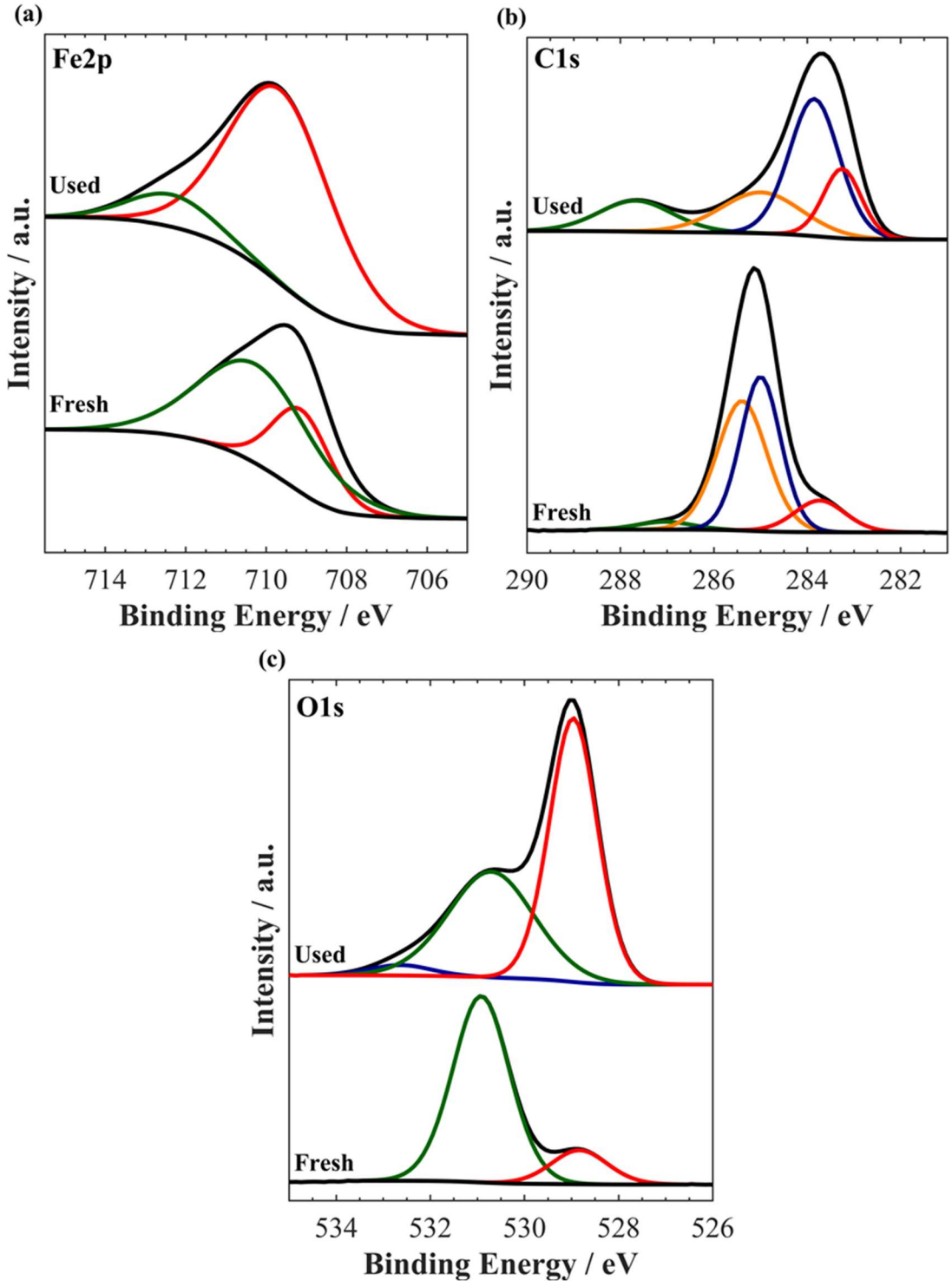

Figure 6-2. High resolution XPS spectra of (a) Fe2p, (b) C1s and (c) O1s for fresh and used FeO_x.

Table 6-1. XPS data corresponding to Figure 6-2.

		Binding Energy (eV)	
		Fresh	Used
(a) Fe2p	Fe_2O_3	710.3	713.5
	Fe-carbide	709.1	710.8
(b) C1s	C=O	287.1	288.8
	C-O	285.4	286.1
	C(sp3)	285	285
	Fe-carbide	283.7	284.4
(c) O1s	FeO_x	528.8	530.1
	C-O, C=O	530.9	531.9
	O^{2-}	NA	533.8

6.3.2 *Open-circuit RWGS activity*

The summary of the open-circuit catalytic tests carried out on FeO_x nanowires at a 1:1 CO_2:H_2 reaction mixture is displayed in Figure 6-3. To ensure the catalyst stability, it was left to stabilize under reaction conditions for 12 h at 300 ºC prior to the catalytic experiments. Each point in Figure 6-3 is obtained under isothermal conditions after the catalyst reached a steady-state behaviour (30 - 60 min). As can be seen, the reaction rate of RWGS shows a maximum CO rate at 300 ºC, followed by a drastic decrease at 335 ºC and a slow increase up to 400 ºC. Once H_2 is introduced in the catalytic system at 250 ºC, Fe_2O_3 is reduced to Fe_3O_4 (eq. 6-1) and cannot be reverted unless oxygen is directly supplied to the system [6–8]:

$$3Fe_2O_3 + H_2 \leftrightarrow 2Fe_3O_4 + H_2O \quad \text{6-1}$$

The decrease in rate at 335 ºC is attributed to further reduction of the higher oxidation state iron-oxides (Fe_2O_3 and Fe_3O_4) to FeO (eq. 6-2) according to:

$$Fe_3O_4 + H_2 \leftrightarrow 3FeO + H_2O \quad \text{6-2}$$

Therefore, the catalyst becomes more reduced and less active as the temperature increases as was confirmed earlier, using temperature programmed reduction (TPR) studies. TPR showed the reduction of iron-oxides to FeO between 320-340 ºC due the increase in H_2 dissociation that is able to spillover and reduce the catalyst surface and bulk [8–11]. Furthermore, the transition to a reduced oxidation state of iron is present in the O1s spectrum in Figure 6-2 (c). The further rate increase at 400 ºC is due to an endothermic nature of the reaction.

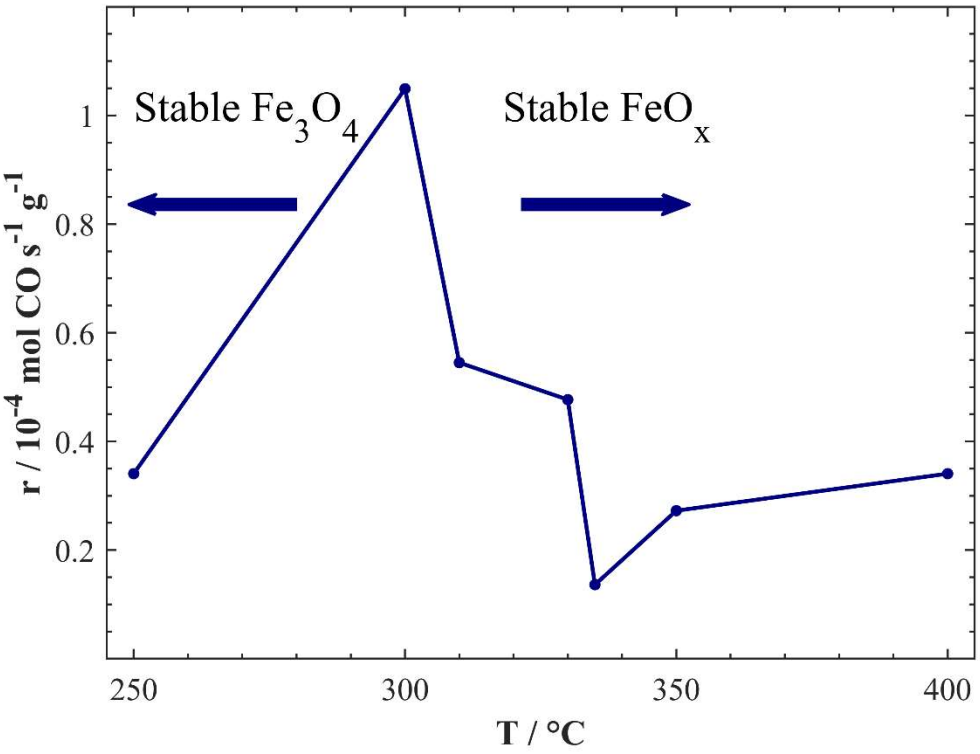

Figure 6-3. Open-circuit RWGS activity of FeO_x/YSZ catalyst. CO_2:H_2 = 1:1, and 100 mL min^{-1}.

The observed change in catalytic activity is affiliated to the alteration in the oxidation state of the FeO_x nanowires transitioning from a highly oxidized state to a more reduced one. Furthermore, metallic iron and Fe-carbides (Fe_xC) could also form under certain reaction conditions as depicted in the following mechanism (eq. 6-3) [4,6]:

$$Fe_2O_3 \rightarrow Fe_3O_4 \rightarrow FeO \rightarrow Fe \rightarrow Fe_xC \qquad 6\text{-}3$$

Overall consisting of a mix of Fe_3O_4, FeO, Fe and Fe_xC, the iron catalyst becomes more reduced as the temperature increases. This reduction characteristic is directly in-line with the current results where starting from 335 °C, the RWGS catalytic activity decreases, signifying a new reduced state that gradually increases to 400°C due the endothermicity of the RWGS reaction, as confirmed from STEM and XPS analysis. The CO_2 conversion and carbon balance, corresponding to the data from Figure 6-3, is summarized in Table D-2. The CO_2 conversion was kept under 1% to ensure electrochemical enhancement activity and due to the small catalytic area of 1 cm^2. The carbon balance decreased as the temperature increased, signifying carbon deposition on FeO_x, specifically on the outer shell (Figure 6-1 (d)).

Iron-oxide nanowires displayed almost 100 % selectivity to CO formation. This is in agreement with the literature on iron-oxide catalysts (*i.e.* Fe_3O_4 and FeO), where the RWGS reaction remains dominant throughout the studied temperature range [5]. The FeO_x behaviour is similar to the cycling of oxygen vacant/filled sites exerted by ceria-based supports, where CO_2 dissociates on the Fe surface into CO and O, where O diffuses into the bulk filling up an oxygen vacant site, that can be later reduced to form H_2O [6,12]. FeO_x catalysts have displayed a high affinity in H_2 adsorption on the surface and the weak adsorption for CO [13]. Thus, the weaker binding energy of CO avoids its hydrogenation into methane which is commonly observed for most other catalysts under atmospheric conditions [13]. Additionally, unlike ceria and other supports, Fe has the ability to store carbon (C) by diffusing it from the surface and into its bulk, forming iron carbide (Fe_xC) [5]. The Fe_xC has been proven to be less active for the RWGS reaction, however, it can never be permanently deactivated since Fe_xC is able to be re-oxidized into an FeO_x phase under direct oxidation, as if the catalyst was newly prepared [7,14]. Thus, for the catalytic system with the high and persistent oxygen storage capacity, CO production remains dominant throughout all the experiments. Confirming with reported results that a form (or a mixture) of iron-oxide is active towards the RWGS reaction and that a more reduced state is less active for the RWGS reaction [5].

6.3.3 *Cyclic Voltammetry*

To further evaluate the oxidation state of FeO_x nanowires cyclic voltammetry (CV) measurements were carried out under the stoichiometric RWGS reaction conditions (*i.e.* CO_2:H_2 = 1:1). Figure 6-4 (a) shows the final cycle of FeO_x at 350 ºC, in a potential window of -1.6 to 1.6 V, at a scan rate of 20 mVs^{-1}. A complete summary of the CV cycles can be found in Figure D-4 (a). In the anodic cycle, the oxidation of Fe to Fe_2O_3 occurs around -0.27 V at the vicinity of the three-phase boundary (TPB) [15]. The small shoulder (a tail) at around +0.2 V is related to the formation of an intermediate oxide, Fe_3O_4 according to eq. 6-4 and 6-5:

$$3FeO + \frac{1}{2}O^{2-}(YSZ) \rightarrow Fe_3O_4 + e^- \quad 6\text{-}4$$

$$2Fe_3O_4 + \frac{1}{2}O^{2-}(YSZ) \rightarrow 3Fe_2O_3 + e^- \quad 6\text{-}5$$

The current growth at around ~0.7 V is due to the oxygen evolution reaction at the TPB from YSZ [16] (eq. 6-6):

$$\frac{1}{2}O^{2-}(YSZ) - 2\,e^- \rightarrow \frac{1}{2}O_2 \quad 6\text{-}6$$

On the cathodic branch there are three cathodic peaks. The first cathodic peak (I) at ~ 0.03 V is affiliated to the reduction of Fe_2O_3 into Fe_3O_4 (eq. 6-7), followed by its reduction to FeO (eq. 6-8) in the second peak (II) at ~ -0.2 V and finally to metallic Fe (eq. 6-9) in the most negative cathodic peak at ~ -0.65 V, peak (III). At higher negative potential the current growth could be associated with electrochemical CO_2 reduction.

$$3Fe_2O_3 + e^- \rightarrow 2Fe_3O_4 + \frac{1}{2}O^{2-} \quad 6\text{-}7$$

$$Fe_3O_4 + e^- \rightarrow 3FeO + \frac{1}{2}O^{2-} \quad 6\text{-}8$$

$$FeO + e^- \rightarrow Fe + \frac{1}{2}O^{2-} \quad 6\text{-}9$$

To evaluate the effect holding potential time has on the oxidation state of FeO_x, the first cycle for each parameter is taken. Figure 6-4 (b) zooms to a narrower potential window from -1.6 to 1.6 V and compares a CV from Figure 6-4 (a) with three CV curves obtained after holding the anodic potential at 1.6 V for 0, 5, 30 and 45 min, following by a voltametric sweep from 1.6 V to

-1.6 V and back. The stability of the system is shown in Figure D-4 (b), with an overlap of the last cycle for each test, where there is a slight shift in current as the conductivity of the catalytic system decreases as more catalytic tests are performed. The cathodic peak (I) did not show any increase but a shift to lower values, whereas peak (II) increased and shifted to lower values compared to a zero-holding time. The highest maximum peak current was after 5-min and then it slightly decreased for 30- and 45-min. Peak (III) increased with increasing polarization time that was accompanied by the peak potential decrease. The increase of the cathodic peaks indicated that more iron-oxide was formed anodically and that this oxide growth occurred not only on the surface but also in the bulk of the catalyst.

Figure 6-4 (c), summarizes the maximum current obtained at each cathodic peak. For peak (I) the current is low and changes slightly. Peak (II) displays a maximum current for a holding time of 5 min, which decreases as holding time is prolonged. Peak (III) reached a maximum current at 30 min holding time, indicating that FeO_x of the higher oxidation state (Fe_2O_3) is mainly formed during extended polarization and its quantity increases with time. The charge densities associated with peak (II) and (III) dependent on the holding time are displayed in Figure 6-4 (d). The charge for peak I was negligible (not shown), while peak (II) reached a maximum for a polarization of 5 min and peak (III) at 30 min.

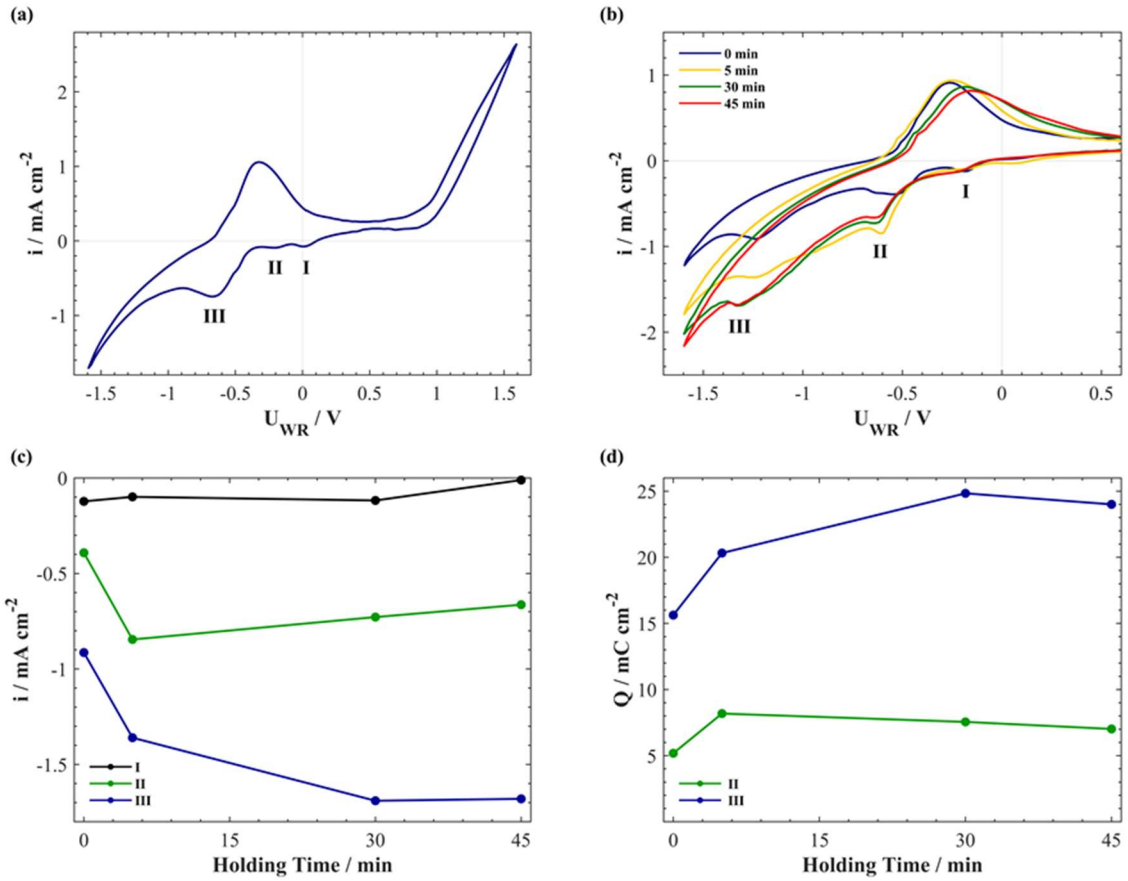

Figure 6-4. Cyclic voltammetry of FeO_x nanowires interfaced with YSZ solid electrolyte under reaction conditions at 350 ºC (a) a stable CV in a wide potential region and (b) CVs after holding potential at 1.6 V for 0, 5, 30 and 45 minutes. Corresponding summary of cathodic peaks for (c) current and (d) charge. CO_2:H_2 = 1:1 and 100 mL min^{-1}.

The maximum shift for peaks (II) and (III) to more negative potentials suggest that reduction process becomes more thermodynamically limited due to the larger amount of iron-oxide present. In the previous studies, using cyclic voltammetry over Pt, Ni and Ag catalysts supported on YSZ [16–19], the oxide formation and bulk (sub-surface) oxygen storage at in the form of metal oxides were linked to the catalytic performance of this materials under open-circuit and EPOC conditions. The existence of stored oxygen in the form of sub-surface oxides was linked with electrochemically induced increase in the catalyst activity and in particular persistent-EPOC behaviour [20].

6.3.4 *Electrochemical promotion of FeO_x nanowires at 300ºC*

Polarization of the FeO_x/YSZ catalyst at 250 ºC did not show a significant response to potential or current application, possibly due to the low production rate of CO at this temperature and endothermic nature of the RWGS reaction, as well as the low conductivity of YSZ. Figure 6-5 shows a transient rate response and the corresponding anodic current to an application of a positive potential of 2 V at 300 ºC under a CO_2:H_2 ratio of 1:1. Positive polarization resulted in the reaction rate decrease represented by a rate enhancement ratio (ρ) of 0.32 and Faradaic efficiency (Λ) of 13. A minimum of 2 h of anodic polarization was required to stabilize the reaction rate. Upon current interruption, 5 h was needed for the reaction to return to its open circuit (O.C.) value. The inhibition of the catalytic activity is related to the oxidation of an active oxide phase, Fe_3O_4, into less active, Fe_2O_3 (eq. 6-5). The formation of Fe_2O_3 is only possible under direct oxygen supply, or during closed-circuit conditions through anodic electro-oxidation [8,21]. Without the supply of O^{2-} to the catalyst, upon potential interruption, the catalyst is slowly reduced under reaction conditions, re-creating oxygen vacancies. The decrease in current value during the applied polarization (Figure 6-5) could indicate the change in conductivity of FeO_x nanowires when higher oxidation state oxides were formed.

Negative polarization had a negligible effect on the CO rate (not shown here), suggesting the FeO_x nanowires were in a promoted state under O.C. conditions. Given the transient behaviour, the active surface area of FeO_x can be estimated using the galvanostatic technique and is described in detail in Chapter 5.3.2. Expressed in moles, the catalytic surface area is estimated to be 8.2 x 10^{-6} mol O (calculated following eq. 5-1) [22]. Overall, at 300 ºC the RWGS reaction showed a decrease in catalytic rate with an increase in potential, sharing a similar behaviour to Ru catalysts for the RWGS reaction under EPOC conditions [23–25].

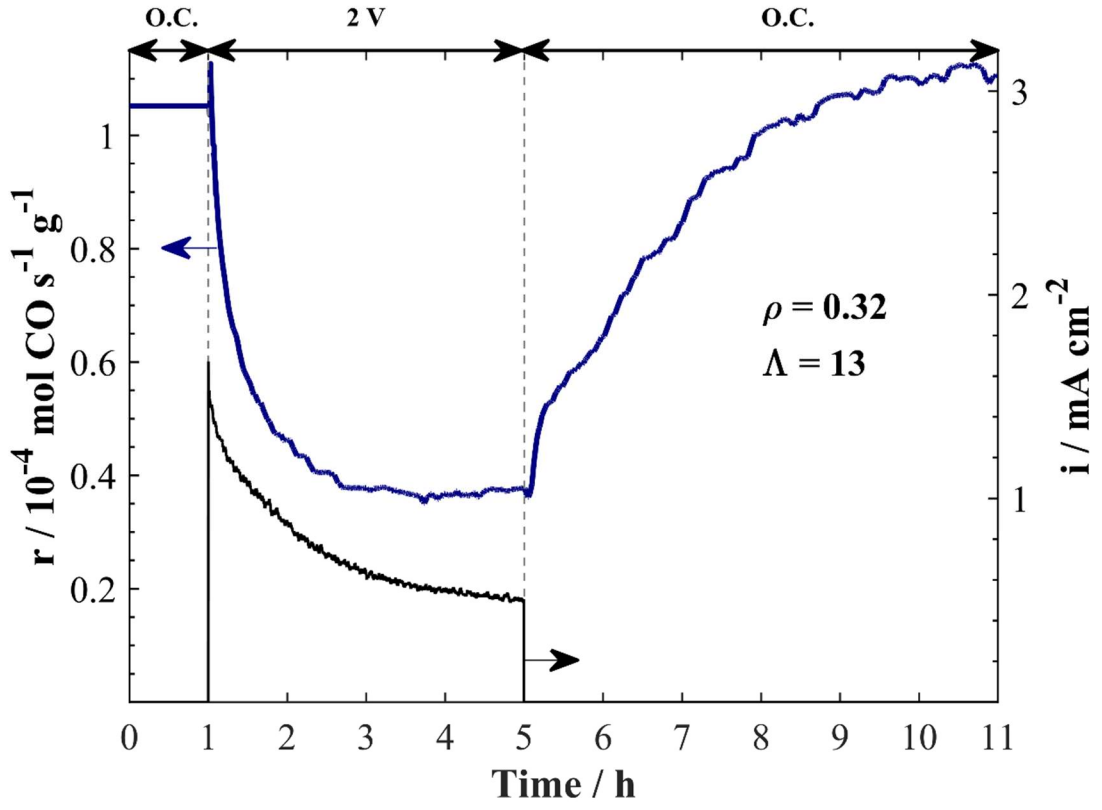

Figure 6-5. Transient reaction rate response of FeO_x nanowires under the application of 2 V at 300 ºC. CO_2:H_2 = 1:1, and 100 mL min^{-1}.

6.3.5 *Electrochemical promotion of FeO_x at 335 and 350 ºC*

According to Figure 6-3, FeO_x nanowires that were mostly present in the Fe_3O_4 state between 250 and 300 ºC undergo partial reduction to FeO that is accompanied by the catalytic rate decrease. Figure 6-6 (a) and (b) shows a transient rate response to the application of 2 V and 500 µA at 335 ºC, respectively. As can be seen, the open-circuit catalytic rate is inferior to the rate observed at 300 ºC (Figure 6-3) confirming that the catalyst is present in a less active reduced state that leads to the formation of carbide sites, rendering the catalyst less active for the RWGS reaction as the oxygen-to-Fe ratio decreases [26]. At this temperature, application of positive polarization (Figure 6-6 (a)) leads to a significant rate increase (ρ_{max} = 4) followed by subsequent decrease and rate stabilization after 1 h at ρ = 2.3 and Λ = 5. The current response directly follows the increase in spike in CO rate, suggesting a change in conductivity from an initial increase followed by a gradual decrease as FeO_x further oxidizes. Further analysis of this effect is evaluated and discussed in Chapters 6.3.6 and 6.3.7, and Figure 6-8 and Figure 6-9. Once potential application is interrupted

after 2 h, the reaction rate showed an interesting behaviour, where instead of decreasing (conventional EPOC) or remaining in its promoted state (persistent electrochemical promotion, p-EPOC behaviour), the rate showed a “new promoted transient” for almost 3 h before returning to its initial open-circuit value. Upon potential interruption, the rate increased first, reached a maximum (γ = 3.4) after 15 min and then slowly returned to its open-circuit value.

Application of constant current, 500 μA shown in Figure 6-6 (b), displayed a similar response to the application of constant potential, with a steady-state value of ρ = 2.2 and Λ = 3, whereas the maximum rate increase corresponded to ρ_{max} = 2.8 for both potential application and interruption (γ = 2.8). For both Figure 6-6 (a) and (b), the corresponding measured current and potential of the FeO_x catalyst followed its oxidation state. In particular, the potential response provided insight on the post-promotional rate increase and slow return to O.C. conditions that could be linked to iron-oxide formation and oxygen storage under polarization. Once the circuit is interrupted the stored oxygen becomes available for the reaction and could act as an oxygen promoter for the RWGS reaction on the iron-based catalyst. This will be further discussed later.

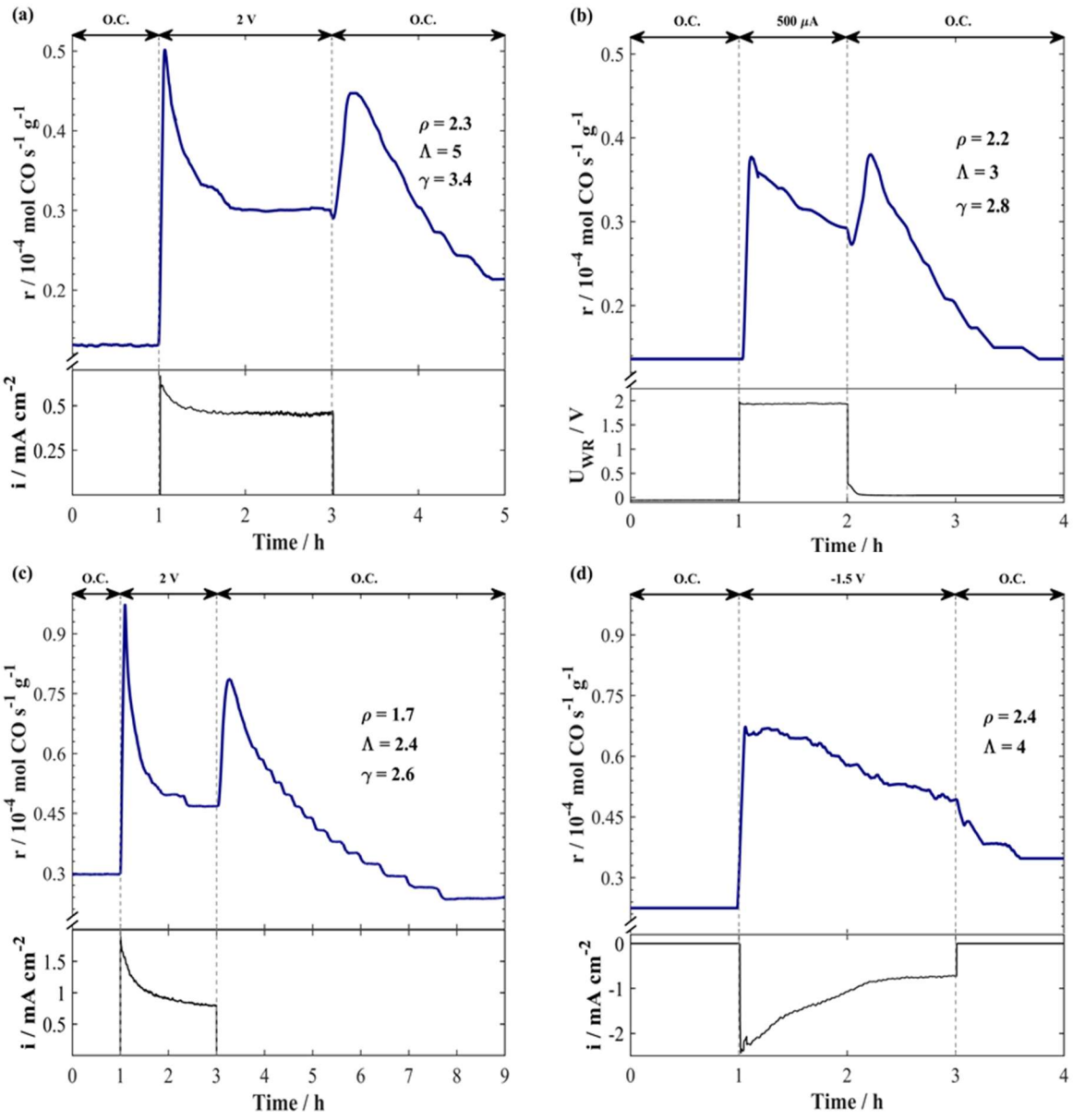

Figure 6-6. Transient response at 335 ºC for (a) 2 V and (b) 500 μA application and at 350 ºC (c) 2 V and (d) -1.5 V application. CO_2:H_2 = 1:1, and 100 mL min^{-1}. The lower figures show the corresponding current or potential response.

Figure 6-6 (c) shows a rate increase under application of 2 V at 350 ºC, leads to a CO enhancement rate of ρ_{max} = 3.8, ρ = 1.7, Λ = 2.4 and γ = 2.6. Following similar behaviour to the effect at 335 ºC, it varied with a larger return to O.C. conditions of 5 h. Thus, confirming the reproducibility of the double CO rate increase. Negative application in Figure 6-6 (d) leads to the reduction of the FeO_x catalyst by forcing $O^{\delta-}$ to migrate towards the YSZ through the three-phase

boundary (eq. 6-8 and 6-9). Thus, the catalyst is in a more reduced state, which in turn increases the cycling exchange of O originating from the dissociation of CO_2 into CO and O, overall increasing the coverage of CO_2 on the surface. Application of -1.5 V for 2 h shows a rate enhancement response of $\rho = 2.4$ and $\Lambda = 4$, that gradually decreases in response with the current. Thus, the RWGS reaction rate at 335 and 350 ºC follows inverted-volcano behaviour due to increase in CO rate under positive and negative polarization, affiliated to the weak adsorption of CO_2 and H_2 [23].

6.3.6 *Electrochemical promotion of FeO_x at 400 ºC*

Investigating further at 400 ºC, the application of a constant current of 1 mA and -1 mA, and their respective potential responses are displayed in Figure 6-7 (a) and (b), respectively. Upon positive current application at 1 h, the CO rate experiences a rate increase similar to the behaviour exerted at 335 and 350 ºC, which takes about the same time to reach a promoted steady-state of $\rho = 1.7$ and $\Lambda = 2.5$, with a $\rho_{max} = 2.1$. Upon current interruption at 3 h, there is again a spike in CO rate along with a delay in potential response, which requires 1 h to return to the O.C. rate, where it is slightly greater than the initial O.C. rate. Upon the application of -1 mA, an increase in CO rate occurs for about 5 min ($\rho_{max} = 2$), where it eventually stabilizes with $\rho = 1.5$ and $\Lambda = 2$. The initial increase in CO rate could be due to the weakening in binding energy of CO_2 that reacts with the Fe-carbide to generate CO. This is affiliated to the quicker response (7 min) when compared with positive potential (39 min). Overall, at 400 ºC, the RWGS reaction experience yet again inverted-volcano behaviour.

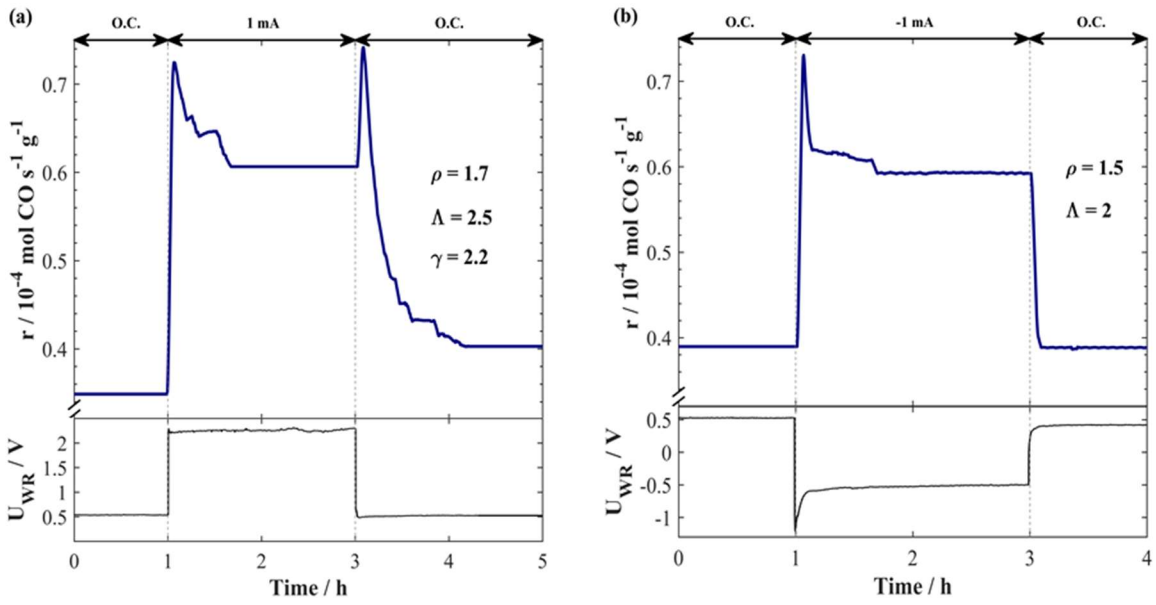

Figure 6-7. Transient rate response of FeO_x nanowires to the application of (a) 1 mA and (b) -1 mA at 400 ºC. CO_2:H_2 = 1:1 and 100 mL min^{-1}. The lower figures show the corresponding potential response.

The rate increase after the current or potential interruption were investigated by varying the length of polarization at a constant current of 1 mA for 15, 30, and 45 min (Figure 6-8). The O.C. conditions of 1:1 (CO_2:H_2) were held for 4 h between each test, allowing sufficient time for the catalyst to reach the steady-state. Application of current for 15 min, does not produce a steady-state. After initial rate increase, the rate continues to decline during 15 min and after the current interruption the catalyst slowly returned to its initial state. Current application for 30 and 45 min, results in a promoted steady-state, in agreement with the transients from Figure 6-6 and Figure 6-7. It is evident that the post-promotional rate increase is higher for longer polarization time (γ_{30min} = 1.9 and γ_{45min} = 2.2) indicating that more oxygen promoters were stored in the form of iron-oxide of higher oxidation states. Upon current interruption the stored oxygen ions become available as reaction promoters, because the electrochemically formed iron-oxide is no longer stable. Oxygen availability results in continuous promotion of the RWGS reaction until the oxygen reservoir remains. The return of the catalyst to O.C. state also depends on the duration of polarization and was slower for longer polarization confirming that extended polarization lead to larger oxygen reservoir inside the FeO_x bulk. The depletion of the oxygen storage and return to O.C. conditions

after polarization are dependent on the time of polarization, in agreement with CV results in Figure 6-4 (b).

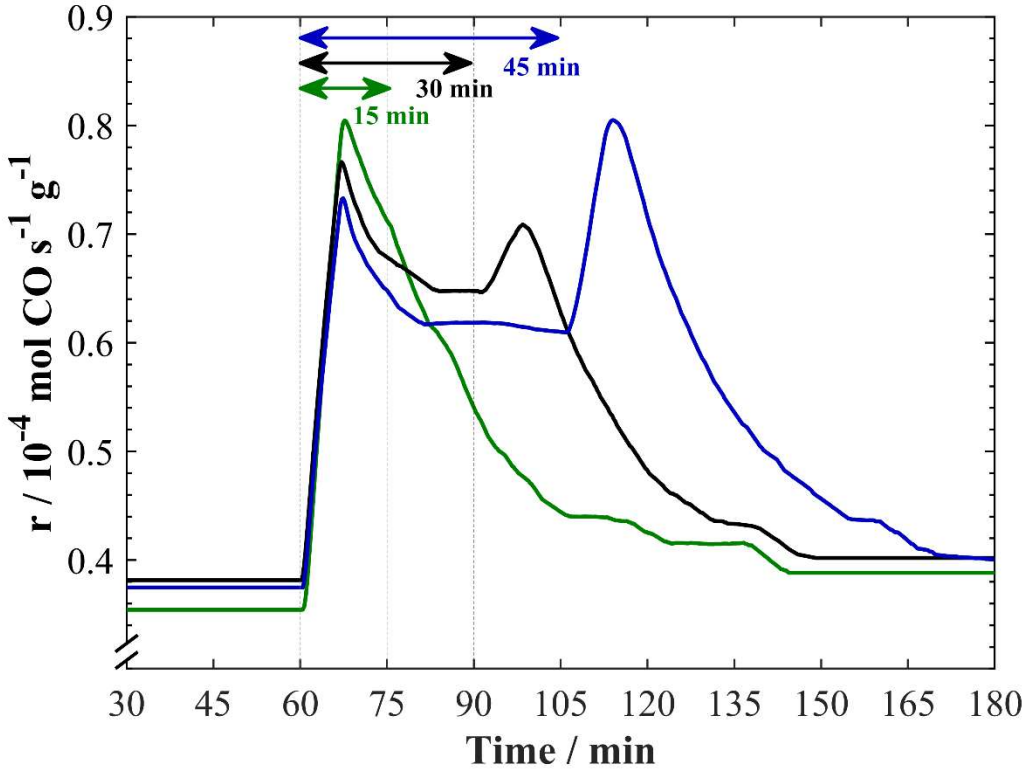

Figure 6-8. Transient response of FeO_x nanowires under the application 1 mA at 400 ºC, varying the polarization time for 15, 30 and 45 minutes as indicated in the figure. CO_2:H_2 = 1:1, and 100 mL min^{-1}.

6.3.7 *Elucidation of carbide formation*

In this section, we further investigated the considerable rate increase during the first minutes of positive polarization, observed at 335, 350 and 400 °C under positive polarization. To this end, the catalyst was first left in the stoichiometric reaction mixture under O.C. for 12 h and then the reaction mixture was switched to He and positive potential of 2 V was applied. Figure 6-9 shows the CO catalytic rate response under O.C. and during polarization. Under O.C. the reaction rate is zero for both temperatures. Given that above 335°C, the electrochemical behaviour was similar up to 400 °C, 350 °C was selected to be compared with 300 °C, where the initial increase was negligible. Upon application of 2V at 300 and 350 ºC under He exclusively, an increase in the

CO rate occurs at both temperatures. At 350 ºC, the rate increase is greater due to the greater amount of Fe-carbide species formed at elevated temperatures, displayed by the larger current response value that decreases as FeO_x becomes more oxidized. CO_2 and CO production occurred; however, only CO production is reported since it directly influences the CO rate during reaction experiments. This confirms the presence of the inactive Fe-carbide that can be activated in-situ through electro-oxidation of oxygen from the YSZ solid electrolyte for the RWGS reaction. Furthermore, removing the need to reactivate the catalyst through the direct supply of oxygen.

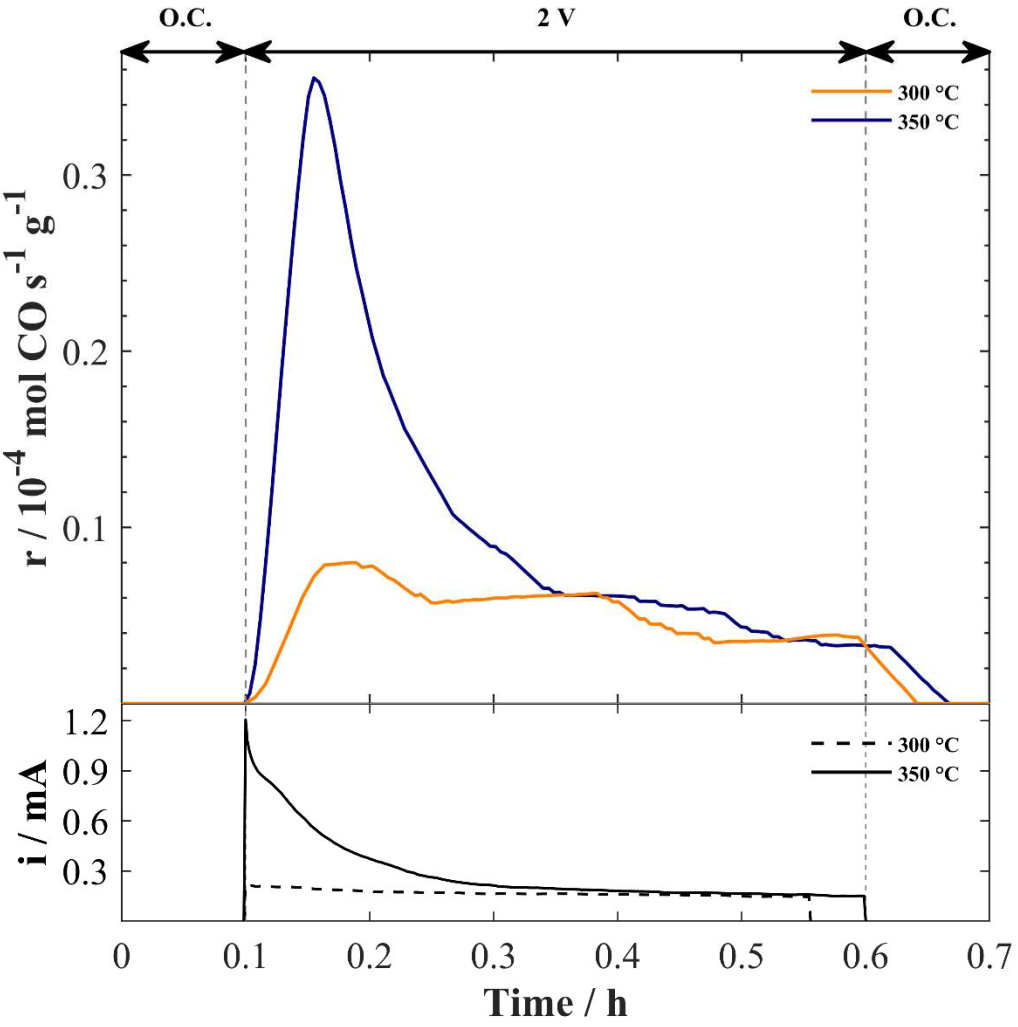

Figure 6-9. CO catalytic rate response to a positive applied potential of 2V under He at 300 ºC and 350 ºC. The lower figure shows the corresponding current response. 100 mL min^{-1}.

Our results demonstrate that during the RWGS reaction between 300 and 400 °C, FeO_x exists in various oxidation states and also as iron carbide. This strongly influences the catalytic activity of FeO_x nanowires under open-circuit and under polarization. We found that the catalyst oxidation state and catalytic activity can be in-situ controlled by applying current or potential resulting in a significant RWGS rate increase at 335-400 °C and rate decrease below 335 ºC. The application of positive polarization at 300 °C led to the decrease in CO rate and negligible rate change during negative polarization, because at this temperature the most active Fe_3O_4 oxidation state is stable. The temperature increases above 335 °C results in partial reduction of FeO_x and formation of less active reduced FeO phase. The overall electrochemical behaviour at 335 ºC and above for positive and negative application is referred to as inverted-volcano behaviour since there is an increase in CO production in both cases. CO rate is in positive order for both electron donor and acceptor reactants, or CO_2 and H_2, respectively. Thus, the reactants experience a weak adsorption with the catalyst surface, making them more prone for a quick dissociation, formation and desorption. Which is in line with the nature of the reactants, which follow simple dissociation into CO, O and H species, and desorb as CO and H_2O on FeO_x [12]. Positive polarization above 335 °C resulted in interesting electrochemical promotion behaviour, where two rate maxima were observed. The initial rate maximum was attributed to Fe_xC oxidation, whereas the second maximum, after current or potential interruption was related to the release of the stored O^{2-} promoters that significantly alter the reaction rate resulting in permanent-EPOC (p-EPOC). Negative polarization above 335 ºC showed an increase in CO production. The removal of $O^{\delta-}$ from the FeO_x surface/bulk lead to a reduced catalyst consisting of additional oxygen vacant sites that are available for the dissociation of CO_2 into CO and O to take place. Furthermore, the rate is enhanced electrochemically through the ease of adsorbing the electronegative CO_2 molecule over H_2 and in turn increasing its coverage over the surface.

6.4 Conclusion

Our findings show that Fe-oxide nanowires can be electrochemically promoted for the RWGS reaction in the temperature range of 300 - 400 °C. Under the reaction conditions FeO_x exists in various oxidation states, where active phases are: Fe_3O_4, FeO and metallic Fe, while fully oxidized Fe_2O_3 and Fe-carbide have shown to inhibit the reaction. We demonstrated that the small current or potential can influence and control the oxidation state of FeO_x nanowires, as well as iron carbide formation and decomposition. The inactive state of Fe-carbide that forms under open-

circuit reaction conditions can be activated in-situ through the direct supply of oxygen from YSZ in favour of the RWGS reaction. Thus, removing the need of an oxidation/reduction step to reactivate the catalyst. The application of negative potential in all cases, resulted in a rate increase of CO production. The initial increase in the CO rate is affiliated with the carbon formed during reaction conditions and the rate increase after polarization is halted is associated to the reduction of oxygen reservoir of FeO_x formed upon polarization according to the persistent-EPOC mechanism [20,27]. Therefore, our work demonstrated an importance of in-situ controlling the oxidation state of inexpensive iron catalyst to ensure efficiency of the RWGS reaction.

References

[1] E. Ruiz, P.J. Martínez, Á. Morales, G. San Vicente, G. De Diego, J.M. Sánchez, Electrochemically assisted synthesis of fuels by CO2 hydrogenation over Fe in a bench scale solid electrolyte membrane reactor, Catal. Today. 268 (2016) 46–59. doi:10.1016/j.cattod.2016.02.025.

[2] E.A. Baranova, C. Bock, D. Ilin, D. Wang, B. MacDougall, Infrared spectroscopy on size-controlled synthesized Pt-based nano-catalysts, Surf. Sci. 600 (2006) 3502–3511. doi:10.1016/j.susc.2006.07.005.

[3] M.S.E. Houache, E. Cossar, S. Ntais, E.A. Baranova, Electrochemical modification of nickel surfaces for efficient glycerol electrooxidation, J. Power Sources. 375 (2018) 310–319. doi:10.1016/j.jpowsour.2017.08.089.

[4] F. Bonnet, F. Ropital, P. Lecour, D. Espinat, Y. Huiban, L. Gengembre, Y. Berthier, P. Marcus, Study of the oxide/carbide transition on iron surfaces during catalytic coke formation, Surf. Interface Anal. 34 (2002) 418–422. doi:10.1002/sia.1330.

[5] D.H. Kim, S.W. Han, H.S. Yoon, Y.D. Kim, Reverse water gas shift reaction catalyzed by Fe nanoparticles with high catalytic activity and stability, J. Ind. Eng. Chem. 23 (2014) 67–71. doi:10.1016/j.jiec.2014.07.043.

[6] V. V Galvita, H. Poelman, V. Bliznuk, C. Detavernier, G.B. Marin, CeO 2 -Modified Fe 2 O 3 for CO 2 Utilization via Chemical Looping, Ind. Eng. Chem. Res. 52 (2013) 8416–8426. doi:10.1021/ie4003574.

[7] J.S. Hwang, K. Jun, K. Lee, Deactivation and regeneration of Fe-K/alumina catalyst in CO2 hydrogenation, 208 (2001) 217–222.doi:1 0.1016/S0926-860X(00)00701-8

[8] J. Zieliński, I. Zglinicka, L. Znak, Z. Kaszkur, Reduction of Fe2O3 with hydrogen, Appl. Catal. A Gen. 381 (2010) 191–196. doi:10.1016/j.apcata.2010.04.003.

[9] M. Albrecht, U. Rodemerck, M. Schneider, M. Bröring, D. Baabe, E. V. Kondratenko, Unexpectedly efficient CO2 hydrogenation to higher hydrocarbons over non-doped Fe2O3, Appl. Catal. B Environ. 204 (2017) 119–126. doi:10.1016/j.apcatb.2016.11.017.

[10] Y.H. Choi, Y.J. Jang, H. Park, W.Y. Kim, Y.H. Lee, S.H. Choi, J.S. Lee, Carbon dioxide Fischer-Tropsch synthesis: A new path to carbon-neutral fuels, Appl. Catal. B Environ. 202 (2017) 605–610. doi:10.1016/j.apcatb.2016.09.072.

[11] D. Zhang, J. Luo, J. Wang, X. Xiao, Y. Liu, W. Qi, D.S. Su, W. Chu, Ru/FeOx catalyst performance design: Highly dispersed Ru species for selective carbon dioxide hydrogenation, Chinese J. Catal. 39 (2018) 157–166. doi:10.1016/S1872-2067(17)62967-X.

[12] A.G. Kharaji, A. Shariati, M.A. Takassi, A novel γ-alumina supported fe-mo bimetallic catalyst for reverse water gas shift reaction, Chinese J. Chem. Eng. 21 (2013) 1007–1014. doi:10.1016/S1004-9541(13)60573-X.

[13] T. Osaki, N. Narita, T. Horiuchi, T. Sugiyama, H. Masuda, K. Suzuki, Kinetics of reverse water gas shift (RWGS) reaction on metal disulfide catalysts, J. Mol. Catal. A Chem. 125 (1997) 63–71. doi:10.1016/S1381-1169(97)00080-0.

[14] C.S. Chen, W.H. Cheng, S.S. Lin, Enhanced activity and stability of a Cu/SiO2 catalyst for the reverse water gas shift reaction by an iron promoter., Chem. Commun. (Camb). (2001) 1770–1771. doi:10.1039/b104279n.

[15] G.J. Bignold, Cyclic voltammetry at the iron electrode in high temperature aqueous sodium hydroxide solutions, Corros. Sci. 12 (1972) 145–154. doi:10.1016/S0010-938X(72)90874-8.

[16] M. Fee, S. Ntais, A. Weck, E.A. Baranova, Electrochemical behavior of silver thin films interfaced with yttria-stabilized zirconia, J. Solid State Electrochem. 18 (2014) 2267–2277. doi:10.1007/s10008-014-2477-0.

[17] C.G. Vayenas, A. Ioannides, S. Bebelis, Solid electrolyte cyclic voltammetry for in situ investigation of catalyst surfaces, J. Catal. 129 (1991) 67–87. doi:10.1016/0021-9517(91)90010-2.

[18] S.G. Neophytides, C.G. Vayenas, TPD and cyclic voltammetric investigation of the origin of electrochemical promotion in catalysis, J. Phys. Chem. 99 (1995) 17063–17067. doi:10.1021/j100047a001.

[19] D. Tsiplakides, C.G. Vayenas, Temperature Programmed Desorption of Oxygen from Ag Films Interfaced with Y 2 O 3 -Doped ZrO 2, 251 (1999) 237–251. doi:10.1006/jcat.1999.2522

[20] S. Souentie, C. Xia, C. Falgairette, Y.D. Li, C. Comninellis, Investigation of the "permanent" electrochemical promotion of catalysis (P-EPOC) by electrochemical mass spectrometry (EMS) measurements, Electrochem. Commun. 12 (2010) 323–326. doi:10.1016/j.elecom.2009.12.031.

[21] M. Niemelä, M. Nokkosmäki, Activation of carbon dioxide on Fe-catalysts, Catal. Today. 100 (2005) 269–274. doi:10.1016/j.cattod.2004.09.061.

[22] S. Ladas, S. Kennou, S. Bebelis, C.G. Vayenas, Origin of non-faradaic electrochemical modification of catalytic activity, J. Phys. Chem. 97 (1993) 8845–8848. doi:10.1021/j100137a004.

[23] S. Brosda, C.G. Vayenas, J. Wei, Rules of chemical promotion, Appl. Catal. B Environ. 68 (2006) 109–124. doi:10.1016/j.apcatb.2006.07.021.

[24] D. Theleritis, S. Souentie, A. Katsaounis, C.G. Vayenas, Hydrogenation of CO2 over Ru electropromoted catalysts, ACS Catal. 2 (2012) 770–780. doi:dx.doi.org/10.1021/cs300072a.

[25] I. Kalaitzidou, A. Katsaounis, T. Norby, C.G. Vayenas, Electrochemical promotion of the hydrogenation of CO2 on Ru deposited on a BZY proton conductor, J. Catal. 331 (2015) 98–109. doi:10.1016/j.jcat.2015.08.023.

[26] J. Liu, G. Zhang, X. Jiang, J. Wang, C. Song, X. Guo, Insight into the role of Fe5C2 in CO2 catalytic hydrogenation to hydrocarbons, Catal. Today. (2020). doi:10.1016/j.cattod.2020.07.032.

[27] C. Falgairette, A. Jaccoud, G. Fóti, C. Comninellis, The phenomenon of "permanent" electrochemical promotion of catalysis (P-EPOC), J. Appl. Electrochem. 38 (2008) 1075–1082. doi:10.1007/s10800-008-9554-y.

Appendix D - Supplementary Information for Chapter 6

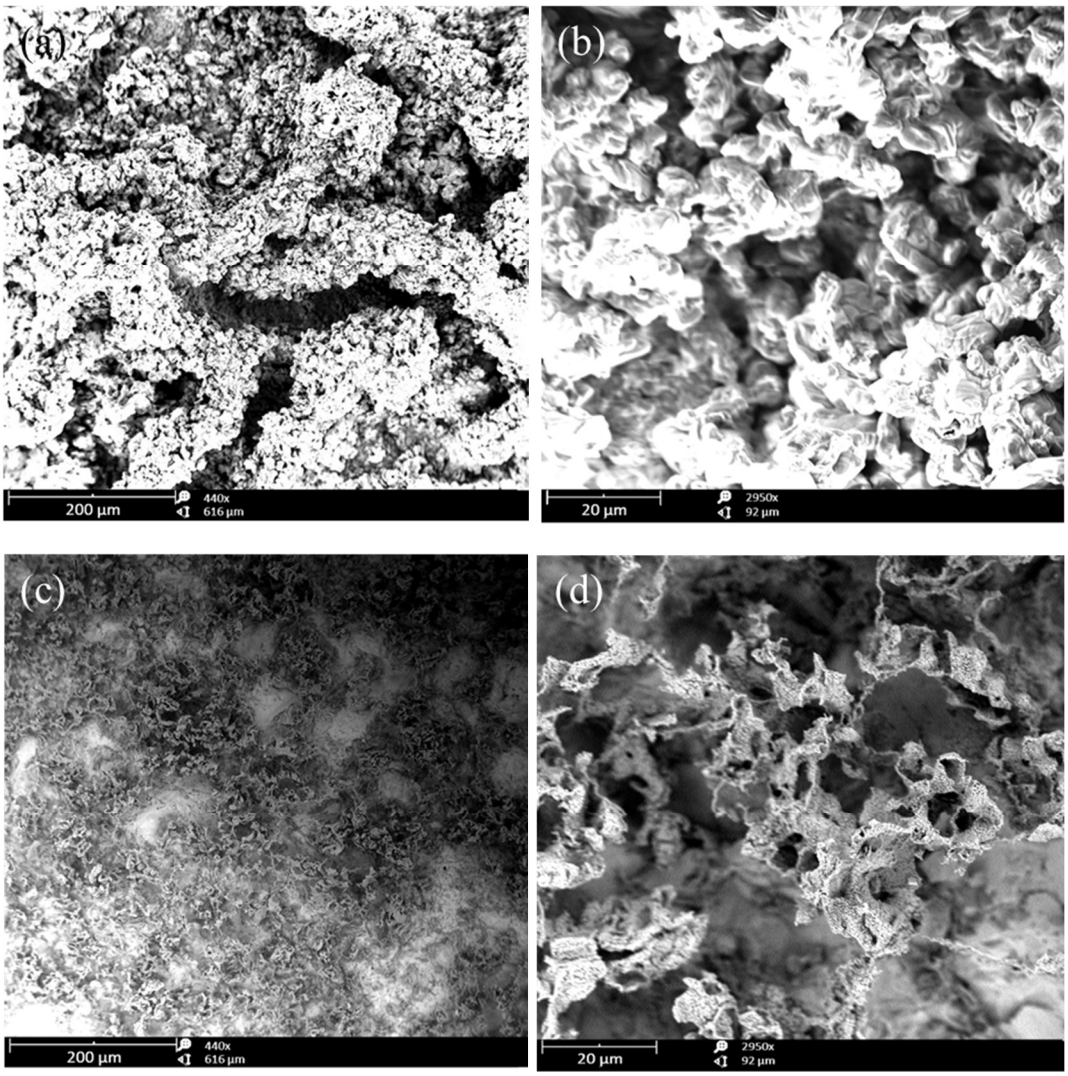

Figure D-1. SEM images of FeO_x dispersed catalyst (a) and (b) fresh and (c) and (d) used.

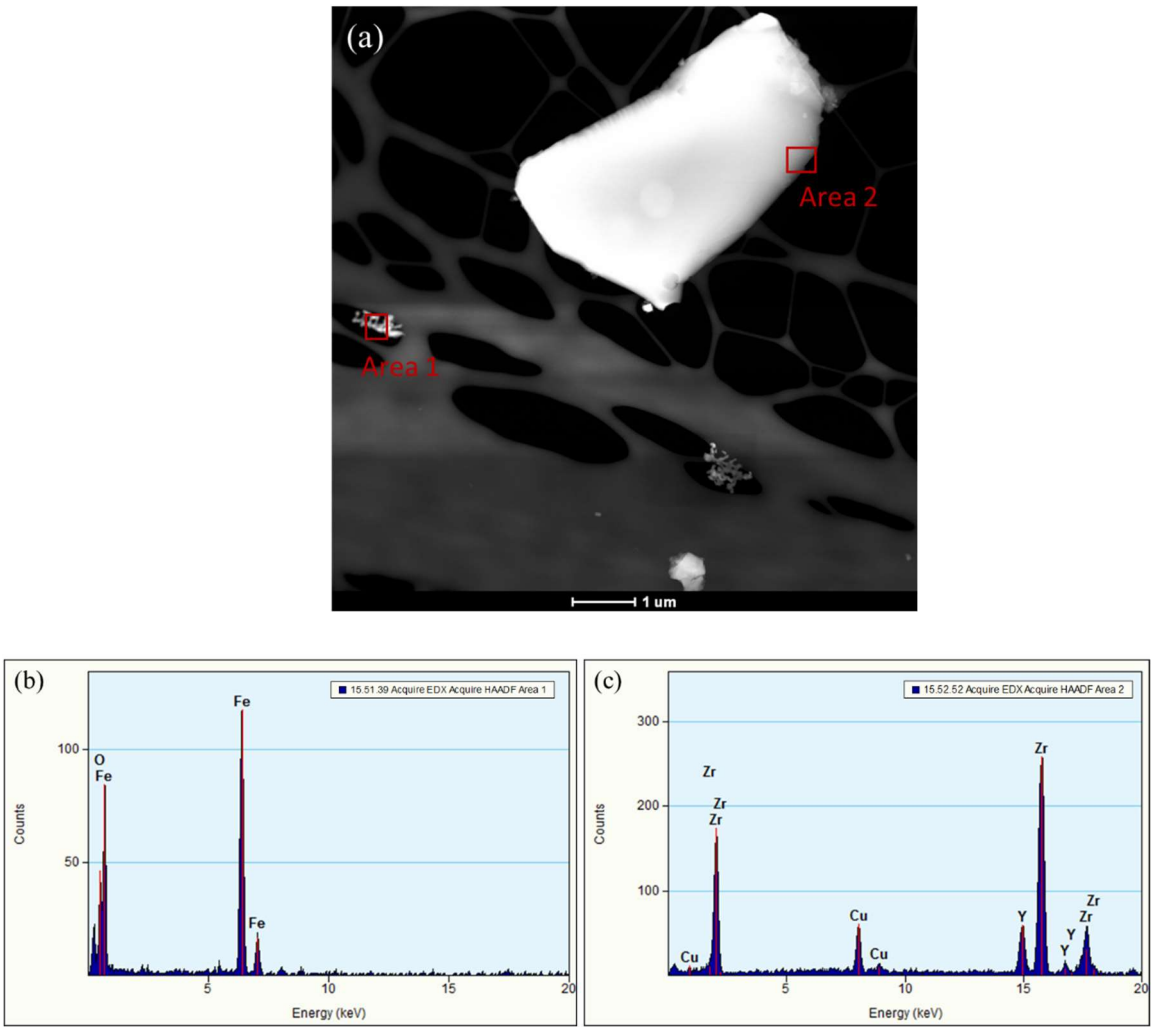

Figure D-2. STEM of (a) FeO_x particle (area 1) and YSZ (area 2), (b) EDX mapping of area 1 and (c) area 2.

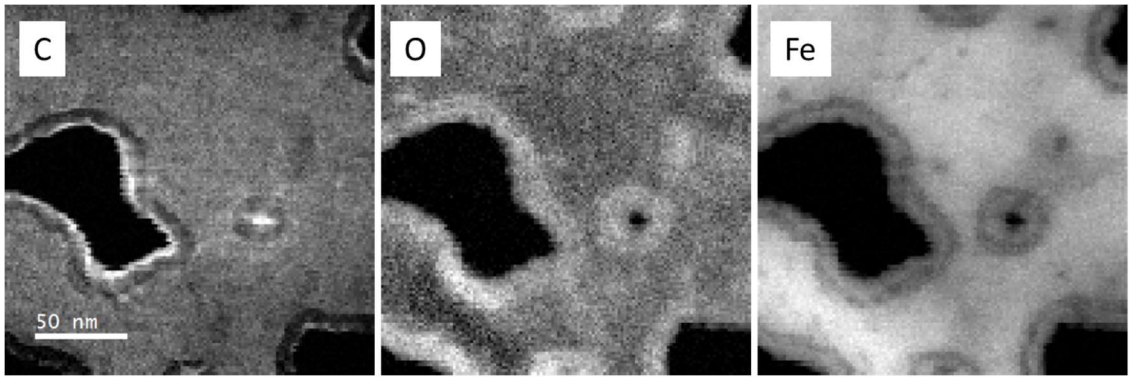

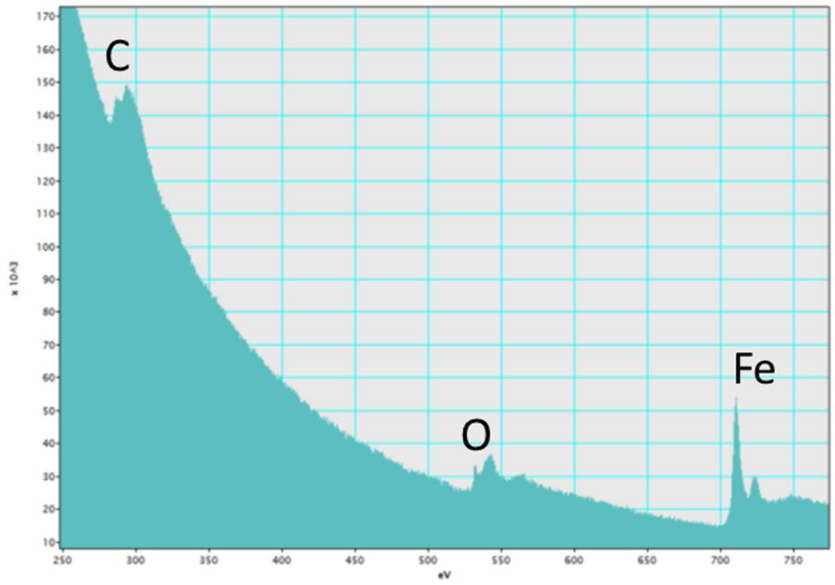

Figure D-3. EELS mapping and spectrum of the used FeO_x.

Table D1, summarizes the carbon balance for Figure 6-3, Figure 6-5-Figure 6-9 following equation D-1. The carbon balance for Figure 6-3, the open-circuit RWGS activity, was referenced to the CO_2 input. For Figure 6-5 to Figure 6-9, the carbon balance was measures as the difference between O.C. values and polarization. For example, 100% carbon balance signifies no change in the carbon amount from O.C. to the ρ value.

$$C\ balance\ (\%) = \frac{[CO_{2,in}] + [CO_{out}]}{[CO_{2,in}]} \qquad D-1$$

From the O.C. RWGS activity, the carbon balance decreases as temperature increases, signifying the formation of carbon deposition. In terms of the electrochemical tests, the carbon balance increases for the ρ_{max} values, signifying a release of carbon from the catalyst. The ρ values display a slight change, while γ display a slight decrease in the carbon balance related to the stored oxygen species being replaced with carbide

Table D-1. Carbon balance Summary for Figure 6-3,Figure 6-5, Figure 6-6, Figure 6-7, Figure 6-8 and Figure 6-9.

		CO_2 Conversion (%)	Carbon Balance (%)
Figure 6-3	250 °C	0.14	100
	300 °C	0.42	99.8
	335 °C	0.05	99.4
	350 °C	0.11	99
	400 °C	0.14	98.6

	Conditions	ρ_{max} (%)	ρ (%)	γ (%)
Figure 6-5	300 °C	100	100.02	100
Figure 6-6	335 °C 500 μA	100.6	100.06	99.67
	335 °C 2 V	100.3	100.02	99.8
	350 °C 2 V	100.7	100.07	99.5
	350 °C -1.5 V	100	100	100
Figure 6-7	400 °C 1 mA	100.7	100.2	99.5
	400 °C -1 mA	100.4	100.1	100
Figure 6-8	15 min	100.9	NA	99.5
	30 min	101	100.8	99.3
	45 min	102.2	101.4	99.1
Figure 6-9	300 °C 2 V	102.8	NA	NA
	350 °C 2 V	104	NA	NA

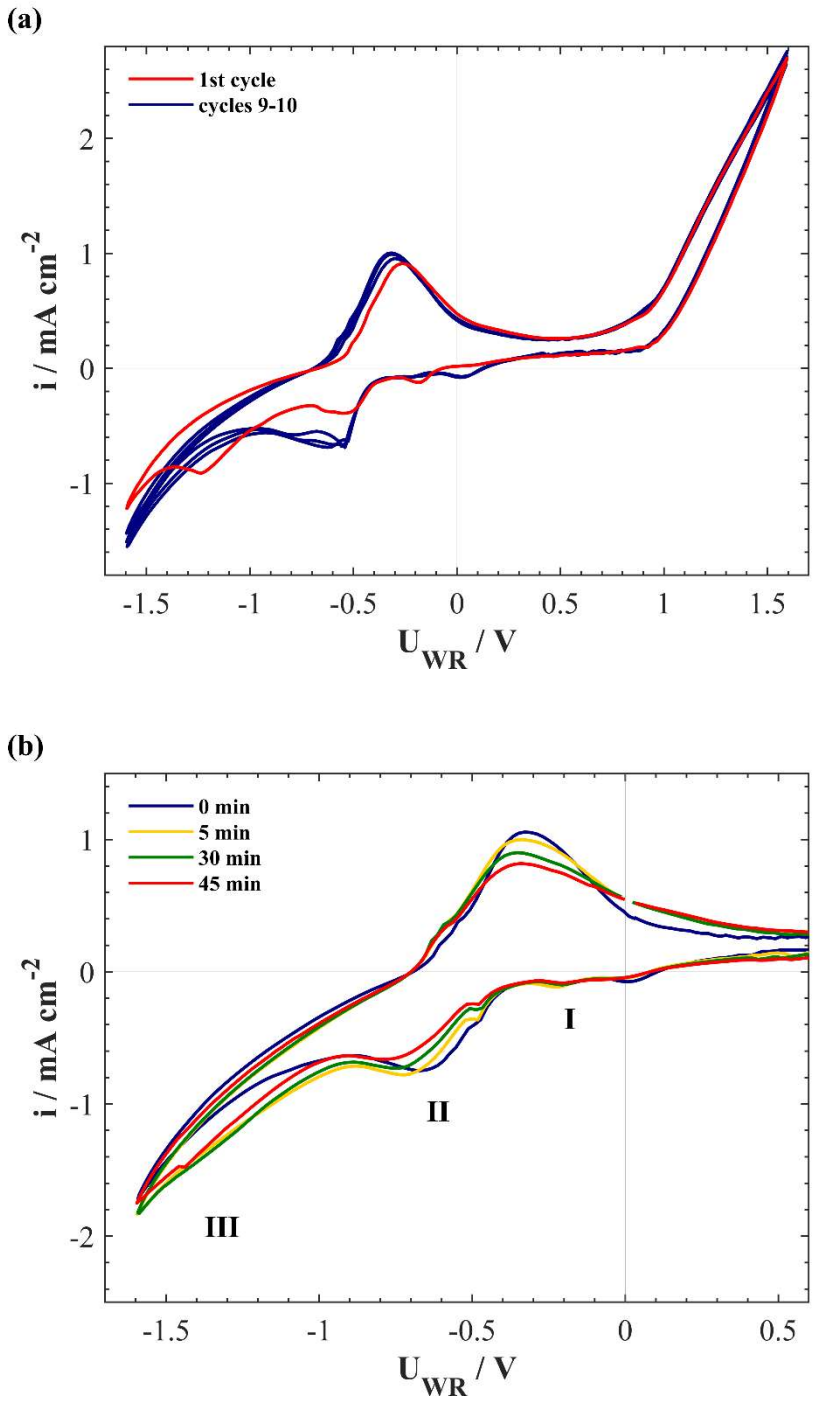

Figure D-4. Cyclic voltammetry of FeO_x nanowires interfaced with YSZ solid electrolyte under reaction conditions at 350 ºC. (a) Summary of no fold CV for 10 cycles and (b) last CV cycle after holding potential at 1.6V for 0, 5, 30 and 45 minutes. CO_2:H_2 = 1:1 and 100 mL min^{-1}.

Chapter 7 : The role of Ru clusters in Fe carbide suppression for the reverse water gas shift reaction over electropromoted Ru/FeO_x catalysts

Adapted from: ***C. Panaritis****, J. Zgheib, M. Couillard, E. A. Baranova, Electrochemistry Communications, 119 (2020), 106824.*

Abstract

The formation of an iron carbide phase has been shown to inhibit the efficiency of Fe-based catalysts in the initial step of adsorbing carbon dioxide (CO_2). In this study, we evaluate the effect of adding Ru clusters (20% at.) to FeO_x nanowires deposited on yttria-stabilized zirconia (YSZ) for the reverse water gas shift (RWGS) reaction carried out at 300–400 °C under atmospheric conditions. STEM shows that Ru-FeO_x formed a bi-phase structure with Ru clusters (1.5–2 nm) supported on FeO_x nanowires (5 nm) that remain as mixed oxides after the reaction. Open-circuit catalytic measurements demonstrated that addition of Ru increased the catalytic activity and stabilized high selectivity (>99%) towards CO. The synergetic effect of Ru and FeO_x was further emphasized through electrochemical polarization, which led to a reversible catalytic activity increase of up to 2.4 times. The addition of Ru inhibits the formation of inactive Fe carbide by acting as the reducing component and stabilizing the FeO_x active state. This results in an improved and lasting catalytic performance and makes Ru/FeO_x catalysts attractive for industrial applications.

7.1 Introduction

Herein, we modified FeO_x nanowires with Ru clusters to form a Ru/FeO_x bi-phase catalyst for the RWGS reaction. We carried out STEM characterizations for the fabricated and used Ru/FeO_x and catalytic testing under open-circuit and EPOC conditions at 300–400 °C. Anodic and cathodic polarization were conducted under stoichiometric (CO_2:H_2 = 1:1) and reducing (CO_2:H_2 =1:7) conditions to evaluate the change in catalytic behaviour. Furthermore, we studied the effect of persistent or permanent EPOC [1] over Ru/FeO_x catalysts at 400 °C under reducing conditions.

7.2 Experimental

7.2.1 *Synthesis of Ru/FeO_x*

The Ru/FeO_x catalyst used in this study was synthesized through a two-step polyol method. The first step consisted of fabricating FeO_x nanowires by mixing iron (III) nitrate ($Fe(NO_3)_3$) (nanohydrate, Fischer Scientific) with ethylene glycol (EG) and tetramethylammonium hydroxide (TMAOH) as described in Chapter 6.2.1. The second step consisted of preparing a solution containing ruthenium chloride ($RuCl_3$) (anhydrous, Sigma Aldrich) by mixing the precursor with TMAOH, for a final pH of 12, then adding ethylene glycol to reach the desired volume. The obtained Ru precursor salt solution was then mixed with the FeO_x nanowire solution and then TMAOH was added to reach a pH of 12. After that, the solution was stirred at room temperature for 30 min, refluxed for 3 h at 160 ˚C and cooled down to room temperature. The final mixture was dark brown in colour with a pH of ~7.5. The nominal atomic composition of the catalyst was 20 to 80 at. % of Ru to FeO_x.

7.2.2 *Characterization of Ru nanoparticles on FeO_x nanowires*

The Ru/FeOx catalyst was analyzed through scanning transmission electron microscopy (STEM) before and after reaction. Energy-Dispersive X-ray spectroscopy (EDX) was used to study the used sample after reaction. A FEI Titan3 80-300 TEM operated at 300 keV, equipped with a CEOS aberration corrector (for the probe-forming lens) and an EDX spectrometer (EDAX Analyzer, DPP-II) were used. The samples were prepared following the procedure reported in Chapter 4.2.2.

7.2.3 *Reaction Experiment*

The total flow rate of 100 mL min^{-1} consisted of CO_2 (Linde, 99.99%), H_2 (Linde, 100 %) and He (Linde, 100 %) at 1.5 kPa, 1.5–10.5 kPa and 88–97 kPa, respectively. CO_2:H_2 ratios of 1:1 and 1:7 were examined to compare stoichiometric and reducing conditions, respectively. The analysis of gases and electrochemical tests were done following the same procedure as Chapter 4.2.3.

7.3 Results & Discussion

7.3.1 *Characterization*

STEM images of fresh (just prepared) and used (after reaction) Ru/FeO_x catalyst are shown in Figure 7-1 (a) and (b), respectively. In agreement with our earlier results in Chapter 6.3.1, the FeO_x nanowires have a diameter of 5 nm and range in length from 5 to 50 nm, while the average

size of the Ru clusters is ~1 nm (as shown in Chapter 4.3.1). The morphology shows Ru clusters supported on FeO_x, which will be denoted as Ru/FeO_x. Figure 7-1 (b) shows Ru/FeO_x after reaction, where various FeO_x planes are exposed: Fe_3O_4 (111), FeO (111) and FeO (220), corresponding with *d*-spacings of 4.8 Å, 2.5 Å and 1.6 Å, respectively [2,3]. The size of FeO_x does not significantly increase, even though the particles have agglomerated. Ru is indistinguishable, but can be associated with an amorphous structure represented by the bright area in Figure 7-1 (b) (circled by a red dashed line). The presence of Ru is confirmed through EDX analysis (see Figure 7-1 (c-f)), while the elemental Cu and Mo originate from the sample holder.

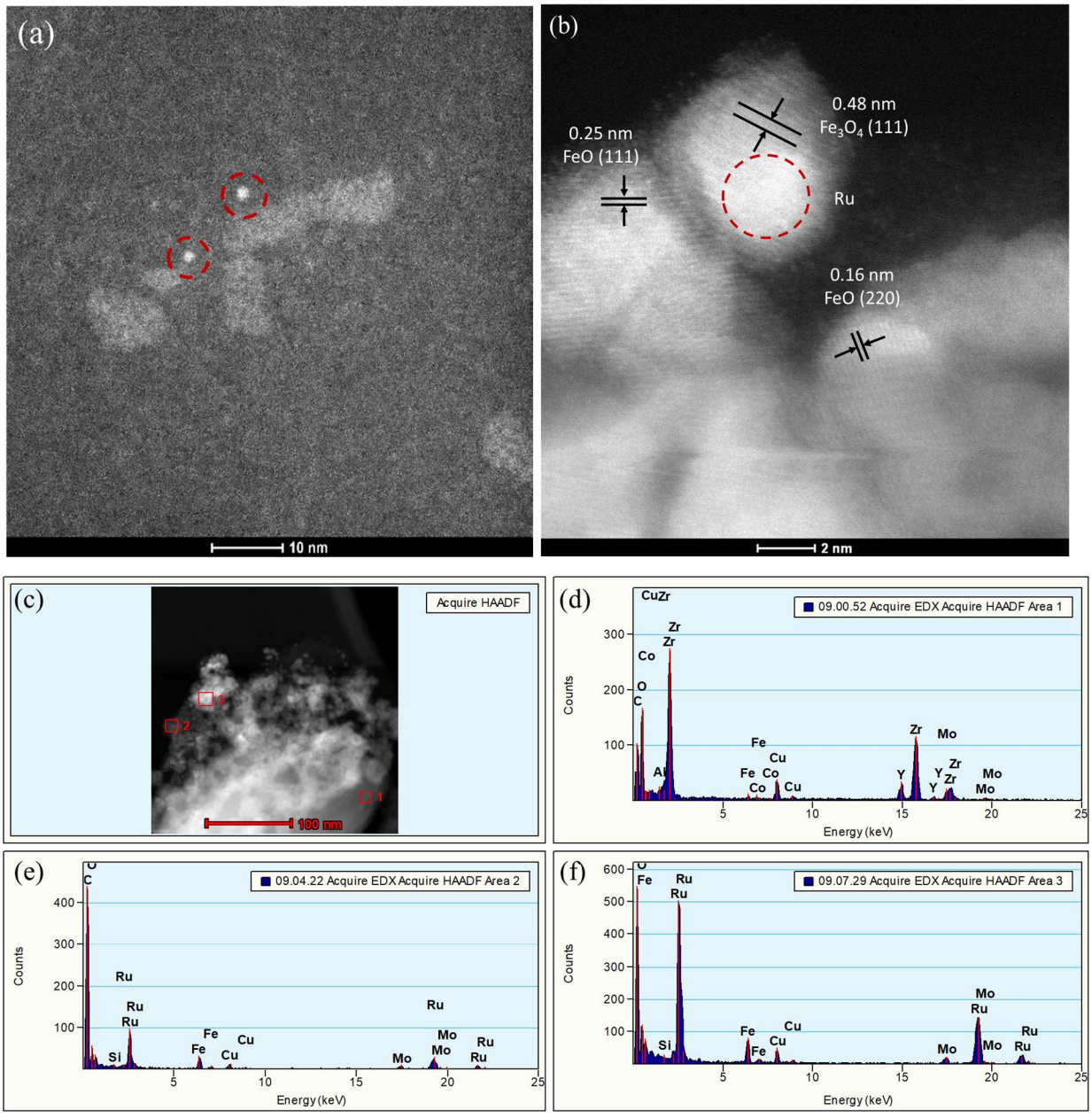

Figure 7-1. STEM image of (a) a fresh colloidal solution of Ru clusters on Fe oxide nanowires and (b) spent Ru/FeO_x on YSZ, where Ru is represented by the bright spots circled by a dashed red line. EDX mapping (c) and the corresponding compositions (d)-(f) for the red squares marked in (c).

7.3.2 *Open-circuit Catalytic Activity*

To establish the effect of Ru on FeO_x, we compared the catalytic activity of FeO_x and Ru/FeO_x for CO_2:H_2 ratios of 1:1 and 1:7 (Figure 7-2 (a) and (b), respectively). In Figure 7-2 (a), the catalytic activity of FeO_x reached a maximum CO rate at 300 °C, followed by a lower CO rate at 335 °C which then increased with temperature. The catalytic activity associated with Ru/FeO_x increased with temperature, overtaking the CO rate of FeO_x at ~330 °C. Increasing the reducing conditions to CO_2:7H_2 (Figure 7-2 (b)) results in a similar pattern for FeO_x with a decrease in overall catalytic activity, where the CO rate reached a maximum at 300 °C, decreased at 350 °C and then increased with temperature. Ru/FeO_x outperformed FeO_x at ~325 °C and continued to do so up to 400 °C. As shown in Chapters 4 and 5, free-standing Ru nanoparticles produce CH_4 when used as a nanofilm deposited on YSZ and barium-zirconate yttria (BZY) solid electrolytes. Thus, when combined with FeO_x the methanation reaction is inhibited, causing the catalytic activity to be > 99% selective for CO.

The initial high reaction rate of monometallic FeO_x is linked to the existence of an Fe_3O_4 active phase at 300 °C, which is reduced to a mixture of Fe_3O_4–FeO as the temperature is increased. In terms of Ru/FeO_x, the CO rate follows the same trend for both 1:1 and 1:7, which is to increase as a function of temperature. The increased CO rate associated with Ru/FeO_x is due to the synergetic effect between Ru and FeO_x, in which Ru has the ability to dissociate H_2 into atomic H, providing the opportunity for a spillover onto the FeO_x nanowires, thus generating oxygen vacancies. FeO_x acts as a catalyst for the adsorption of CO_2 and its subsequent cleavage into CO and O. The dissociated O is used to fill the oxygen vacancies to repeat the process all over again [4]. Thus, for monometallic FeO_x, all sites compete for the activation of CO_2 and H_2, while the addition of Ru provides sites for H_2 adsorption.

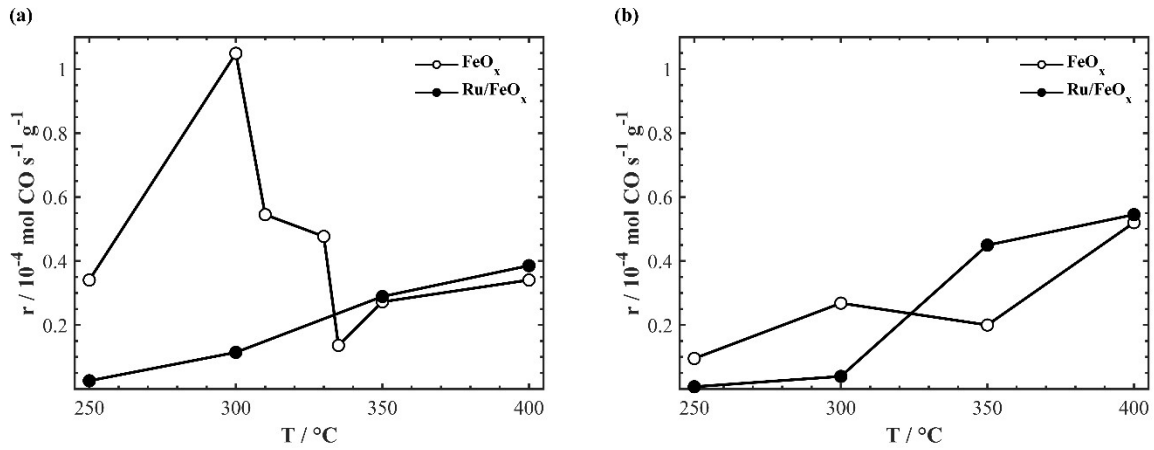

Figure 7-2. Summary of the open-circuit catalytic rate on FeO_x/YSZ and Ru/FeO_x/YSZ. The CO_2:H_2 ratios were (a) 1:1 and (b) 1:7.

7.3.3 *Electrochemical Promotion of Ru/FeO_x*

Given that the RWGS is an endothermic reaction, the electrochemical promotion experiments were undertaken at 350 and 400 °C. Figure 7-3 (a) shows the transient response for an applied potential of 1.5 V at 350 °C with CO_2:H_2 = 1:1. Upon anodic polarization of the Ru/FeO_x catalyst, oxygen ions migrate from YSZ to the Ru/FeO_x catalyst electrode, resulting in a CO rate increase of up to 1.6 times with an apparent Faradaic efficiency $\Lambda = 3$. When the potential was interrupted, the CO rate returned to the initial O.C. rate value.

Cathodic polarization resulted in the migration of O^{2-} from Ru/FeO_x through YSZ to the Au counter electrode. Figure 7-3 (b) shows the rate response upon negative -1.5 V polarization, which led to a CO rate increase of 2.4 with $\Lambda = 0.5$. Under polarization for 2 h, the reaction rate gradually increased due to the reduction of FeO_x, thus influencing the adsorption of CO_2 and subsequent dissociation into CO and O. After current interruption the rate remained in a promoted state ($\gamma = 2.3$) and another 2 h were required for it to return to its less active FeO_x initial state. Thus, based on the EPOC rules established by Brosda *et al.* [5], both positive and negative polarization resulted in an increase in the CO rate corresponding to inverted volcano behaviour, associated with weak adsorption of the electron donor (H_2) and acceptor (CO_2) on the catalyst surface [6].

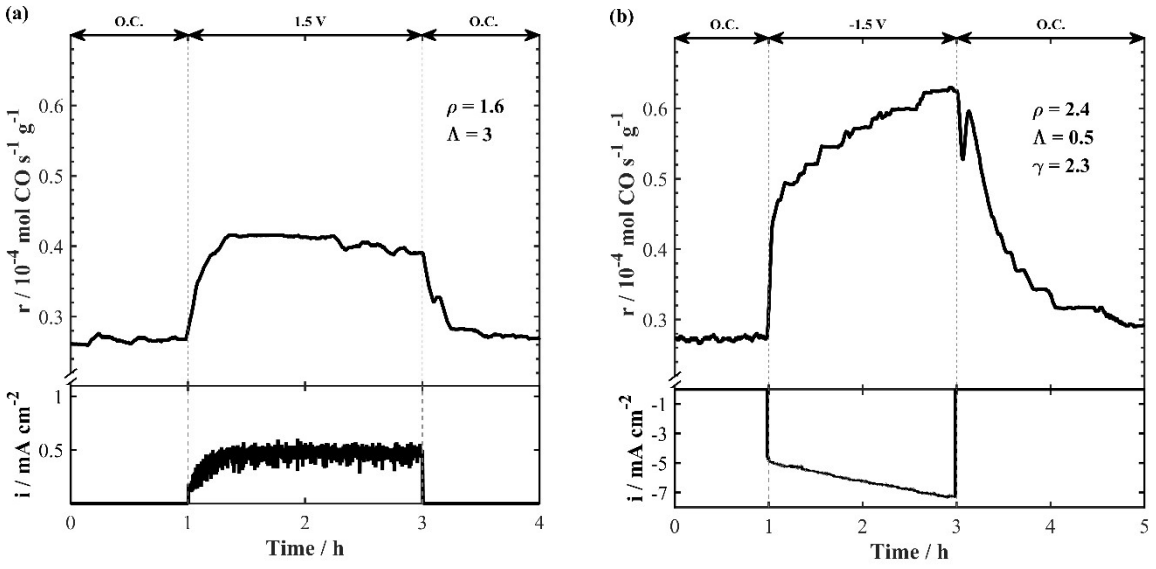

Figure 7-3. Transient reaction rate response of Ru/FeO_x upon anodic (a) 1.5 V and cathodic (b) -1.5 V applied potential with CO_2:H_2 = 1:1 at 350 °C.

The catalytic activity of Ru/FeO_x with stoichiometric (CO_2:H_2 = 1:1) and reducing (CO_2:H_2 = 1:7) gas compositions was evaluated under galvanostatic conditions at 400 °C. Figure 7-4 (a) displays the catalytic response under stoichiometric conditions when 1 mA current is applied. The CO rate initially increased due to the oxidation of inactive Fe_xC – this stage lasts for ~9 min before it stabilizes in a promoted state with ρ = 1.2 and Λ = 1.04. Once the current is interrupted, oxygen stored in the form of FeO_x is made available for the reaction, resulting in an increased reaction rate and a persistent EPOC value of γ = 1.6 for 1 h before it returns to the O.C. value. For an applied current of -1 mA (Figure 7-4 (b)), after 1 h the CO rate increased with ρ = 1.2 and Λ = 0.6. When the current is interrupted at 2 h, the p-EPOC is γ = 1.4 and requires 30 min to return to the O.C. value.

Figure 7-4 (c) and (d) display the effect of reducing conditions (ratio of CO_2:$7H_2$) with applied currents of 1 and –1 mA, respectively. Figure 7-4 (c) shows that positive current application leads to a constant increase in the CO rate with ρ = 1.4 and Λ = 2.2. Once current is interrupted at 3 h, there is p-EPOC (γ = 2.3) for 1 h before it returns to the O.C. value. This is similar behaviour to FeO_x when used on its own at 400 °C for CO_2:H_2 = 1:1. Figure 7-4 (d) displays the transient response under negative current –1 mA, with a steady-state rate increase of 1.2 with a Λ value of 3.4. When the current is interrupted there is a slight p-EPOC (γ = 1.3), which lasts

less than 5 min. The high potential response is due to the decrease in oxygen ion conductivity of YSZ after extended catalytic testing. Because oxygen ions act as sacrificial promoters during the EPOC experiments they are continuously consumed and not replaced due to the absence of oxygen in the reaction feed. This therefore leads to YSZ reduction and a decrease in its conductivity. Regeneration of the YSZ by exposing it to an oxygen atmosphere could be envisaged in practical applications.

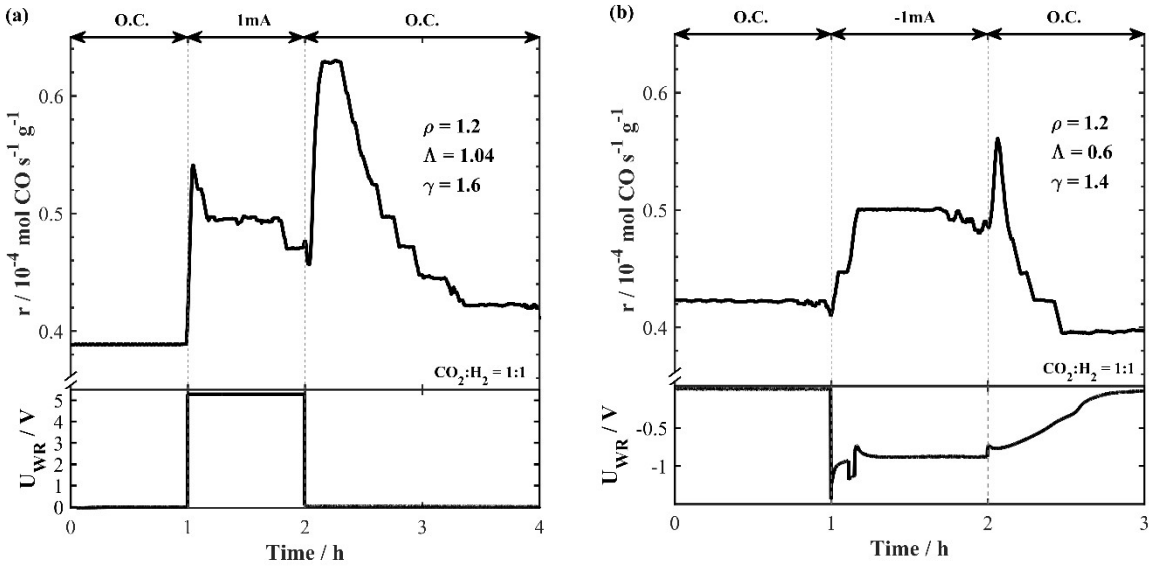

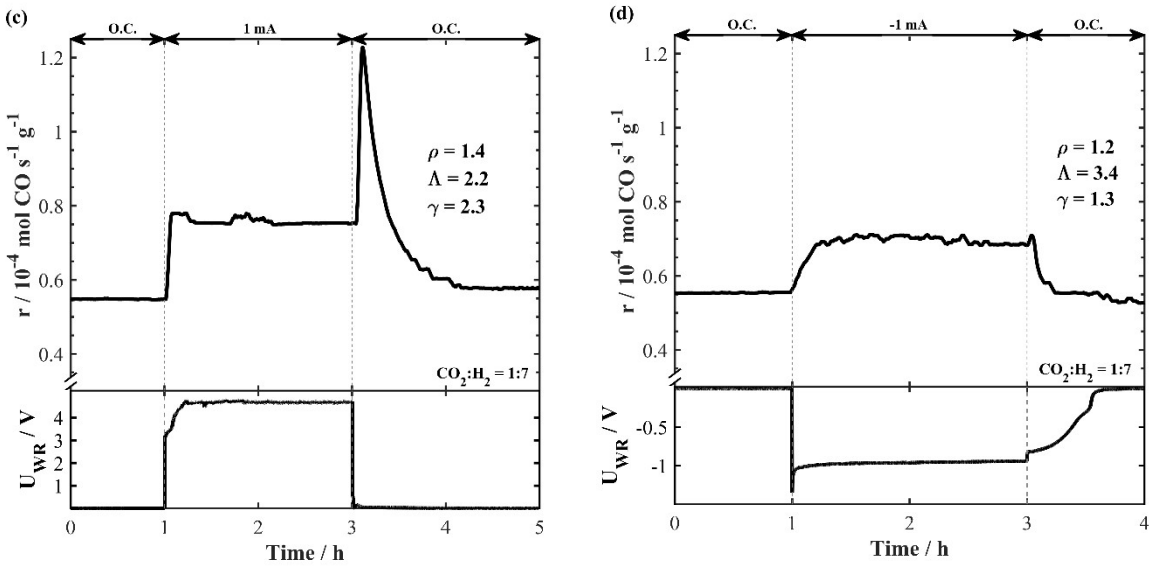

Figure 7-4. Transient rate responses of Ru/FeO_x under galvanostatic conditions at 400 °C: left-hand side (a,c) +1 mA and right-hand side (b,d) –1 mA. The gas composition is indicated in each panel.

To elucidate the persistent EPOC effect occurring after current interruption at 400 °C, Ru/FeO_x catalysts were polarized for 5, 15 and 30 min (see Figure 7-5). Between each polarization, the open-circuit conditions were maintained for 2 h to ensure that the reaction rate is at a steady state. The slight initial increase in the CO rate occurring in all cases can be attributed to the oxidation of the Fe_xC phase, which forms in small amounts compared to monometallic FeO_x due to the presence of Ru clusters which inhibit the formation of iron carbide. The longer the polarization time, the greater the storage of oxygen in FeO_x, resulting in a longer persistent EPOC once the current is interrupted. The corresponding persistent enhancement ratios are $\gamma_{5min} = 1.3$, $\gamma_{15min} = 1.35$, and $\gamma_{30min} = 1.5$. Similar conclusions were drawn for monometallic FeO_x, indicating that FeO_x is an active component.

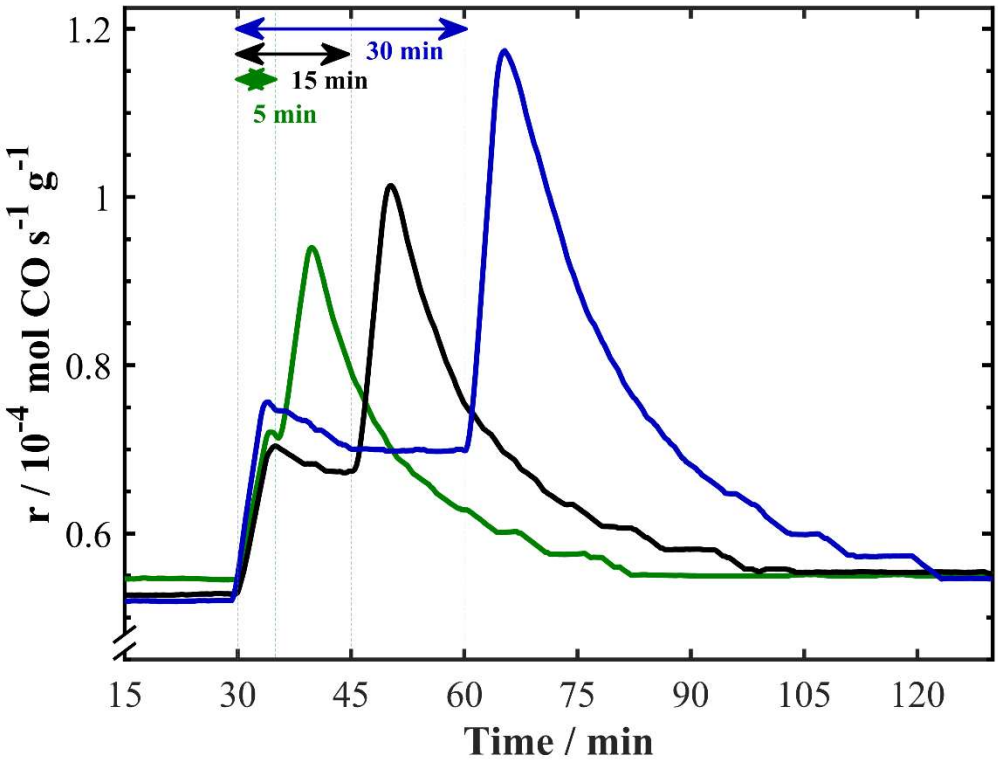

Figure 7-5. Transient rate response to application of 1 mA for 5, 15 and 30 min at CO_2:H_2 = 1:7 and 400 °C.

7.3.4 *Effect of adding Ru*

The addition of Ru to FeO_x results in a dual functioning catalyst, where Ru acts as a site for H_2 adsorption and FeO_x for CO_2 adsorption and dissociation [4,7]. The dissociation of H_2 on Ru allows for controlled H spillover onto FeO_x. A metal–support interaction effect is established between Ru clusters and FeO_x which improves the CO rate at increased temperature and results in new electrochemical behaviour. A direct comparison of Ru/FeO_x and FeO_x is shown in Figures E1 and E2 in Appendix E. Although Ru influences the reaction rate, the FeO_x prevails, ensuring that the selectivity for CO is > 99%.

Compared with monometallic FeO_x, the absence of an initial CO rate increase once the anodic potential or current is applied indicates that a negligible amount of the Fe_xC phase is formed in Ru/FeO_x. This is further confirmed in the STEM image in Figure 7-1 (b), which shows that the proximity of Ru to the FeO_x facets influences its oxidation state: Fe_3O_4 (111) is present near Ru,

while FeO (111) and FeO (220) facets are exposed when Ru is absent. Furthermore, no carbon was detected on the STEM images, unlike the monometallic FeO_x which forms a FeO_x-C core-shell structure (Figure 6-1). This suggests that Ru inhibits the formation of iron carbide (Fe_xC) by providing active sites for H_2 adsorption and dissociation, with H remaining on Ru, halting the reduction of FeO_x into Fe_xC. Figure E3 compares the ρ_{max} values of Ru/FeO_x and FeO_x, which are associated with the formation of Fe carbide.

Ru/FeO_x shows new p-EPOC behaviour compared to FeO_x under negative polarization, which indicates that the adsorption strength of H on Ru is weakened [8]. The weakening of the H bond and increase in CO_2 activation on FeO_x allow H to spillover from Ru to reduce FeO_x sites without both reactants competing for the same sites. FeO_x is reduced to an active state during the polarization that persists after current interruption before returning to its initial less active FeO_x state.

7.3.5 *Conclusion*

Our findings show that addition of Ru clusters to FeO_x decreases the formation of inactive FeC_x, as confirmed in open-circuit and EPOC experiments. Ru is shown to improve the redox reaction taking place on FeO_x by adsorbing H_2 and supplying H to FeO_x, in the temperature range 250–400 °C. A synergistic effect occurs between Ru and FeO_x, which enables FeO_x to remain in an active state for the RWGS reaction (> 99% selective to CO) and increase by 2.4 times during polarization. Overall, the addition of Ru nanoparticles in a two-step synthesis enhances FeO_x performance in redox reactions that can be applied to industrial scale applications where catalytic stability and susceptibility to carbide formation are crucial.

References

[1] C. Falgairette, A. Jaccoud, G. Fóti, C. Comninellis, The phenomenon of “permanent” electrochemical promotion of catalysis (P-EPOC), J. Appl. Electrochem. 38 (2008) 1075–1082. doi:10.1007/s10800-008-9554-y.

[2] B. Leszczynski, A.A.E.-G. George C. Hadjipanayis, K. Załęski, A.M. Zbigniew Śniadecki, M. Jarek, S. Jurga, A. Skumiel, The influence of oxidation process on exchange bias in egg-shaped FeO/Fe3O4 core/shell nanoparticles, J. Magn. Magn. Mater. 416 (2016) 269–274. doi:http://dx.doi.org/10.1016/j.jmmm.2016.05.023.

[3] A. Lak, J. Dieckhoff, F. Ludwig, J.M. Scholtyssek, O. Goldmann, H. Lünsdorf, D. Eberbeck, A. Kornowski, M. Kraken, F.J. Litterst, K. Fiege, P. Mischnick, M. Schilling, Highly stable monodisperse PEGylated iron oxide nanoparticle aqueous suspensions: A nontoxic tracer for homogeneous magnetic bioassays, Nanoscale. 5 (2013) 11447–11455. doi:10.1039/c3nr02197a.

[4] D. Zhang, J. Luo, J. Wang, X. Xiao, Y. Liu, W. Qi, D.S. Su, W. Chu, Ru/FeOx catalyst performance design: Highly dispersed Ru species for selective carbon dioxide hydrogenation, Chinese J. Catal. 39 (2018) 157–166. doi:10.1016/S1872-2067(17)62967-X.

[5] S. Brosda, C.G. Vayenas, J. Wei, Rules of chemical promotion, Appl. Catal. B Environ. 68 (2006) 109–124. doi:10.1016/j.apcatb.2006.07.021.

[6] D. Theleritis, S. Souentie, A. Katsaounis, C.G. Vayenas, Hydrogenation of CO2 over Ru electropromoted catalysts, ACS Catal. 2 (2012) 770–780. doi:dx.doi.org/10.1021/cs300072a.

[7] S. Kattel, P. Liu, J.G. Chen, Tuning Selectivity of CO2 Hydrogenation Reactions at the Metal/Oxide Interface, J. Am. Chem. Soc. 139 (2017) 9739–9754. doi:10.1021/jacs.7b05362.

[8] D. Theleritis, S. Souentie, A. Siokou, A. Katsaounis, C.G. Vayenas, Hydrogenation of CO2 over Ru/YSZ electropromoted catalysts, ACS Catal. 2 (2012) 770–780. doi:10.1021/cs300072a.

Appendix E - Supplementary Information for Chapter 7

Figure E-1 and Figure E-2 display the Ru/FeO_x transients from the current study compared with FeO_x from Chapter 6. Figure E1 (a) and (b) compares Ru/FeO_x with FeO_x at CO_2:H_2 = 1:1 at 350 °C. Figure E-2 (a) and (b) compares Ru/FeO_x with FeO_x at CO_2:H_2 = 1:1 at 400 °C. The open-circuit activity for Ru/FeO_x is greater than FeO_x, however under polarization FeO_x outperforms Ru/FeO_x. Both catalysts display similar behaviour with a slight initial CO increase and persistent-EPOC effect after current interruption. For negative polarization (Figure E-2 (b)), again FeO_x outperforms Ru/FeO_x during polarization, with the addition of p-EPOC for Ru/FeO_x. Figure E-2 (c) and (d) compares Ru/FeO_x (CO_2:H_2 = 1:7) with FeO_x (CO_2:H_2 = 1:1). As expected with an increase in reducing conditions, the open-circuit and promoted catalytic activity for Ru/FeO_x was greater than FeO_x. As mentioned in the main text, the initial CO increase is absent for Ru/FeO_x and p-EPOC after negative interruption.

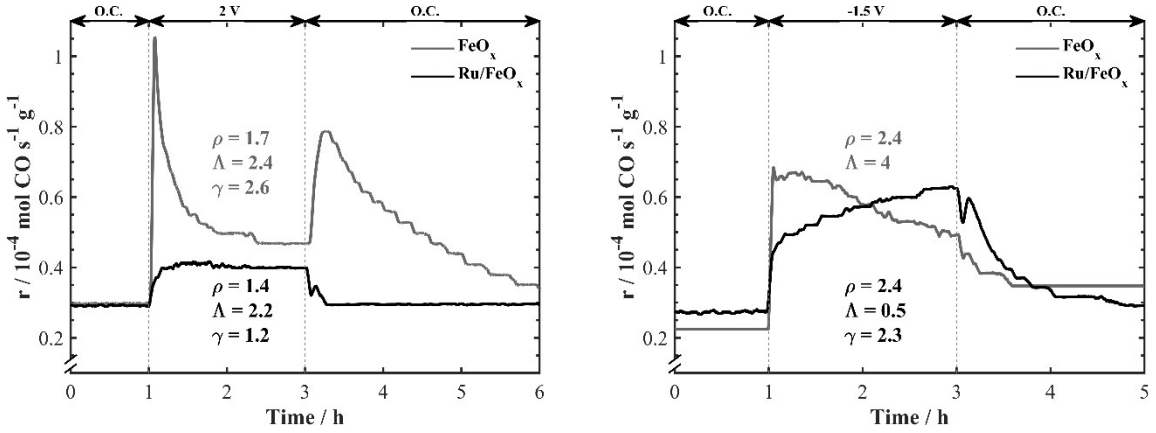

Figure E-1. Transient response 350°C and CO_2:H_2 = 1:1.

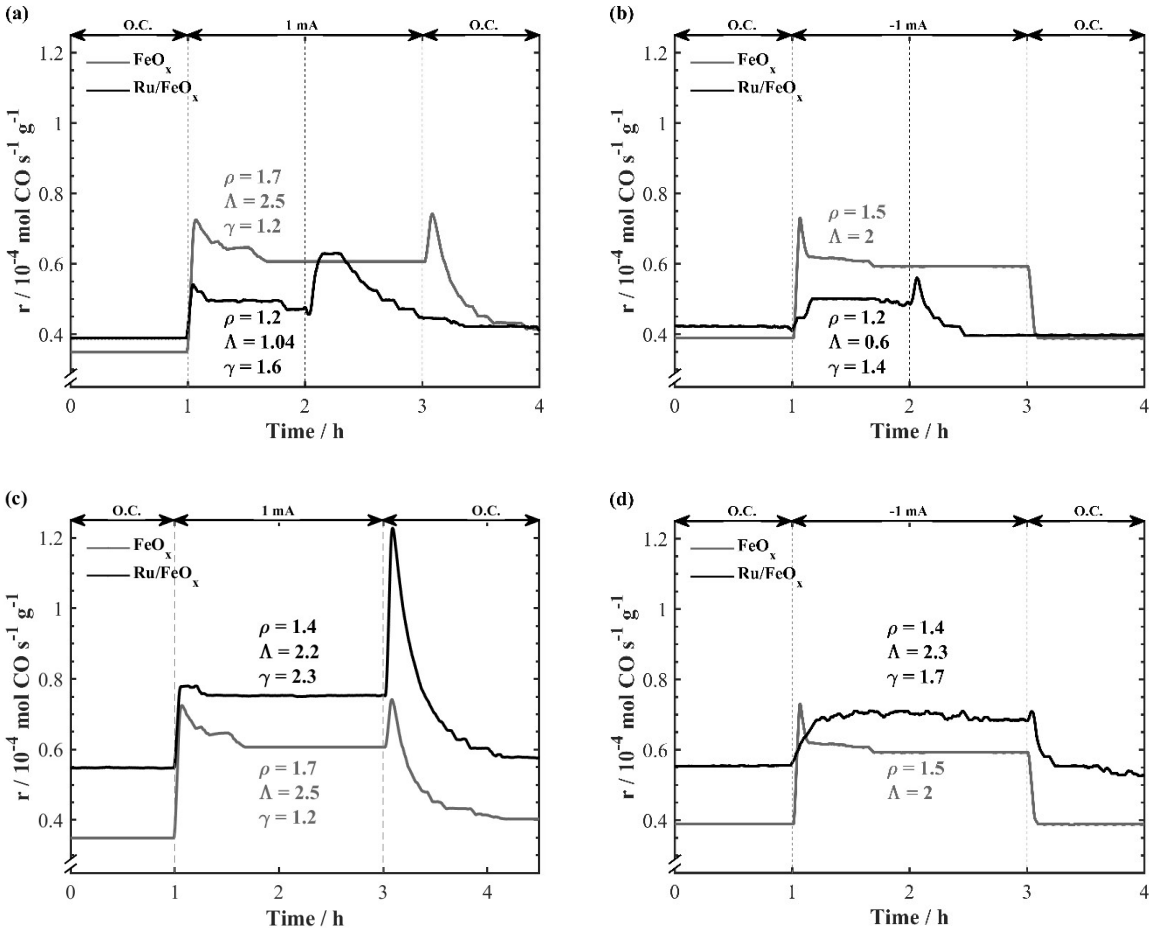

Figure E-2. Transient response 400 °C and (a) and (b) CO_2:H_2 = 1:1 and (c) and (d) CO_2:H_2 = 1:7.

Figure E3 summarizes the ρ_{max} values presented in this study and Chapter 6, which are affiliated to the indication of Fe-carbide (Fe_xC) formation during open-circuit conditions. Figure E3 shows that Fe_xC forms at 335, 350 and 400 °C for FeO_x, and only at 400 °C for Ru/FeO_x. The CO rate increase for FeO_x at 335, 350 and 400°C required 42 min, 48 min and 39 min respectively, to reach steady-state. For Ru/FeO_x the initial CO rate required 9 min to reach steady-state. The longer the initial CO increase the greater the formation of carbon formed under catalytic open-circuit conditions that is oxidized into CO_2 and CO before reaching the FeO_x active state.

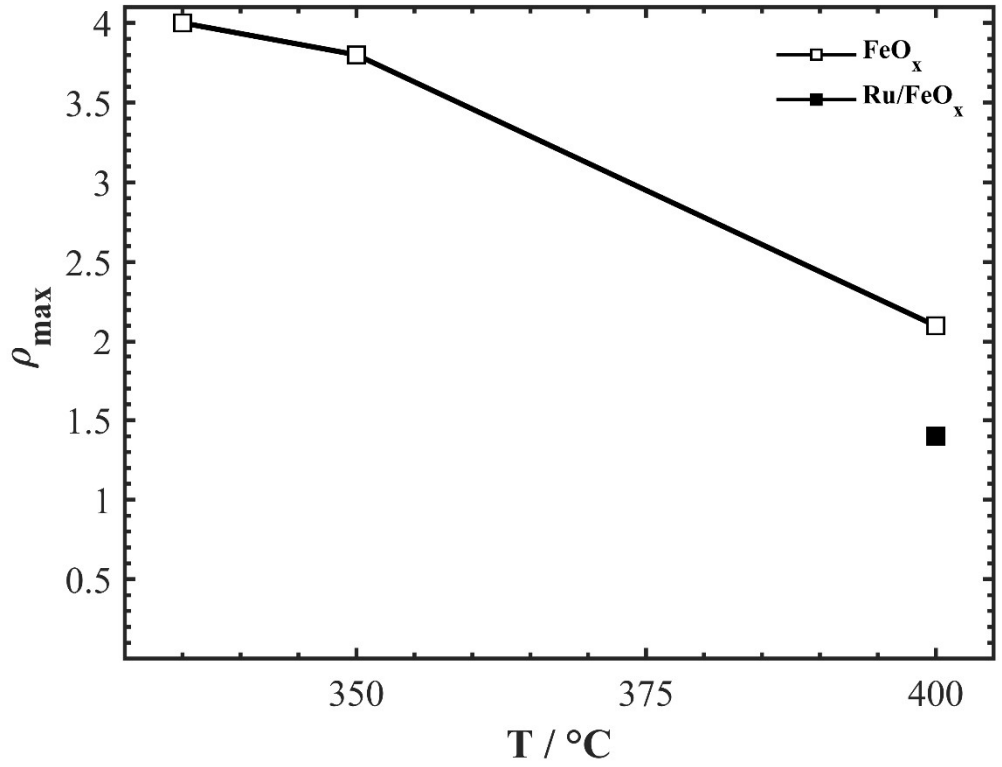

Figure E3. Summary of the maximum enhancement ratios (ρ_{max}) during polarization for FeO_x and Ru/FeO_x.

Chapter 8 : Electrochemical Investigation of the Metal-Support Interaction in FeO_x/CoO_x for the Reverse Water Gas Shift Reaction

***C. Panaritis**, S. Yan, M. Couillard, E. A. Baranova. In preparation for submission.*

Abstract

The transformation of CO_2 into CO is a crucial step in the manufacturing of carbon-neutral products. Herein, FeO_x nanowires prepared by the polyol synthesis method supported on Co_3O_4 semiconductor are investigated for the reverse water gas shift from 200-400 °C under atmospheric conditions. Enhancement of FeO_x/CoO_x (5 wt.%) was attained through the metal-support interaction effect. STEM images display an interface between both transition metals, forming an oxide bridge. The FeO_x/CoO_x (5 wt.%) composite displayed high catalytic activity with high selectivity to CO (>99%), 1.4-fold increase over Co_3O_4 and 20-times improvement over FeO_x/Al_2O_3. Under anodic and cathodic polarization, the catalytic activity decreased due to the disruption of the active state of the catalyst, confirming that the catalyst is already in a promoted state. The deposition of the FeO_x/CoO_x follows a feasible method that can adhere to a rough surface as a thin film and suitable for industrialized processes.

8.1 Introduction

Doping Fe with Co has shown to enhance RWGS catalytic activity due to the improvement in catalyst reducibility, the formation of a mixed-oxide synergetic relationship and the facilitation of electron hopping between both metals [1]. Under reaction conditions H_2 partially reduces the oxide state forming an oxygen vacancy allowing CO_2 to adsorb and dissociate into CO, and repeating the process all over again.

In this study, FeO_x nanowires from Chapter 6 are deposited on Co_3O_4 in a packed-bed reactor and deposited on the YSZ electrolyte for the RWGS reaction to investigate its metal-support interaction effect. The structure of FeO_x/CoO_x was investigated through physicochemical characterizations and was examined from 200-400°C under CO_2:H_2 ratios of stoichiometric (1:1), reducing (1:7) and oxidizing (3:1) conditions. FeO_x/CoO_x was compared alongside FeO_x/Al_2O_3 to

display the advantage Co_3O_4 has on enhancing the catalytic rate. The EPOC effect is used as a tool to interpret the enhancement performance of FeO_x on CoO_x.

8.2 Experimental

8.2.1 *Synthesis of FeO_x/CoO_x*

The FeO_x nanowires were prepared through the polyol synthesis method following the same procedure described Chapter 6.2.1. The FeO_x were deposited on commercially purchased Co_3O_4 (Sigma - Aldrich, Cobalt (II,III) oxide nanopowder, <50 nm particle size (TEM), 99.5% trace metals basis and specific surface area (SSA) = 40-70 m^2/g) through the wet deposition method. FeO_x colloidal solution was mixed vigorously with Co_3O_4 in deionized water for 48 h, to ensure adequate dispersion. The final loading of FeO_x was 5 wt.% on Co_3O_4, and is herein referred to as FeO_x/CoO_x (5 wt.%). Additionally, FeO_x was deposited through the same procedure on Al_2O_3 (40-50 nm particle size and SSA = 32-40 m^2/g).

8.2.2 *Characterization of FeO_x nanowires on Co_3O_4*

The morphology and size of the as-prepared and used FeO_x/CoO_x catalyst was performed through scanning transmission electron microscopy (STEM). The presence and distribution of the Fe and Co were confirmed through energy-dispersive X-ray spectroscopy (EDX) and energy electron loss spectroscopy (EELS). STEM, EDX and EELS analysis were conducted following the same procedure described in Chapter 4.2.2.

8.2.3 *Reaction Experiment*

Reaction experiments took place in a fixed-bed reactor (4 mm inner diameter) and an electrochemical cell, as described in Chapter 3.2.4 and 4.2.3, respectively. Each catalyst loading was 30 mg. The total flow rate of the reactor was 100 mL/min consisting of CO_2 (Linde, 99.99%), H_2 (Linde, 100 %) and Ar (Linde, 100 %), the flow rates were adjusted for each condition, where Ar was used as the balance. CO_2 varied from 1.5-4.5 KPa, H_2 from 1.5-10.5 KPa and Ar from 88-97 KPa to measure RWGS stoichiometric conditions (CO_2:H_2 = 1:1), reducing conditions (CO_2:H_2 = 1:7) and oxidizing conditions (CO_2:H_2 = 3:1). The catalysts were pretreated under oxygen for 1 h followed by H_2 for 12 h at 350°C. Temperature was held at each reported temperature for about 30 minutes to reach a steady-state and the reported results demonstrate the final temperature cycle when a steady-state was achieved. The product gases were measured using a quadrupole mass

spectrometer (QMS, Ametek Proline DM 100) to measure output CO_2, H_2, CO, CH_4, H_2O, and Ar [2].

8.2.4 *Electrochemical Cell*

YSZ solid electrolyte was prepared and used the same way as described in Chapter 4.2.3. Directly opposing the counter electrode on the opposite side FeO_x/CoO_x was deposited in an area of 1 cm^2. The FeO_x/CoO_x powder was diluted in isopropanol and was deposited via micropipette where it was dried at 100 °C for 1 min between deposits. The final mass loading of FeO_x/CoO_x and Co_3O_4 were 0.75, 1.5 and 3 mg. A gold mesh was mechanically pressed onto the FeO_x/CoO_x film to ensure electron conductivity. Three gold wires were connected to each electrode respectively connected to the potentiostat-galvanostat (Arbin Instruments, MSTAT) in order to undertake the electrochemical tests. The enhancement ratio (ρ), apparent Faradaic efficiency (Λ) and permanent-EPOC (γ) abide to eq. 1-10, 1-11 and 1-12, respectively.

8.3 Results & Discussion

8.3.1 *Physicochemical Characterization*

Displayed in Figure 8-1 are the STEM images of FeO_x deposited as FeO_x on Co_3O_4, with a lattice spacing of 5Å (0.5 nm) and 2Å (0.2nm), corresponding to α-Fe_2O_3 (0112) and Co_3O_4 (400) [3–5]. FeO_x has a greater oxidation state than CoO_x, suggesting that Co_3O_4 oxidizes the FeO_x into α-Fe_2O_3. Due to the reducing conditions of the reaction, the fully oxidized state of the catalyst will change and is further referred to as FeO_x. Energy dispersive X-ray mapping (EDX) in Figure F-1 from Appendix F displays the presence of Fe and Co, with no other impurities. Energy electron loss spectroscopy (EELS) in Figure F-2 confirms the presence of Fe, Co and O, with a seemingly fine distribution layer of Fe over the Co spinel structure. The spent catalyst after reaction and polarization is displayed in the TEM image in Figure 8-1 (c) with an average particle size of 40-80 nm (histogram Figure F-3), represented by the dark spots. The transparent section of the TEM image represents carbon in the form of graphene and in some sections as carbon nanotubes (CNT). The EELS mapping in Figure 8-1 (e) and (f), corresponds to the orange box in the STEM image in Figure 8-1 (d). The top left image in Figure 8-1 (f) represents the C portion and again in blue in Figure 8-1 (f). The Fe, Co and O composition overlap without further mixing with the C portion, suggesting that the catalyst was able to manufacture CNT (Ø = 20 - 50 nm) with a lattice spacing of 0.375 nm corresponding to the (0002) plane of graphitic carbon [6–8]. The Fe, Co, and O

composition remained similar to the as-prepared sample (Figure F-2). A recent study by Espinos *et al.* [9], employed the EPOC effect to decompose CH_3OH into CNTs on the surface of Ni catalyst using the K-Al_2O_3 solid electrolyte. Through negative polarization the addition of K^+ on the surface of Ni allowed CH_3OH to break down and form graphene. While the formation of carbon structures is interesting, it is not the purpose of this study and will be further explored in the future.

SEM images of the fresh and used samples are shown in Figure F-4 (a) and (b), respectively. FeO_x/CoO_x displays a porous structure. The used catalyst (Figure F-4 (b)) displays the formation of larger clusters that remained porous suggesting that the reaction temperatures did not sinter the catalyst, nor contribute to agglomeration, signifying that the loading of FeO_x remained in the nano range during and after reaction. To distinguish the presence of FeO_x, SEM images of fresh and used CoO_x are displayed in Figure F-4 (c) and (d). Similar structure is observed for the fresh and used sample, signifying that FeO_x does not affect the overall porosity of the structure.

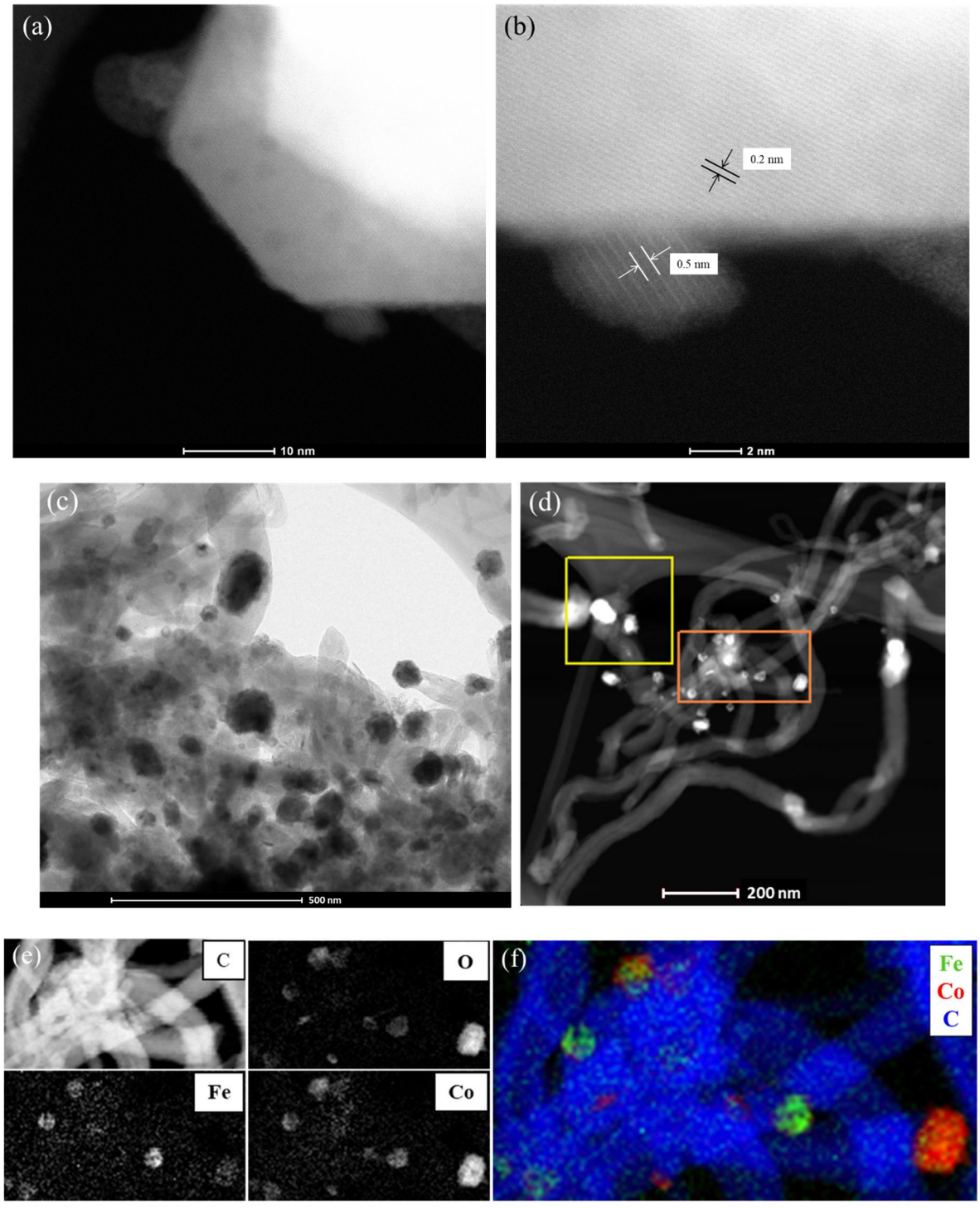

Figure 8-1. STEM image of the (a) and (b) as-prepared, and (c) TEM and (d) STEM image of spent FeO_x/CoO_x with corresponding elemental composition (e) and (f).

8.3.2 *FeO_x/CoO_x RWGS catalytic performance*

The catalytic activity for FeO_x/CoO_x (5 wt.%) was compared against Co_3O_4 and FeO_x/Al_2O_3 (5 wt.%) in the packed-bed reactor at 200-400 °C for a CO_2:H_2 ratio of 1:1, 1:7, and 3:1, associated with Figure 8-2 (a), (b) and (c) respectively. Al_2O_3 on its own was not active in the evaluated temperature range and was only active above 550 °C (not shown here). FeO_x/Al_2O_3 (5 wt.%) was selected as the inert support to be compared to the FeO_x/CoO_x catalytic activity. Co_3O_4 and Al_2O_3 share a similar specific surface area of 40-70 m^2/g and 32-40 m^2/g, respectively, that will shed light on the MSI effect between FeO_x and Co_3O_4.

Figure 8-2 (a) displays the stoichiometric conditions, FeO_x/CoO_x and Co_3O_4 convert CO_2 at ~5.5% and ~6.5%, respectively, which outperform FeO_x/Al_2O_3 at ~0.3% at 400 °C. Co_3O_4 is also an active catalyst for the RWGS reaction, it slightly outperforms FeO_x/CoO_x under 1:1 affiliated to its size (40-50 nm) active sites exposure [1,10]. FeO_x supported on Al_2O_3 displayed minimal CO_2 conversion, suggesting that the structural promotion does not enhance the catalytic properties of FeO_x as opposed to Co_3O_4. Under reducing conditions (Figure 8-2 (b)), at 400°C FeO_x/CoO_x converts CO_2 at ~18%, while Co_3O_4 converts CO_2 at ~12%. The rich H_2 atmosphere favours the reducibility of the catalyst ensuring oxygen vacancies are generated and take part as CO_2 activation sites. FeO_x supported on Co_3O_4 further improves the CO_2 activation process, due to its favourability to CO_2 [11,12]. Figure 8-2 (c) displays oxidizing conditions (CO_2:H_2 = 3:1), where FeO_x/CoO_x, Co_3O_4, and FeO_x/Al_2O_3 activate CO_2 with a conversion of ~15, ~11, and ~0.5 %, respectively, at 400 °C. FeO_x/CoO_x outperforms Co_3O_4 reaching the equilibrium conversion of ~15%. H_2 reduces the catalyst and generates oxygen vacancies by forming H_2O, while FeO_x affinity to activate CO_2 is enhanced. In oxidizing and reducing conditions, the catalytic activity of FeO_x/Al_2O_3 is non-existent. The inactivity of Al_2O_3 is due to its non-reducibility as shown by Bobadilla *et al*., when compared with reducible support TiO_2 which has shown its ability to cycle oxygen [13].

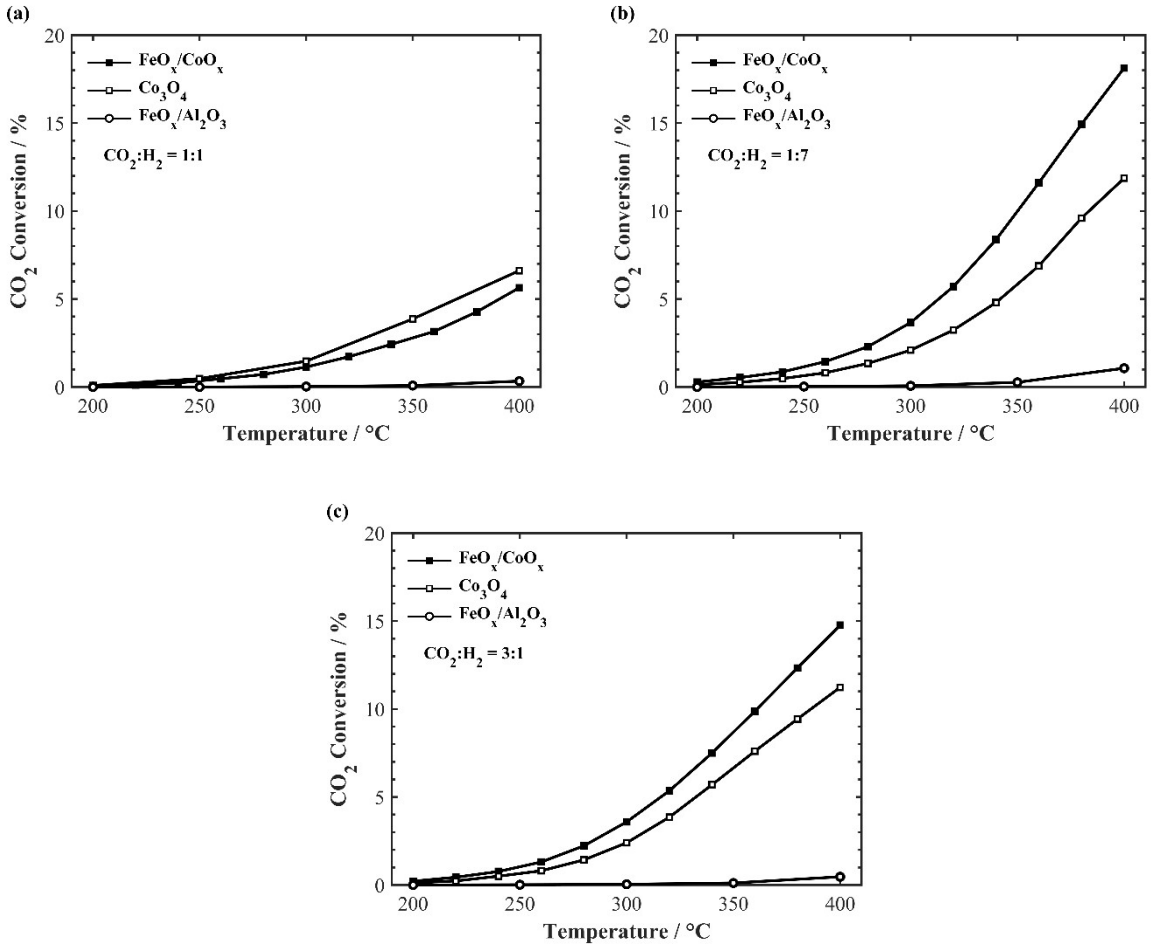

Figure 8-2. Catalytic activity for FeO_x/CoO_x, Co_3O_4 and FeO_x/Al_2O_3 in the packed-bed reactor for a CO_2:H_2 ratio of (a) 1:1, (b) 1:7 and (c) 3:1. 30 mg of catalyst and 100 mL min^{-1}.

The enhanced catalytic activity attributed to FeO_x/CoO_x is due to the MSI at the metal-oxides interface between FeO_x and CoO_x. The MSI effect promotes the catalytic activity for metals at the nanoscale, where oxygen ions from CoO_x are able to backspillover on FeO_x and spillover from FeO_x onto Co_3O_4. The FeO_x-CoO_x interface is displayed in Figure 8-1 (a) and (b), acting more than a structural support and forming a strong-metal support interaction connecting both metals. After the reaction the presence of FeO_x on CoO_x remains intact (EELS Figure F1 (e)-(f)) with a slight increase in the average particles size from 40 nm to 60 nm (Figure F-3). Similar conclusions have been drawn by Zhou *et al.*, where a synergistic effect between the two oxides has been proposed where CuO_x/CeO_x work together to alter each other's oxidation state by creating electron deficient states [14]. Lin *et al.*, show that FeO_x/CeO_2 forms a strong oxide interaction (Fe-O-Ce) which allows Fe to remain in a partially oxidized state to dissociate CO_2 [15].

The Fe_3O_4 state has been demonstrated through density function theory (DFT) calculations to be the CO_2 activation step for FeO_x [12]. Mono-metallic FeO_x, where above 335 °C a reduced state of FeO_x that formed under reaction conditions, rendered it less active for the RWGS reaction (Chapter 6). Temperature programmed reduction (TPR) characterizations conducted by various groups for FeO_x and CoO_x, demonstrate that the metal-oxide state in dominate under 450 °C, explaining the increased catalytic activity from 250-400 °C [16–18]. Co has been shown to fully reduced at 460 °C, this has been observed in the current study when the temperature was brought up to 450 °C and the catalytic activity drastically decreased (not shown here), confirming that a reduced state does not favour the RWGS reaction [19]. Due to the greater amount of CoO_x over FeO_x the oxidation state of the composite is dependent on CoO_x remaining active up to 400 °C before transitioning to a reduced state [1]. The CoO state was confirmed in Chapter 5 with X-ray Diffraction (XRD) analysis for Ru/Co_3O_4 after CO_2 hydrogenation conditions at 450 ºC.

8.3.3 *Effect of Polarization*

The effect of polarization on FeO_x/CoO_x was evaluated for the catalyst film loadings of 1.5 mg and 0.75 mg under stochiometric, oxidizing and reducing conditions at 350 and 400°C, for anodic and cathodic polarization (Figure 8-3). Operating at 350°C and above, Co_3O_4 is conductive, allowing it to close the electric circuit and direct the movement of $O^{\delta-}$ to and away from FeO_x. Co_3O_4 disperses on YSZ, allowing it adhere to the surface and form a dispersed film exposing FeO_x nanoparticles. A catalytic loading of 3 mg did not produce an electrochemical response, nor did Co_3O_4 on its own, signifying that the presence of dispersed FeO_x was responsible for the change in catalytic activity under polarization.

Initially, the open-circuit catalytic activity for FeO_x/CoO_x and Co_3O_4 deposited on YSZ as a thin film (0.75 mg/cm^2) are summarized in Figure F-5 (a)-(c). Similar catalytic behaviour is observed as in Figure 8-3, where FeO_x/CoO_x outperforms Co_3O_4 by 25-30%. A loading of 0.75 mg of FeO_x/CoO_x improved its catalytic rate by ~3-3.5-fold over 1.5 mg due to the greater dispersion and exposure of active sites. Furthermore, the catalytic activity of FeO_x/CoO_x surpassed FeO_x on its own on YSZ by 2000% (normalized to the amount of FeO_x), as shown in Chapter 6.

Figure 8-3 displays the electrochemical transients for a FeO_x/CoO_x loading of 1.5 mg at 350 and 400 °C for a potential difference of 2V and -2V under stoichiometric, reducing and oxidizing reaction conditions. In Figure 8-3 (a) at 350°C and 2V, the CO rate decreased in all

conditions by an average of 10% (*i.e.* $\rho \approx 0.9$) after 2h, which return to initial open-circuit (O.C.) values after potential interruption. For the application of -2V (Figure 8-3 (b)), the removal of $O^{\delta-}$ from FeO_x results in the CO rate to decrease by an average of 11% that does not return to O.C. value. The new O.C. value suggests a persistent-EPOC (p-EPOC) effect equal to $\gamma \approx 0.88$, due to the reduction of FeO_x inhibiting the RWGS reaction. The CO rate under stochiometric and reducing conditions behave similarly, signifying that the reaction is zero order in H_2, which can be affiliated to reduced FeO_x as opposed to a higher oxidation state under oxidizing conditions.

Figure 8-3 (c) shows a decrease in catalytic activity for 2V at 400°C, where the CO rate was suppressed for stoichiometric (ρ=0.86) and oxidizing (ρ=0.9) conditions. Increase in temperature improved the reaction under reducing conditions and was minimally affected by polarization (ρ=0.94). For the application of -2V in Figure 8-3 (d), the stoichiometric RWGS and oxidizing conditions are minimally influenced by the removal of $O^{\delta-}$, displaying a slow permanent decrease in the CO rate which continues after potential interruption. However, under reducing conditions, the CO rate experiences a significant decrease of 15% that returns slightly to O.C. values. Thus, increasing the temperature to 400 °C favours reducing conditions along with negative polarization leads to a less active FeO_x state. Furthermore, theoretical studies performed by Wang *et al*., have shown the abundance of H on reduced iron surfaces leads to the inhibition of CO_2 adsorption, explaining the decrease in catalytic activity [20].

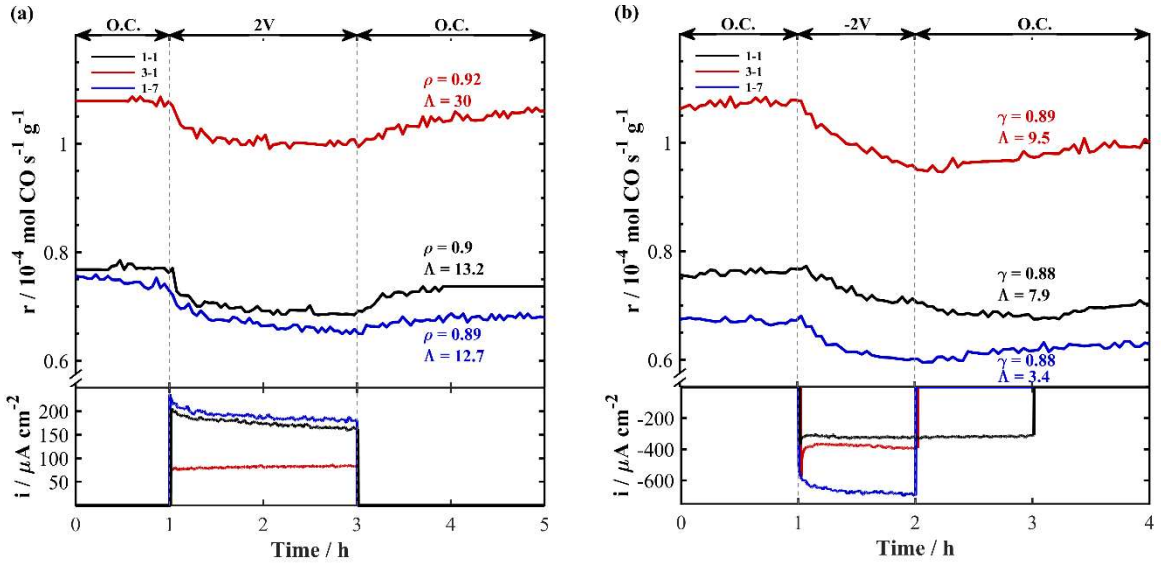

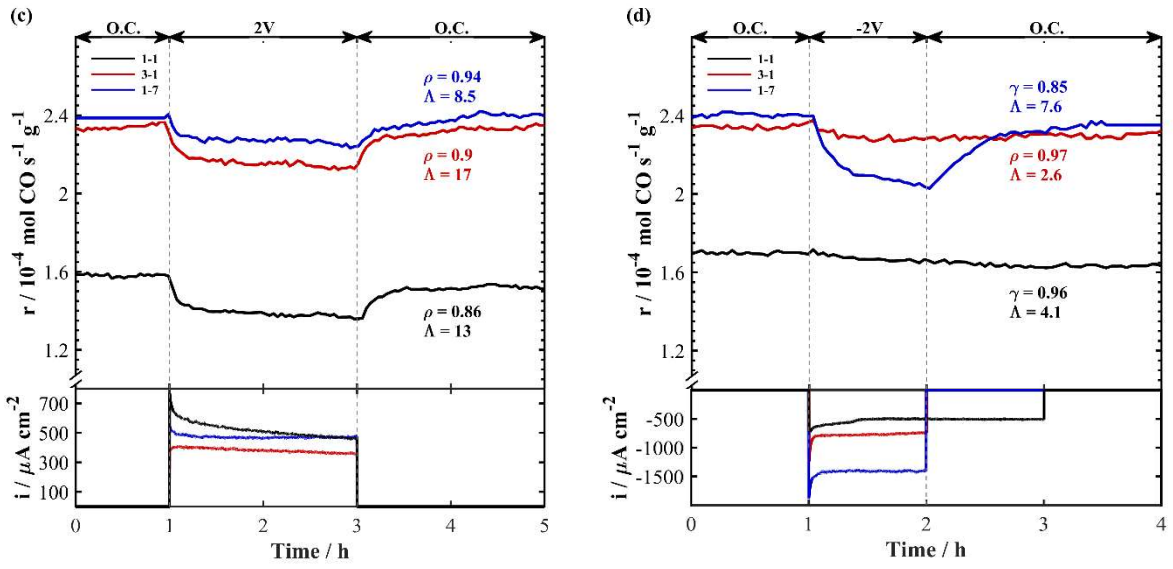

Figure 8-3. Transient response for FeO_x/Co_3O_4 (5 wt.%) for 1.5mg loading at (a) 2V and (b) -2V at 350 °C, and (c) 2V and (d) -2V at 400 °C.

Through the application of 2V, the catalytic activity experiences a suppression in the CO rate in all cases. All transients are Non-Faradaic due to $\rho \neq 1$ and $\Lambda > 1$, signifying that the change in CO rate is associated to the change in the catalytic activity and is not solely electrochemical [21]. All EPOC experiments follow volcanic behaviour, meaning that polarization causes the reactants CO_2 (electron acceptor) and H_2 (electron donor) to strongly adsorbed on the surface [22]. Increase in temperature could potentially lead to a promoted effect during polarization, as shown for mono-metallic FeO_x when above 335°C. Additionally, unlike FeO_x/YSZ, carbon was detected as graphene in the spent catalyst (Figure 8-1 (c)) that could have occurred under reaction conditions and could have been invoked through polarization, future studies will explore this new phenomenon. Nonetheless, the presence of graphene/CNTs did not hinder the catalytic activity, allowing the catalyst to convert CO_2 into CO, while simultaneously manufacturing carbon.

Given the various transients, the dispersion of the FeO_x/CoO_x can be estimated through the Galvanostatic Technique [23]. Using the equation (eq. 5-1), the number of moles of the catalyst that takes part in the reaction can be estimated. Calculating the galvanostatic transient gives an indication of the active surface area of the catalytic film in terms of the uptake of the moles of oxygen which take part in the reaction. Comparing the average uptake in moles of oxygen (N_G) shows that negative polarization results in a 6-fold improvement with 4.32×10^{-6} mol O over

$6.33x10^{-7}$ mol O for positive polarization. The N_G and τ are summarized in Table F-1. The greater active surface area for the negative polarization suggests removal of O^{2-} from FeO_x/CoO_x leads to a more exposed reduce catalyst surface but not necessarily more active (*i.e.* $\gamma < 1$), which is in line with previous studies showing metallic Fe and Co to be less active [24].

8.3.4 *Effect of Self-Sustained Electro-Promotion for non-noble metals*

Given the high catalytic activity exhibited by FeO_x/CoO_x when compared to Co_3O_4 and FeO_x/Al_2O_3, FeO_x/CoO_x is promoted due to the MSI between FeO_x and CoO_x, similar to MIEC and ionically conductive supports. Monometallic FeO_x supported on the mixed-ionically conductor samarium-doped ceria (SDC) from Chapter 3 and FeO_x/CeO_2 by Yin *et al.,*[24] displayed catalytic activity only occurred above 450 °C. Above 450 °C the backspillover of ionic species from the MIEC supports promote the reaction through the MSI effect. As opposed to the exchange of oxygen between FeO_x and CoO_x that occurs at lower temperatures and can be in-situ controlled at 350 °C.

Under polarization, the forceful addition and removal of O^{2-} to and from FeO_x/CoO_x results in the alteration in the catalyst composition shifting to more oxidized state during positive polarization and more reduced state for negative polarization, overall inhibiting the RWGS reaction. The addition of $O^{\delta-}$ leads to the disruption in the redox reaction, inhibiting the creation of oxygen vacancies. While the removal of $O^{\delta-}$, reduces the catalyst, resulting in a permanent suppression in the CO rate after current interruption. Given the decrease in CO rate suggests that FeO_x/CoO_x is able to achieve its own active state during open-circuit conditions that can be disrupted with the influence of electrical stimuli. Thus, given the suppression behaviour of FeO_x/CoO_x under the EPOC effect, the catalyst is in a self-sustained electro-promotion (SSEP) state.

The SSEP phenomenon is dependent on the difference in work function between the metal-oxides, causing oxygen to migrate between FeO_x and CoO_x through the sharing of electrons/oxides, altering the redox properties of the catalyst [25]. Thus, the spillover and backspillover of oxygen species occurs as the state changes with response to the redox reactions. The SSEP was initially observed with ionically conductive supports, now it is observed with the semiconductor Co_3O_4 which shares similar conductivity properties as a MIEC. When compared with the catalytic activity of MIEC on its own, Co_3O_4 activates CO_2 and H_2 favourably with a 5-

fold conversion over bare supports like CeO_2 and Sm-doped CeO_2 (Chapter 3). The added benefit is that Co_3O_4 is an active metal for the RWGS while allowing electronic conduction above 350 °C to promote FeO_x during the RWGS reaction.

The correlation between the work function and oxidation state has been reported by Greiner *et al.*, for metal films [26]. They demonstrate that the work function increases as a function of oxidation state, thus the higher oxidation state - the higher the work function. As the various oxidation states of $Fe_2O_3/Fe_3O_4/FeO/Fe$ and $Co_3O_4/CoO/Co$ alternate from one form to another, they work together in unison under reaction conditions to exchange oxygen species between them in a promoted state to favour the RWGS reaction.

To put in perspective the SSEP enhancement for FeO_x/CoO_x, Figure 8-4 compares the open and closed-circuit catalytic rates of previous EPOC experiments employing, Rh [27], Ru [21,28,29], Ru-Co [30], FeO_x, Ru/FeO_x and Co[31]. The highest catalytic rate was taken for each study at the given temperature as CO mol s^{-1} g^{-1} produced for a CO_2:H_2 ratio of 1:1 (Figure 8-4 (a)) and 1:7 (Figure 8-4 (b)). In both figures, the catalytic activity of FeO_x/CoO_x (represented by the circle marker) outperforms most previous studies. Ru nanoparticles (Chapter 5) deposited on BZY outperform FeO_x/CoO_x due to the BZY support: spontaneous H^+ migration and a rough surface leading to high dispersion. The improved catalytic activity for FeO_x/CoO_x is affiliated to the catalyst already being in a promoted state; dual catalyst functionality, high catalyst dispersion and metal-support electron/oxygen sharing.

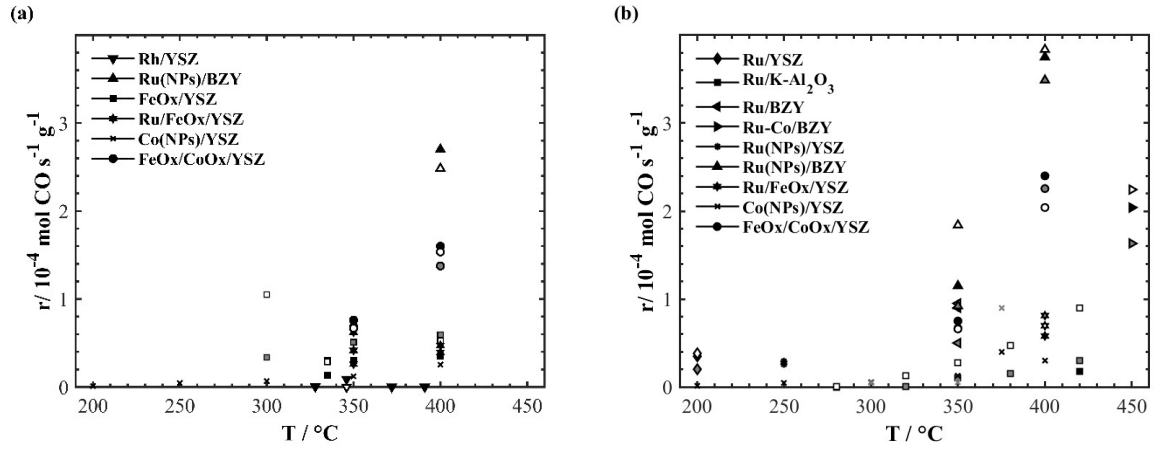

Figure 8-4. Comparative summary of past and current data for the RWGS for various catalyst: Rh/YSZ [27], Ru/YSZ[21], $Ru/K\text{-}Al_2O_3$ [28], Ru/BZY [29], Ru-Co/BZY[30], Ru(NPs)/YSZ

(Chapter 4), Ru(NPs)/BZY (Chapter 5), FeO_x/YSZ (Chapter 6), Ru/FeO_x/YSZ (Chapter 7), Co(NPs)/YSZ [31] and FeO_x/CoO_x/YSZ. Black filled markers represent OCP conditions, no fill represent positive polarization and gray represents negative polarization.

Overall, this is a promising application at the industrial level, due to inexpensive metals, high conversion at lower temperatures and high CO_2 concentration conversion. High CO_2 concentration sources with minimal H_2 can lead to the absence of H_2 gas and instead employ H^+ ions, from the protonic solid electrolyte yttria-doped barium zirconate (BZY). Furthermore, the semi-conductivity of Co_3O_4 acts as catalyst, high dispersion support, transfers electrons, alters the oxidation state and can manipulate the movement of electrons during polarization. This provides a great advantage in applying FeO_x/CoO_x on a larger scale, along with its feasibility in depositing as a semi-conductor film to various surfaces.

8.4 Conclusion

Our findings show that FeO_x nanowires combined with commercially available Co_3O_4 leads to the self-sustained electro-promotion effect for the RWGS reaction from 200-400 °C. STEM images displayed a contact between FeO_x and CoO_x facilitating oxygen exchange for a prmoted catalytic activity. Results display a superior CO_2 conversion for FeO_x/CoO_x (5 wt.%) over Co_3O_4 and FeO_x/Al_2O_3 (5 wt.%). The application of anodic and cathodic polarization led to the suppression of the CO rate, affiliated to the alteration in the FeO_x state from highly oxidized (anodic) or highly reduced (cathodic) conditions, suggesting a disruption in its active phase. This is the first time the SSEP has been observed for non-noble metals and the use of a metal-oxide/metal-oxide catalyst. This provides an approach to be applied to the industrial level to convert large concentrations of CO_2 while being highly active and economically feasible.

References

[1] S. Sengupta, A. Jha, P. Shende, R. Maskara, A.K. Das, Catalytic performance of Co and Ni doped Fe-based catalysts for the hydrogenation of CO2 to CO via reverse water-gas shift reaction, J. Environ. Chem. Eng. 7 (2019) 102911. doi:10.1016/j.jece.2019.102911.

[2] P. Perreault, E. Robert, G.S. Patience, Experimental Methods in Chemical Engineering: Mass Spectrometry—MS, Can. J. Chem. Eng. 97 (2019) 1036–1042. doi:10.1002/cjce.23466.

[3] L.W. Finger, R.M. Hazen, Crystal structure and isothermal compression of Fe2O3, Cr2O3, and V2O3 to 50 kbars, J. Appl. Phys. 51 (1980) 5362–5367. doi:10.1063/1.327451.

[4] F. Kraushofer, Z. Jakub, M. Bichler, J. Hulva, P. Drmota, M. Weinold, M. Schmid, M. Setvin, U. Diebold, P. Blaha, G.S. Parkinson, Atomic-Scale Structure of the Hematite α-Fe2O3(11-02) "r-Cut" Surface, J. Phys. Chem. C. 122 (2018) 1657–1669. doi:10.1021/acs.jpcc.7b10515.

[5] L. Wang, H. Liu, Y. Chen, S. Yang, Reverse water–gas shift reaction over co-precipitated Co–CeO2 catalysts: Effect of Co content on selectivity and carbon formation, Int. J. Hydrogen Energy. 42 (2017) 3682–3689. doi:10.1016/j.ijhydene.2016.07.048.

[6] C.H. Kiang, M. Endo, P.M. Ajayan, G. Dresselhaus, M.S. Dresselhaus, Size effects in carbon nanotubes, Phys. Rev. Lett. 81 (1998) 1869–1872. doi:10.1103/PhysRevLett.81.1869.

[7] B. Liu, H. Yao, R.A. Daniels, W. Song, H. Zheng, L. Jin, S.L. Suib, J. He, A facile synthesis of Fe3C@mesoporous carbon nitride nanospheres with superior electrocatalytic activity, Nanoscale. 8 (2016) 5441–5445. doi:10.1039/c6nr00604c.

[8] E. Zhang, J. Wang, B. Wang, X. Yu, H. Yang, B. Lu, Unzipped carbon nanotubes for aluminum battery, Energy Storage Mater. 23 (2019) 72–78. doi:10.1016/j.ensm.2019.05.030.

[9] J.P. Espinós, V.J. Rico, J. González-Cobos, J.R. Sánchez-Valencia, V. Pérez-Dieste, C. Escudero, A. De Lucas-Consuegra, A.R. González-Elipe, Graphene Formation Mechanism by the Electrochemical Promotion of a Ni Catalyst, ACS Catal. (2019) 11447–11454. doi:10.1021/acscatal.9b03820.

[10] Y. Shen, Z. Cao, Z. Xiao, An efficient support-free nanoporous Co catalyst for reverse water-gas shift reaction, Catalysts. 9 (2019) 423. doi:10.3390/catal9050423.

[11] X. Nie, L. Meng, H. Wang, Y. Chen, X. Guo, C. Song, DFT insight into the effect of potassium on the adsorption, activation and dissociation of CO2 over Fe-based catalysts, Phys. Chem. Chem. Phys. 20 (2018) 14694–14707. doi:10.1039/c8cp02218f.

[12] X. Liu, C. Cao, P. Tian, M. Zhu, Y. Zhang, J. Xu, Y. Tian, Y.F. Han, Resolving CO2 activation and hydrogenation pathways over iron carbides from DFT investigation, J. CO2 Util. 38 (2020) 10–15. doi:10.1016/j.jcou.2019.12.014.

[13] L.F. Bobadilla, J.L. Santos, S. Ivanova, J.A. Odriozola, A. Urakawa, Unravelling the Role of Oxygen Vacancies in the Mechanism of the Reverse Water-Gas Shift Reaction by Operando DRIFTS and Ultraviolet-Visible Spectroscopy, ACS Catal. 8 (2018) 7455–7467. doi:10.1021/acscatal.8b02121.

[14] G. Zhou, F. Xie, L. Deng, G. Zhang, H. Xie, Supported mesoporous Cu/CeO2-δ catalyst for CO2 reverse water–gas shift reaction to syngas, Int. J. Hydrogen Energy. 45 (2020) 11380–11393. doi:10.1016/j.ijhydene.2020.02.058.

[15] L. Lin, S. Yao, N. Rui, L. Han, F. Zhang, C.A. Gerlak, Z. Liu, J. Cen, L. Song, S.D. Senanayake, H.L. Xin, J.G. Chen, J.A. Rodriguez, Conversion of CO2 on a highly active and stable Cu/FeOX/CeO2 catalyst: Tuning catalytic performance by oxide-oxide interactions, Catal. Sci. Technol. 9 (2019) 3735–3742. doi:10.1039/c9cy00722a.

[16] J. Zieliński, I. Zglinicka, L. Znak, Z. Kaszkur, Reduction of Fe2O3 with hydrogen, Appl. Catal. A Gen. 381 (2010) 191–196. doi:10.1016/j.apcata.2010.04.003.

[17] C.W. Tang, C. Bin Wang, S.H. Chien, Characterization of cobalt oxides studied by FT-IR, Raman, TPR and TG-MS, Thermochim. Acta. 473 (2008) 68–73. doi:10.1016/j.tca.2008.04.015.

[18] M.K. Gnanamani, G. Jacobs, H.H. Hamdeh, W.D. Shafer, F. Liu, S.D. Hopps, G.A. Thomas, B.H. Davis, Hydrogenation of Carbon Dioxide over Co-Fe Bimetallic Catalysts, ACS Catal. 6 (2016) 913–927. doi:10.1021/acscatal.5b01346.

[19] C. Yang, S. Liu, Y. Wang, J. Song, G. Wang, S. Wang, Z.-J. Zhao, R. Mu, J. Gong, The Interplay between Structure and product selectivity of CO2 hydrogenation, Angew. Chemie Int. Ed. 131 (2019) 11364–11368. doi:https://doi.org/10.1002/anie.201904649.

[20] H. Wang, X. Nie, Y. Chen, X. Guo, C. Song, Facet effect on CO2 adsorption, dissociation and hydrogenation over Fe catalysts: Insight from DFT, J. CO2 Util. 26 (2018) 160–170. doi:10.1016/j.jcou.2018.05.003.

[21] D. Theleritis, S. Souentie, A. Katsaounis, C.G. Vayenas, Hydrogenation of CO2 over Ru electropromoted catalysts, ACS Catal. 2 (2012) 770–780. doi:dx.doi.org/10.1021/cs300072a.

[22] S. Brosda, C.G. Vayenas, J. Wei, Rules of chemical promotion, Appl. Catal. B Environ. 68 (2006) 109–124. doi:10.1016/j.apcatb.2006.07.021.

[23] C.G. Vayenas, S. Bebelis, C. Pliangos, S. Brosda, D. Tsiplakides, Electrochemical Activation of Catalysis, Springer US, 2001.

[24] G. Yin, X. Yuan, X. Du, W. Zhao, Q. Bi, F. Huang, Efficient Reduction of CO2 to CO Using Cobalt–Cobalt Oxide Core–Shell Catalysts, Chem. - A Eur. J. 24 (2018) 2157–2163. doi:10.1002/chem.201704596.

[25] R.J. Isaifan, E.A. Baranova, Effect of ionically conductive supports on the catalytic activity of platinum and ruthenium nanoparticles for ethylene complete oxidation, Catal. Today. 241 (2015) 107–113. doi:10.1016/j.cattod.2014.03.061.

[26] M.T. Greiner, L. Chai, M.G. Helander, W.M. Tang, Z.H. Lu, Transition metal oxide work functions: The influence of cation oxidation state and oxygen vacancies, Adv. Funct. Mater. 22 (2012) 4557–4568. doi:10.1002/adfm.201200615.

[27] S. Bebelis, H. Karasali, C.G. Vayenas, Electrochemical promotion of CO2 hydrogenation on Rh/YSZ electrodes, J. Appl. Electrochem. 38 (2008) 1127–1133. doi:10.1007/s10800-008-9574-7.

[28] M. Makri, A. Katsaounis, C.G. Vayenas, Electrochemical promotion of CO2 hydrogenation on Ru catalyst-electrodes supported on a K-β″-Al2O3 solid electrolyte, Electrochim. Acta. 179 (2015) 556–564. doi:10.1016/j.electacta.2015.03.144.

[29] I. Kalaitzidou, A. Katsaounis, T. Norby, C.G. Vayenas, Electrochemical promotion of the hydrogenation of CO2 on Ru deposited on a BZY proton conductor, J. Catal. 331 (2015) 98–109. doi:10.1016/j.jcat.2015.08.023.

[30] A. Kotsiras, I. Kalaitzidou, D. Grigoriou, A. Symillidis, M. Makri, A. Katsaounis, C.G. Vayenas, Electrochemical promotion of nanodispersed Ru-Co catalysts for the hydrogenation of CO 2, Appl. Catal. B Environ. 232 (2018) 60–68. doi:10.1016/j.apcatb.2018.03.031.

[31] D. Zagoraios, S. Tsatsos, S. Kennou, C.G. Vayenas, G. Kyriakou, A. Katsaounis, Tuning the RWGS Reaction via EPOC and In Situ Electro-oxidation of Cobalt Nanoparticles, ACS Catal. 10 (2020) 14916–14927. doi:10.1021/acscatal.0c04133.

Appendix F - Supplementary Information for Chapter 8

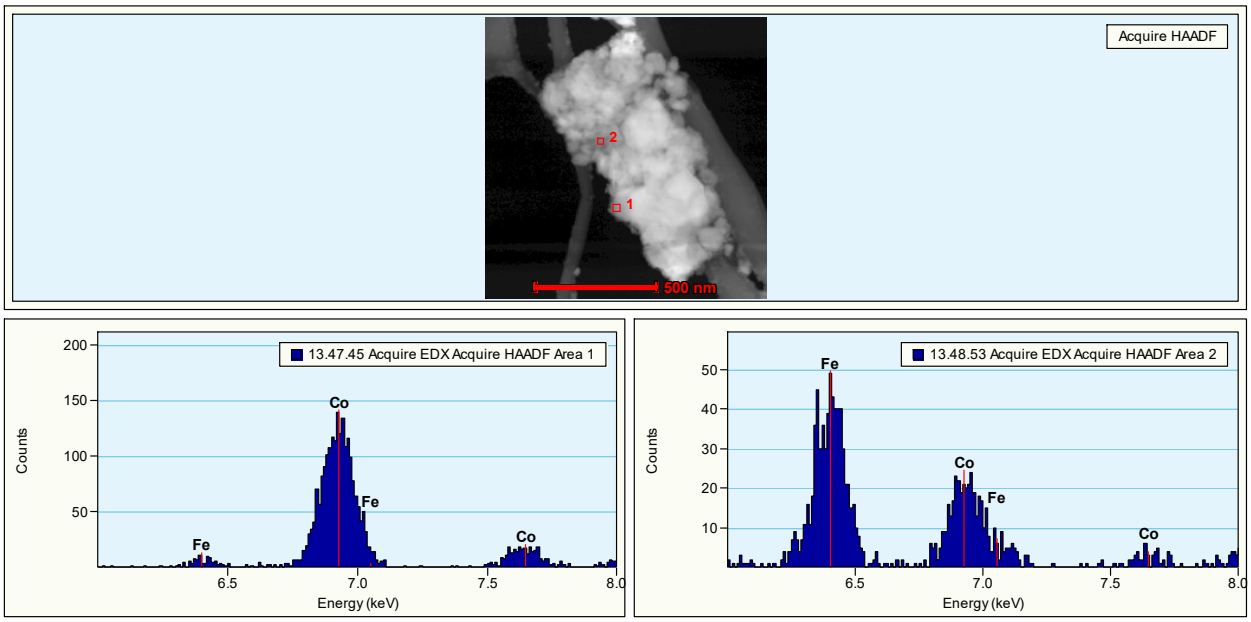

Figure F-1. Energy dispersive X-ray spectroscopy (EDX) of the fresh sample

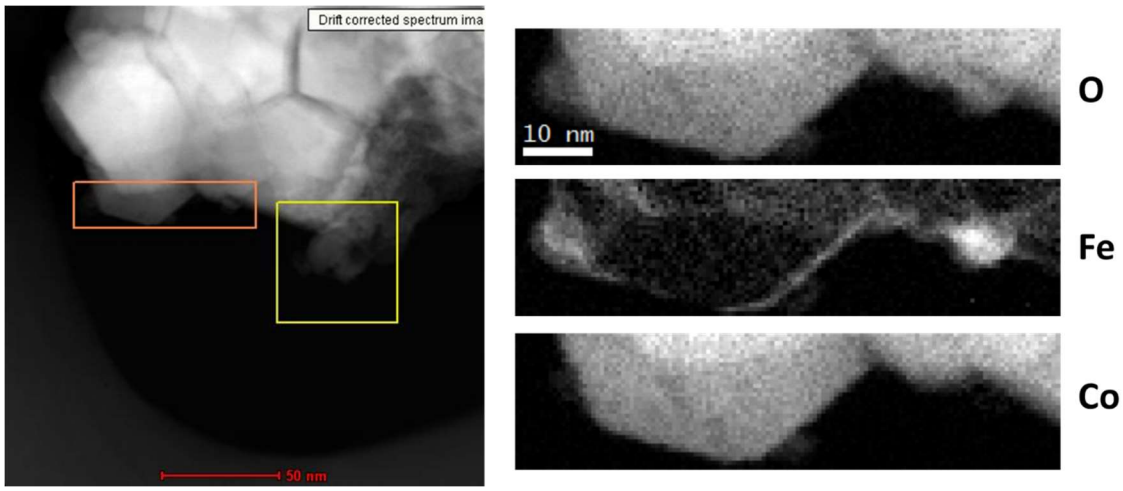

Figure F-2. Energy electron loss spectroscopy (EELS) of FeO_x/CoO_x (5 wt.%) before reaction.

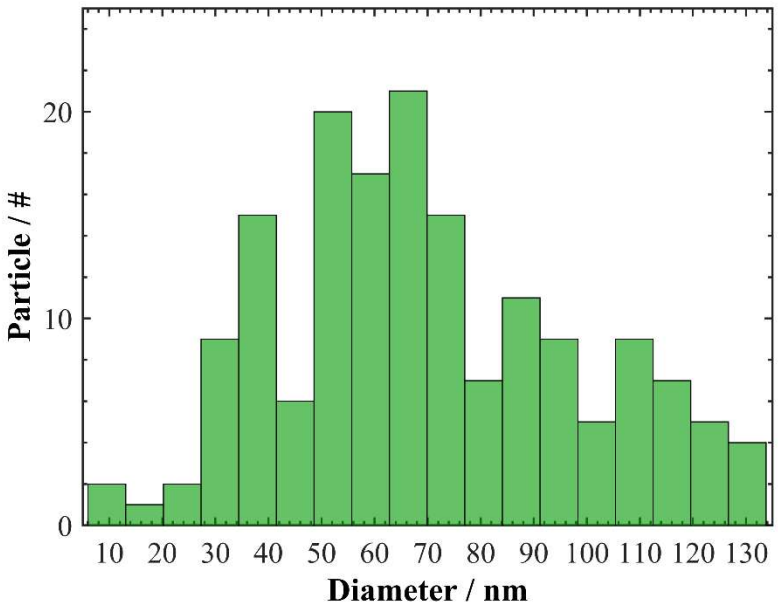

Figure F-3. Distribution of spent FeO_x/CoO_x (5 wt.%).

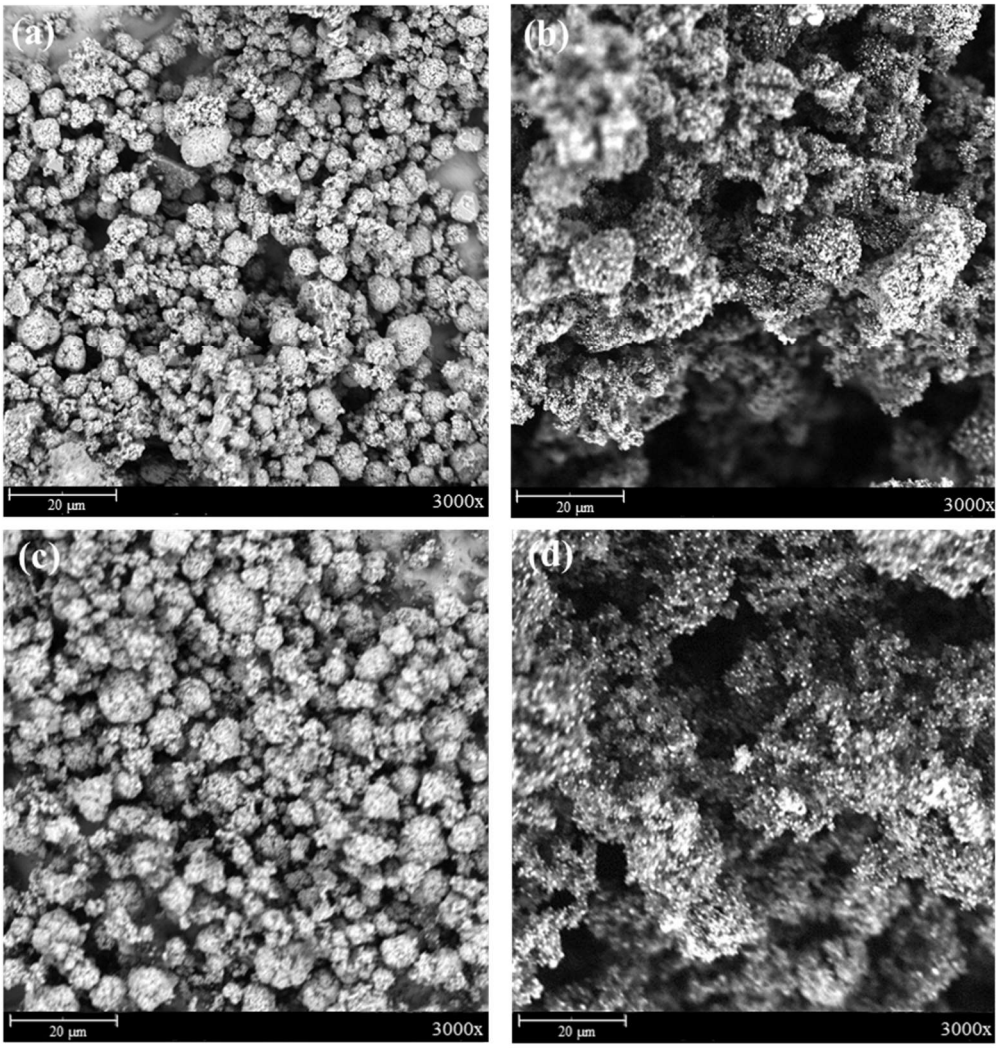

Figure F-4. SEM images of (a) fresh and (b) used FeO_x/CoO_x and (c) fresh and (d) used Co_3O_4.

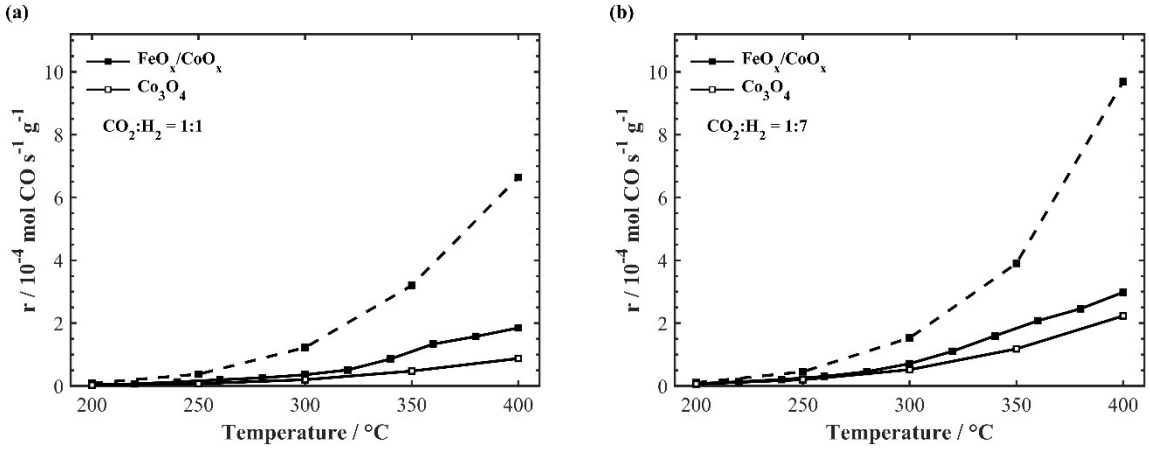

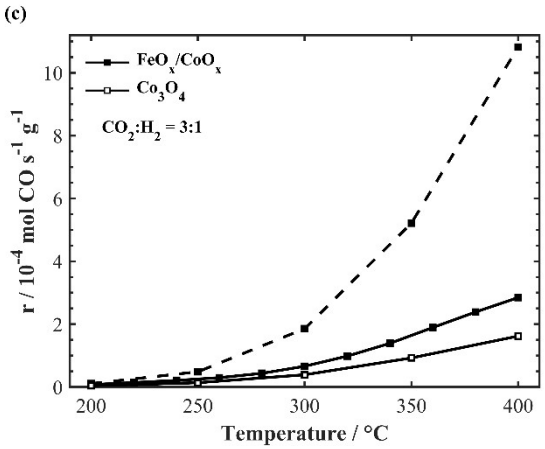

Figure F-5. Open-circuit catalytic activity in the EPOC (CSTR) reactor for FeO_x/CoO_x and Co_3O_4 for a loading of 3mg (solid line) and FeO_x/CoO_x loading of 0.75 mg (dashed line) for a CO_2:H_2 ratio of (a) 1:1, (b) 1:7 and (c) 3:1.

The EPOC response for a FeO_x/CoO_x film loading of 0.75 mg is displayed in Figure F6 (a) and (b) at 400 °C for 2V and -2V, respectively. The catalyst did not experience a response to potential at 350 °C possibility due to the high dispersion of the catalyst on YSZ which was not able to fully close the electrical circuit forming islands even with the addition of a gold mesh. Polarization of 2V at 400°C was less effective for oxidizing and reducing conditions with a ρ=0.98 for both, while for 1-1 the CO rate decreased by 7% and returned to O.C. values once potential was interrupted. For negative polarization (Figure F6 (b)), the CO rate followed similar behaviour as the catalyst loading of 1.5 mg, thus, following a decrease in CO rate and permanent-EPOC suppression after potential interruption with an average of γ = 0.95.

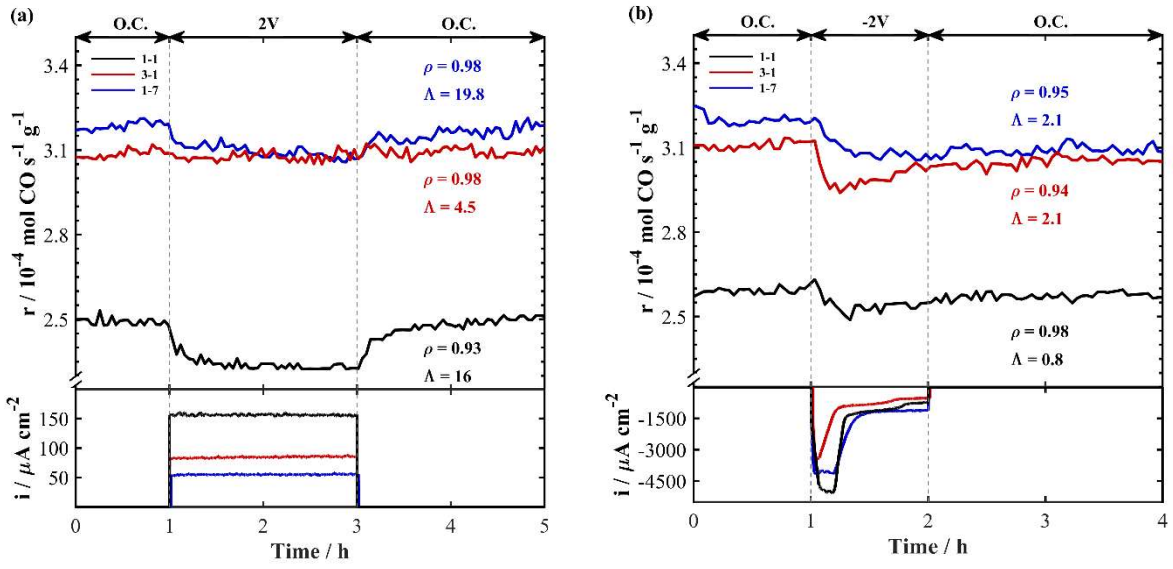

Figure F-6. Transient response for FeO_x/CoO_x (5 wt.%) for 0.75 mg loading for (a) 2V and (b) -2V application difference at 400 °C.

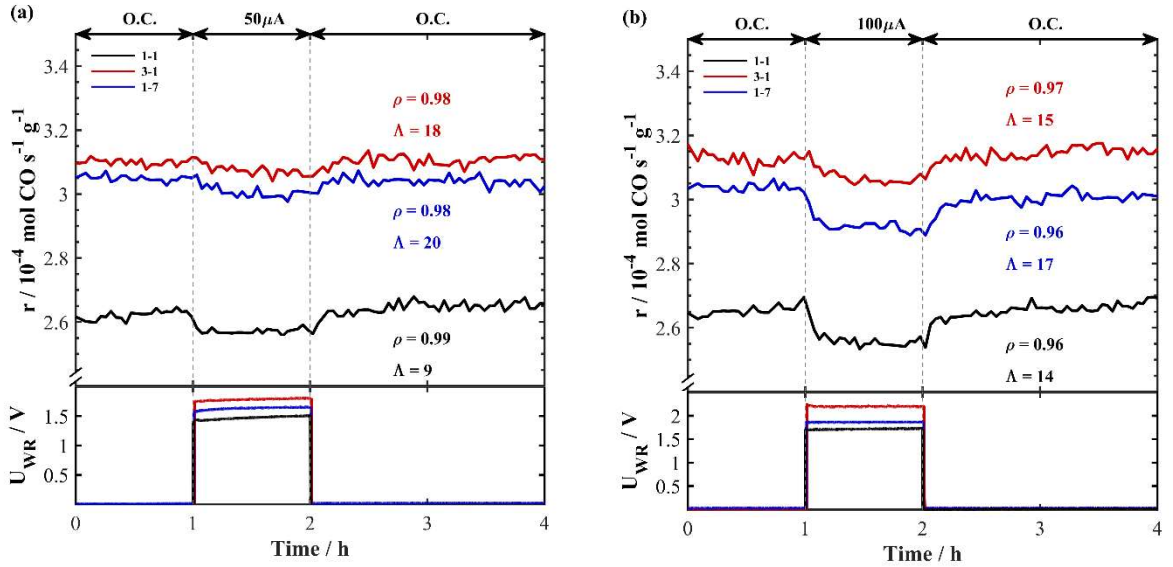

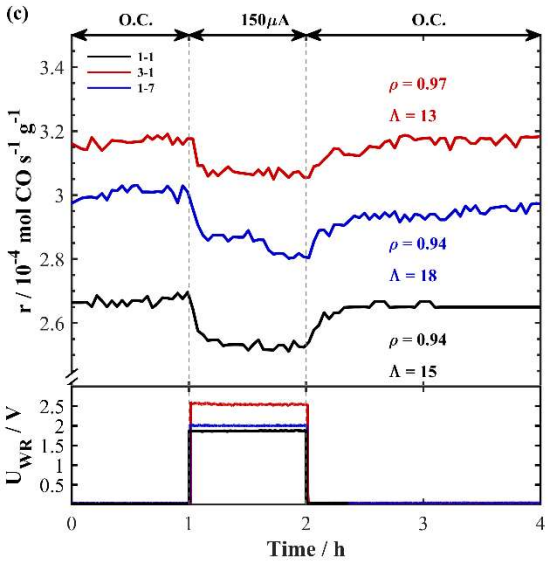

Figure F-7. Transient response to the effect of current (a) 50 μA, (b) 100 μA, and (c) 150 μA.

Table F-1. Summary of the galvanostatic transient

Figure	Temperature (°C)	Loading	Potential	CO_2:H_2 ratio	τ (s)	N_G (mol O)
3 (a)	350	1.5 mg	2V	1:1	396	$3.95x10^{-7}$
				1:7	900	$1.9x10^{-6}$
				3:1	1008	$4.1x10^{-7}$
3 (b)	350	1.5 mg	-2V	1:1	900	$9.13x10^{-7}$
				1:7	1368	$4.6x10^{-6}$
				3:1	1404	$2.7x10^{-6}$
3 (c)	400	1.5 mg	2V	1:1	324	$1x10^{-6}$
				1:7	180	$4.4x10^{-7}$
				3:1	432	$9.1x10^{-7}$
3 (d)	400	1.5 mg	-2V	1:1	2520	$6.5x10^{-6}$
				1:7	792	$5.8x10^{-6}$
				3:1	443	$1.8x10^{-6}$
4 (a)	400	0.75 mg	2V	1:1	468	$3.8x10^{-7}$
				1:7	324	$1.4x10^{-7}$
				3:1	324	$9.1x10^{-8}$
4 (b)	400	0.75 mg	-2V	1:1	360	$9.2x10^{-6}$
				1:7	828	$2.0x10^{-6}$
				3:1	324	$5.33x10^{-6}$

Chapter 9 : Conclusion and Recommendation

9.1 Conclusions & Contributions

Since beginning this study over 4 years ago, the field of CO_2 conversion has evolved exponentially. The future of research and development in recycling CO_2 is headed in the right direction, however there still remains a long way to go before overcoming the ongoing crisis. As climate disasters worsen in terms of change in weather patterns and the inability to grow certain foods, to name a few, the demand and need for fossil-fuel free alternatives will increase. Limiting fossil-fuel emissions is not a sustainable option as the global lockdown of the 2020 Covid-19 pandemic demonstrated, where even though the CO_2 emissions decreased for the year, one year does fix the damage done over the last 80 years. Thus, to ensure a sustainable future and rely on current infrastructures, the development of a carbon-neutral product to replace fossil-fuels and meet the regulations put in place during the 2015 Paris Climate Agreement is required. In the time of this writing the Covid-19 pandemic is still ongoing and I hope that once it is over, that renewable energy and clean technologies will be part of the new "normal" and replace the demand for fossil-fuels.

Building on the idea of a sustainable future, the goal of this thesis was to develop and evaluate nano-structured catalytic systems paired with the MSI and EPOC phenomena to enhance the RWGS reaction. Focusing on the RWGS reaction, the employment of nanoparticles and the electrochemical polarization allowed to increase the catalytic conversion and govern the selectivity of the reaction towards CO. Each chapter encompasses those approaches with the following conclusions:

- In Chapter 3, Ru_xFe_{100-x} bimetallic nanoparticles (1-2 nm) of various compositions (x=20, 45, 80) were synthesized through the polyol synthesis method and are deposited on mixed-ionic electronic conductive (CeO_2, SDC, etc.), ionically conductive (YSZ) and inactive supports (C). The metal-support interaction between RuFe nanoparticles and the oxygen-conductive supports have shown to enhance the catalytic rate due to the backpillover of O^{2-} ions from the support onto the catalyst. The addition of Fe improved stability and did not hinder the catalytic activity of Ru, allowing less precious noble metal to be used.

- In Chapter 4, free-standing Ru nanoparticles were deposited as the catalyst-working electrode on the ionically conductive solid electrolyte YSZ. Employing the EPOC phenomenon, an electrochemical response of nanoparticles is achieved for the first time towards the RWGS reaction. To provide insight on the effect polarization has on the Ru catalyst, DFT calculations were performed. Polarization has shown to influence the binding energy of the CO molecule, associated with the change in reaction selectivity between the RWGS reaction and the methanation reaction. A strong correlation between the experimental and theoretical study were established, allowing the DFT model to be used in future studies.
- In Chapter 5, compares free-standing Ru nanoparticles with supported Ru nanoparticles on Co_3O_4 deposited on BZY. The use of the BZY solid electrolyte improved the selectivity towards the RWGS reaction due to the spontaneous migration of H^+ from BZY onto Ru. Applying the EPOC phenomenon improved the RWGS reaction under negative polarization (H supplied to Ru) and resulted in a p-EPOC behaviour. The use of Ru/Co_3O_4 showed a higher catalytic rate towards CO by acting as a dual catalyst. The use of Co_3O_4 allowed to highly dispersed nanoparticles and close the electrochemical circuit to allow the ionic species to promote the Ru nanoparticles.
- In Chapter 6, for the first time free-standing FeO_x nanowires were synthesized through the polyol method are deposited on YSZ and are electropromoted towards the RWGS reaction. The in-situ electrochemical supply of O^{2-}on the surface altered the oxidation state to Fe_3O_4 and FeO making it an active state towards the RWGS reaction. The inactive state of iron-carbide (confirmed STEM images and XPS spectra) is reversed under the direct supply of O^{2-} species. This demonstrates the importance of in-situ controlling the oxidation state of the catalyst to promote the RWGS reaction.
- In Chapter 7, free-standing FeO_x nanowires were doped with Ru clusters synthesized through a 2-step polyol method were deposited on YSZ and electrochemically promoted for the RWGS reaction. The synergetic effect between Ru and FeO_x was found to suppress the formation of Fe_xC by allowing FeO_x to remain in an active state ensuring catalytic stability and avoiding the transformation into inactive Fe_xC. This is appealing for industrial application since susceptibility to carbon formation can be avoided with minimal doping of Ru nanoparticles.

- In Chapter 8, FeO_x nanowires deposited on Co_3O_4 displayed an improved metal-support interaction under reaction conditions. The EPOC phenomenon is used as a tool to alter the state of the catalyst and remove it from its promoted state. Finally, FeO_x/CoO_x displayed one of the highest RWGS catalytic activity employing only non-noble metals among the previous studied catalysts for the EPOC effect and provided a way to store carbon in the form of CNTs. This catalyst brings the process to a more practical approach affiliated with the use of non-noble metals and high catalytic activity.

9.2 Recommendations

As in any scientific research, one discovery brings forth a new set of hypotheses and ideas. This thesis begins by showcasing the benefits of using the Ru-based noble metal nano-structured catalysts for the RWGS reaction employing the MSI and EPOC phenomena and ends by putting in place a new chapter in the EPOC community. Nearing the mid-point of the thesis the discovery of promoting non-noble metals has led to set of fundamental and exciting possibilities for electrocatalytic reactions in the gas-phase. While this discovery is very exciting, it is only the beginning of possible application and a greater understanding of the materials and mechanism is required. Therefore, here are some recommendations for future researchers in the academic and industrial community:

- Having made progress in the advancement in the usage of non-noble metals specifically Fe as a doping agent or mono-metallic use, I recommend that future project continue with Fe as the main component with the incorporation of additional non-noble metals like Co, copper (Cu), and nickel (Ni).
- Future researchers should explore the EPOC effect with additional DFT studies using the model provided from Chapter 4. The model can apply to various types of metal slabs ranging from metallic to partially and fully oxidized forms. This model is not specific to just CO_2 reactions, it can be applied to all reactions covered by the EPOC effect and electrochemical polarization.
- To provide experimental conclusions to the DFT study in Chapter 4, I recommend future studies focus on the in-situ characterization the effect of potential has on the surface of the catalyst. This can be done through Polarization Modulation Infrared Reflection Absorption Spectroscopy (PMIRRAS) to analyze the changes in binding energy of surface specie. This

will provide experimental evidence to support the findings of the DFT calculations and additional support the EPOC theory that polarization on the catalytic surfaces causes a change in work function and binding energy for catalytic reaction.

- Focusing on improving the RWGS reaction rate, I recommend further studies to evaluate the effect of the other solid electrolytes containing different type of ionic species, specifically H-ion conducting supports like BZY and doped-versions of it. Additionally, I suggest to explore the effect of a rough surface, which can provide a greater surface area for nanoparticles to be dispersed and increase the contact of the three-phase boundary between the catalyst and solid electrolyte to promote the reaction.
- Incorporate promoting species like Na during the synthesis to promote the reaction during the reaction. Employ NaOH in the polyol method instead of TMAOH to increase the CO_2 conversion. This is focused more for practical large-scale application as opposed to studying the properties of the metal itself.
- Knowing the RWGS reaction is the first step in the synthesis of hydrocarbons through the FT synthesis; I recommend future studies focus on the development of a reactor and catalytic system that can directly reduce and hydrogenate CO_2 into hydrocarbon, instead of 2-step process (*i.e.* RWGS and then FT). This will allow to combine two steps into one and reduce the need for separating the gases from the feed. Additionally, the EPOC effect can be employed to tailor the selectivity of one end-product over the other.
- Study the use of a solid electrolyte of different shapes that can provide a more practical application. As opposed to using a three-electrode cell. A reactor setup where the gold mesh (current collector) on the working electrode is removed and the connection to the catalyst-working electrode is bypassed completely. Thus, following a cylindrical cell, the catalyst is coated on the inner surface while the electrodes on painted on the outside of the ring. This will drastically lower the sensitivity and cost of the electrochemical cell.
- The formation of the carbon nanotubes (CNTs) mentioned in Chapter 8 (Figure 8-1 (c)) can be further explored to provide insight on the contributing factors on its formation like the CO_2:H_2 ratios, temperature, and effect of polarization. The formation of CNTs have shown to be possible in a recent EPOC study for the decomposition of CH_3OH. Thus, understanding how CNTs are formed with CO_2 under polarization can result in a way to store carbon and convert CO_2 into CO and other various products. Once the mechanism

and conditions to form CNTs is established, focus can change to methods in separating the CNTs from the catalyst.

Scholarly Contributions

Publications

Panaritis, C., Zgheib, J., Couillard, M. & Baranova, E.A. (2020) The role of Ru clusters in Fe carbide suppression for the reverse water gas shift reaction over electropromoted Ru/FeO_x catalysts. Journal of Electrochemistry Communications. (PhD Work)

Panaritis, C.*, Hajar, Y.*, Treps, L., Michel, C., Baranova, E.A., & Steinmann, S. (2020) Demystifying the Atomistic Origin of the Electric Field Effect on Methane Oxidation. Journal of Phyical Chemistry Letters.11: 6976-6981. (PhD Work)

Zagoraios, D.*, **Panaritis, C.*,** Krassakopoulou, A., Baranova, E.A., Katsaounis, A., & Vayenas., C. (2020) Electrochemical promotion of Ru nanoparticles deposited on a proton conductor electrolyte during CO_2 hydrogenation. Journal of Applied Catalysis B: Environmental. 276: 119148. (PhD Work)

Panaritis, C., Michel, C., Couillard, M., Baranova, E.A., & Steinmann, S. (2020) Elucidating the role of electrochemical polarization on the selectivity of the CO_2 hydrogenation reaction over Ru. Journal of Electrochemica Acta. 350: 136405. (PhD Work)

Panaritis, C., Zgheib, J., Ebrahim SAH., Couillard, M., & Baranova, E.A. (2020) Electrochemical in-situ activation of Fe-oxide nanowires for the reverse water gas shift reaction. Journal of Applied Catalysis B: Environmental. 269: 118826. (PhD Work)

Panaritis, C., Edake, M., Couillard, M., Einakchi, R. & Baranova, E. A. (2018) Insight towards the role of ceria-based supports for reverse water gas shift reaction over RuFe nanoparticles. Journal of CO_2 Utilization. 26: 350–358. (MASc Work)

In preparation:

Panaritis, C., Yang, S., Couillard M., & Baranova, E.A., (2020) Electrochemical Investigation of the Metal-Support Interaction in FeO_x/CoO_x for the Reverse Water Gas Shift Reaction. To be submitted.

Conferences and Poster Presentations

Panaritis, C.*, Couillard, M., & Baranova E.A. (2020). Electrochemically Enhancing Nanostructured Fe-Oxide/Co_3O_4 for the Reverse Water Gas Shift Reaction. ECS Meeting and Exhibit, May 10-15, 2020, Montreal, Canada. Meeting, Canadian and oral presentation. (PhD Work)

Panaritis, C.*, Zgheib, J., Ebrahim SAH., Couillard, M., & Baranova, E.A. (2020). Electrochemical Enhancement of Fe-Oxide Nanowires for the Reverse Water Gas Shift Reaction. University of Ottawa Poster Competition. Poster Presentation. (PhD Work)

Panaritis, C.*, Silver, J., Couillar, M., & Baranova E.A. (2019). Tuning the Activation of CO_2 Using Fe-Oxide Catalysts Through an Electrochemical Approach. CCEC Conference, October 20-23, 2019, Halifax, Canada. Canadian Chemical Engineering Conference. Conference, Canadian and oral presenation. (PhD Work)

Panaritis, C.*, Zgheib, Z., Ebrahim, S.A., & Baranova E.A. (2019) Electrochemical Promotion of Fe-Nanostructured Catalysts for the Conversion of CO_2 through the Reverse Water Gas Shift Reaction. CCCE Conference, June 3 - 7, 2019, Quebec City, Canada. Canadian Chemistry Conference and Exhibition. Conference, Canadian and oral presentation. (PhD Work)

Panaritis, C.*, Baranova E.A., Michel, C., & Steinmann, S. (2018) Electrochemical Promotion of Catalysis for CO_2 Hydrogenation on Ru-Based Catalyst Using Ionically Conducting Ceramics. AiMES 2018 Meeting, September 30 - October 4, 2018, Cancun Mexico. The Electrochemical Society. 48: 1685. Conference, international and oral presentation. (PhD Work)